University of Liège, Belgium
Aerospace and Mechanical Engineering Department

Numerical Modeling and Experimental Identification of Mistuned Multi-Stage Bladed Assemblies

PhD Thesis Dissertation submitted in partial fulfilment of the requirements for the degree of Doctor in Engineering Sciences

by

Florence Nyssen

March 2016

Members of the Examination Committee

Pr. Ludovic Noëls (President of committee)
Université de Liège

Pr. Jean-Claude Golinval (Supervisor)
Université de Liège

Pr. Gaëtan Kerschen
Université de Liège

Pr. Greg Dimitriadis
Université de Liège

Pr. Fabrice Thouverez
Ecole Centrale de Lyon, France

Pr. Alain Batailly
Ecole Polytechnique de Montréal, Canada

Dr. Scott Cogan
Université de Franche-Comté, France

Dr. Jean de Cazenove
SAFRAN Aero Boosters

Abstract

In gas turbines engines, the axial flow compressors are made of a succession of rotating disks that carry blades. Although the blades are designed to be identical, small variations appear between the blades, known as mistuning, due to manufacturing tolerances, in-service wear... Mistuning leads to important changes in the dynamical properties of the structures with respect to the tuned case, such as localization of the vibration energy in a few blades only and amplification of the forced response.

In the field of turbomachinery, the optimization of the mass is a sensitive design criterion. To this purpose and also to improve aerodynamic performances, aircraft engine manufacturers tend to design one-piece bladed disks. These one-piece technologies bring obvious advantages in terms of performance, cost and mass reduction but are challenging for the mechanical design because the effects of mistuning are exacerbated due to the low damping level of the structure, the higher disk flexibility, and to the blade/disk coupling.

The thesis focuses on multi-stage systems of mistuned bladed disks. Two aspects are investigated: experimental identification of mistuning in multi-stage structures, and numerical analysis and developments to reduce computational times for multi-stage systems of bladed disks.

An experimental validation and extension of the component mode mistuning (CMM) identification method is proposed. A testing procedure is developed, using base excitation and laser measurements on each blade. The experimental tests are conducted on mock-up mono-stage and two-stage academic bladed structures. Validation of the mistuning identification is performed by adding small masses to the structure. Both stiffness and mass modifications are successfully retrieved. The geometry of the structure is also accurately acquired by an optical measurement system. The identified mistuning is compared with the geometrical one. The observed differences are shown to be due to non-uniformities in the boundary conditions that disturb the first measured mode shapes.

Multi-stage analyses for industrial structures require high computational times and resources. Numerical analyses are performed to reduce computational times for the statistical predictions of the forced response amplification. Nonparametric modeling of uncertainties is used to handle the case of multi-stage structures, and the predicted amplification factor is compared with the one obtained by the well-established CMM parametric approach. A combination of both methods is also proposed to obtain accurate results with reduced computational resources. Then, a characterization of the interstage coupling is performed. The differences between the mono-stage and multi-stage predictions for the amplification factor are found to be related to the energy localized in the drum. Analytical developments conducted on a two-stage lumped mass model are used to propose a coupling criterion based on equivalent parameters. Finally, the influence of the aerodynamic coupling is also briefly studied for different drum stiffnesses.

Acknowledgements

First, I wanted to thank my advisor Professor Jean-Claude Golinval, who conscientiously follows the evolution of my research works and advices me during my thesis.

Many thanks to the Professor Bogdan Epureanu (University of Michigan, MI,USA) and the Professor Robert Kielb (Duke University, NC, USA) who kindly welcome me in their respective Universities. They both help me during my thesis with their expert and valuable advices.

I also wanted to acknowledge the members of my thesis committee, Professors Ludovic Noëls, Gaëtan Kerschen and Greg Dimitriadis, for their relevant remarks during the committee meetings. The Professor Maarten Arnst also follows me carefully during my thesis, and is gratefully thanked. The external members of the examination committee, the Professors Fabrice Thouverez and Alain Batailly, Dr. Scott Cogan and Dr. Jean de Cazenove are also acknowledged for accepting to participate to the examination committee.

I gratefully thank the Belgian National Fund for Scientific Research (F.R.S.-FNRS) for its financial support through the Aspirant FNRS grant. I also acknowledge the University of Liège for the logistical support and the grants allowing me to take part in several conferences. The Zonta International foundation and the ASME committees are also thanked for their supporting grants.

I acknowledge the company Techspace Aero (SAFRAN group), and more particularly Régis Viguié who helps me to build the thesis application form for the FNRS grant and Jérôme Nadaud for its technical support during my thesis. The V2i S.A. company is also acknowledged for its support.

I also express my gratitude to the A&M MDF (Méthode de fabrication) laboratory from the University of Liège for the manufacturing of the two academic structures used in the thesis for the experimental tests.

Finally, I would like to thank my colleagues, my friends and my family for their support.

Contents

1 Introduction **1**
- 1.1 General context . . . 1
- 1.2 Objectives of the thesis . . . 2
- 1.3 Outline . . . 2

2 Dynamics of bladed assemblies **5**
- 2.1 Introduction . . . 5
- 2.2 Dynamical properties of bladed disks . . . 6
- 2.3 Modal analysis of a cyclic symmetric structure . . . 8
- 2.4 Main dynamic analysis tools . . . 12
  - 2.4.1 Zig-Zag diagram . . . 12
  - 2.4.2 SAFE/ZZENF diagram and Campbell diagram . . . 12
- 2.5 Modeling of mono-stage bladed structures . . . 19
  - 2.5.1 Cyclic symmetry formulation . . . 19
  - 2.5.2 Equation of motion . . . 21
  - 2.5.3 Cyclic boundary conditions . . . 21
- 2.6 Mistuning in mono-stage bladed disks . . . 22
  - 2.6.1 Frequency splitting . . . 22
  - 2.6.2 Mode localization . . . 22
  - 2.6.3 Maximum amplitude increase . . . 23
  - 2.6.4 Aerodynamic stability . . . 25
- 2.7 Reduced order model for mono-stage bladed disks . . . 25
  - 2.7.1 Component Mode Synthesis (CMS) . . . 25
  - 2.7.2 Component Mode Based (CMB) method . . . 26
  - 2.7.3 Secondary Modal Analysis Reduction Technique (SMART) . . . 27
  - 2.7.4 Subset of Nominal Modes (SNM) approach . . . 27
  - 2.7.5 Fundamental Mistuning Model (FMM) . . . 28
  - 2.7.6 Asymptotic Mistuning Model (AMM) . . . 29
  - 2.7.7 Petrov's method . . . 29
  - 2.7.8 Component Mode Mistuning (CMM) method . . . 30
  - 2.7.9 Integral Mode Mistuning (IMM) . . . 30
  - 2.7.10 Nodal Energy Weighted Transformation (NEWT) . . . 31
  - 2.7.11 Static Mode Compensation (SMC) method . . . 32
  - 2.7.12 Nonparametric modeling . . . 32
  - 2.7.13 Mbaye's method . . . 33
  - 2.7.14 Modified Modal Domain Analysis (MMDA) . . . 34
- 2.8 Mistuning identification method for mono-stage bladed disks . . . 34
  - 2.8.1 CMB identification (CMB ID) method . . . 35

2.8.2 FMM identification (FMM ID) method . . . 35
2.8.3 CMM identification (CMM ID) method . . . 36
2.8.4 Best-achievable-eigenvectors based method . . . 37
2.8.5 Nonparametric identification method . . . 38
2.8.6 MMDA identification (MMDA ID) method . . . 38
2.9 Dynamics of multi-stage bladed structures . . . 39
2.10 Modeling of multi-stage bladed structures . . . 40
2.10.1 Equations in the physical basis . . . 41
2.10.2 Cyclic symmetry formulation . . . 41
2.10.3 Equations in the cyclic basis . . . 42
2.10.4 Restriction on the compatibility of the harmonics . . . 42
2.11 Mistuning in multi-stage bladed disks . . . 44
2.12 Reduced order model for multi-stage bladed disks . . . 44
2.12.1 Extended SMART method . . . 45
2.12.2 Song's method . . . 45
2.12.3 Laxalde's method . . . 46
2.12.4 Extended MMDA method . . . 47
2.13 Mistuning identification method for multi-stage bladed disks . . . 47
2.14 Conclusion . . . 48

3 Mistuning identification for the mono-stage structure 51
3.1 Introduction . . . 51
3.2 Component Mode Mistuning (CMM) method . . . 51
3.2.1 Reduced-order model . . . 52
3.2.2 Inverse reduced-order model . . . 55
3.2.3 Identification using the experimental data . . . 56
3.3 Experimental testing procedure . . . 56
3.4 Experimental vibration measurements . . . 57
3.4.1 Presentation of the tested structure . . . 57
3.4.2 Verification of CMM assumptions . . . 59
3.4.3 Measurements using a laser vibrometer . . . 59
3.5 Validation of the identified mistuning . . . 64
3.6 Conclusion . . . 68

4 Experimental mistuning identification in a multi-stage drum 69
4.1 Introduction . . . 69
4.2 Component mode mistuning (CMM) method for multi-stage structure . . . 70
4.2.1 Reduced-order models (ROMs) . . . 70
4.2.2 Inverse reduced-order models (IROMs) . . . 74
4.2.3 Identification using experimental data . . . 77
4.3 Example of an academic multi-stage drum . . . 78
4.4 Experimental stiffness mistuning identification . . . 80
4.5 Validation of the experimental mistuning identification . . . 83
4.5.1 Identification of the perturbed stiffness mistuning . . . 87
4.5.2 Validation of the identification . . . 87
4.5.3 Mass mistuning identification . . . 89
4.6 Sensitivity of the identification method . . . 89
4.7 Conclusion . . . 91

5 Geometric mistuning and model updating 93
5.1 Introduction 93
5.2 Test set-up for the optical measurement of the geometry 95
5.3 Geometry measurement 96
5.3.1 Mono-stage academic structure 96
5.3.2 Multi-stage academic structure 98
5.4 Construction of the finite element model 100
5.4.1 Mono-stage academic structure 100
5.4.2 Multi-stage academic structure 105
5.5 Comparison of the frequency and geometric mistuning 106
5.5.1 Mono-stage academic structure 107
5.5.2 Multi-stage academic structure 107
5.6 Update of the clamping conditions 108
5.6.1 Mono-stage academic structure 110
5.6.2 Multi-stage academic structure 112
5.7 Conclusion 116

6 Parametric and nonparametric modeling of mistuned multi-stage bladed structures 117
6.1 Introduction 117
6.2 Nonparametric modeling of mistuned multi-stage structure 118
6.2.1 Mean (tuned) reduced model 118
6.2.2 Nonparametric model of random uncertainties for blade mistuning . 123
6.2.3 Forced response computation 124
6.3 Application on a two-stage academic structure 124
6.4 Proposed approach 128
6.5 Comparison with the CMM parametric approach 131
6.6 Influence of the number of retained harmonics 134
6.7 Conclusion 135

7 Influence of multi-stage coupling 137
7.1 Introduction 137
7.2 Analysis of the influence of the interstage structure on a lumped mass model 138
7.3 Application on an academic structure 145
7.3.1 Comparison of the dynamical properties between the mono-stage and multi-stage academic structures 146
7.3.2 Influence of the drum stiffness and coupling criterion in the academic structure 155
7.4 Difference on the mono- and multi-stage amplification factor with the drum stiffness 158
7.5 Conclusion 161

8 Aerodynamic coupling 163
8.1 Introduction 163
8.2 Single blade flutter 164
8.3 Multi-airfoils (cascade) flutter 167
8.4 Aerodynamic model 169
8.5 Studied structure 172
8.6 Structural and aerodynamic coupling 173

8.7 Influence of errors in the aerodynamic coefficients 178
8.8 Conclusion 179

9 Conclusions and perspectives 181
9.1 Contributions of the thesis 181
  9.1.1 Experimental identification of mistuning in multi-stage structure . . 181
  9.1.2 Numerical analyses and developments 182
9.2 Perspectives 183

A Design and presentation of the studied structures 185
A.1 Introduction 185
A.2 Design of the academic bladed structures 185
A.3 Presentation of the mono-stage academic structure 187
  A.3.1 Construction of the finite element model 187
  A.3.2 SAFE diagram 188
  A.3.3 Deformation energy for each mode shapes 189
  A.3.4 Clamped blade properties 191
A.4 Presentation of the multi-stage academic structure 193
  A.4.1 Construction of the finite element model 193
  A.4.2 SAFE diagram 194
  A.4.3 Deformation energy for each mode shape 196
  A.4.4 Clamped blade properties 201

B Drawing of the academic structures 203

C Comparison of finite element models with different refining 207
C.1 Mono-stage academic structure 207
C.2 Multi-stage academic structure 209

D Influence of the microaccelerometer on the measurements 211
D.1 Measurements using microaccelerometers 211
  D.1.1 Test set-up 211
  D.1.2 Stabilization diagram 212
  D.1.3 Frequencies and mode shapes 214
D.2 Comparison between the measurement with the accelerometers and with the laser 218

E Construction of the finite element model based on geometry measurements 223

Bibliography 229

List of Publications 243

Nomenclature

Acronym

1B	First bending mode
1BT	First bending torsion mode
1T	First torsion mode
2B	Second bending mode
2BT	Second bending torsion mode
2S1	Stripe mode 1
2S2	Stripe mode 2
2T	Second torsion mode
3B	Third bending mode
3BT	Third bending torsion mode
BAE	Best achievable eigenvectors
CAD	Computer aided design
CFD	Computational fluid dynamic
CMB	Component-mode-based
CMM	Component mode mistuning
CMS	Component mode synthesis
CNC	Computer numerical control
DOF	Degree of freedom
EO	Engine order
FE	Finite element
FMM	Fundamental model of mistuning
FRF	Frequency response function

HCF	High cycle fatigue
ID	Identification
IROM	Inverse reduced order model
LED	Light emitting diode
MAC	Modal assurance criterion
MMDA	Modified modal domain analysis
MSF	Modal scale factor
NC	Nodal circle
ND	Nodal diameter
PDF	Probability density function
Plane B	Plane bending mode
POD	Proper orthogonal decomposition
ROM	Reduced order model
RPM	Revolution per minute
SAFE	Singh's Advanced Frequency Evaluation
SE	Superelement
SMART	Secondary modal analysis reduction technique
SNM	Subset of nominal modes
ZZENF	Zig-Zag shaped Excitation line in the Nodal diameter versus Frequency diagram

Symbols

α	Pitch DOF
$\bar{S}_k^R$	Damping coefficient of blade k
$\mathbf{\Lambda}^{CB}$	Generalized stiffness matrix of the cantilevered blade
$\mathbf{\Lambda}_0$	Generalized stiffness matrix
$\mathbf{\Lambda}_s^{CB}$	Generalized stiffness matrix of the cantilevered blade of stage s
$\mathbf{\Lambda}_{ns}$	Modal stiffnesses of the retained internal vibration modes of each blade n of stage s
$\mathbf{\Lambda}'_{ns}$	Perturbed $\mathbf{\Lambda}_{(n,s)}$ matrix
$\mathbf{\Phi}$	Tuned mode shapes matrix

$\mathbf{\Phi}^{CB}$	Cantilevered blade modes for the nominal blade
$\mathbf{\Phi}_k$	k^{th} eigenvector of the system
$\mathbf{\Phi}_r^{CB}$	r^{th} cantilevered blade modes
$\mathbf{\Phi}_s^{CB}$	Cantilevered blade modes for the nominal blade of stage s
$\mathbf{\Phi}_{exp}$	Tuned displacement of the measured DOF
$\mathbf{\Phi}_{ns}$	Tuned mode-shapes restricted to the DOF of blade n of stage s
$\mathbf{\Phi}_n$	Tuned mode-shapes restricted to the DOF of blade n
$\mathbf{\Phi}_n^M$	Mistuned mode-shapes of the DOF of blade n
$\mathbf{\Phi}_{s,r}^{CB}$	r^{th} cantilevered blade modes of stage s
$\mathbf{\Psi}$	Mode matrix
$\mathbf{\Psi}^n$	Mode matrix of blade n
$\mathbf{\Psi}^{ns}$	Mode matrix of blade n of stage s
Δf_a	Aerodynamic frequency spread
Δf_s	Structural frequency spread
δ	Normal distribution law perturbation
Δ_n	Inter-blade phase angle
δ_n^k	Perturbation in the clamping stiffness of sector n
$\delta_{nonparam}^s$	Dispersion parameter of stage s for the nonparametric approach
δ_{param}^s	Dispersion parameter of stage s for the parametric approach
Γ	Gamma distribution law
γ	Damping coefficient
$\hat{\mathbf{A}}$	Mistuning matrix
$\hat{\mathbf{f}}_{js}$	Cyclic force vector associated to harmonic j for stage s
$\hat{\mathbf{f}}_j$	Cyclic force vector associated to harmonic j
$\hat{\mathbf{x}}$	Displacement vector in cyclic components
$\hat{\mathbf{x}}_j$	Harmonic j of the displacement vector in cyclic components
$\hat{\mathbf{x}}_{js}$	Harmonic j of the displacement vector of stage s in cyclic components
$\hat{\mathbf{x}}_s$	Displacement vector of stage s in cyclic components
$\hat{S}$	Stability parameter

λ	Eigenvalues of the system
λ_k	k^{th} eigenvalue of the system
$\lambda^{\delta}_{n,r}$	Eigenvalue deviation of the r^{th} cantilevered blade mode of blade n
$\lambda^{\delta}_{ns,r}$	Eigenvalue deviation of the r^{th} cantilevered blade mode of blade n of stage s
$\mathbf{A}$	Mass, stiffness or damping matrix
$\mathbf{A}^d$	Mass, stiffness or damping matrix restricted to the disk DOF
$\mathbf{A}^m$	Aerodynamic matrix
$\mathbf{A}^d_{red}$	Reduced mass, stiffness or damping matrix restricted to the disk DOF
$\mathbf{A}^n_{red}$	Reduced mass, stiffness or damping matrix restricted to the DOF of blade n
$\mathbf{A}^{n,s'}_{red}$	Perturbed reduced mass, stiffness or damping matrix for blade n of stage s
$\mathbf{A}^{ns}_{red}$	Reduced mass, stiffness or damping matrix restricted to the DOF of blade n of stage s
$\mathbf{C}$	Damping matrix
$\mathbf{C}_{js}$	Cyclic damping matrix associated to harmonic j for stage s
$\mathbf{C}_j$	Cyclic damping matrix associated to harmonic j
$\mathbf{C}_s$	Damping matrix of stage s
$\mathbf{F}$	Modal participation factor of the load $\mathbf{f}$
$\mathbf{f}$	Force vector
$\mathbf{F}^m$	Aerodynamic modal force due to blade motion
$\mathbf{F}^w$	External excitation modal force
$\mathbf{f}_s$	Force vector of stage s
$\mathbf{G}^{ns}_A$	Random positive-definite symmetric matrix for the mass, stiffness or damping matrix of blade n of stage s
$\mathbf{I}$	Identity matrix
$\mathbf{j}_s$	Set of cyclic harmonics on stage s
$\mathbf{K}$	Stiffness matrix
$\mathbf{K}^{\delta}$	Perturbation in the stiffness matrix
$\mathbf{K}^{CB}$	Cantilevered blade stiffness matrix
$\mathbf{K}_0$	Tuned stiffness matrix
$\mathbf{K}_r$	Reduced stiffness matrix

$\mathbf{K}_r'$	Mistuned reduced stiffness matrix
$\mathbf{K}_r^0$	Contribution of the disk and static modes in the reduced stiffness matrix
$\mathbf{K}_r^{s\prime}$	Mistuned reduced stiffness matrix of stage s
$\mathbf{K}_r^s$	Reduced stiffness matrix of stage s
$\mathbf{K}_{js}$	Cyclic stiffness matrix associated to harmonic j for stage s
$\mathbf{K}_j$	Cyclic stiffness matrix associated to harmonic j
$\mathbf{K}_{ns}$	Stiffness matrix restricted to the DOF of blade n of stage s
$\mathbf{K}_{ns}^\delta$	Perturbed stiffness matrix restricted to the DOF of blade n of stage s
$\mathbf{K}_n$	Stiffness matrix restricted to the DOF of blade n
$\mathbf{K}_n^\delta$	Perturbed stiffness matrix restricted to the DOF of blade n
${\mathbf{K}_{red}^s}'$	Perturbed reduced stiffness matrix for stage s
$\mathbf{K}_{red}^s$	Reduced stiffness matrix for stage s
$\mathbf{K}_s$	Stiffness matrix of stage s
$\mathbf{K}_s^{CB}$	Cantilevered blade stiffness matrix of stage s
$\mathbf{L}_A^{ns}$	Upper real matrix of the Cholesky decomposition of the mass, stiffness or damping matrix of blade n of stage s
$\mathbf{L}_G^{ns}$	Upper triangular random perturbation matrix for the mass, stiffness or damping matrix of blade n of stage s
$\mathbf{M}$	Mass matrix
$\mathbf{M}^\delta$	Perturbation in the mass matrix
$\mathbf{M}_0$	Tuned Mass matrix
$\mathbf{M}_{js}$	Cyclic mass matrix associated to harmonic j for stage s
$\mathbf{M}_j$	Cyclic mass matrix associated to harmonic j
$\mathbf{M}_{ns}$	Mass matrix restricted to the DOF of blade n of stage s
$\mathbf{M}_{ns}^\delta$	Perturbed mass matrix restricted to the DOF of blade n of stage s
$\mathbf{M}_s$	Mass matrix of stage s
$\mathbf{p}$	Modal coordinates
$\mathbf{p}^I$	Imaginary part of $\mathbf{p}$
$\mathbf{p}^R$	Real part of $\mathbf{p}$
$\mathbf{Q}_{ns}$	Modal participation factors of blade n of stage s

$\mathbf{Q}_n$	Modal participation factor of blade n
$\mathbf{R}^n$	Rotation matrix of blade n
$\mathbf{R}^{ns}$	Rotation matrix of blade n of stage s
$\mathbf{T}_k$	Travelling wave with k nodal diameters
$\mathbf{w}_j$	Fourier vector associated to harmonic j
$\mathbf{w}_{js}$	Fourier vector of stage s associated to harmonic j
$\mathbf{x}$	Displacement vector
$\mathbf{x}_n$	Displacement vector of sector n
$\mathbf{x}_s^\Gamma$	Restriction of the displacement vector of stage s to the interstage DOFs
$\mathbf{x}_{exp}$	Physical displacement at the measured DOF
$\mathbf{x}_{ns}$	Displacement vector of sector n of stage s
$\mathbf{x}_n^a$	Response of blade n for the aerodynamic coupling only case
$\mathbf{x}_n^b$	Response of blade n when structural and aerodynamic coupling are considered
$\mathbf{x}_n^s$	Response of blade n for the structural coupling only case
$\mathbf{x}_s$	Displacement vector of stage s
$\mathcal{E}$	Expected value
$\mathcal{F}$	Fourier matrix
$\mathcal{F}_{\mathbf{j}s}$	Fourier matrix of stage s restricted toa given set of harmonics $\mathbf{j}$
$\mathcal{F}_s$	Fourier matrix of stage s
$\mu_{ns,r}^\delta$	Perturbation in the generalized mass of the r^{th} mode of blade n of stage s
Ω	Rotational speed
ω	Frequency
ω_n	n^{th} natural frequency
ϕ_n	Angular position of blade n
$\Re$	Real part
ρ	Density
Σ	Blade/disk interface DOF
Σ_n	Blade/disk interface DOF for blade n
Σ_s	Blade/disk interface DOF of stage s

Σ_{ns}	Blade/disk interface DOF for blade n
$\tilde{m}^K$	Rank of the matrix $\mathbf{K}^s_{red}$
Ξ	Damping coefficient
ζ	Damping ratio
a_r	Aerodynamic coefficients
AF	Amplification factor
AF_{ID}	Amplification factor obtained using the identified mistuning
$AF^{\star}_{ID}$	Amplification factor obtained using a perturbed mistuning pattern
C	Relative frequency spread between structural and aerodynamic coupling
c	Chord
E	Young's modulus
E^a	Global error for the aerodynamic coupling only (a) case
E^s	Global error for the structural coupling only (s) case
E^s_b	Energy ratio localized in the blade for stage s
E^s_d	Energy ratio localized in the disk for stage s
e^a_n	Error on the FRF of blade n with only the aerodynamic coupling term
e^s_n	Error on the FRF of blade n with only the structural coupling term
E_{AF}	Error on the amplification factor
E_{ID}	Error on the identified mistuning
f_{exp}	Measured frequencies
f'_{exp}	Perturbed measured frequencies
f^a_{max}	Maximum frequencies when only the aerodynamic coupling is considered
f^s_{max}	Maximum frequencies when only the structural coupling is considered
f^a_{mean}	Mean frequencies when only the aerodynamic coupling is considered
f^s_{mean}	Mean frequencies when only the structural coupling is considered
f^a_{min}	Minimum frequencies when only the aerodynamic coupling is considered
f^s_{min}	Minimum frequencies when only the structural coupling is considered
h	Plunge DOF
I_α	Mass moment of inertia of the blade

K	Maximum number of nodal diameters
k^{ji}	Stiffness between blade$i$ of stage 1 and blade j of stage 2
k_0	Initial clamping stiffness
K_α	Pitch spring stiffness
k_b^s	Equivalent stiffness between the blade and the disk of the reference sector of stage s
k_c	Coupling stiffness
k_d^s	Equivalent stiffness between adjacent disk sectors of stage s
K_h	Plunge spring stiffness
k_n	Mistuned clamping stiffness of sector n
k_{cl}^s	Clamping stiffness of the reference sector of stage s
$l\,(t)$	Lift
$m\,(t)$	Aerodynamic moment
m	Number of retained modes
m_b^s	Equivalent mass of the blade of the reference sector of stage s
m_d^s	Equivalent mass of the disk of the reference sector of stage s
m_{ID}	Identified mistuning
$m_{ID}^\star$	Mistuning identified with perturbed input data
m_{ID}^{Acc}	Mistuning identified using a microaccelerometer
m_{ID}^L	Mistuning identified using a laser vibrometer
N	Number of blades in a mono-stage structure
n	Blade index
N^{CB}	Number of retained cantilevered blade modes
N_A	Size of $\mathbf{A}_{red}^{ns}$
N_s	Number of blades of stage s in a multi-stage structure
$ndofb_{ns}$	Total number of DOF of blade n of stage s
$ndof$	Total number of DOF
$p\,(t)$	Force due to the added mass effect
$r\,(t)$	Moment due to the added mass effect

R	Set of retained cantilevered blade modes
S	Number of stages
s	Stage index
U	Air speed
W_k	Influence coefficient of blade k
w_n	Traveling wave seen by blade n
w_r	Complex modal force coefficient
$W^s_{nonparam}$	Dispersion indicator of stage s for the nonparametric approach
W^s_{param}	Dispersion indicator of stage s for the parametric approach
x^{ns}_b	Displacement of blade n of stage s
x_c	Position of the center of mass
x^{ns}_d	Displacement of disk sector n of stage s
x_f	Position of the fluxural axis

Chapter 1

Introduction

1.1 General context

In gas turbine engines, the axial flow compressor consists of a multi-stage unit composed of rotating disks that carry blades (Figure 1.1). Although the blades are designed to be identical, manufacturing variations and in-service wear cause the blades to be slightly different, which confines most of the vibration energy to only a few blades. This phenomenon is known as *mistuning*. In a forced excitation configuration, this implies the occurrence of much higher vibrating levels that can significantly impact the High Cycle Fatigue behavior of the structure. The mistuning phenomenon appears in rotationally periodic structures, which can be found in many applications: e.g., centrifugal compressors, gear wheels, turbomachinery bladings, etc.

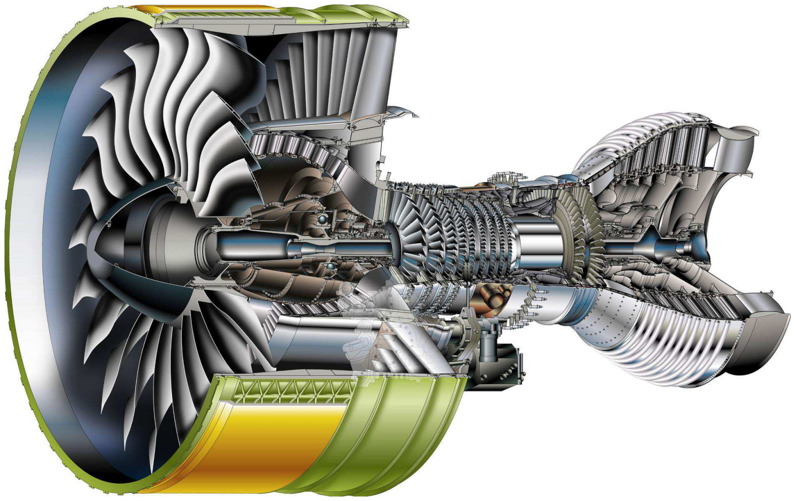

Figure 1.1: Aircraft engine (GP7200) [1].

In the field of turbomachinery, the optimization of the mass is a sensitive design criterion. To this purpose and also to improve aerodynamic performances, aircraft engine manufacturers tend to design one-piece bladed disks (called *blisks*). Blisks may be integrally cast, machined from a solid piece of material, or made by welding individual blades to the rotor disk. These one-piece technologies bring obvious advantages in terms of performance, cost and mass reduction but are challenging for the mechanical design. In the case of blisks, the effects of mistuning are exacerbated due to the low damping level of the structure, the higher drum flexibility, and to the blade/drum coupling.

So far, most of the existing studies on mistuning analysis have focused on single stage structures. However, the development of one-piece multi-stage structures has significantly increased the influence of the interstage coupling that cannot be neglected anymore in the numerical models. As a consequence, it appears that multi-stage structures may present higher amplification factor than those related to single stage configurations. Due to the poor literature on this matter, this feature requires additional analyses to be carried out, in particular on industrial configurations.

1.2 Objectives of the thesis

The existing theoretical developments enable the analysis of the dynamical response of multi-stage structures. However, they have to be validated through experimental investigations. Nowadays, experimental modal identification of cyclically periodic structures is still highly challenging due to the numerous sources of mistuning (geometrical tolerances, variations of the material properties, presence of nonlinearities, wear...). This renders the data processing and the analysis of the measurements very complex. The thesis aims at developing a testing procedure and to propose guidelines for improving the measurement quality in presence of mistuning for both single and multi-stage structures. These experimental tests are conducted on mock-ups mono-stage and multi-stage structures.

Although these theoretical developments permit to retrieve the dynamical behavior of the structure, the required computation time remains considerable and not possible to handle in practice. Such studies are not possible on industrial-type structures and are still limited to academic cases. Indeed, theoretically, a complete modal basis is necessary to characterize a mistuned mode. The higher the number of modes, the more accurate the results, but at the expense of a significant increase of the computational time and size of the structural matrices. In this context, the industry is still using mono-stage analysis. This thesis aims to quantify the error between mono-stage and multi-stage predictions, in order to establish a criterion guiding the industrial engineers and to determine in an efficient way the need or not of a complete multi-stage numerical analysis.

1.3 Outline

In Chapter 2, the dynamics of tuned bladed disks is explained, for both mono-stage and multi-stage structures. The influence of mistuning on the dynamic behavior of bladed structures is described. The existing reduced order modeling techniques and the corresponding mistuning identification methods are reviewed for mono-stage and multi-stage structures. The comparison of all methods enables to select the most appropriated one for the studies in the thesis.

In Chapter 3, an existing identification method is applied on the mono-stage academic structure. The aim is to establish a simple test procedure to identify mistuning in bladed structures. The identification method is validated by adding small masses on the structure.

In Chapter 4, the procedure for experimental mistuning identification is extended for multi-stage structure. An experimental modal analysis is performed on a two-stage monobloc academic bladed rotor. The frequency response function is measured using a base excitation with an electrodynamic shaker and one measurement point per blade of each stage is acquired. Numerical and experimental validations are presented. The method is then generalised to take into account both mass and stiffness mistuning. The sensibility of the proposed method to noise is also quantified.

In Chapter 5, an optical measurement is used to obtain the precise geometry of the both academic structures. A geometrical mistuning is associated to each blade. Since the structures are one-piece manufactured, the material properties can be assumed to be uniform, and there are no bounded connexions between the blades and the drum. Thus, the main source of mistuning for these two structures is the geometry variations due to the manufacturing process. The geometric mistuning is compared with the one experimentally identified for both mono-stage and multi-stage academic blisks in Chapters 3 and 4 respectively using vibration tests. Non-uniformities in the boundary conditions are analyzed in detail.

In Chapter 6, a nonparametric approach for modeling uncertainties in bladed structures is extended for multi-stage structure. This nonparametric approach takes into account errors due to uncertainties in the modal parameters but also errors due to uncertainties in the model. Both mono-stage and multi-stage predictions for the amplification of the forced response are evaluated and compared. Then, a comparison of the nonparametric results with the widely used parametric approaches is performed. A combination of the two methods is also proposed to reduce the computational times.

In Chapter 7, a characterization of the interstage coupling in multi-stage bladed structures is performed. More particularly, the effect of the drum flexibility on the eigenfrequencies and mode shapes is evaluated. The differences between the mono-stage and multi-stage results are quantified. In parallel, the strain energy located in the drum and in the blades is computed for different values of the drum stiffness. The aim is to establish a criterion based on equivalent parameters to determine, depending on the localization of the energy in the structure, when a multi-stage finite element analysis is necessary instead of only computing the different mono-stage models separately. Then, the frequency response function is computed for the mono-stage and multi-stage models, and the corresponding amplification factors. The resulting error on the amplification factor is also computed for different mistuning levels.

In Chapter 8, the influence of the aerodynamic coupling on the forced response is evaluated. Both structural and aerodynamic coupling terms are considered here. The influence on the predicted amplification factor when neglecting the structural or the aerodynamic coupling term is analyzed for different values of drum Young's modulus.

Chapter 2

Dynamics of bladed assemblies

In this Chapter, the dynamics of tuned bladed disks is described for mono-stage and multi-stage structures. The existing modeling methods are briefly explained. The influence of mistuning on the dynamic behavior of mono-stage and multi-stage structure is also recalled, and the existing mistuning identification methods are reviewed.

2.1 Introduction

In the ideal case, bladed disks are cyclically symmetric structures consisting in a group of identical sub-structures called sectors forming a ring. Figure 2.1 shows an example of a cyclically symmetric structure with its reference sector. The cyclic symmetry property can be exploited in the finite element models to reduce drastically the computational time and resources, in a linear framework, by considering one sector instead of the entire assembly.

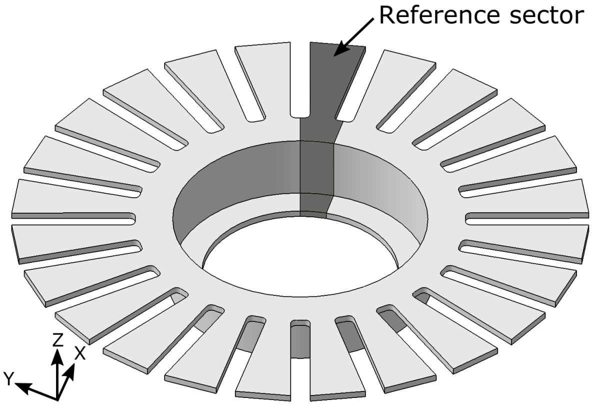

Figure 2.1: Cyclically symmetric structure and its reference sector.

In addition to the cyclic symmetry, a second assumption is usually made in the field of turbomachinery i.e., that the different stages are isolated and dynamically independent. This second assumption is made to allow the use of smaller and independent finite element models, one for each stage, instead of simultaneously solving the whole coupled problem with all stages together. This can be relaxed by using carefully chosen boundary conditions to represent constraints normally imposed by adjacent stages, but this approach may not accurately describe the disk/drum flexibility locally at the interstage boundaries. It may lead to an inconsistent representation of the interaction between families of disk- and blade-dominated modes which is a critical factor to determine the sensitivity of a design to mistuning in veering regions [2].

Even if each stage is designed to be cyclically symmetric, small random blade-to-blade variations appear in practice due to manufacturing tolerances, irregularities in the material properties, wear during use, etc. These small variations, known as mistuning, disturb dramatically the dynamic behavior of bladed disks [3]. The different reduced-order modeling techniques that have been developed to compute the dynamic behavior of mistuned bladed disks with reduced computational time [4–16] are reviewed in this Chapter. These reduced-order models (ROMs) enable to construct low-order models of bladed disks based on the global finite element model of the structures. Using ROMs enables to run a large number of simulations with random mistuning patterns in order to retrieve the statistical distribution of the amplification of the forced response amplitudes for given amounts of mistuning.

In parallel, identification methods have been developed to identify mistuning from the experimental frequency response of bladed structures [15, 17–19]. A usual assumption consists in proportional mistuning i.e., the variation of each blade is considered to be proportional to the stiffness of the tuned sector. First studies tested separately each individual blade to determine their deviation from the nominal design [10, 17]. However, additional mistuning is introduced when blades are assembled on the disk. Many bladed disks are now manufactured in one-piece, known as integrally bladed disks or blisks. Several methods have been developed to identify mistuning from measurements of the response of the entire bladed disk rather than on individual and isolated blades. Early works were based on lumped parameter models in order to identify the structural parameters of blades [20, 21]. More recently, identification methods based on ROMs have been developed [18, 19, 22–27]. These methods are recalled in this Chapter.

2.2 Dynamical properties of bladed disks

Cyclic symmetric structures have specific dynamical properties. Three types of vibration modes can be distinguished for the disk:

- Nodal diameters modes: the mode shape is sinusoidal in the circumferential direction and the vibration nodes form diametrical lines on the structure (Figure 2.2(a)).
- Nodal circles modes: the vibration nodes form circles on the structure (Figure 2.2(b)).
- Hybrid modes: combination of the previous two (Figure 2.2(c)).

A mode shape of a disk/drum is therefore characterized by specifying the number of nodal diameters (ND) and nodal circles (NC).

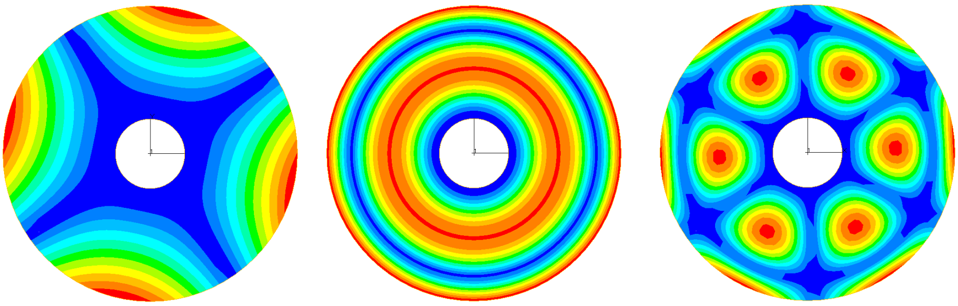

(a) 2ND (b) 1NC (c) 1NC-3ND

Figure 2.2: Mode with 2 nodal diameters - 2ND (a), Mode with 1 nodal circle - 1NC (b), Mode with 1 nodal circle and 3 nodal diameters - 1NC-3ND (c).

Regarding the blades modes, they are similar to those of beams and rectangular plates, clamped at their basis for rotors and clamped at both sides for stators.

A iB mode is a mode with i max deflection spots (1B mode in Figure 2.3(a) for a rotor blade and in Figure 2.4(a) for a stator blade, 2B mode in Figure 2.3(b) for a rotor blade and in Figure 2.4(b) for a stator blade). A iT mode is a mode with i layers of max deflection spots (1T mode in Figure 2.3(c) for a rotor blade and in Figure 2.4(c) for a stator blade, 2T mode in Figure 2.3(d) for a rotor blade and in Figure 2.4(d) for a stator blade). Stripe modes iSj are modes with i layers of max deflection spots and j horizontal lines of max deflection spots (2S1 mode in Figure 2.3(e) for a rotor blade and in Figure 2.4(e) for a stator blade, 2S2 mode in Figure 2.3(f) for a rotor blade and in Figure 2.4(f) for a stator blade). Plane bending modes are characterized by deformation in the plane of the blade (Figure 2.3(g) for a rotor blade and in Figure 2.4(g) for a stator blade).

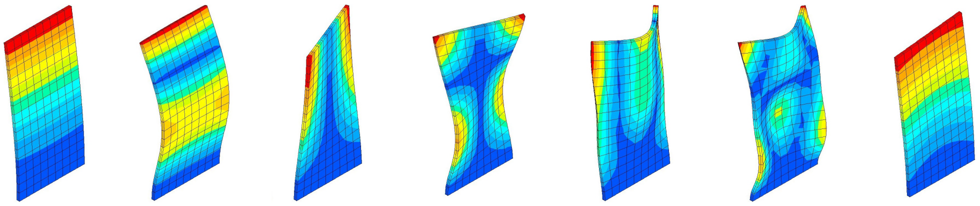

(a) 1B (b) 2B (c) 1T (d) 2T (e) 2S1 (f) 2S2 (g) Plane B

Figure 2.3: Blade modes for a rotor blade.

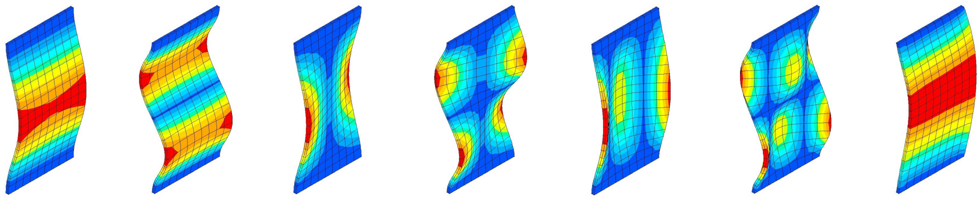

(a) 1B (b) 2B (c) 1T (d) 2T (e) 2S1 (f) 2S2 (g) Plane B

Figure 2.4: Blade modes for a stator blade.

2.3 Modal analysis of a cyclic symmetric structure

Consider a simplified system of a cyclic symmetric structure. Its modal characteristics can be studied using a discrete model with N identical masses and stiffnesses (Figure 2.5).

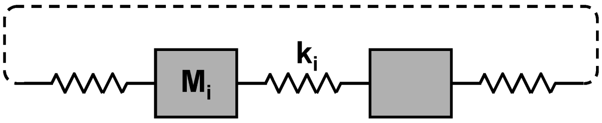

Figure 2.5: Discretisation of a cyclic symmetric structure.

The equation of motion is given by

$$\mathbf{M}\ddot{\mathbf{x}} + \mathbf{K}\mathbf{x} = \mathbf{0} \ , \tag{2.1}$$

where $\mathbf{M}$ is the mass matrix (diagonal, the elements contain the mass of the N sectors) and $\mathbf{K}$ is the stiffness matrix (cyclic symmetry). Because of the cyclic symmetry of the problem, the eigenvalues are double $\lambda_k = \lambda_{N-k}$ (these solutions are called "degenerate solutions"), except λ_0, which corresponds to a motion of the whole structure and where all sectors vibrate in phase, which is equivalent to a mode with 0 nodal diameters, and in the case of an even number of blades, $\lambda_{N/2}$ in which all sectors vibrate in phase opposition to each other, which is equivalent to a mode of $\frac{N}{2}$ diameters (these two solutions are called "non-degenerate solutions") [28].

At each eigenvalue λ_k is associated an eigenvector of the undamped system $\mathbf{\Phi}_k$. The orthogonal eigenvectors $\mathbf{\Phi}_k$ and $\mathbf{\Phi}_{N-k}$, associated with double eigenfrequencies λ_k et λ_{N-k}, appear as stationary orthogonal modes. They have the same number of nodal diameters [29] and are shifted by a quarter period. Thus, these orthogonal modes are generally referred to cosine and sine modes. These eigenvectors form a basis of linearly independent vectors. Therefore, any linear combination of two modes corresponding to the same eigenfrequency is also a mode of vibration. By linear combination of the eigenvectors $\mathbf{\Phi}_k$ and $\mathbf{\Phi}_{N-k}$ (corresponding to the stationary cosine and sine), a rotating excitation can be constructed as

$$\begin{aligned} \mathbf{T}_k &= \mathbf{\Phi}_k + i \ \mathbf{\Phi}_{N-k} \\ \mathbf{T}_{N-k} &= \mathbf{\Phi}_k - i \ \mathbf{\Phi}_{N-k} \ , \end{aligned}$$

the + sign corresponding to a forward traveling wave (Figure 2.6), and the – sign to a backward traveling wave (Figure 2.7).

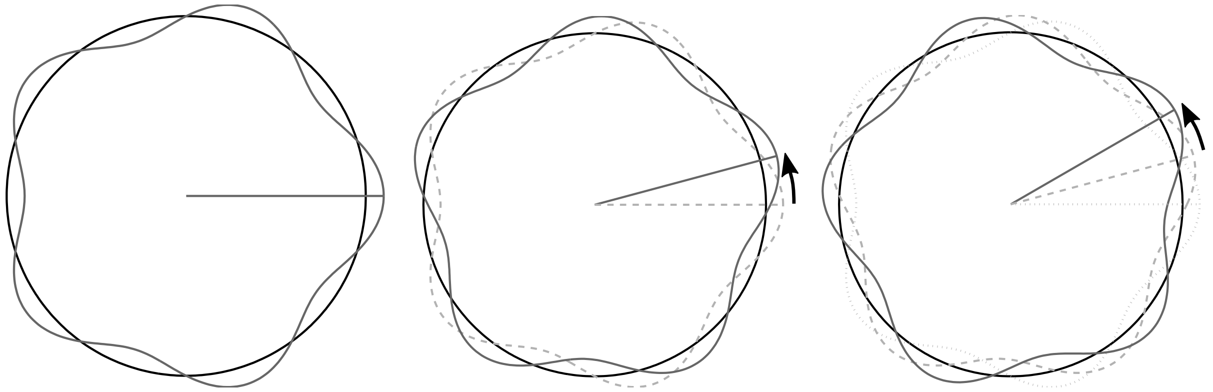

(a) t_1 (b) $t_2 > t_1$ (c) $t_3 > t_2$

Figure 2.6: Forward traveling wave.

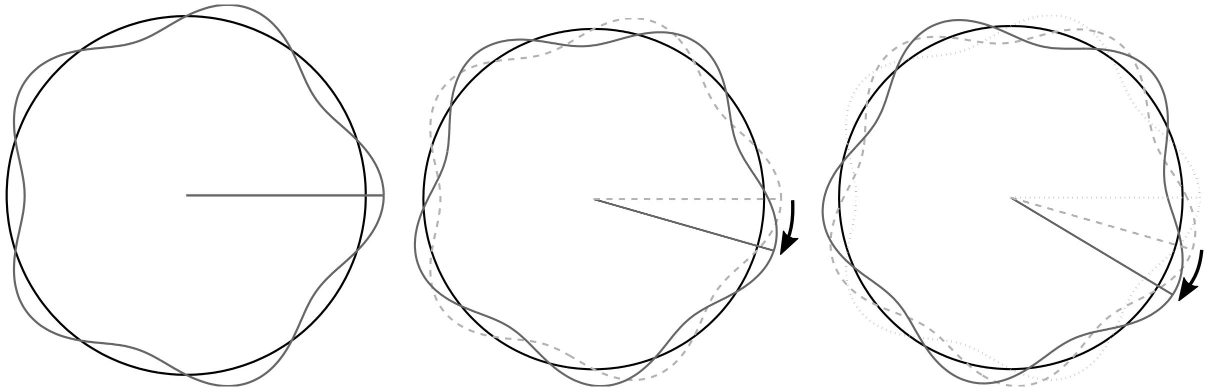

(a) t_1 (b) $t_2 > t_1$ (c) $t_3 > t_2$

Figure 2.7: Backward traveling wave.

The only harmonics to consider in the modal analysis are those between 0 and K, where

$$K = \begin{cases} \frac{N}{2} & \text{if } N \text{ is even} \\ \frac{N-1}{2} & \text{if } N \text{ is odd} \end{cases} . \tag{2.2}$$

For larger orders than K, we can associate with any order p the number of nodal diameters $N - p$. This corresponds to the aliasing of the discrete Fourier series [30].

The aliasing phenomenon can also be understood using the Nyquist-Shannon sampling theorem [31]

$$f_{sampling} = 2 f_{max} \ , \tag{2.3}$$

where $f_{sampling}$ is the sampling frequency and f_{max} the maximum frequency that can be detected.

In the case of cyclically symmetric structures, blades can be seen as samples, and the Nyquist-Shannon theorem can be rewritten as

$$N = 2K \ , \tag{2.4}$$

with N the number of blades and K the maximum numbers of nodal diameters.

Figure 2.8 permits to understand graphically the aliasing of the discrete Fourier series. A 36 blades structure is considered for this example. A mode with 10 ($= p$) and 26 ($N - p = 36 - 10$) nodal diameters are drawn. Figure 2.8 shows that whatever the blade considered (the blades are represented by black dots, distant from each other 360°/36 = 10°), the amplitude seen by the blades is identical for 10 and 26 nodal diameters modes. Therefore, exciting a $N - p$, $N + p$, ... nodal diameters is equivalent than exciting a p nodal diameter mode.

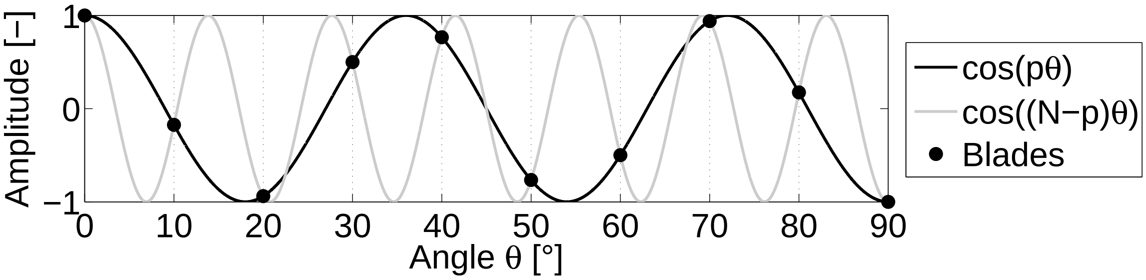

Figure 2.8: Illustration of the aliasing for a bladed structure with 36 blades, considering a mode with 10 ($= p$) and 26 ($= N - p = 36 - 10$) nodal diameters on $[0 - 90]°$.

The aliasing phenomenon can also be understood using more physical considerations. When all blades vibrate in phase, the observed mode is a 0 nodal diameter mode (Figure 2.9). In the case of a 1 nodal diameter mode, two phase changes are observed, identified by radial lines forming a mode with 1 nodal diameter. Remember that each nodal diameters mode appears in pairs. Similarly, for a 2 nodal diameters mode, each group of blades vibrates in phase opposition with respect to the adjacent groups of blades (Figure 2.10). Four phase changes are observed, forming 2 nodal diameters. Figure 2.11 shows the two orthogonal modes with 3 nodal diameters (6 phase changes can be seen). Following this reasoning, the maximum number of nodal diameters that can be observed corresponds to a configuration where a shift of 180° is observed between each blade. The situation with N phase changes (Figure 2.12) corresponds to a $\frac{N}{2}$ nodal diameters mode (in the case of an even number of blades).

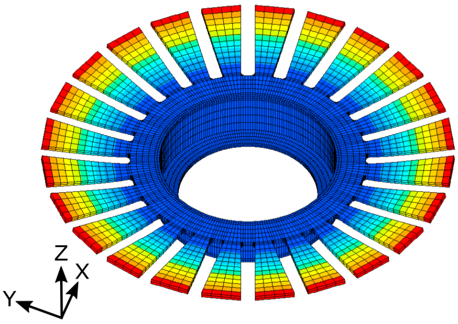

Figure 2.9: Mode with 0 nodal diameter.

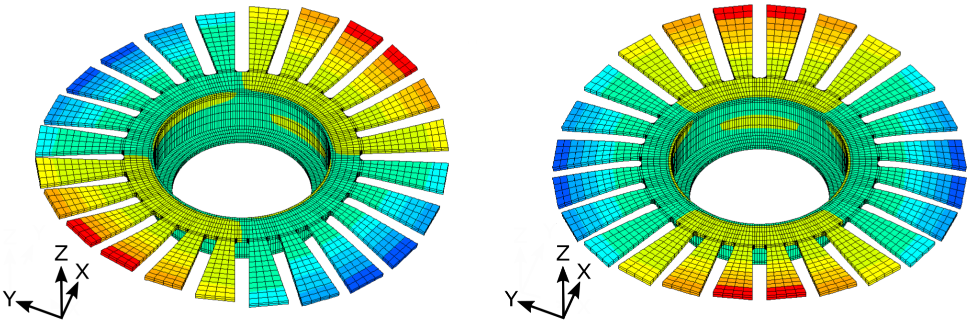

Figure 2.10: Two orthogonal modes with 2 nodal diameters.

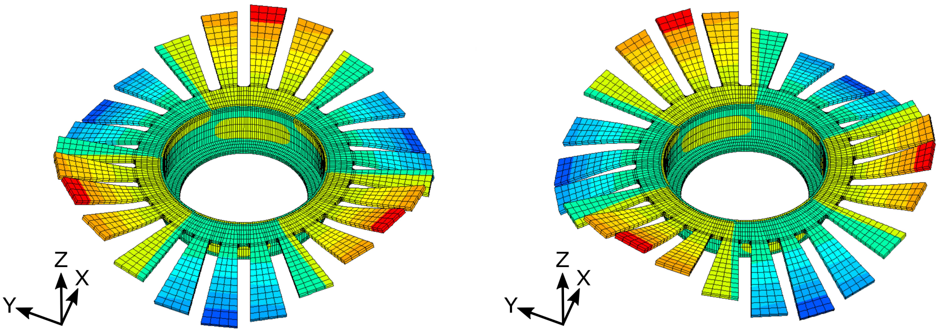

Figure 2.11: Two orthogonal modes with 3 nodal diameters.

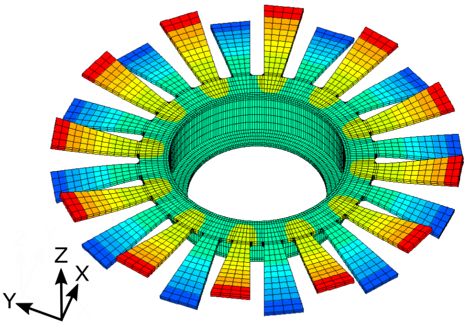

Figure 2.12: Mode with $\frac{N}{2} = 12$ diameters.

2.4 Main dynamic analysis tools

The Zig-Zag diagram, the SAFE diagram and the Campbell diagram are three important tools used for the dynamic analysis of bladed structure. These diagrams are explained in detail in this Section.

2.4.1 Zig-Zag diagram

The Zig-Zag diagram is a tool used in the field of turbomachinery that associates the numbers of nodal diameters excited by the same excitation order. Figure 2.13 shows a Zig-Zag diagram for an even and an odd number of blades (10 and 9 blades respectively). An excitation of order p excites modes with $d = |kN - p|$ nodal diameters, with k such that $0 < |kN - p| < \frac{N}{2}$ for N even or $\frac{N-1}{2}$ for N odd.

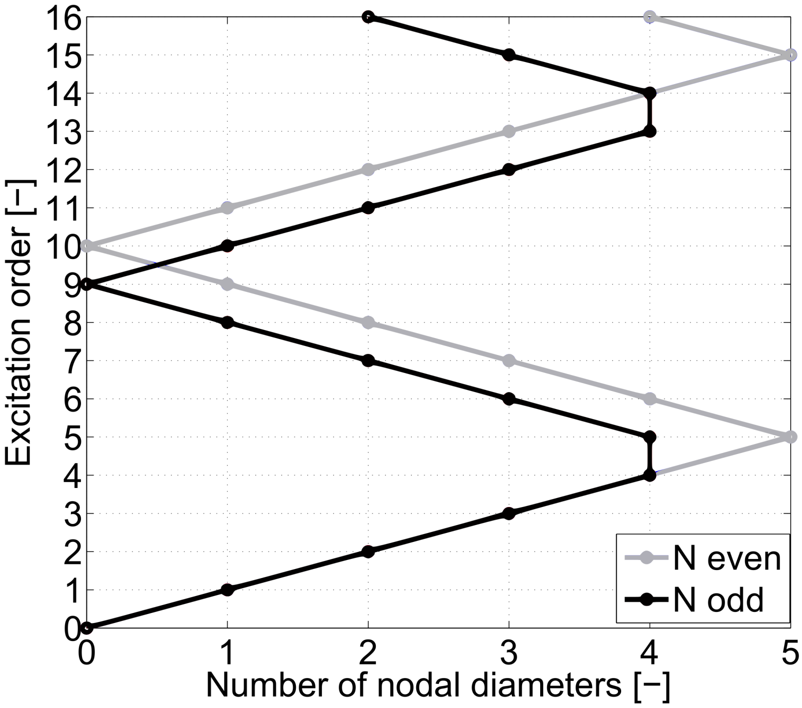

Figure 2.13: Zig-Zag diagram.

2.4.2 SAFE/ZZENF diagram and Campbell diagram

The SAFE or ZZENF diagram and the Campbell diagram are two complementary tools used to prevent resonances of the structure.

Evolution of the eigenfrequencies

The mode shapes, associated to a particular eigenfrequency, are grouped in mode families. Each mode family is characterized by a similar blade deformation. The eigenfrequencies ω evolve with the rotational speed Ω and the number of nodal diameters p for the same mode family, due to stiffening or softening effects. Therefore, a three dimensional diagram (Ω, p, ω) can be constructed, as shown in Figure 2.14, characterizing the evolution of the frequencies for a mode family. One mode family is therefore represented by a surface. The two dimensional projections of the surface in the (p, ω) plane, called "SAFE/ZZENF" plane and in the (Ω, ω) plane, called "Campbell" plane, as shown in Figures 2.15(a) and 2.15(b) respectively.

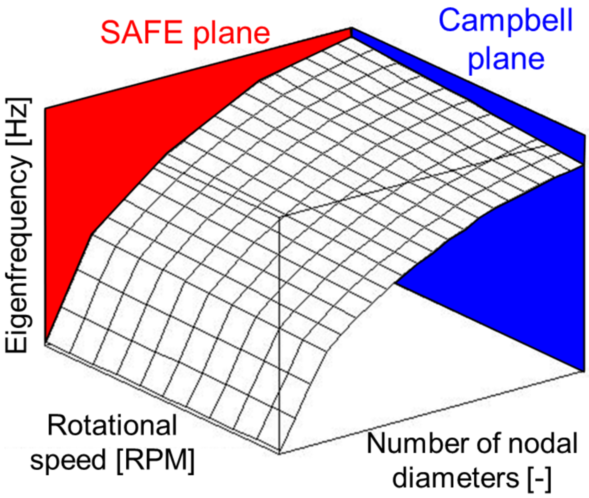

Figure 2.14: 3D representation of a mode family [32, 33].

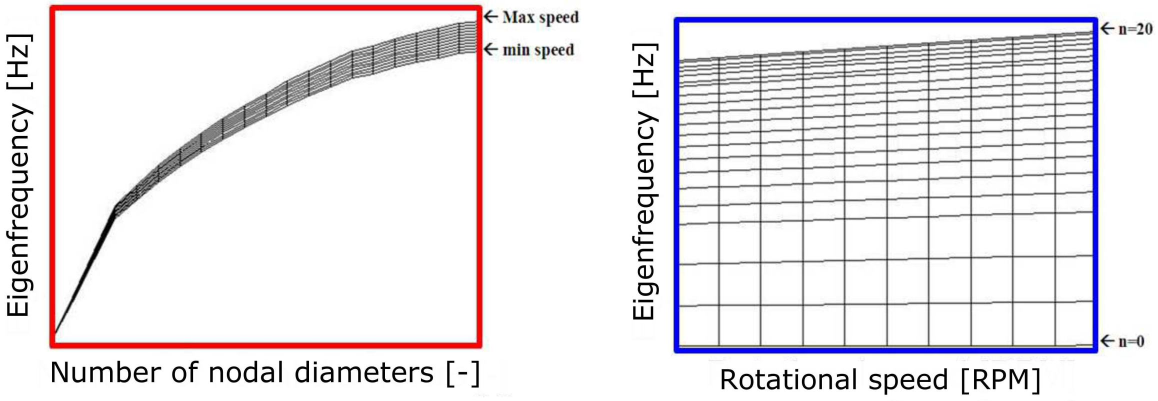

(a) SAFE/ZZENF plane

(b) Campbell plane

Figure 2.15: 2D projections of the evolution of the mode family in the SAFE/ZZENF plane (a) and in the Campbell plane (b) [32, 33].

Aerodynamic excitation

In turbomachinery, bladed structures are mainly submitted during their revolution to aerodynamic forces. The obstacles (such a stator, discharge valve...), uniformly distributed in the upstream or downstream airflow, generate pressure fluctuations along the circumference. Because of the rotation of the rotor parts, each sector of the bladed structure is submitted to a periodic force, which can be decomposed as a series of harmonics using the Fourier decomposition (as illustrated in Figure 2.16). The frequency of the harmonics ω depends on the rotation speed Ω (expressed in RPM) of the structure and on the number of obstacles N_{obst} present on a complete revolution, such as

$$\omega = \frac{N_{obst}\ \Omega}{60}\ [\text{Hz}]\ . \tag{2.5}$$

The excitation frequencies are whole multiple of the passing frequency of the stator blades. These excitation frequencies are said "synchronous" with the rotor rotational speed. The number of obstacles N_{obst} is commonly referred as "Engine Order" (EO).

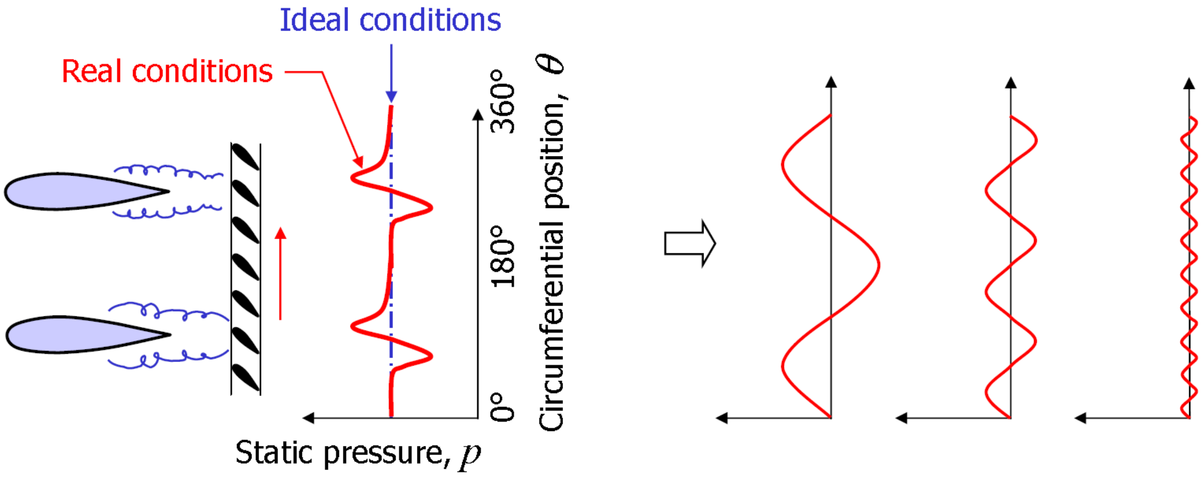

Figure 2.16: Pressure fluctuation due to obstacles in the upstream airflow [34].

The excitation frequency given by Equation (2.5) can be represented using a three dimensional diagram, as shown in Figure 2.17. The 2D projections in the SAFE/ZZENF plane and in the Campbell plane are given in Figures 2.18(a) and 2.18(b) respectively.

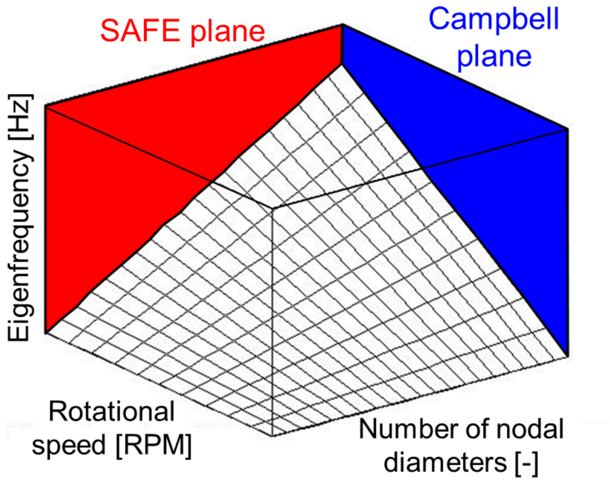

Figure 2.17: 3D representation of the evolution of a mode family [32, 33].

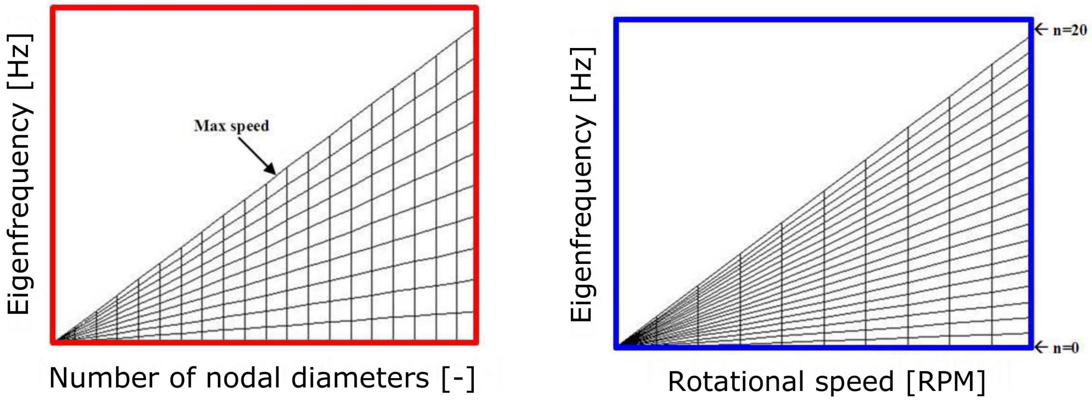

(a) SAFE/ZZENF plane

(b) Campbell plane

Figure 2.18: 2D projections of the evolution of the excitation in the SAFE/ZZENF plane (a) and in the Campbell plane (b) [32, 33].

Resonance conditions

Two conditions are required for a structure to enter in resonance:

- The first condition is that the frequency of the exciting force is equal to the natural frequency of the bladed structure (frequency matching). This first condition can be verified using the Campbell diagram.

- The second condition is that the number of nodal diameters of the mode coincides to the harmonic of the excitation (shape matching). This first condition can be verified using the SAFE/ZZENF diagram.

Campbell diagram

The Campbell diagram is a widely used tool to predict resonances. This diagram gives the evolution of the eigenfrequencies with respect to the rotational speed. Figure 2.19 shows the Campbell diagram, which superimpose the curves of Figures 2.15(b) and 2.18(b). It enables to localize the coincidences between the eigenfrequencies and the main harmonics of the engine rotational speed (black dots in Figure 2.19 that gives the intersections between the lines of evolution of the eigenfrequencies and the excitation lines), and therefore, enables to determine the *probable* resonances.

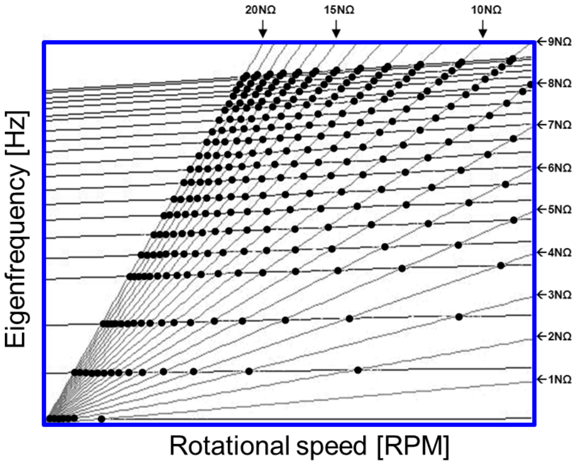

Figure 2.19: Example of Campbell diagram [32, 33].

The coincidence of eigenfrequencies with the excitation has been widely used to determine resonance. However, experiences based on turbines have demonstrated that only a few points among the black dots in Figure 2.19 leads to high response levels that provide concern for the blading reliability. Indeed, the Campbell diagram is not directly exploited in the case of bladed structures because of the compatibility condition between the shape of the excitation and the shape of the considered modes. This second condition reduces the *probable* resonances to a restricted set of *possible* resonances. This set of resonances can be obtained by the intersection of the three dimensional graph of the evolution of the eigenfrequencies of a mode family (Figure 2.14) and the three dimensional graph of the evolution of the excitation frequency (Figure 2.17), as shown in Figure 2.20. The *possible* resonances are given by the intersection between both surfaces (black dots in Figure 2.20).

By projection of the diagram of Figure 2.20 in the Campbell plane, one obtains the graph in Figure 2.21, where only the *possible* resonances are noted by black dots (frequency and shape matching).

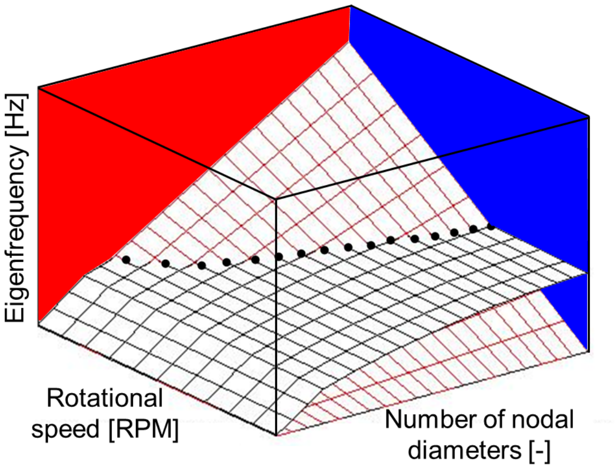

Figure 2.20: Set of *possible* resonances obtained by the intersection of the modal plane and the excitation plane [32, 33].

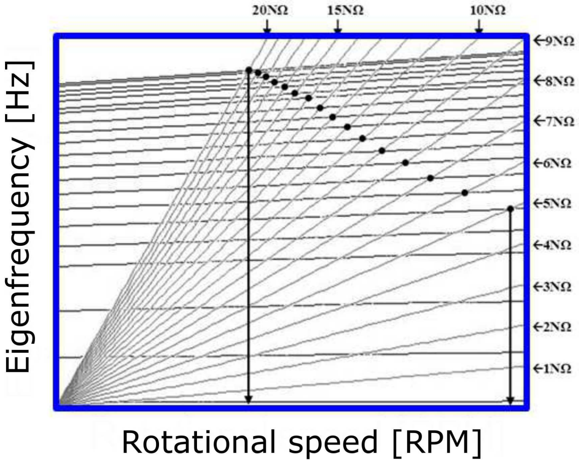

Figure 2.21: Campbell diagram with the *possible* resonances localized using black dots [32, 33].

SAFE/ZZENF diagram

The SAFE (Singh's Advanced Frequency Evaluation) diagram [32, 33], or the ZZENF (Zig-Zag shaped Excitation line in the Nodal diameter versus Frequency diagram) diagram [35, 36] are two identical tools respectively developed based on graphical and mathematical approaches. These diagrams give the evolution of the eigenfrequencies of a bladed structure with respect to the number of nodal diameters.

Figure 2.22 shows the SAFE diagram, which superimposes the curves of Figures 2.15(a) and 2.18(a), or can be seen as the projection of Figure 2.20 in the SAFE plane. Only the *possible* resonances are selected. In general, the SAFE diagram is plotted for one particular rotational speed. One plane is therefore considered in three dimensional graph in Figure 2.23(a) and projected on the SAFE plane (Figure 2.23(b)).

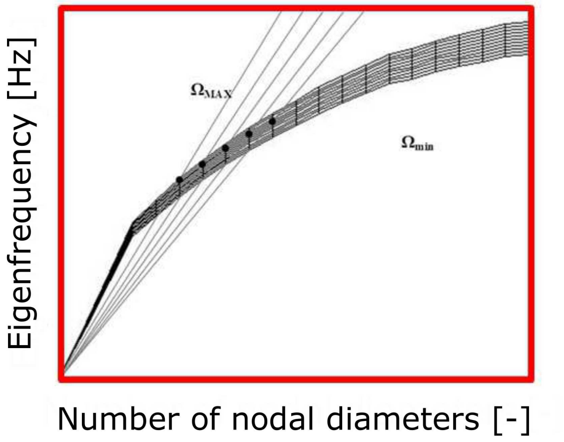

Figure 2.22: SAFE diagram for all rotational speeds.

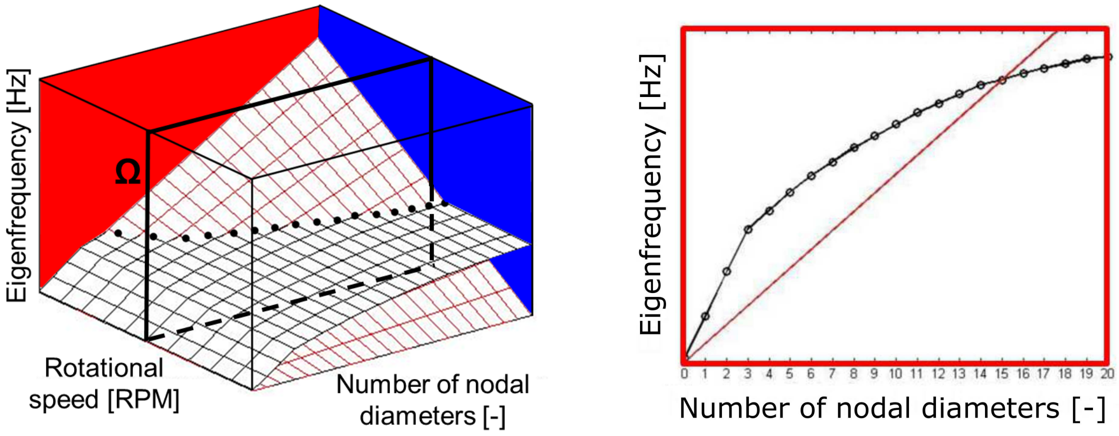

(a) 3D diagram

(b) SAFE/ZZENF diagram

Figure 2.23: 3D evolution of the eigenfrequencies and of the excitation frequency with one rotational speed selected (a) and SAFE diagram (b) [32, 33].

An example of a SAFE diagram is shown in Figure 2.24, with the excitation lines superimposed. Because of the aliasing phenomenon (Section 2.4.1), it has been shown that a p engine order excitation also excites $N-p$, $N+p$, ... nodal diameters modes.

All eigenfrequencies and associated mode shapes can be classified in three families [28]: families with mainly blade deformation, families with high participation of the disk/drum/shroud in the mode deformation, and mixed modes. It is possible, for some modes, to follow the evolution of the eigenfrequencies with respect to the number of nodal diameters on the SAFE diagram. Usually, the eigenfrequencies vary more for low numbers of nodal diameters. For these modes, the disk/drum/shroud has a larger participation in the mode shape, and the evolution of the number of nodal diameters modify the disk/drum/shroud stiffness (Figure 2.24, disk/drum/shroud modes). The modes for which the frequencies almost not evolve with the number of nodal diameters correspond to modes with a dominant blade deformation (Figure 2.24, blade modes).

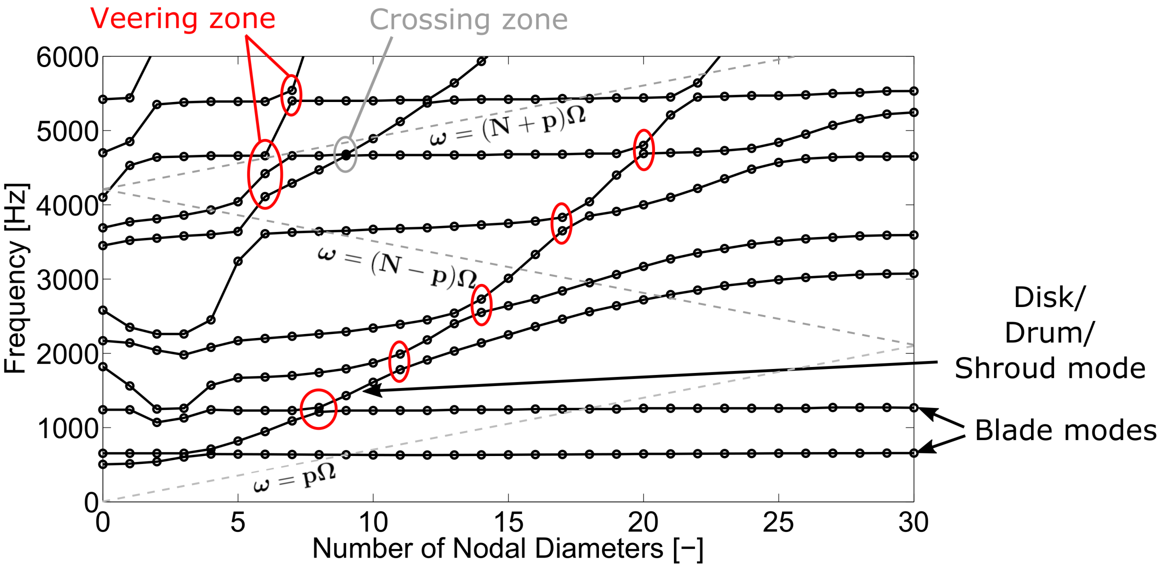

Figure 2.24: Example of SAFE diagram.

Moreover, the regions where the eigenfrequencies with the same number of nodal diameters become close can be dangerous. Indeed, important energetic exchanges can occur between the modes, involving other modes and the disk/drum. The zones are called "veering zones" (when the frequencies become close but does not cross), or "crossing zones" (when the frequencies become close and crossed), and are illustrated in Figure 2.24.

2.5 Modeling of mono-stage bladed structures

Finite element models of bladed disks are constructed taking into account the cyclic symmetric property of the structure. The formulation adopted here follows the presentation performed by Laxalde [16].

2.5.1 Cyclic symmetry formulation

Consider a cyclic symmetric structure composed of N identical sectors, as illustrated in Figure 2.25 with the reference sector in gray. The displacement vector of the structure $\mathbf{x}$ can be split as

$$\mathbf{x} = [\ \mathbf{x}_1, \mathbf{x}_2, ..., \mathbf{x}_N\ ]^T \quad , \tag{2.6}$$

where $\mathbf{x}_n$ $(n = 1, ..., N)$ is the displacement vectors associated to the n^{th} sector.

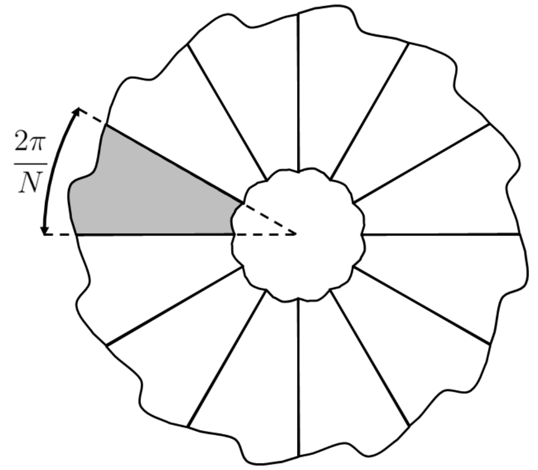

Figure 2.25: Cyclic symmetric structure with the reference sector in gray [16].

Given the rotational periodicity of cyclic structures, the mode shapes are such that each sector has the same deflection with a constant phase difference from the adjacent sectors. This phase angle is $\frac{2\pi(n-1)}{N}$, where $n = 1, ..., N$, is the number of nodal diameters of the considered mode. Therefore, the displacement vector of sector $n = 2, ..., N$ can be obtained from the displacement vector of a reference sector 1.

Consider the displacement vector of sector n ($n \in [1, ..., N]$). Using the discrete Fourier transform, $\mathbf{x}_n$ can be related to the cyclic components $\hat{\mathbf{x}}_j$ (associated with harmonic $j \in [1, N]$) as

$$\hat{\mathbf{x}}_j = \sum_{n=1}^{N} \mathbf{x}_n \; e^{-i\frac{2\pi(j-1)(n-1)}{N}} \qquad \text{and} \qquad \mathbf{x}_n = \frac{1}{N}\sum_{j=1}^{N} \hat{\mathbf{x}}_j \; e^{i\frac{2\pi(j-1)(n-1)}{N}} \; . \tag{2.7}$$

Introducing the Fourier vector

$$\mathbf{w}_j = \left(1, e^{-i\frac{2\pi(j-1)}{N}}, ..., e^{-i\frac{2\pi(j-1)(N-1)}{N}}\right) \; , \tag{2.8}$$

Equation (2.7) can be simplified as

$$\hat{\mathbf{x}} = \sum_{n=1}^{N} \mathbf{w}_n \otimes \mathbf{x}_n \qquad \text{and} \qquad \mathbf{x} = \frac{1}{N}\sum_{j=1}^{N} \mathbf{w}_j^{\star} \otimes \hat{\mathbf{x}}_j \; , \tag{2.9}$$

where $\hat{\mathbf{x}}$ is the vector which concatenates cyclic components vectors $\hat{\mathbf{x}}_j$ and the symbol * refers to conjugate-transpose.

Finally, introducing the Fourier matrix

$$\mathcal{F} = \begin{bmatrix} \mathbf{w}_1 \\ \mathbf{w}_2 \\ \mathbf{w}_3 \\ \vdots \\ \mathbf{w}_N \end{bmatrix} = \begin{pmatrix} 1 & 1 & 1 & \dots & 1 \\ 1 & e^{-i\frac{2\pi}{N}} & e^{-i\frac{2\pi 2}{N}} & \dots & e^{-i\frac{2\pi(N-1)}{N}} \\ 1 & e^{-i\frac{2\pi 2}{N}} & e^{-i\frac{2\pi 4}{N}} & \dots & e^{-i\frac{2\pi 2(N-1)}{N}} \\ \vdots & & & \ddots & \vdots \\ 1 & e^{-i\frac{2\pi(N-1)}{N}} & e^{-i\frac{2\pi 2(N-1)}{N}} & \dots & e^{-i\frac{2\pi(N-1)(N-1)}{N}} \end{pmatrix} , \tag{2.10}$$

Equation (2.9) can be further simplify as

$$\hat{\mathbf{x}} = (\mathcal{F} \otimes \mathbf{I})\,\mathbf{x} \qquad \text{and} \qquad \mathbf{x} = \frac{1}{N}\,(\mathcal{F}^{\star} \otimes \mathbf{I})\,\hat{\mathbf{x}} \ . \tag{2.11}$$

2.5.2 Equation of motion

The dynamical problem for the complete structure is given by

$$\mathbf{M}\ddot{\mathbf{x}} + \mathbf{C}\dot{\mathbf{x}} + \mathbf{K}\mathbf{x} = \mathbf{f} \ . \tag{2.12}$$

The quantities $\mathbf{x}$ and $\mathbf{f}$ can be defined with cyclic components using Equation (2.7). Equation (2.12) can be written in the cyclic basis as a set of sub-problems for each harmonic j ($j = 1, ..., N$) as

$$\mathbf{M}_j\ddot{\hat{\mathbf{x}}}_j + \mathbf{C}_j\dot{\hat{\mathbf{x}}}_j + \mathbf{K}_j\hat{\mathbf{x}}_j = \hat{\mathbf{f}}_j \ , \tag{2.13}$$

where $\mathbf{M}_j$, $\mathbf{C}_j$ and $\mathbf{K}_j$ are respectively the mass, damping and stiffness cyclic matrices for the harmonic j obtained from the matrices of the reference sector, and $\hat{\mathbf{f}}_j$ is the cyclic force vector for the harmonic j.

For each harmonic, the definition of boundary conditions must be added to these sub-problems (Section 2.5.3).

2.5.3 Cyclic boundary conditions

For each sub-problem of Equation (2.13), cyclic boundary conditions are defined. The displacement vector $\mathbf{x}_n$ can be decomposed in:

- degrees of freedom of the left boundary ${}^{l}\mathbf{x}_n$;
- degrees of freedom of the right boundary ${}^{r}\mathbf{x}_n$;
- internal degrees of freedom ${}^{i}\mathbf{x}_n$.

The boundary conditions consist in the compatibility of the displacement at the interface of the different sectors (Figure 2.26) i.e.,

$$^{l}\mathbf{x}_1 = {}^{r}\mathbf{x}_2, \qquad {}^{l}\mathbf{x}_2 = {}^{r}\mathbf{x}_3, \qquad \ldots, \qquad {}^{l}\mathbf{x}_N = {}^{r}\mathbf{x}_1 \ . \tag{2.14}$$

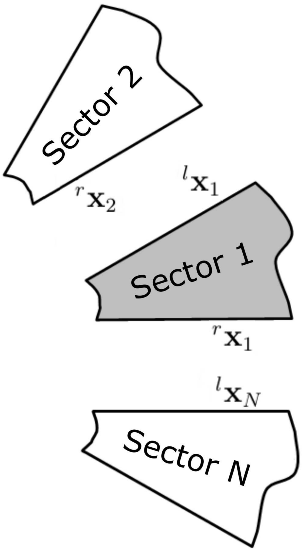

Figure 2.26: Illustration of the principle of the boundary conditions.

2.6 Mistuning in mono-stage bladed disks

Bladed disks present in reality small random blade-to-blade variations due to many factors as manufacturing tolerances, irregularities in the material properties or wear during use. These small discrepancies drastically affect the dynamic behavior of the bladed assemblies. The main effects of mistuning are explained below.

2.6.1 Frequency splitting

A notable effect of mistuning is the separation of the natural frequencies initially confused in the tuned structure. According to Ewins [37], if the frequency separation is greater than the modal damping (for a percentage of critical damping) factor, it is possible to observe the two modes separately. This phenomenon increases the number of peaks in the frequency response [38, 39].

2.6.2 Mode localization

For a mistuned structure, the mode shapes are not pure nodal diameter modes anymore but have multiple harmonic contents [3]. These modes can therefore be excited by all engine orders of excitation. Moreover, the mode shapes present a localization of the vibration energy about a few number of blades, as illustrated in Figure 2.27. This localization phenomenon can also lead to an increase of the vibration amplitude and stresses of these blades compared to the tuned case, which increases the risk of High Cycle Fatigue (HCF) failures. This phenomenon is more likely to occur on a structure with high spectral density [40, 41].

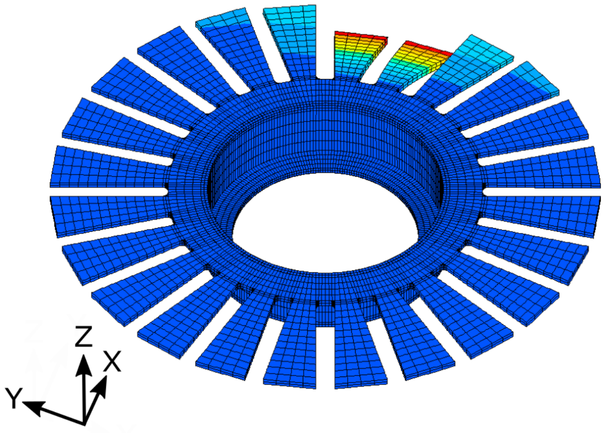

Figure 2.27: A localized mode shape for a mistuned bladed disk.

Mode localization depends only on the ratio between the mistuning strength and the coupling strength [42]. Mode localization increases indeed monotonically with increasing the mistuning or decreasing the structural coupling between substructures.

2.6.3 Maximum amplitude increase

The maximum vibration amplitude of the forced response presents a peak value with respect to mistuning or coupling strength for moderately weak interblade coupling (Figure 2.28) [43–49]:

- For weak values of the interblade coupling, each blade can be considered as an individual mistuned oscillator, and the mistuned response does not differ significantly from the ideal case.

- If the interblade coupling increase, the vibration energy can be transmitted between all the blades. In particular, the vibration energy from the different blades can localized to the maximum responding one in the assembly. This leads to a large increase of the vibration amplitude of some blades.

- If the coupling further increases, the vibration energy can be easily transferred between the blades and the localization phenomenon decreases, yielding tuned-like response levels.

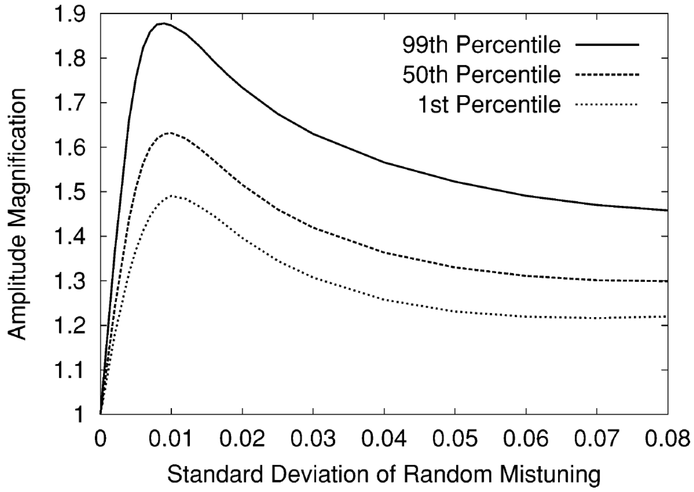

Figure 2.28: Amplitude magnification as a function of mistuning strength [3].

Bladed disks are submitted to high dynamic loads due to fluctuating gas forces. Because of the localization phenomenon and of the amplification of the forced response amplitude, mistuning increases the risk of High Cycle Fatigue (HCF) failures [50]. Numerous studies have been conducted in order to quantify the amplification of the maximum response level. The *amplification factor* is defined in different ways:

- The most used definition is the ratio between the largest amplitude response of the mistuned disk and the largest amplitude response of the tuned case [51].
- The ratio between the largest amplitude response of the mistuned disk and the largest amplitude response of a mistuned clamped blade alone [52–54].
- The ratio between the maximum amplitude and the mean amplitude over all sectors.

Since mistuning is a random phenomenon, statistics are generally used to determine the amplification factor distribution and his maximal value. Monte Carlo simulations can be used for example. Since mistuning is inevitable, numerous researches have been conducted to quantify the maximum level amplitude increase in forced response of bladed disk assemblies.

Whitehead [55] estimates analytically the maximum amplification factor, known as Whitehead factor:

$$\frac{1}{2}\left(1+\sqrt{N}\right) \ , \tag{2.15}$$

where N refers to the number of blades.

2.6.4 Aerodynamic stability

Mistuning can have beneficial effects with aeroelastic instabilities [56–60]. Mistuning can be intentionally introduced to stabilize the vibrations in the case of blade flutter.

2.7 Reduced order model for mono-stage bladed disks

First works on mistuning effects were based on lumped parameter models. These models are based on cyclic chains of spring-mass oscillators. The simplest model consists in a chain of N single-degree-of-freedom oscillators coupled by linear springs. Other oscillators can be added at each sector to model both blade and disk degrees of freedom. The mistuning is then modeled as small random perturbations to the stiffnesses or the masses of the blade degrees of freedom. These simple models enable to understand the dynamic behavior of bladed disks. The influence of mistuning can be investigated using statistical methods [61]. For example, mode localization, coupling, or forced response increase can be explained with these models.

The lumped-parameter models characterize qualitatively the dynamic behavior of mistuned bladed disks. For predicting quantitatively the response of a real structure, the use of the finite element model is needed. The finite element model consists usually in one sector of the bladed disk and a cyclic symmetric property is considered. But the presence of mistuning changes the response of the structure and the cyclic symmetry. A full finite element model is necessary (with millions of degrees of freedom) and Monte Carlo simulations become infeasible. Therefore, reduction techniques are used to generate reduced-order models from a parent finite element model for a frequency range of interest. The first reduced order models (ROMs) were constructed based on the component mode synthesis (CMS) method [62–64] or similar component-mode-based techniques. The basic principle of CMS method is that the structure is divided in different components (typically the disk and the blades), which are treated separately. Different types of boundary conditions can be then imposed, such as fixed or free blade/disk interfaces. For the free interface methods, constraint modes can be added to take into account the interface motion. The second generation of reduced order models consists in the system modes methods. These methods express the mistuning by means of tuned mode shapes of the bladed system in a specific frequency range. The existing ROMs are reviewed in this Section.

2.7.1 Component Mode Synthesis (CMS)

Irretier [4] applied the CMS method with free-interface of Craig and Chang [65, 66] to construct a reduced order model for bladed disks. Good results were obtained comparing to the parent finite element model. Then, Zheng and Wang [5] used the free-interface CMS method for shrouded disks. Ottarson [67] improved the method since he found that a blade mode can be represented using a basis of cantilevered blade modes and a set of blade modes induced by the disk vibration. This set of modes can be found using a finite element analysis where the mass density of the blades is set to zero, which will give disk-induced static shapes for the blades. In this improved approach, constraint modes are no more needed at the blade/disk interfaces, even in the case of fixed-interface methods. The modes of the disk component included the motion of the blade, and satisfied the displacement compatibility condition at the blade/disk interface. This hybrid CMS method enables to obtain a reduced order model of low size. Pierre and coworkers [7, 9] further improved the method. It has been shown that a reduced order model of size 10 N gives accurate results for a parent finite element model of a bladed disk with N sectors. However, the main drawback of this method is the non-accurate representation of the coupling between the disk and the blade, which is extremely important for mistuning studies (Section 2.6). The assumptions, advantages and drawbacks of the method are summarized below.

Assumptions:

- Small mistuning
- Mistuning simulated by changes in blades Young's modulus or equivalently specific changes in the stiffness matrix

Advantages:

- First ROM: good results obtained comparing to the parent FE model

Drawbacks:

- Numerous DOF needed to couple substructures (blades and disk) ⟶ rather large ROMs
- Non-accurate representation of the disk/blade coupling

2.7.2 Component Mode Based (CMB) method

Yang and Griffin [68] proposed the component-mode-based (CMB) method, in which the degrees of freedom at the interface between the blades and the disk are treated as rigid body. Therefore, no constraints modes at the blade/disk interface have to be computed. The method has a good accuracy, and allows a direct modeling of the mistuning in terms of perturbed blade stiffness and mass matrices or in terms of mistuned blade eigenfrequencies. The main drawback of the method also consists in a non-accurate representation of the coupling between the disk and the blade due to the assumptions on the blade/disk interface, which strongly influences the effects of mistuning (Section 2.6). The assumptions, advantages and drawbacks of the method are summarized below.

Assumptions:

- Rigid blade root motion
- Mistuning modeled in terms of perturbed blade stiffness and mass matrices or in terms of mistuned blade eigenfrequencies

Advantages:

- Structural fidelity comparable to the one of a FE model of the entire bladed disk system with significantly improved computational efficiency

Drawbacks:

- Non-accurate representation of the disk/blade coupling

2.7.3 Secondary Modal Analysis Reduction Technique (SMART)

Bladh et al. [11,12] developed the secondary modal analysis reduction technique (SMART), which enables to better capture the effect of the blade/disk interface motion. The finite element model is first reduced using Craig-Bampton method. Then, the interface degrees of freedom are condensed through a second modal analysis on the intermediate CMS model [66, 69–73]. The Craig-Bampton method is adapted for cyclic symmetric structures, which leads to a really compact reduced order model (size of the model is of the order of N, where N is the number of blades of the bladed disk). The mistuning is introduced as a deviation of the cantilevered blade mass or stiffness. The assumptions, advantages and drawbacks of the method are summarized below.

Assumptions:

- Mistuning modeled as a deviation of the cantilevered blade mass or stiffness
- Small mistuning $\longrightarrow$ no mode shapes modification, only frequency deviation $\longrightarrow$ mistuned mode shapes represented by a linear combination of tuned mode shapes

Advantages:

- ROM of small size (the order of the number of blades)
- Accurate results for both free and forced response
- Good results in veering zones

Drawbacks:

- Method complexity

2.7.4 Subset of Nominal Modes (SNM) approach

Yang and Griffin [8] developed the subset of nominal modes (SNM) method. Unlike the previous methods, the disk and the blades are not considered here as separated substructures as for the component-mode-based approaches, but as a whole structure. The basic assumption of the method is that the mistuned mode shapes can be represented by a finite sum (or "subset") of tuned mode shapes [74]. Therefore, the reduced order model is constructed using modes in the frequency range of interest, including a family of blade-dominated modes, typically with at least one mode per nodal diameter to span the space of the mistuned modes. The modes with remote frequencies are neglected, which involves an error inversely proportional to the frequency deviation. This enables in fact to provide a Fourier basis using tuned system modes to represent mistuned mode shapes [75, 76]. The reduced model has a number of degrees of freedom equal to the number of retained modes i.e., as small as the number of blades N of the bladed disk. The mistuning is then introduced in the model as a perturbation in the mass and stiffness matrices of the blades, which is expressed in the system coordinates using an appropriate coordinate transformation. The reduced order model generated using the SNM method remains highly accurate comparing to the parent finite element model, with reduced computational cost. The assumptions, advantages and drawbacks of the method are summarized below.

Assumptions:

- Small mistuning ⟶ no modification of the mode shapes, only frequency deviations ⟶ mistuned mode shapes represented by a linear combination of tuned mode shapes

Advantages:

- Simple implementation
- High accuracy, even in veering zones
- Converge to the exact solution when the number of retained DOF increases

Drawbacks:

- Basic method comparing to the numerous evolutions that have been performed after based on this method

2.7.5 Fundamental Mistuning Model (FMM)

Feiner and Griffin [13] proposed the fundamental model of mistuning (FMM), which is a simplification of the SNM method (Section 2.7.4) for the case of an isolated family of blade-dominated modes. With this additional assumption, only a set of tuned system eigenfrequencies are required, and the mistuning is introduced by defining frequency deviations of each sector. However, because of this simplifying assumption, the method is not accurate near veering zones or regions with high modal density. The assumptions, advantages and drawbacks of the method are summarized below.

Assumptions:

- Small mistuning ⟶ no modification of the mode shapes, only frequency deviations ⟶ mistuned mode shapes represented by a linear combination of tuned mode shapes
- Study of an isolated family of blade-dominated modes

Advantages:

- Simple implementation
- High accuracy for an isolated family of blade modes
- Mistuning can be applied on the all sector (blade + disk, and not on the blades only)

Drawbacks:

- Strong assumptions
- Not applicable in veering zones and regions with high modal density

2.7.6 Asymptotic Mistuning Model (AMM)

Martel et al. [77–79] proposed the asymptotic mistuning model (AMM) consisting in a further reduction of the FMM approach (Section 2.7.5). Comparing to the FMM method that can only account for modal families with nearly identical frequencies, the AMM method allows to describe the dynamics associated with more general modal families. The model is derived from the complete mistuned problem using an asymptotic expansion that exploits the smallness of the mistuning and the damping. The assumptions, advantages and drawbacks of the method are summarized below.

Assumptions:

- Small mistuning and damping
- Valid for a single mode family

Advantages:

- Not limited to mode families with nearly identical frequencies
- Accurate method

Drawbacks:

- Strong assumptions

2.7.7 Petrov's method

Petrov et al. [80–82] developed a different approach for modeling mistuned bladed disks. The method computes the mistuned forced response using the tuned forced response and a modification matrix, constructed using the frequency response function matrix of the tuned system and a mistuning matrix. Even if the method is defined in the physical coordinates, it is not mandatory to retain all physical degrees of freedom of the blades. Only a few active degrees of freedom can be retained by introducing lumped masses, dampers, and springs attached to some degrees of freedom of the blades which represent the effect of mistuning. Moreover, the tuned frequency response function can be computed using a restricted number of system modes. The assumptions, advantages and drawbacks of the method are summarized below.

Assumptions:

- Mistuning effects represented by lumped masses, dampers, and springs attached to some DOF

Advantages:

- Exact expression
- Computational cost for mistuning calculations not dependant on the size of the original sector model as the solution is obtained at active coordinates

- Reduced model corresponding to the active coordinates as accurate as the initial sector model represented by its natural frequencies and mode shapes

Drawbacks:

- Complexity of the method
- Mistuning defined in the physical space

2.7.8 Component Mode Mistuning (CMM) method

Lim et al. [14] proposed the component mode mistuning (CMM) method, a reduced order model combining both system modes based and component mode synthesis methods. The system is divided in different substructures: one for the tuned bladed disk and N to introduce mistuning for each blade. For the tuned bladed disk, a set of tuned system modes is used to provide a Fourier basis to generate the reduced order model, as in the SNM method (Section 2.7.4). Then, the mistuned substructures are assembled using a component mode synthesis method. The blade alone motion is represented by a set of cantilevered blade modes and optionally the interface modes (Craig–Bampton constraint modes [64] for the degrees of freedom fixed in the cantilevered blade model). Modal participation factors enable to project the blade mistuning into the reduced order model, which is an extension of method proposed by Bladh et al. [9] (Section 2.7.3). The mistuning is introduced as a perturbation of the mass or stiffness in the modal space. It can be proportional (identical for all modes of a given blade) or non-proportional (different for each type of cantilevered blade modes of a given blade). Therefore, a high accuracy is obtained using the CMM method, even in the veering zones where different mode families are involved. Moreover, because of the possibility of introducing a non-proportional mistuning, the method is applicable for high frequencies. The assumptions, advantages and drawbacks of the method are summarized below.

Assumptions:

- Small displacements at the interface blades/disk

Advantages:

- Accurate results, even in veering regions
- General method (small and large mistuning, proportional or not)

Drawbacks:

- More complex method

2.7.9 Integral Mode Mistuning (IMM)

Vargiu et al. [83] proposed an extension to CMM (Section 2.7.8) known as integral mode mistuning (IMM) to address mistuning that may occur at the blade/disk interface or throughout the sector. Vargiu et al. replaced the cantilevered blade modes in the mistuning projection by normal modes of a full sector with free interfaces. The accuracy of IMM is similar to CMM when only sector mistuning is applied, but can also produce accurate results for a system with root mistuning. The assumptions, advantages and drawbacks of the method are summarized below.

Assumptions:

- Small mistuning

Advantages:

- Accurate results
- Take into account root and sector mistuning

Drawbacks:

- Not validated experimentally

2.7.10 Nodal Energy Weighted Transformation (NEWT)

Fitzner et al. [84] proposed the nodal energy weighted transformation (NEWT) approach, which consists in a combination of the CMM (Section 2.7.8) and SNM (Section 2.7.4) methods. The NEWT method assumes as in CMM and SNM methods that the mistuned mode shapes can be written as a linear combination of the tuned mode shapes. Instead of considering cantilevered blade modes for the mistuning projection, a subset of tuned system modes of one sector is used. The NEWT reduced order model shows a good accuracy (comparable to the CMM method) and can be improved by increasing the number of projection modes. The response of all modes can be well predicted even for not blade dominated modes. The assumptions, advantages and drawbacks of the method are summarized below.

Assumptions:

- Small mistuning ⟶ mistuned mode shapes represented by a linear combination of tuned mode shapes
- No mistuning at sector interfaces

Advantages:

- High accuracy, which can be improved by adding more projection modes
- Accurate prediction even for not blade dominated modes

Drawbacks:

- Not validated experimentally
- Arbitrary process for the projection modes selection

2.7.11 Static Mode Compensation (SMC) method

Lim et al. [23] proposed the static mode compensation (SMC) method to model bladed disks with large geometrical deviations from a nominal design. The proposed approach employs a mode-acceleration method with static mode compensation. The basis vectors consist in a combination of tuned system normal modes compensated by static modes. For higher frequency ranges, static modes are replaced by quasi-static modes to take into account inertia effects. Ganine et al. [85] improved the SMC method by replacing the quasi-static set of modes with inexact solutions of the linear Jacobi-Davidson correction equations. This enables to obtain an accurate method even in the veering zones. The proposed SNC method shows a better convergence than methods based on tuned system normal modes. The assumptions, advantages and drawbacks of the method are summarized below.

Assumptions:

- Geometrical mistuning
- Basis of mistuned mode shapes constructed as a combination of tuned mode shapes with quasi-static mode compensation

Advantages:

- Good convergence
- Does not required an expensive modal analysis of the mistuned system
- Compact method
- Accurately description of structures with geometrical mistuning
- Accurate in veering zones

Drawbacks:

- Not validated experimentally
- High computational time for small mistuning projection

2.7.12 Nonparametric modeling

Soize [86] developed an approach known as a nonparametric modeling of random uncertainties. This method is based on the entropy optimization principle. Capiez and Soize [87] particularized the nonparametric approach to the case of cyclically symmetric structures. In this approach, both eigenfrequencies deviations and uncertainties on the blade mode shapes are modeled. Moreover, the nonparametric probabilistic approach enables to model both data and model uncertainties while parametric approaches take into account only model uncertainties. The nonparametric approach is constructed using a mean reduced model, and using a probability model for symmetric positive-definite real random matrices constructed using the entropy maximization principle with the available information. The assumptions, advantages and drawbacks of the method are summarized below.

Assumptions:

- Blades only coupled by the disk
- Disk fixed on a part of its boundary
- Mistuning statistically independent from blade to blade

Advantages:

- Both data and model uncertainties are modeled
- Both eigenfrequencies deviations and uncertainties on the blade mode shapes are modeled

Drawbacks:

- Large size of matrices

2.7.13 Mbaye's method

Mbaye et al. [88–90] proposed a nonparametric modeling method that takes into account variations in geometry instead of a variation in the mechanical properties (mass or stiffness). The finite element model of each sector with geometry modifications is supposed to be known. The method uses the mode shapes of each sector and imposes linear constrains to satisfy the displacement compatibility conditions at the interface between sectors. Each sector matrix is therefore reduced by its own cyclic modes. Since the FE models of each sector are assumed to be known, the method is adapted for intentional mistuning only, and no identification method is associated. The influence of non-intentional mistuning is estimated using probabilistic methods. The assumptions, advantages and drawbacks of the method are summarized below.

Assumptions:

- Reduction of each sector mass and stiffness matrix by its own modes
- Linear constraints applied on common boundaries between sectors to make the displacement field admissible on the entire bladed disk

Advantages:

- Simple method
- Accurate results
- Geometric mistuning
- Applicable for large mistuning

Drawbacks:

- FE model of each sector required
- Only valid for intentional mistuning (no identification method associated)

2.7.14 Modified Modal Domain Analysis (MMDA)

Sinha [91–93] proposed the Modified Modal Domain Analysis (MMDA), which takes into account geometrical mistuning. The MMDA approach is an adaptation of the SNM method (Section 2.7.4). The perturbation is assumed to be located on the blades only. Unlike stiffness mistuning, geometrical mistuning involves a significant change in the mode shapes, which makes the other approaches (i.e., that take into account only stiffness mistuning) inappropriate. The problem is not the assumption that a mistuned mode shape is represented by a linear combination of tuned mode shapes, but the number of retained tuned modes which is too low because the method requires the finite element model of each different geometry. The assumptions, advantages and drawbacks of the method are summarized below.

Assumptions:

- Perturbation located on the blades only

Advantages:

- Simple method (based on SNM method)
- Accurate results
- Geometric mistuning
- Applicable to large mistuning

Drawbacks:

- FE model of each blade geometry required

2.8 Mistuning identification method for mono-stage bladed disks

For bladed disks with inserted blades, the eigenfrequencies of each individual blade can be directly measured experimentally to get the mistuning pattern of the structure [10,20,94]. However, constructors orientate now to one-piece bladed disk called blisk, for which the blades cannot be removed from the assembly. Mistuning identification methods have been developed in order to retrieve mistuning of each blade using experimental measurements.

The identification methods usually take the inverse form of the reduced order modeling techniques. Knowing the eigenfrequencies and mode shapes of the tuned finite element model and the experimental eigenfrequencies and mode shapes, the identification methods enables to retrieve the mistuning of the structure.

2.8.1 CMB identification (CMB ID) method

Judge et al. [40, 95, 96] developed the first identification method. The method is based on the CMS reduced order modeling technique developed by Bladh et al. [11] (Section 2.7.3). A second model reduction was performed in order to condense the degrees of freedom of the disk and of the blades/disk interfaces. Only the blade modal stiffnesses are retained in the model. The input data of the proposed method are the eigenfrequencies and mode shapes of the tuned finite element model, and either the experimental eigenfrequencies and mode shapes or the experimental forced responses [96]. Using the set of measurements, the mistuning of each blade can be retrieved. The assumptions, advantages and drawbacks of the method are summarized below.

Assumptions:

- Small mistuning ⟶ no mode shapes modification, only frequency deviation ⟶ mistuned mode shapes represented by a linear combination of tuned mode shapes

Advantages:

- Validated experimentally
- Modal stiffness mistuning
- Accurate results
- Two methods, the first for lowly damped structures and/or with low modal density, and the second for higher damping and/or high modal density

Drawbacks:

- Complex method
- For the case of higher damping and/or high modal density, three sets of measurement required, especially with intentional mistuning
- Not validated in veering zones or for different mode families simultaneously

2.8.2 FMM identification (FMM ID) method

Feiner and Griffin [18, 19] proposed two identification methods based on the FMM method (Section 2.7.5). The first method (the basic FMM ID method) required as input data the tuned eigenfrequencies of the structure. The second one (the advanced FMM ID method) identifies the mistuning of each blade, but also the tuned eigenfrequencies based on experimental measurements. This second approach is especially useful to validate the finite element model of the tuned bladed structure. In both methods, the mistuning is defined as a variation of the sector's eigenfrequencies instead of a variation of the blade eigenfrequencies only. However, the approach is limited to the case of an isolated family of blade-dominated modes. Accurate results are obtained for both mistuning identification and forced response prediction when this restricted assumption is respected. The assumptions, advantages and drawbacks of the method are summarized below.

Assumptions:

- Small mistuning ⟶ no mode shapes modification, only frequency deviation ⟶ mistuned mode shapes represented by a linear combination of tuned mode shapes
- Study of an isolated family of blade-dominated modes

Advantages:

- Simple method
- Two methods, and the advanced one only requires experimental measurements as input data
- Mistuning defined as a variation of the sector's eigenfrequencies instead the blade only (able to represent a mistuning due to geometrical changes or material properties variations)
- Accurate results for an isolated blade-mode family
- Validated experimentally [97]

Drawbacks:

- Very restrictive assumptions (isolated family of blade-dominated modes ⟶ veering regions to proscribe)

2.8.3 CMM identification (CMM ID) method

Lim et al. [98, 99] proposed an identification technique based on the CMM method (Section 2.7.8). The CMM method has the advantages to get accurate results even in veering regions where different mode families participate in the response. The proposed identification method retrieves the variations in the modal parameters (mass or stiffness) of each blade, but also the cyclic modeling error due to the differences between the tuned finite element model and the virtual tuned system associated to the tested structure. Madden et al. [27] further worked on the CMM ID method in order to select the experimental modes to improve the precision of the identification. The assumptions, advantages and drawbacks of the method are summarized below.

Assumptions:

- Small mistuning ⟶ no mode shapes modification, only frequency deviation ⟶ mistuned mode shapes represented by a linear combination of tuned mode shapes
- Small displacements at the blade/disk interface

Advantages:

- Not limited to one isolated modes family, applicable in veering zones and for high frequencies
- Excellent results
- Validated experimentally

Drawbacks:

- Not validated experimentally in veering zones or for different mode families simultaneously

2.8.4 Best-achievable-eigenvectors based method

Pichot et al. [24,25,100] proposed an identification method based on the "Best Achievable Eigenvectors" (BAE) [101,102] of all experimental mode shapes combined with a regulation technique. A reduced order model is constructed based on the Benfield and Hruda reduction method [103] adapted to bladed disk modeling. Mistuning is introduced as a perturbation of the cantilevered blade modes. The identification is based on the inversion of the equation of motion in order to determine the mistuning parameters. First, an expansion technique is applied on the measured data. Then, a regulation method is used to minimise the effect of measurements noise or of non-considered nonlinearities. This step consists in a projection of the experimental mode shapes on a subspace spanned by the mistuned model, which enables to improve the representativeness of the experimental modes and limits the influence of noise in the measurements. The assumptions, advantages and drawbacks of the method are summarized below.

Assumptions:

- Small mistuning
- Mistuning defined as a deviation in the Young's modulus of each blade (perturbation of the cantilevered-blade modes)
- Global measurements of a system of modes necessary

Advantages:

- Simple method
- Validated on different numerical cases and on an experimental case

Drawbacks:

- Iterative selection of the measured modes
- Proportional mistuning

2.8.5 Nonparametric identification method

Based on the probability distribution of the amplification factor of the forced response, the method proposed by Soize and Capiez [104, 105] retrieves the blade geometrical tolerances. A probabilistic model of the blade geometry is constructed a priori, which enables to estimate a value for the dispersion parameters of the nonparametric model in function of the blade tolerance. The dispersion parameters are constructed based on the blade nonparametric probabilistic model, which can be expressed analytically. The identification criterion consists in equalizing the dispersion parameters of the blade geometry's probabilistic model and the dispersion parameters of the blade nonparametric probabilistic model. A relationship giving the dispersion parameters of the blade nonparametric probabilistic model as a function of the blade tolerance is constructed. Then, the nonparametric probabilistic model is used with the identified values of the dispersion parameters in order to evaluate the amplification factor of the forced response. Several iterations are performed for different tolerances. Fixing a probability of the amplification factor, it is possible to characterize the optimal tolerances of the blades. The assumptions, advantages and drawbacks of the method are summarized below.

Assumptions:

- Blade only coupled by the disk
- Mistuning statically independent from blade to blade

Advantages:

- Blade geometrical tolerances retrieved based on a probability distribution of the amplification factor
- Validated numerically

Drawbacks:

- Not validated experimentally
- Iterative method

2.8.6 MMDA identification (MMDA ID) method

Bhartiya et al. [106] developed a mistuning identification method based on the MMDA method (Section 2.7.14). Sinha [91] has used a proper orthogonal decomposition (POD) of CMM data to identify the independent vibratory parameters (mistuning parameters). The identification method enables to retrieve these geometric mistuning parameters. Two versions of the method are proposed, the first one based on eigenfrequencies and mode shapes, and the second one based on forced responses. Accurate results have been obtained even when the assumed mean geometry is different from the true mean geometry and with large errors in damping estimation. The assumptions, advantages and drawbacks of the method are summarized below.

Assumptions:

- Mistuning parameters identification using the mode shapes and eigenfrequencies of the mistuned structure
- Rayleigh damping
- Mistuned system modes represented as a linear combination of tuned system modes and modes of the system perturbed along specific POD features

Advantages:

- Geometric mistuning
- Large damping
- Identification using modal and harmonic analysis
- Validated numerically

Drawbacks:

- Not validated experimentally

2.9 Dynamics of multi-stage bladed structures

Bladed disks are usually studied as isolated systems, but there are in reality connected to adjacent stages in a multi-stage rotor. In current practice, a finite element model is constructed for each stage separately, imposing either fully clamped conditions or axial restraints alone, or modeling adjacent stages as uniformly distributed masses and stiffnesses to preserve cyclicity. However, applying constraints to the boundary degrees of freedom of a single stage could not faithfully capture the boundary conditions of the actual stage-to-stage connection.

Only few works have been performed on multi-stage structures. The effect of the interstage coupling is not well established.

Bladh et al. [2] have shown on a finite element model that connecting a second stage to a single-stage bladed disk can significantly affect the dynamic behavior of the first stage predicted with the single-stage analysis. Most mode shapes were confined to either stage, relatively few modes exhibit significant participation of both stages (system modes), as shown in Figure 2.29. Multi-stage effects due to the interstage coupling were shown to occur mainly in veering regions (Figure 2.30), where the motion of the disk is dominant. The presence of the adjacent stage alters inter-blade coupling through the disk, which governs to a large extent the severity of vibration energy localization (Section 2.6).

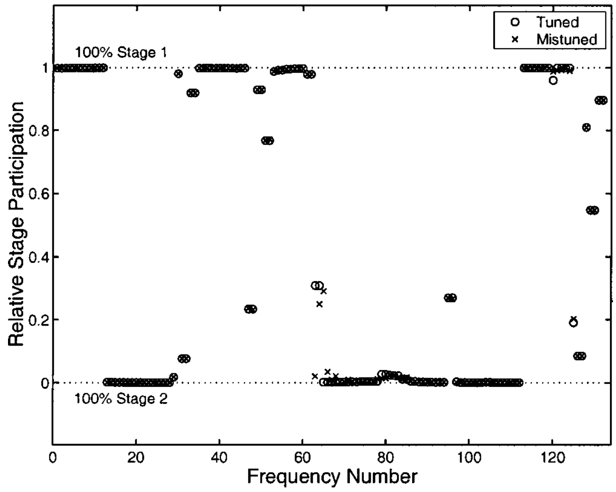

Figure 2.29: Stage 1 strain energies relative to total multi-stage strain energies for "tuned" and blade mistuned multi-stage modes below 8000 Hz [2].

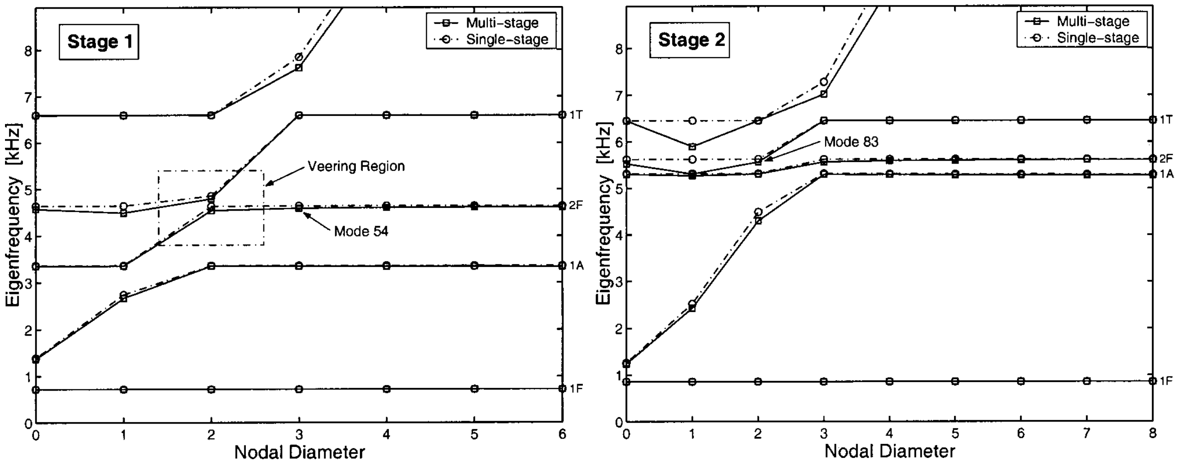

(a)

(b)

Figure 2.30: Natural frequencies versus number of nodal diameters for the tuned stage 1 (a) and stage 2 (b) model with fixed interstage boundaries, and for the "tuned" multi-stage model for modes confined to stage 1 (a) or stage 2 (b) [2].

2.10 Modeling of multi-stage bladed structures

Consider a multi-stage system of S cyclic structures with the same axis of rotational symmetry. In absence of mistuning, each sub-structure is composed of N_s identical sectors. The same approach can be considered for each stage of the whole structure but interstage compatibility conditions must be added. The formulation adopted here follows the presentation performed by Laxalde [16].

2.10.1 Equations in the physical basis

The equations of motion of each stage s ($s = 1, ..., S$) may be written as

$$\mathbf{M}_s\ddot{\mathbf{x}}_s + \mathbf{C}_s\dot{\mathbf{x}}_s + \mathbf{K}_s\mathbf{x}_s = \mathbf{f}_s \ , \tag{2.16}$$

where:

- $\mathbf{M}_s$, $\mathbf{C}_s$ and $\mathbf{K}_s$ are the structural mass, damping and stiffness matrices of substructure s;
- $\mathbf{x}_s$ is the vector containing the degrees of freedom of stage s;
- $\mathbf{f}_s$ is the external force vector on stage s.

The multi-stage assembly is obtained by compatibility conditions on the displacements at each interface Γ between stages α and β in the physical base:

$$\mathbf{x}_\alpha^\Gamma - \ \mathbf{x}_\beta^\Gamma = 0 \ , \tag{2.17}$$

where $\mathbf{x}_\alpha^\Gamma$ and $\mathbf{x}_\beta^\Gamma$ correspond to the restriction of the degrees of freedom vectors of the stages α and β respectively to the interstage degrees of freedom.

2.10.2 Cyclic symmetry formulation

The characteristic quantities (displacement, load...) are written in a cyclic basis using a discrete Fourier transform, following the same approach than in the single stage case. Consider the displacement vector $\mathbf{x}_{ns}$ of each sector $n \in [1, N_s]$ of the stage $s \in [1, S]$. $\mathbf{x}_{ns}$ can be related to the cyclic components $\hat{\mathbf{x}}_{js}$ (associated with harmonic $j \in [1, N_s]$) as

$$\hat{\mathbf{x}}_{js} = \sum_{n=1}^{N_s} \mathbf{x}_{ns} \ e^{-i\frac{2\pi(j-1)(n-1)}{N_s}} \qquad \text{and} \qquad \mathbf{x}_{ns} = \frac{1}{N_s}\sum_{j=1}^{N_s} \hat{\mathbf{x}}_{js} \ e^{i\frac{2\pi(j-1)(n-1)}{N_s}} \ . \tag{2.18}$$

Introducing the Fourier vector

$$\mathbf{w}_{js} = \left(1, e^{-i\frac{2\pi(j-1)}{N_s}}, ..., e^{-i\frac{2\pi(j-1)(N_s-1)}{N_s}}\right) \ , \tag{2.19}$$

Equation (2.18) can be simplified as

$$\hat{\mathbf{x}}_s = \sum_{n=1}^{N_s} \mathbf{w}_{ns} \otimes \mathbf{x}_{ns} \qquad \text{and} \qquad \mathbf{x}_s = \frac{1}{N_s}\sum_{j=1}^{N_s} \mathbf{w}_{js}^\star \otimes \hat{\mathbf{x}}_{js} \ , \tag{2.20}$$

where $\hat{\mathbf{x}}_s$ is the vector which concatenates cyclic components vectors $\hat{\mathbf{x}}_{js}$ and the symbol * refers to conjugate-transpose. Finally, introducing the Fourier matrix of stage s

$$\mathcal{F}_s = \begin{bmatrix} \mathbf{w}_{1s} \\ \mathbf{w}_{2s} \\ \mathbf{w}_{3s} \\ \vdots \\ \mathbf{w}_{Ns} \end{bmatrix} = \begin{pmatrix} 1 & 1 & 1 & \dots & 1 \\ 1 & e^{-i\frac{2\pi}{N_s}} & e^{-i\frac{2\pi 2}{N_s}} & \dots & e^{-i\frac{2\pi(N_s-1)}{N_s}} \\ 1 & e^{-i\frac{2\pi 2}{N_s}} & e^{-i\frac{2\pi 4}{N_s}} & \dots & e^{-i\frac{2\pi 2(N_s-1)}{N_s}} \\ \vdots & & & \ddots & \vdots \\ 1 & e^{-i\frac{2\pi(N_s-1)}{N_s}} & e^{-i\frac{2\pi 2(N_s-1)}{N_s}} & \dots & e^{-i\frac{2\pi(N_s-1)(N_s-1)}{N_s}} \end{pmatrix} , \tag{2.21}$$

Equation (2.9) can be further simplify as

$$\hat{\mathbf{x}}_s = (\mathcal{F}_s \otimes \mathbf{I})\, \mathbf{x}_s \qquad \text{and} \qquad \mathbf{x}_s = \frac{1}{N_s} (\mathcal{F}_s^\star \otimes \mathbf{I})\, \hat{\mathbf{x}}_s \ . \tag{2.22}$$

2.10.3 Equations in the cyclic basis

The equation of motion (2.16) can be written in the cyclic basis for each stage s as

$$\mathbf{M}_{js}\ddot{\hat{\mathbf{x}}}_s + \mathbf{C}_{js}\dot{\hat{\mathbf{x}}}_s + \mathbf{K}_{js}\hat{\mathbf{x}}_s = \hat{\mathbf{f}}_{js} \ , \tag{2.23}$$

in which cyclic matrices $\mathbf{M}_{js}$, $\mathbf{C}_{js}$ and $\mathbf{K}_{js}$ associated to harmonic j for stage s are obtained from the matrices of the reference sector to which cyclic boundary conditions have been applied, and $\hat{\mathbf{f}}_{js}$ is the cyclic force vector for the harmonic j for stage s.

The interface compatibility conditions in Equation (2.17) between two stages α and β in the cyclic basis become

$$\frac{1}{N_\alpha} \sum_{j_\alpha=1}^{N_\alpha} \mathbf{w}_{j_\alpha \alpha} \otimes \ \hat{\mathbf{x}}^\Gamma_{j_\alpha \alpha} - \frac{1}{N_\beta} \sum_{j_\beta=1}^{N_\beta} \mathbf{w}_{j_\beta \beta} \otimes \ \hat{\mathbf{x}}^\Gamma_{j_\beta \beta} = 0 \ , \tag{2.24}$$

or

$$\frac{1}{N_\alpha} (\mathcal{F}_\alpha \otimes \mathbf{I}) \ \hat{\mathbf{x}}^\Gamma_\alpha - \frac{1}{N_\beta} (\mathcal{F}_\beta \otimes \mathbf{I}) \ \hat{\mathbf{x}}^\Gamma_\beta = 0 \ , \tag{2.25}$$

in which cyclic harmonics of the two adjacent stages $\hat{\mathbf{x}}^\Gamma_\alpha$ and $\hat{\mathbf{x}}^\Gamma_\beta$ are coupled.

2.10.4 Restriction on the compatibility of the harmonics

The key point here consists in neglecting the distinct harmonics between the stages [30].

The set of fundamental harmonics is defined with respect to the stage with the smallest number of sectors (stage 1 for example): $k \in [1, N_1]$. The correspondence between the harmonics of the two stages is then defined according to a congruence rule corresponding to the aliasing of the Fourier transform (Figure 2.31).

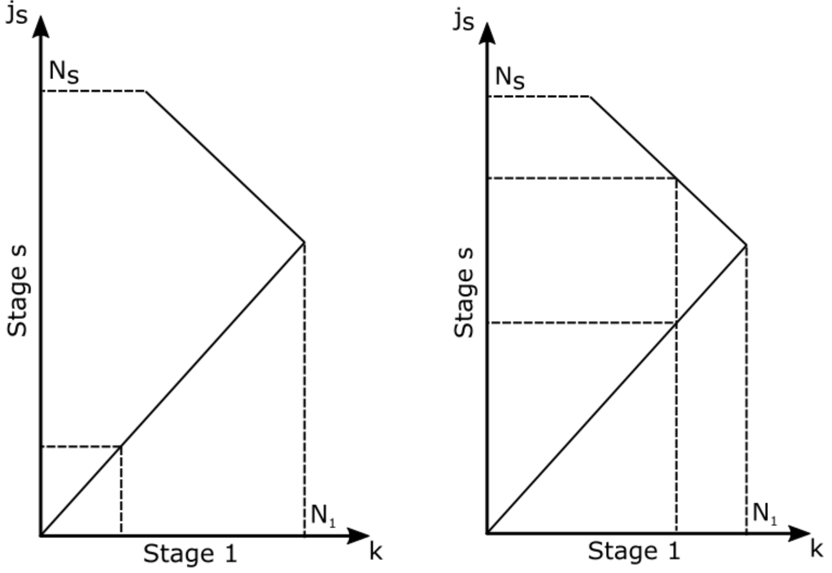

(a) (b)

Figure 2.31: Illustration of the rule concerning the correspondence between the harmonics of the two stages; (a) case of small harmonic index ($\mathbf{j}_s = k$) and (b) aliasing case ($\mathbf{j}_s = [k, 2N_1 - k]$) [16].

This defines a set of cyclic harmonics on stage s, denoted $\mathbf{j}_s$, conformable to the fundamental cyclic harmonic k,

$$\mathbf{j}_s = \left\{ j_{s,p} = (-1)^p (k-1) + 2 \left\lfloor \frac{p+1}{2} \right\rfloor N_s + 1, p \in \mathbb{N} \mid 1 \leq j_{s,p} \leq N_s \right\} , \tag{2.26}$$

which corresponds to aliasing in the discrete Fourier transform.

This restriction of coupling between equivalent harmonics k and $\mathbf{j}_s(k)$ means that only compatible harmonic motions are considered. Hence, Equation (2.25) is restricted to these compatible harmonics $\mathbf{j}_\alpha(k)$ and $\mathbf{j}_\beta(k)$ as

$$\frac{1}{N_\alpha} \sum_{j_\alpha \in \mathbf{j}_\alpha(k)} \mathbf{w}_{j_\alpha \alpha} \otimes \hat{\mathbf{x}}^{\Gamma}_{j_\alpha \alpha} - \frac{1}{N_\beta} \sum_{j_\beta \in \mathbf{j}_\beta(k)} \mathbf{w}_{j_\beta \beta} \otimes \hat{\mathbf{x}}^{\Gamma}_{j_\beta \beta} = 0 , \tag{2.27}$$

or defining Fourier matrices associated with a given set of harmonics $\mathbf{j} = (j_1, ..., j_n)$ as

$$\mathcal{F}_{\mathbf{j}s} = \begin{bmatrix} \mathbf{w}_{j_1 s} \\ \vdots \\ \mathbf{w}_{j_n s} \end{bmatrix} , \tag{2.28}$$

Equation (2.27) becomes

$$\frac{1}{N_\alpha}\left(\mathcal{F}_{\mathbf{j}_\alpha \alpha} \otimes \mathbf{I}\right)\ \hat{\mathbf{x}}^{\Gamma}_{j_\alpha \alpha} - \frac{1}{N_\beta}\left(\mathcal{F}_{\mathbf{j}_\beta \beta} \otimes \mathbf{I}\right)\ \hat{\mathbf{x}}^{\Gamma}_{j_\beta \beta} = 0\ , \tag{2.29}$$

in which vectors $\hat{\mathbf{x}}^{\Gamma}_{\mathbf{j}s}$ refer to the concatenation of vectors $\hat{\mathbf{x}}^{\Gamma}_{j_i s}$ for all $j_i \in \mathbf{j}$.

2.11 Mistuning in multi-stage bladed disks

To date, only few works have been conducted on mistuning in multi-stage assemblies. Bladed disks are usually studied as isolated systems. However, the presence of the other stage affects the dynamic behavior of the structure, and more particularly modifies the disk/drum flexibility. An important implication of the modified disk/drum flexibility is that the characteristics of the eigenfrequency veerings are also modified. This veering modification means that the mixture of blade and disk/drum dominance (i.e., the disk/drum-blade modal interaction) among the two mode pairs representing the veering is altered. This modification of the disk/drum-blade modal interaction may have a critical impact on mistuning sensitivity. Figure 2.30 gives an example of Bladh's results [2]. The single-stage model predicts a strongly localized mode, while the "actual" multi-stage mode shape exhibits a much milder deviation from a tuned, spatially extended behavior. Thus, from a mistuning sensitivity perspective, multi-stage dynamic analyses may be needed in order to yield sufficiently accurate representations of disk/drum flexibility and structural interstage coupling.

Avalos and Mignolet [107] developed an analytic formulation for the maximum amplification of blade response due to mistuning in multi-stage assemblies. This formula is an extension of the Whitehead factor in the multi-stage case:

$$\frac{1}{2}\left(1 + \sqrt{N_1 + N_2\left(\frac{g_2}{g_1}\right) + \ldots}\right)\ , \tag{2.30}$$

where N_s is the number of blades on stage s and $g_s = \mathbf{f}_s^T\ \mathbf{M}_s^{-1}\ \mathbf{f}_s$ with $\mathbf{f}_s$ the external force vector applied on stage s and $\mathbf{M}_s$ its mass matrix. For identical stages, this maximum equals the Whitehead limit observed with single stage structures but with a number of blades equal to sum of the numbers of blades of the coupled stages.

2.12 Reduced order model for multi-stage bladed disks

Some mono-stage reduced order modeling methods have been extended for multi-stage structures. The challenge is that the number of sectors of each stage is different, which breaks the cyclic symmetry property of the structure.

2.12.1 Extended SMART method

Bladh et al. [12] extended the SMART approach (Section 2.7.3) for the case of multi-stage structures. The assumptions, advantages and drawbacks of the method are summarized below.

Assumptions:

- Small mistuning ⟶ no mode shape modification, only frequency deviation ⟶ mistuned mode shapes represented by a linear combination of tuned mode shapes

Advantages:

- Accurate results

Drawbacks:

- Method complexity
- CMS strategy difficult to use in a design process

2.12.2 Song's method

Song et al. [108, 109] proposed a multi-stage reduced order modeling approach based on component mode synthesis (CMS) method (Section 2.7.1). Each stage is treated as a separated component, which retains the cyclic symmetry property. The computation of the component modes and of the constraint modes of each stage can be performed using the finite element model of its reference sector. However, the stages have different numbers of blades. To connect the stages together, a common basis of interface modes is defined using the Fourier series (the interface is axisymmetric). The constraint modes of each stage are projected on this common basis and the displacement compatibility condition is enforced. Then, in order to further reduce the size of the model, a second modal analysis is performed on the assembled model, which enables to retain only a small number of multi-stage modes. The resulting reduced order model has a compact size and keep a high accuracy comparing to the parent finite element model. In order to introduce mistuning, Song et al. [26] adapted the CMM method (Section 2.7.8) using the tuned single-stage modes as a basis for the mistuned model. The assumptions, advantages and drawbacks of the method are summarized below.

Assumptions:

- Small displacements at the interface blades/disk
- Common basis of interface modes defined using a Fourier basis, and displacement compatibility imposed

Advantages:

- General method (small and large mistuning, proportional or not)

Drawbacks:

- CMS strategy difficult to use in a design process

2.12.3 Laxalde's method

Laxalde et al. [110,111] developed a reduced order modeling method for multi-stage structures similar to Song's method (Section 2.12.2), and applied it for modal analysis and forced response computation. The method uses cyclic symmetry reduction to model each stage, and the interstage coupling is obtained by imposing the displacements compatibility condition at the interface. Sternschüss et al. [112–115] extended the method proposed by Laxalde et al. [110,111], representing the inter-sector elements as super-elements and where the stages are coupled by intermediate rings, which remove the problem of incompatible meshes (as illustrated in Figure 2.32). The mistuning is introduced as a modification of the modal stiffness of the blades. The perturbation is then projected in the global model space of the whole structure [16].

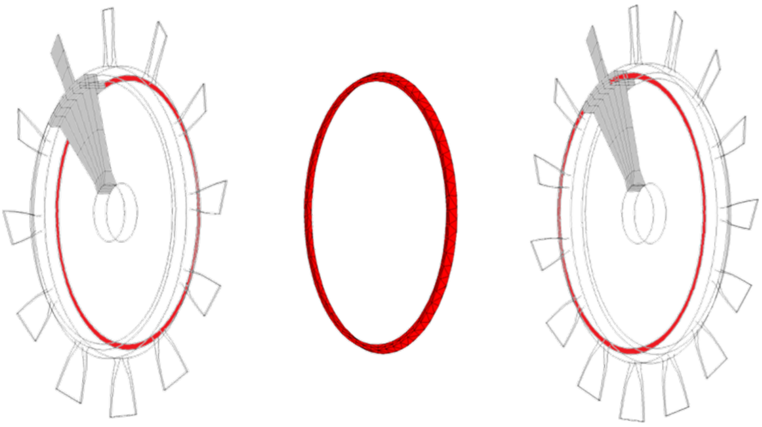

Figure 2.32: Stages coupled by intermediate rings [112].

The assumptions, advantages and drawbacks of the method are summarized below.

Assumptions:

- Linear applications (extended later by the authors to nonlinear with Fourier methods [116])
- Coupling achieved by enforcing continuity of displacements (or other variables) on the interstage boundary in the common physical base
- One-to-one nodal diameter coupling: neglect the coupling between "distinct" nodal diameters of each stage's base

Advantages:

- Direct handling of the sector FE model
- Realistic interstage coupling based on a cyclic recombination of the interface on the chosen nodal diameter
- Applicable for any dynamical problems in free and forced responses

Drawbacks:

- Method complexity
- Methodology looking for mono-harmonic (same harmonic index for both the disks) solution only and does not find multi-harmonic solutions normally present in the exact solution

2.12.4 Extended MMDA method

Sinha [117, 118] extended the MMDA method (Section 2.7.14) to create reduced order model for multi-stage structures with geometric mistuning from a parent finite element model. The method was first validated on a mistuned multi-stage lumped parameter model, in which stages were connected by discrete spring elements. The method was then applied on an academic two-stage bladed structure. The assumptions, advantages and drawbacks of the method are summarized below.

Assumptions:

- Perturbation located on the blade only

Advantages:

- Simple method
- Accurate results
- Geometric mistuning
- Applicable to large mistuning

Drawbacks:

- FE model of each blade geometry required

2.13 Mistuning identification method for multi-stage bladed disks

Song et al. [26, 119] extended the CMM identification method (Section 2.8.3) for the case of multi-stage structures. The deviation of the cantilevered blade eigenfrequencies of each blade of each stage are retrieved using measurement data. More modes have to be retained for multi-stage structures than for mono-stage ones, more particularly when strong coupled modes are present in the frequency range of interest. Therefore, a large number of measurement points is required. The assumptions, advantages and drawbacks of the method are summarized below.

Assumptions:

- Small mistuning (cantilevered blade mode shapes considered the same as that of the tuned cantilevered blade)
- Strain energy due to blade boundary displacement negligible

Advantages:

- Not limited to an isolated mode family
- Validated numerically

Drawbacks:

- Validated numerically without any signal noise
- Not validated experimentally
- Large numbers of measurement points required
- High number of retained modes needed

2.14 Conclusion

Tables 2.1, 2.2, 2.3 and 2.4 summarise the reduced order modeling and identification methods for both cases of mono-stage and multi-stage structures.

For mono-stage structures, the reduced order modeling techniques can be separated in two groups with different mistuning modeling approaches. Mistuning can be modelled as a perturbation of the modal properties of the blades (CMS, CMB, SMART, SNM, FMM, AMM, Petrov, CMM, IMM, NEWT and nonparametric methods), or as geometrical variations (SNC, Mbaye's and MMDA methods). The thesis focuses on the first category, which involves reduced computational times comparing to the ones with geometric mistuning. Among the different available techniques, the CMM method has several advantages. Small and large mistuning can be taken into account, the method enables to associate different mistuning values for each cantilevered blade modes, which gives accurate results even in veering zones, and an extension for multi-stage structure is available. An identification method is also associated to the reduced order modeling method. However, no experimental identification has been performed on a multi-stage structure to validate the method. In the followings, an experimental test procedure has been developed to perform mistuning identification. An extension of the method is also proposed for mass mistuning identification.

The nonparametric approach differs from the other methods (CMS, CMB, SMART, SNM, FMM, Petrov and CMM) in the way of introducing the uncertainties in the model. Both data and model uncertainties are taken into account in the method. In the followings, the nonparametric method is extended to handle multi-stage structures. The extended nonparametric approach is then compared to the CMM multi-stage method.

	Year	Small mistuning	Large mistuning	Proportional mistuning	Geometric mistuning	Veering zones
CMS	1983	✓	X	✓	X	X
CMB	1997	✓	✓	✓	X	X
SMART	2001	✓	X	✓	X	✓
SNM	2001	✓	X	✓	X	✓
FMM	2002	✓	X	✓	X	X
AMM	2008	✓	X	✓	X	X
Petrov	2002	✓	✓	✓	X	✓
CMM	2003	✓	✓	✓	X	✓
IMM	2011	✓	X	✓	X	✓
NEWT	2013	✓	X	✓	X	✓
SNC	2004	✓	✓	✓	X	✓
Non-param	2004	✓	✓	✓	X	✓
Mbaye	2010	✓	✓	X	✓	✓
MMDA	2007	✓	✓	X	✓	✓

Table 2.1: Comparison of the mono-stage reduced order modeling methods.

	Year	Small mistuning	Large mistuning	Proportional mistuning	Geometric mistuning	Veering zones	Validated experimentally
CMB ID	2001	✓	✓	✓	X	X	✓
FMM ID	2004	✓	X	✓	X	X	✓
CMM ID	2009	✓	✓	✓	X	✓	✓
BAE ID	2006	✓	-	✓	X	X	✓
MMDA ID	2004	✓	-	X	✓	✓	X
Non-param ID	2011	✓	✓	X	✓	✓	X

Table 2.2: Comparison of the mono-stage identification methods.

	Year	Small mistuning	Large mistuning	Proportional mistuning	Geometric mistuning	Veering zones
SMART	2001	✓	X	✓	X	✓
Song/CMM	2005	✓	✓	✓	X	✓
Laxalde	2007	✓	✓	✓	X	✓
MMDA	2008	✓	✓	X	✓	✓

Table 2.3: Comparison of the multi-stage reduced order modeling methods.

	Year	Small mistuning	Large mistuning	Proportional mistuning	Geometric mistuning	Veering zones	Validated experimentally
CMM ID	2001	✓	✓	✓	X	✓	X

Table 2.4: Summary of the multi-stage identification method.

Chapter 3

Mistuning identification for the mono-stage structure

In this Chapter, an efficient testing procedure is established to identify mistuning in a blisk using the CMM identification method. The tested structure is a mono-stage academic blisk. A based excitation with laser measurements is used. The experimental identification is validated by adding small masses on the structure.

3.1 Introduction

Different reduced-order modeling techniques have been developed to compute the dynamic behavior of mistuned bladed disks with reduced computational time [4–16]. These reduced-order models (ROMs), presented in Section 2.7, consist of low-order models of bladed disks based on the global finite element model of the structures. Using ROMs enables to run a large number of simulations with random mistuning patterns in order to retrieve the statistical distribution of the amplification of the forced response amplitudes for given amounts of mistuning. In parallel, identification methods have been developed to identify mistuning from the experimental frequency response of bladed structure [15, 17–19]. These methods have been reviewed in Section 2.8.

In this Chapter, the component mode mistuning (CMM) method developed by Lim [15] is used, in which the mistuning identified for each blade is represented as the variation of the cantilevered blade frequency. The theoretical developments of the CMM method are recalled at the beginning of this Chapter. An experimental modal analysis is performed on a mono-stage academic blisk in order to apply Lim's mistuning identification method. The frequency response function (FRF) is measured in terms of transmissibility using a base excitation with an electrodynamic shaker. The response of the structure is measured on each blade with a laser vibrometer.

3.2 Component Mode Mistuning (CMM) method

Lim [15] developed in his thesis two distinct approaches, known as Component Mode Mistuning (CMM) methods: a general method involving large models and potentially long computation times, and a simplified version of this method based on the work of Yang and Griffin [74] and Bladh [9]. The second approach, which is used in this work, is a simplified version that may be considered assuming that the blade mistuning is small compared to nominal properties in the modal domain, and that the bladed disk has normal modes closely spaced in a frequency range. The second assumption means that the tuned modes outside of the frequency range of interest can be ignored in modeling the mistuned system.

In the direct approach, a reduced-order model (ROM) is constructed based on the CMM method. The theoretical developments are given in Section 3.2.1. Based on this ROM, the mistuned properties, such as the mistuned eigenfrequencies and the mistuned mode shapes, can be computed for a given mistuning pattern (as illustrated in Figure 3.1 on the left).

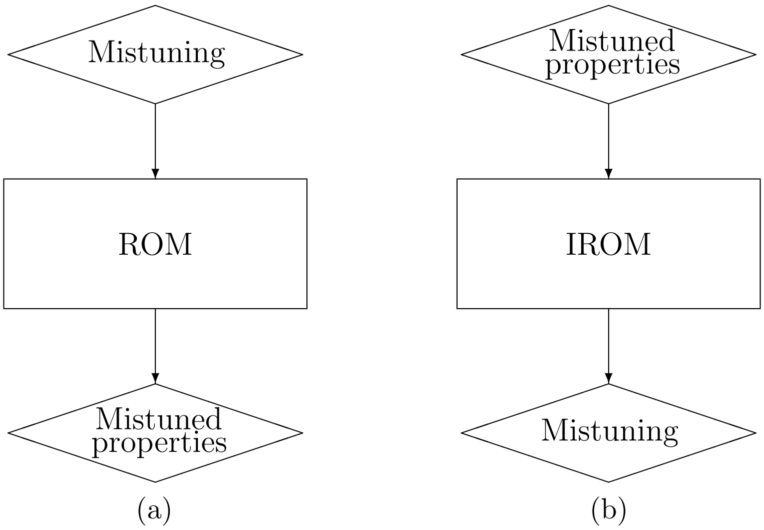

Figure 3.1: CMM: Direct problem (a) and inverse problem (b).

In the case of the inverse problem, developed in Section 3.2.2, the mistuned eigenfrequencies and mode shapes are given by the experiments, and the inverse reduced-order model (IROM) enables to retrieve the mistuning of the structure (as illustrated in Figure 3.1 on the right).

3.2.1 Reduced-order model

The equations of motion in the physical space are given by

$$\mathbf{M}\ddot{\mathbf{x}} + \mathbf{C}\dot{\mathbf{x}} + \mathbf{K}\mathbf{x} = \mathbf{f} \ , \tag{3.1}$$

where $\mathbf{M}$, $\mathbf{C}$ and $\mathbf{K}$ are respectively the mass, damping and stiffness matrices, $\mathbf{x}$ is the displacement vector, and $\mathbf{f}$ is the force vector. Equation (3.1) can be projected in the modal space using

$$\mathbf{x} = \mathbf{\Phi} \ \mathbf{p} \ , \tag{3.2}$$

where $\mathbf{\Phi}$ is the tuned mode shapes of the system (the number of retained modes in the $\mathbf{\Phi}$ matrix is noted m), and $\mathbf{p}$ is the modal coordinates, and defining $\mathbf{F} = \mathbf{\Phi}^T \mathbf{f}$ the modal participation factor of the load $\mathbf{f}$:

$$\mathbf{\Phi}^T \mathbf{M} \mathbf{\Phi} \; \ddot{\mathbf{p}} + \mathbf{\Phi}^T \mathbf{C} \mathbf{\Phi} \; \dot{\mathbf{p}} + \mathbf{\Phi}^T \mathbf{K} \mathbf{\Phi} \; \mathbf{p} = \mathbf{F} \; , \tag{3.3}$$

or in the frequency domain, and considering a modal damping (γ is the damping coefficient),

$$- \omega^2 \mathbf{\Phi}^T \mathbf{M} \mathbf{\Phi} \; \mathbf{p} + (1 + i\gamma) \, \mathbf{\Phi}^T \mathbf{K} \mathbf{\Phi} \; \mathbf{p} = \mathbf{F} \; . \tag{3.4}$$

The mistuning is then introduced in the equations of motion. A small mistuning is considered here i.e., the perturbation of the nominal modal properties of the system is small. This implies that the mistuned mode shapes can be expressed as a combination of tuned mode shapes in the frequency range of interest. Assuming that the mistuning is represented by a stiffness modification, the mistuned equations of motion can be written as

$$- \omega^2 \mathbf{\Phi}^T \mathbf{M}_0 \mathbf{\Phi} \; \mathbf{p} + (1 + i\gamma) \, \mathbf{\Phi}^T \left(\mathbf{K}_0 + \mathbf{K}^\delta \right) \mathbf{\Phi} \; \mathbf{p} = \mathbf{F} \; , \tag{3.5}$$

in which $\mathbf{M}_0$ and $\mathbf{K}_0$ represent respectively the tuned mass and stiffness matrix, and $\mathbf{K}^\delta$ represents the perturbation in the stiffness matrix due to mistuning.

Then, considering that the mode shapes are mass-normalized, Equation (3.5) becomes

$$- \omega^2 \; \mathbf{I} \; \mathbf{p} + (1 + i\gamma) \left[\mathbf{\Lambda}_0 + \mathbf{\Phi}^T \mathbf{K}^\delta \mathbf{\Phi} \right] \mathbf{p} = \mathbf{F} \; , \tag{3.6}$$

where $\mathbf{I}$ is the identity matrix and $\mathbf{\Lambda}_0$ is the generalized stiffness matrix.

Then, three assumptions are performed in CMM. First, the mistuning is considered to be located on the blades only and not on the disk (as illustrated in Figure 3.2), since a mistuning located on the blades is known to have a larger impact than disk mistuning. This implies that matrix $\mathbf{K}^\delta$ is non-zero only in the blade portion i.e.,

$$\mathbf{\Phi}^T \mathbf{K}^\delta \mathbf{\Phi} = \sum_{n=1}^{N} \mathbf{\Phi}_n{}^T \mathbf{K}_n^\delta \; \mathbf{\Phi}_n \; , \tag{3.7}$$

where N is the number of blades, $\mathbf{K}_n^\delta$ is the stiffness matrix restricted to the degrees of freedom of blade n ($n = 1, ..., N$), and $\mathbf{\Phi}_n$ is the matrix of tuned mode shapes restricted to the degrees of freedom of blade n.

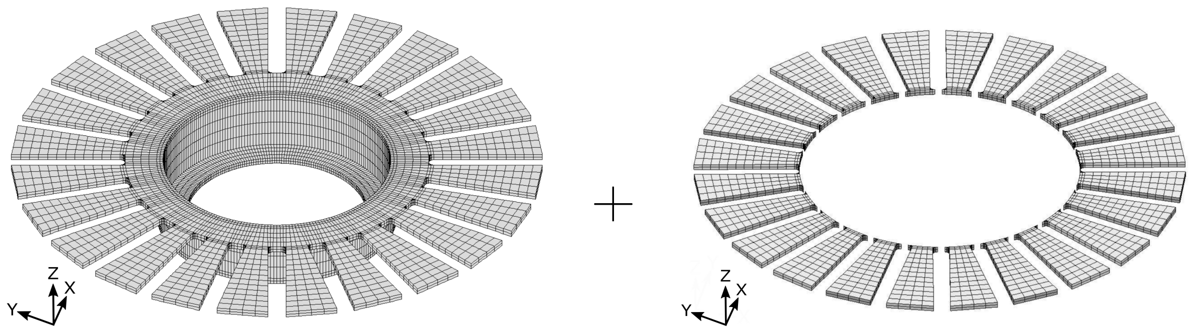

$\mathbf{K}_0$ $\mathbf{K}^{\delta}$

Figure 3.2: Stiffness perturbation only applied on the blade degrees of freedom.

The second assumption in CMM is that the mode shape matrix $\mathbf{\Phi}_n$ of blade n is written as a superposition of cantilevered blade modes i.e.,

$$\mathbf{\Phi}_n = \mathbf{\Phi}^{CB}\mathbf{Q}_n \ , \tag{3.8}$$

where $\mathbf{\Phi}^{CB}$ is the cantilevered blade modes for the nominal blade and $\mathbf{Q}_n$ is the modal participation factor of $\mathbf{\Phi}^{CB}$ into the mistuned mode shape of the blade's degrees of freedom $\mathbf{\Phi}_n^M$. Introducing Equation (3.8) in Equation (3.7) leads to

$$\mathbf{\Phi}^T\mathbf{K}^{\delta}\mathbf{\Phi} = \sum_{n=1}^{N} {\mathbf{Q}_n}^T {\mathbf{\Phi}^{CB}}^T \mathbf{K}_n^{\delta} \ \mathbf{\Phi}^{CB}\mathbf{Q}_n \ . \tag{3.9}$$

The expression ${\mathbf{\Phi}^{CB}}^T\mathbf{K}_n^{\delta} \ \mathbf{\Phi}^{CB}$ in Equation (3.9) have out-of-diagonal terms. However, one tuned cantilevered blade mode is usually dominant if mistuning is small. Therefore, the expression ${\mathbf{\Phi}^{CB}}^T\mathbf{K}_n^{\delta} \ \mathbf{\Phi}^{CB}$ is diagonally dominant and the out-of-diagonal terms, which represent the coupling between cantilevered blade modes, can be neglected. This third assumption enables to simplify Equation (3.9) as

$$\mathbf{\Phi}^T\mathbf{K}^{\delta}\mathbf{\Phi} = \sum_{n=1}^{N} {\mathbf{Q}_n}^T \operatorname{diag}_{r\in R}\left(\lambda_{n,r}^{\delta}\right) \mathbf{Q}_n \ , \tag{3.10}$$

where R is the set of retained cantilevered blade modes and $\lambda_{n,r}^{\delta} = {\mathbf{\Phi}_r^{CB}}^T\mathbf{K}_n^{\delta} \ \mathbf{\Phi}_r^{CB}$ is the eigenvalue deviation of the r^{th} cantilevered blade mode of blade n. Introducing Equation (3.10) in Equation (3.6) yields

$$-\omega^2\mathbf{I}\mathbf{p} + (1+i\gamma)\left[\mathbf{\Lambda}_0 + \sum_{n=1}^{N} {\mathbf{Q}_n}^T \operatorname{diag}_{r\in R}\left(\lambda_{n,r}^{\delta}\right)\mathbf{Q}_n\right]\mathbf{p} = \mathbf{F} \ . \tag{3.11}$$

The computation of the participation factors $\mathbf{Q}_n$ in Equation (3.11) is performed by rewriting Equation (3.8). First, Equation (3.8) is pre-multiplied by ${\mathbf{\Phi}^{CB}}^T\mathbf{K}^{CB}$, such as

$${\mathbf{\Phi}^{CB}}^T\mathbf{K}^{CB}\mathbf{\Phi}_n = {\mathbf{\Phi}^{CB}}^T\mathbf{K}^{CB}\mathbf{\Phi}^{CB}\mathbf{Q}_n \ , \tag{3.12}$$

or

$$\mathbf{\Phi}^{CB^T}\mathbf{K}^{CB}\mathbf{\Phi}_n = \mathbf{\Lambda}^{CB}\mathbf{Q}_n \ , \tag{3.13}$$

where $\mathbf{\Lambda}^{CB}$ is a diagonal matrix containing the squared eigenfrequencies of the cantilevered blade modes. Finally, the expression of the participation factor $\mathbf{Q}_n$ can be written as

$$\mathbf{Q}_n = \mathbf{\Lambda}^{CB^{-1}}\mathbf{\Phi}^{CB^T}\mathbf{K}^{CB}\mathbf{\Phi}_n \ . \tag{3.14}$$

Using Equations (3.11) and (3.14), the mistuned properties of the system can be computed for a given mistuning pattern. All the needed input data can be retrieved from two finite element models:

- The finite element model of the tuned structure, which gives the tuned mode shapes restricted to the blades degrees of freedom, $\mathbf{\Phi}_n$, and the eigenvalues of the multi-stage tuned system in order to obtain $\mathbf{\Lambda}_0$.

- The finite element model of the blade clamped at its basis, which enables to compute the cantilevered blade eigenvalues of in order to construct $\mathbf{\Lambda}^{CB}$, the cantilevered blade modes $\mathbf{\Phi}^{CB}$, and the cantilevered blade stiffness matrix $\mathbf{K}^{CB}$.

3.2.2 Inverse reduced-order model

In this Section, the identification method for the mistuning parameters is presented. The numerical developments are based on the equations in Section 3.2.1.

Reorganizing the terms of Equation (3.11), one obtains

$$\sum_{n=1}^{N} \mathbf{Q}_n{}^T \operatorname{diag}_{r \in R}\left(\lambda^{\delta}_{n,r}\right) \mathbf{Q}_n \ \mathbf{p} = \frac{1}{(1+i\gamma)} \left[\mathbf{F} + \omega^2 \mathbf{I}\mathbf{p} - (1+i\gamma)\,\mathbf{\Lambda}_0 \ \mathbf{p}\right] \ . \tag{3.15}$$

Equation (3.15) is linear in $\lambda^{\delta}_{n,r}$. The number of unknown factors is equal to the number of blades N multiplied by the number of retained cantilevered blade modes N^{CB}. Considering that m modes are measured, Equation (3.15) can be written as

$$\begin{bmatrix} \mathbf{Q}_{1,1}{}^T\mathbf{Q}_{1,1} \ \mathbf{p}_1 & \mathbf{Q}_{1,2}{}^T\mathbf{Q}_{1,2} \ \mathbf{p}_1 & \cdots & \mathbf{Q}_{N,N^{CB}}{}^T\mathbf{Q}_{N,N^{CB}} \ \mathbf{p}_1 \\ \mathbf{Q}_{1,1}{}^T\mathbf{Q}_{1,1} \ \mathbf{p}_2 & \mathbf{Q}_{1,2}{}^T\mathbf{Q}_{1,2} \ \mathbf{p}_2 & \cdots & \mathbf{Q}_{N,N^{CB}}{}^T\mathbf{Q}_{N,N^{CB}} \ \mathbf{p}_2 \\ \vdots & & \cdots & \vdots \\ \mathbf{Q}_{1,1}{}^T\mathbf{Q}_{1,1} \ \mathbf{p}_m & \mathbf{Q}_{1,2}{}^T\mathbf{Q}_{1,2} \ \mathbf{p}_m & \cdots & \mathbf{Q}_{N,N^{CB}}{}^T\mathbf{Q}_{N,N^{CB}} \ \mathbf{p}_m \end{bmatrix} \begin{bmatrix} \lambda^{\delta}_{1,1} \\ \lambda^{\delta}_{1,2} \\ \vdots \\ \lambda^{\delta}_{N,N^{CB}} \end{bmatrix} =$$

$$\frac{1}{(1+i\gamma)} \begin{bmatrix} \mathbf{F}_1 + \omega_1^2 \mathbf{p}_1 - (1+i\gamma)\,\mathbf{\Lambda}_0 \ \mathbf{p}_1 \\ \mathbf{F}_2 + \omega_2^2 \ \mathbf{p}_2 - (1+i\gamma)\,\Lambda_0 \ \mathbf{p}_2 \\ \vdots \\ \mathbf{F}_m + \omega_m^2 \ \mathbf{p}_m - (1+i\gamma)\,\mathbf{\Lambda}_0 \ \mathbf{p}_m \end{bmatrix} \ , \tag{3.16}$$

where $\mathbf{p}_k$, $\mathbf{F}_k$ and ω_k, with $k = 1, ..., m$, are the data related to the k^{th} measured mode, and $\mathbf{Q}_{n,r}$ refers to the r^{th} lines of $\mathbf{Q}_n$. Moreover, if the frequencies ω_k ($k = 1, ..., m$) are chosen to be the eigenfrequencies of the system, the force vector $\mathbf{F}_k$ can be neglected. This group of equations can be divided in a set of real equations and a set of imaginary equations. Since the mistuning parameters are real, they can be obtained by solving both set of equations.

3.2.3 Identification using the experimental data

In the case of the direct problem, the mistuning is known as well as the excitation force. The only unknown factor is the $\mathbf{p}$ vector, which can be determined at each frequency ω. The mistuned FRF can be computed for each mistuning pattern.

However, in the case of the inverse problem, ω, $\mathbf{p}$ and $\mathbf{F} = \mathbf{\Phi}^T\mathbf{f}$ are determined by the experimental tests, and the unknown factors are the $\lambda^{\delta}_{n,r}$ terms. The modal coordinates $\mathbf{p}$ can be computed based on the measured physical displacements as

$$\mathbf{x}_{exp} = \mathbf{\Phi}_{exp} \, \mathbf{p} \ , \tag{3.17}$$

where $\mathbf{x}_{exp}$ contains the physical displacement at the measured degrees of freedom, and $\mathbf{\Phi}_{exp}$ is a matrix that contains the tuned displacements of the measured degrees of freedom. If the matrix $\mathbf{\Phi}_{exp}$ is not a square matrix (i.e., if the number of measured degrees of freedom is larger than $N * N^{CB}$), the modal coordinates $\mathbf{p}$ are obtained by solving the least squares problem.

3.3 Experimental testing procedure

A simple test procedure is established, based on Equation (3.16) of the CMM method:

1. A base excitation is used to excite the structure in the frequency range of interest (other excitation techniques, such as hammer excitation for example, could also be used). The response of the structure is measured on each blade.

2. A stabilization diagram is constructed based on the FRF measured on each blade.

3. The eigenfrequencies and mode shapes can be retrieved using the stabilization diagram.

4. The modal coordinates $\mathbf{p}$ are computed based on the measured physical displacements $\mathbf{x}_{exp}$ using Equation (3.17).

5. Since ω and $\mathbf{p}$ are known from the experimental tests, the unknown factors in Equation (3.16) are the $\lambda^{\delta}_{n,r}$ and the mistuning can be computed.

3.4 Experimental vibration measurements

Experimental tests are performed on a mono-stage academic blisk. The assumptions of the CMM method are discussed and the experimental tests using a laser vibrometer are presented.

3.4.1 Presentation of the tested structure

The considered structure is an academic mono-bloc bladed structure of 24 sectors. As chosen during the design process (Appendix A.2), the structure is made of aluminum. The material and geometric characteristics are given in Table 3.1, and the CAD is shown in Figure 3.3. The detailed geometry of the structure can be found in the Appendix B.

Number of sectors (N) [-]	24
Young's modulus [MPa]	71 000
Density [kg/m^3]	2700
External diameter [mm]	420
Internal diameter [mm]	186
Thickness [mm]	5
Height [mm]	53
Blade length [mm]	86
Blade width [mm]	40

Table 3.1: Material and geometric properties of the mono-stage academic structure.

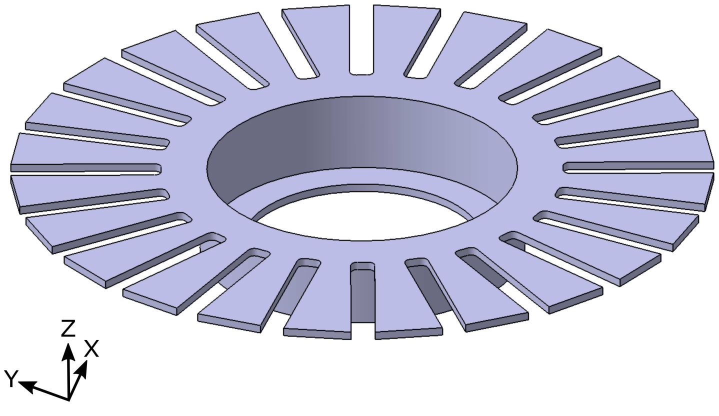

Figure 3.3: CAD of the mono-stage academic bladed structure.

A finite element model of the tuned structure has been constructed using the FE software SAMCEF [120]. The cyclic symmetry property has been applied to reduce the computational time and resources. An analysis on the mesh refining can be found in the Appendix C, in order to get accurate modal properties with reduced computational times. The reference sector of the selected mesh is shown in Figure 3.4(a). The mesh totalizes

8 496 degrees of freedom for the reference sector and is made of hexahedral volumic elements. Then, a recombined mesh (360°) is shown in Figure 3.4(b), with the reference sector in dark gray. This 360° finite element model will be used for the validation process when introducing a different mistuning for each blade, which breaks the cyclic symmetric property of the structure.

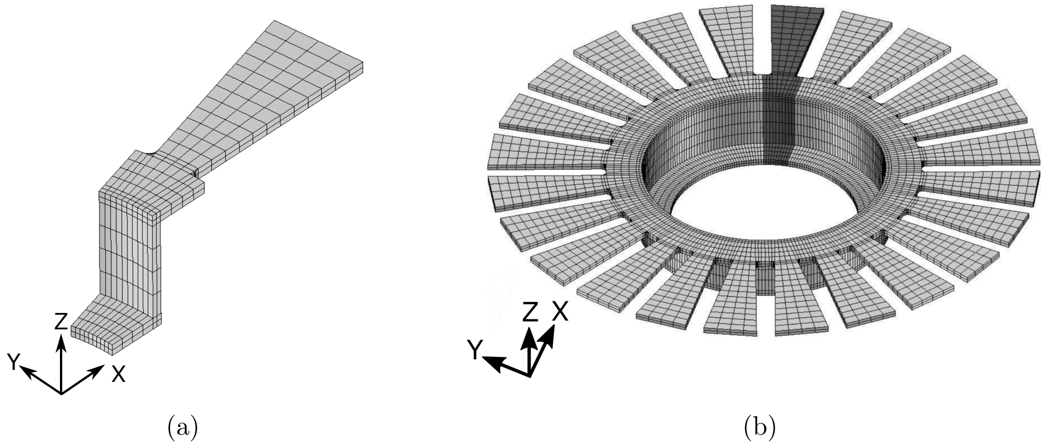

(a) (b)

Figure 3.4: Finite element model of the reference sector of the academic structure (a) and the recombined finite element model with the reference sector in dark gray (b).

The structure is clamped at its basis such that the boundary conditions respect the cyclic symmetry property. For the experiments, 24 (i.e., the number of sectors) fixation points are considered to respect the cyclic symmetry property (Figure 3.5(a)). In the finite element model, the modeling of each bolted connection has not been considered and a 360° clamping is considered (Figure 3.5(b)).

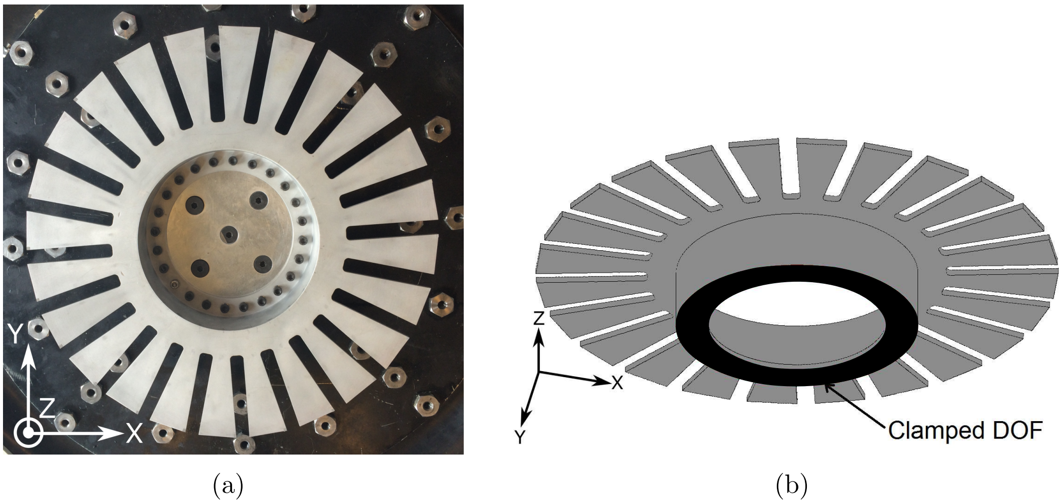

(a) (b)

Figure 3.5: Experimental (a) and numerical (b) clamping conditions.

Based on the cyclic symmetric finite element model, the SAFE diagram (Singh's Advanced Frequency Evaluation diagram i.e., the eigenfrequencies in function of the number of nodal diameters) of the mono-stage structure is constructed. Figure 3.6 shows the SAFE diagram restricted to the first family of mode i.e., the first bending modes of the blades (1B modes).

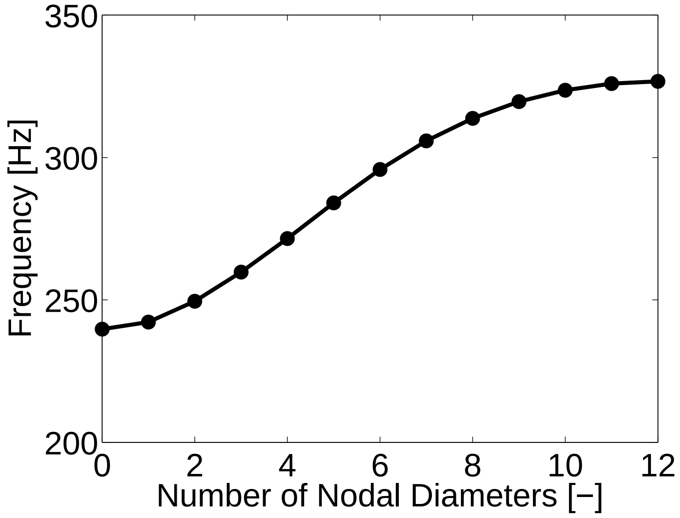

Figure 3.6: SAFE diagram of the academic structure restricted to the 1B mode family.

3.4.2 Verification of CMM assumptions

In the used version of the CMM method, the mistuning is assumed to be small, which is realistic for the considered case. The structure has a simplified geometry and the manufacturing tolerances are indeed of the order of 0.1 mm for blade length of 90 mm, which results in a few percents of blade mistuning, which satisfied the assumption of CMM.

The second assumption of the CMM method is a high modal density. The first family of modes is chosen in this work to apply Lim's identification method because they respond at low frequencies. Therefore, they are more easily experimentally excited with a global excitation (base excitation with a shaker), and this family is well separated from the other ones. The range of frequency is 240 Hz (0 nodal diameter mode) to 320 Hz (12 nodal diameters mode) as can be seen in Figure 3.6. Despite the fact that the modal density seems to be low in comparison to what may be observed on industrial blisks, the CMM method still can be applied because only perturbation in the stiffness matrix is considered and the studied mode family is well isolated.

3.4.3 Measurements using a laser vibrometer

Experimental tests are performed with a laser vibrometer. The laser has the advantage to be a non-contacting device. The measurement is not disturbed by contact or additional masses on the structure. Indeed, the first tests were conducted with a microaccelerometer, and its influence has been analyzed in Appendix D. The impact of the microaccelerometer on the frequency was found to be negligible. However, the errors on the mode shapes were large, which perturbed the identification process.

Test set-up

The academic structure and the test set-up are shown in Figure 3.7. The structure is clamped by its basis with 24 fixation points (as shown in Figure 3.5(a)) in order to keep the cyclic symmetric property: the academic structure has 24 sectors and one fixation point in the center of each sector has been considered. A base excitation is applied with an electrodynamic shaker in the axial direction (Z-axis). A laser vibrometer is used to measure the response of the structure. An accelerometer measures the acceleration of the shaker in order to get the force injected by the shaker. The used acquisition system is LMS Test.Lab [121]. The test is performed at constant temperature (20°C).

A periodic chirp is used to excite the structure, with a resolution of 0.02 Hz. The frequency range is 200 to 400 Hz i.e., the 1B modes. One measurement point is considered on each blade tip.

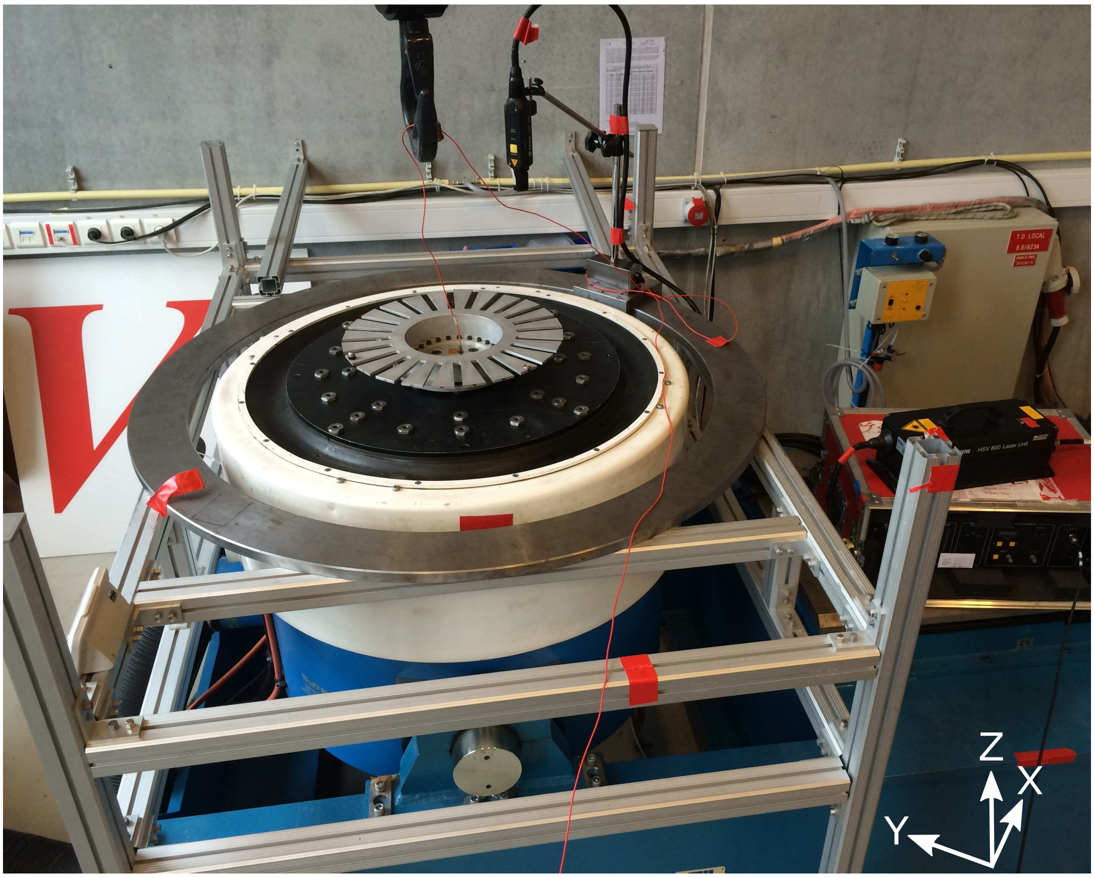

Figure 3.7: Academic structure and test set-up.

Stabilization diagram

Figure 3.8 presents the stabilization diagram obtained using the PolyMax method [122] available in the LMS Test.Lab software [121]. The frequency band is [240-340] Hz i.e., including all the peaks corresponding to 1B modes. The obtained FRF for all measurement points are superimposed. Physical poles can be easily localized since they draw a vertical line of s symbols (s is the symbol corresponding to stabilized poles).

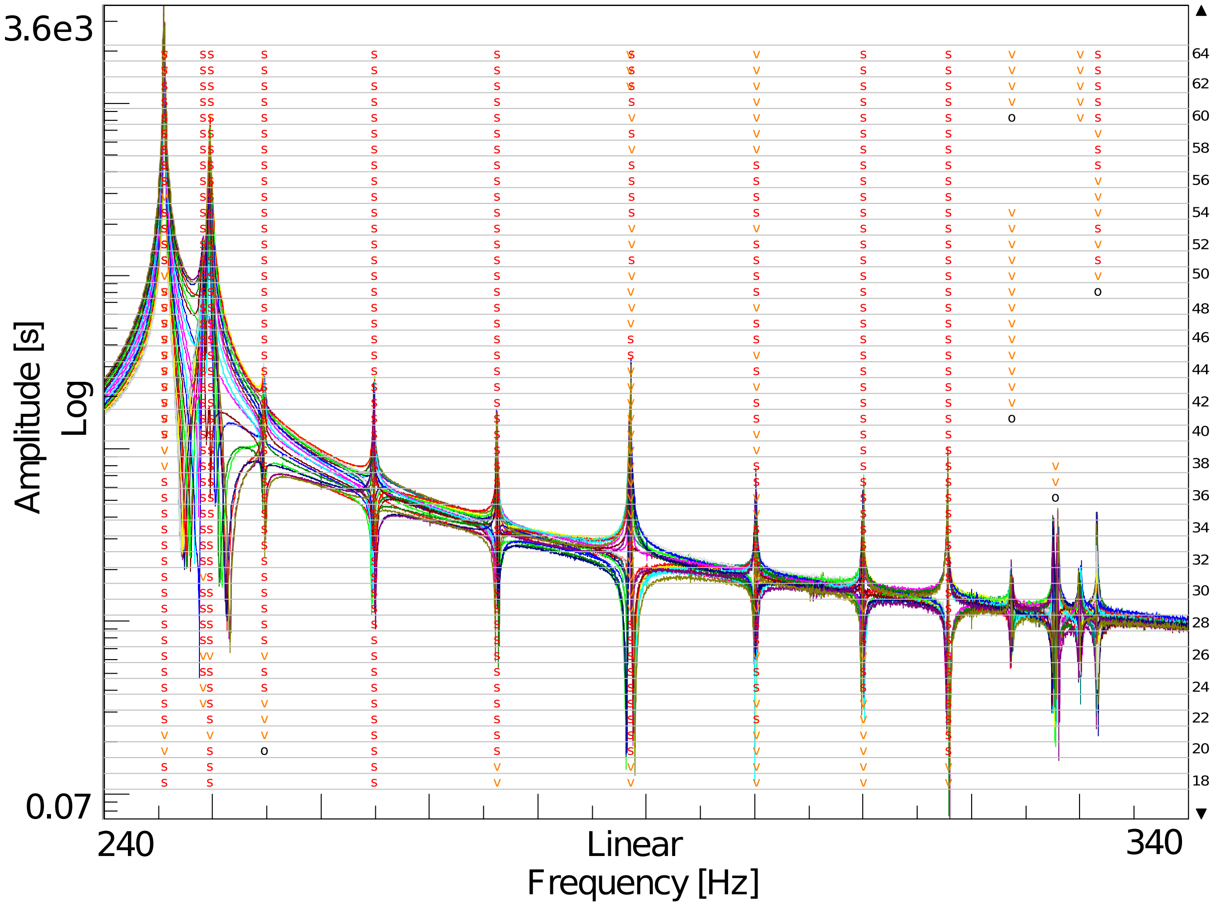

Figure 3.8: Stabilization diagram: 1B modes. Symbols have following meaning: o – new pole; f – stable frequency; d – stable frequency and damping; v – stable frequency and eigenvector; s – all criteria stable.

Frequencies and mode shapes

For each peak of the stabilization diagram, a corresponding frequency and mode shape is computed with the PolyMax method [122]. The frequencies of all 1B modes are given in Table 3.2.

Frequency [Hz]	Main harmonic [-]
245.5	0
249.1 - 249.7	1
254.7	2
264.9	3
276.2	4
288.6	5
300.1	6
310.0	7
317.8	8
323.7	9
327.5 - 328.0	10
330.0	11
331.6	12

Table 3.2: Eigenfrequencies of the 1B modes.

The three 1B modes used for the identification process are the three first modes, at a frequency of 245.5, 249.1 and 249.7 Hz respectively, which are the most excited with the base excitation. Their mode shapes (one measurement point per blade is considered) are respectively presented in Figures 3.9(a), 3.9(b) and 3.9(c) (left column). The harmonic contents of both modes are also given in Figures 3.9(a), 3.9(b) and 3.9(c) (right column). The first mode mainly looks like an umbrella mode since its main component is a 0 nodal diameter. The 1 nodal diameter's harmonic also participates for this mode. The second retained mode has the 1 nodal diameter's harmonic as main component. The 0 and 2 harmonics slightly participate too (a mistuned mode shape can be seen as a linear combination of tuned mode shapes). The third retained mode also has the 1 nodal diameter's harmonic as main component. The 0 and 2 harmonics participate too. The second and third modes are almost orthogonal.

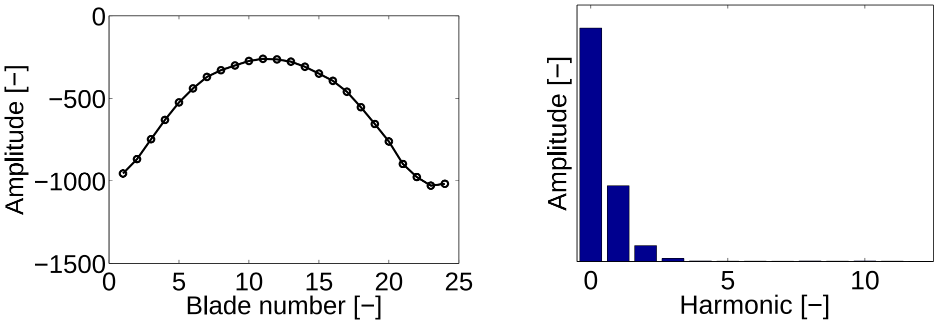

(a) Frequency of 245.5 Hz

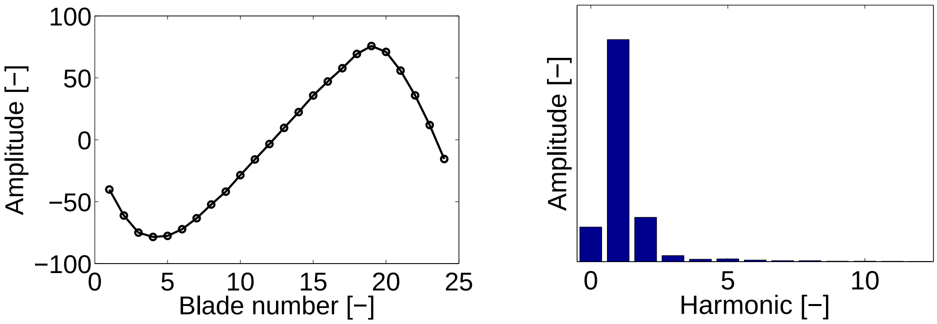

(b) Frequency of 249.1 Hz

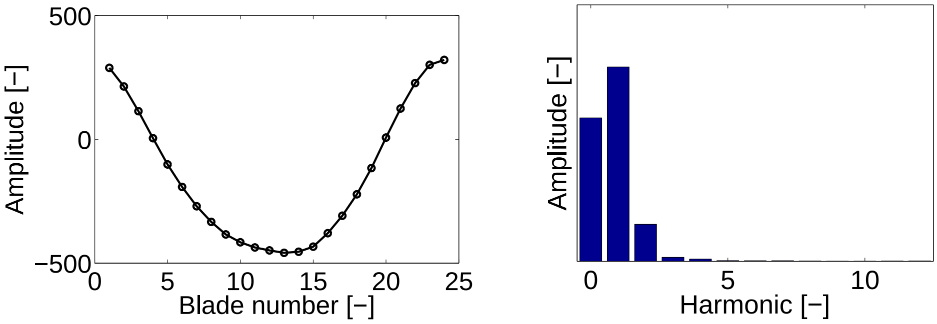

(c) Frequency of 249.7 Hz

Figure 3.9: Mode shapes (left column) and harmonic content (right column) corresponding to the peaks at a frequency of 245.5 Hz (a), 249.1 Hz (b) and 249.7 Hz (c).

The CMM identification method is applied using the three first experimental modes as input data. The obtained mistuning for each blade of the academic structure is presented in Figure 3.10. A mistuning up to 7% is found for blade number 12. These identified values are used in the following Sections to correlate a numerical model with the experimental results on the academic structure.

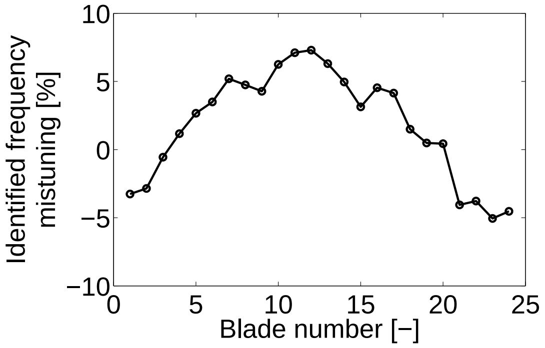

Figure 3.10: Identified mistuning.

3.5 Validation of the identified mistuning

In order to validate the mistuning identification method, the same test procedure is repeated, using a laser vibrometer to measure the response on each blade. The only difference is that small lumped masses are added at the top of some blades as a controlled mistuning, as shown in Figure 3.11. Table 4.2 provides the amount and the location of the additional masses.

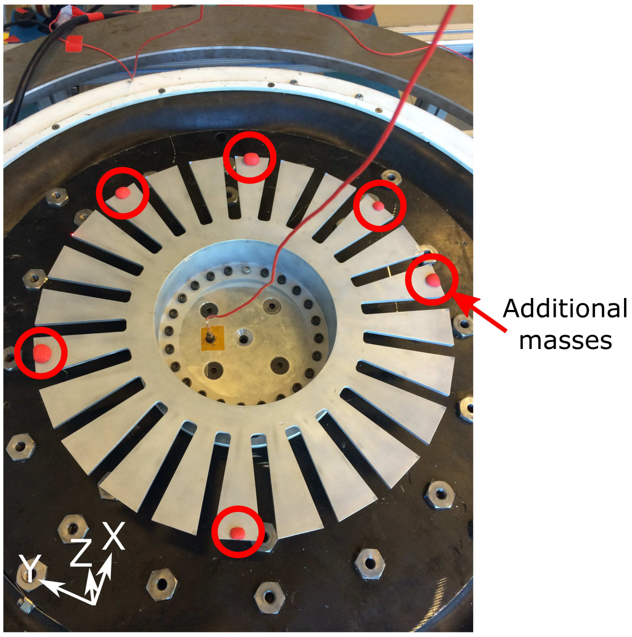

Figure 3.11: Test set-up with small lumped masses added.

The addition of masses on different blades can be seen as a perturbation of the eigenfrequencies, and therefore of the stiffness mistuning, of these blades. The aim of this Section is to identify the mistuning of the perturbed system.

Location [-]	Mass [g]
Blade 2	1.03
Blade 4	0.48
Blade 7	1.96
Blade 10	1.10
Blade 14	2.09
Blade 19	0.42

Table 3.3: Amount and location of the additional masses.

The test conditions remain identical to the ones presented in Section 3.4. The stabilization diagram obtained using the PolyMax method [122] is shown in Figure 3.12. A larger number of peaks is observed compared to the diagram obtained without additional masses since the test structure exhibits a larger mistuning due to the addition of masses. The frequencies and mode shapes of each peak are retrieved with the PolyMax method (shown in Figure 3.13) and used in the identification method to compute the mistuning of each blade for the perturbed system.

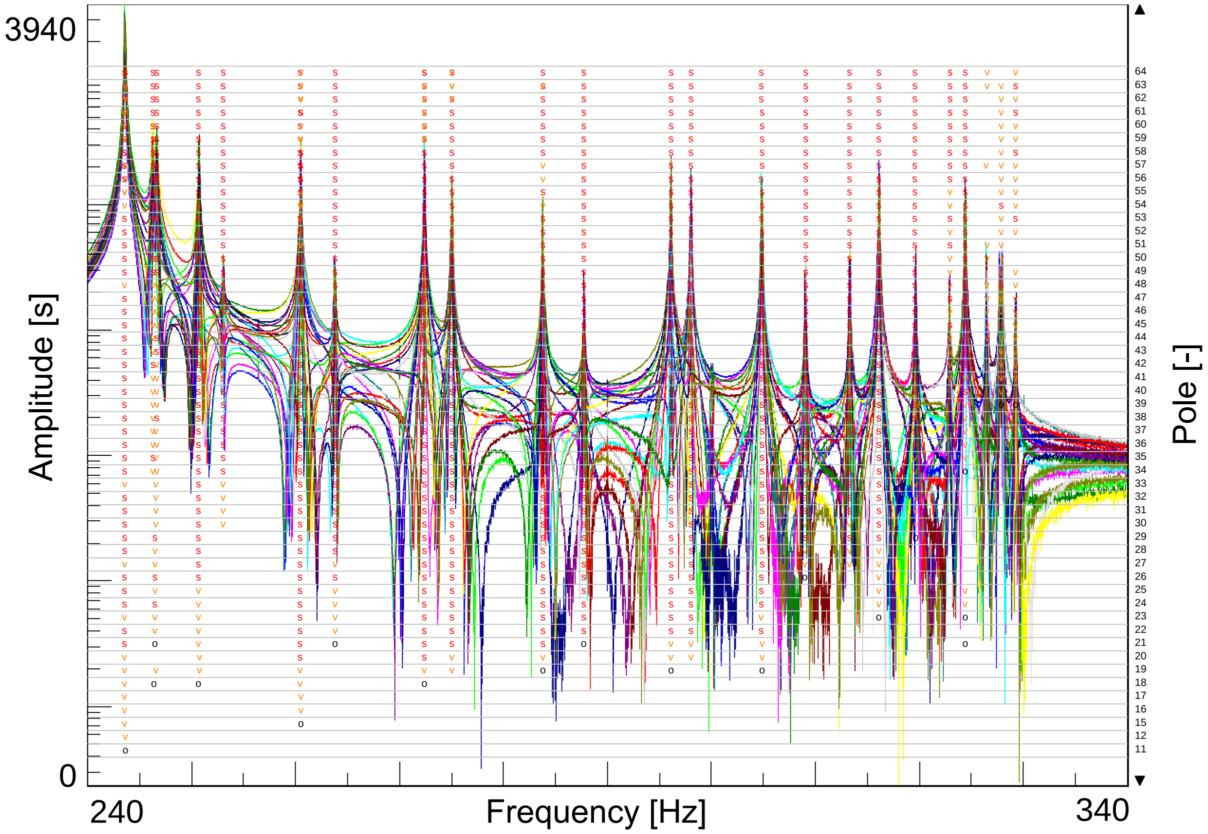

Figure 3.12: Stabilization diagram obtained with the additional masses. Symbols have following meaning: o – new pole; f – stable frequency; d – stable frequency and damping; v – stable frequency and eigenvector; s – all criteria stable.

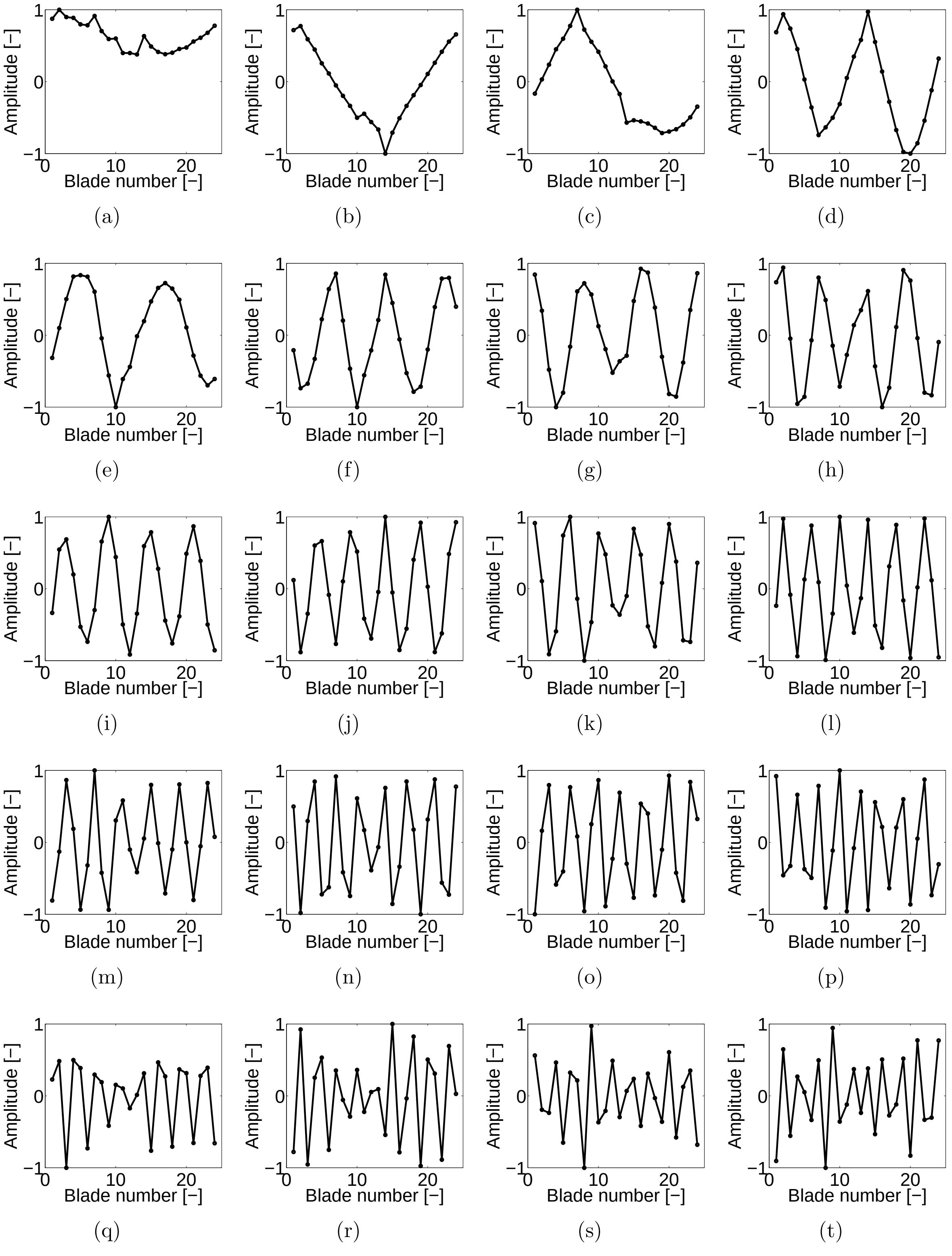

(a) (b) (c) (d) (e) (f) (g) (h) (i) (j) (k) (l) (m) (n) (o) (p) (q) (r) (s) (t)

Figure 3.13: Experimental mode shapes with additional masses.

The same procedure is applied to identify mistuning on the perturbed system i.e., the experimental eigenfrequencies and mode shapes are used to retrieve mistuning. The mistuning obtained using measurements on the perturbed structure is shown in Figure 3.14. The mistuning obtained previously i.e., without masses, is superimposed. The mistuning values become negative for the blades where the masses are located because the addition of mass decreases their clamped blade eigenfrequencies.

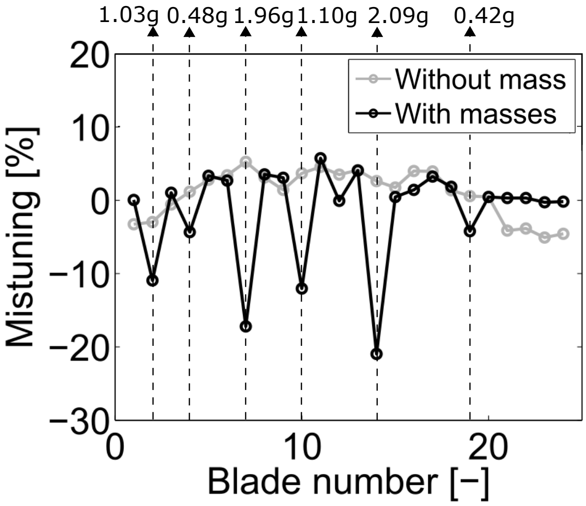

Figure 3.14: Comparison of mistuning obtained with the initial structure and with the structure when adding small lumped masses.

Then, in order to validate the perturbed mistuning, a finite element model is constructed using the SAMCEF software [120]. The finite element model is constructed as followed:

- Since the stiffness mistuning of each blade of the non-perturbed structure has been identified in Section 3.4, a different Young's modulus is applied on each blade in the finite element model, as illustrated in Figure 3.15 (the blades have different colors in Figure 3.15, which correspond to different values of Young's modulus). Therefore, the finite element model represents the structure without masses.
- Then, small lumped masses are added in the finite element model at the same location than the experiment (black circles in Figure 3.15).

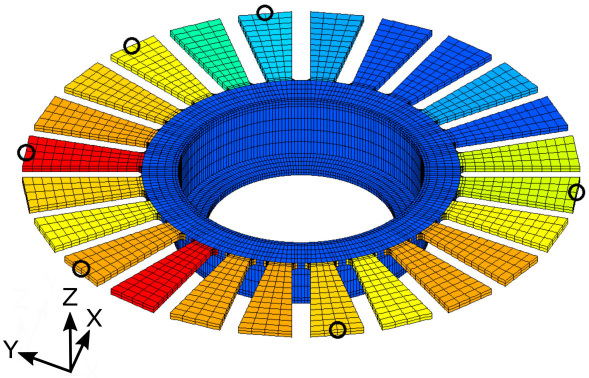

Figure 3.15: Finite element model with the identified mistuning on each blade, and small lumped masses.

Eigenfrequencies and mode shapes are computed for this finite element model, and are used as input of the identification method. Figure 3.16 compares the results obtained with the experimental data with additional masses and the data from the finite element model. The location of the added masses and the mistuning obtained without any masses is also superimposed. A good agreement is obtained between both results, which validates the identification method with the experimental data.

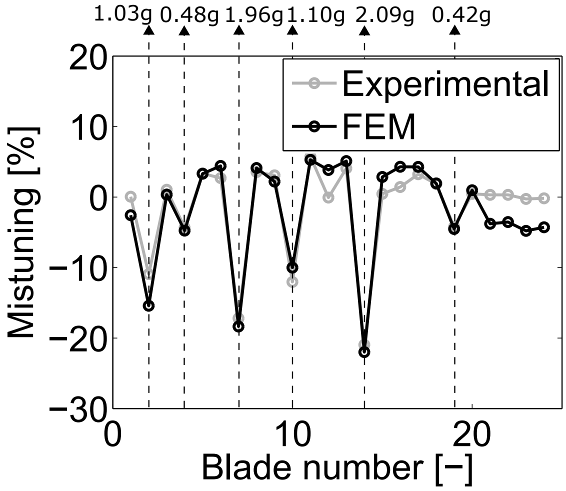

Figure 3.16: Comparison of mistuning obtained with the structure when adding small lumped masses, and with the finite element model.

3.6 Conclusion

The mistuning of a mono-stage and mono-bloc academic bladed structure has been identified experimentally by using the component mode mistuning (CMM) method. A base excitation with an electrodynamic shaker was used to excite the structure in the frequency range of interest. The response was measured on each blade by use of a laser vibrometer.

Then, the test methodology and the identification method have been validated by adding small lumped masses on the structure. These masses disturb manually the structure with a controlled mistuning. The value of the added mistuning has been retrieved using the identification method, which validates it.

The results from this Chapter have enabled to establish and to validate a simple test methodology to identify experimentally mistuning in an academic blisk. In Chapter 4, the identification method will be extended to the case of multi-stage structures and generalized to take into account both stiffness and mass mistunings.

Chapter 4

Experimental mistuning identification in a multi-stage drum

In this Chapter, the component mode mistuning (CMM) method is used for multi-stage assemblies to create a mistuning identification approach. The method is generalised to take into account both mass and stiffness mistuning. The sensitivity of the proposed method to noise is also quantified. An experimental modal analysis is performed on a two-stage monobloc academic bladed drum. The frequency response function is measured using a base excitation with an electrodynamic shaker and one measurement point per blade of each stage is used. The approach is used to identify mistuning in a multi-stage drum. Numerical and experimental results are presented. Results show that the proposed approach is effective even for multi-stage modes.

4.1 Introduction

Lim [15] developed the CMM identification method in which the mistuning identified for each blade is represented as the variation of the cantilevered blade frequency. Song et al. [108, 109] generalized the equations for multi-stage structures. In this work, an identification procedure is developed for multi-stage structures. The equations of the CMM method are also generalized to extend the identification approach to the case of mass mistuning. An experimental modal analysis is performed on a two-stage monobloc academic bladed drum. The proposed method is applied to retrieve the existing mistuning from frequency response functions (FRF) measured using a base excitation and one measurement point per blade (at the tip of each blade). The validation of the results is performed by adding small lumped masses at the tip of some blades. The mistuning of the disturbed structure is identified again and is compared to the results of a finite element model where the same masses are added at the same location. A numerical analysis is performed to investigate the sensitivity of the identification to noise in the measurement data. Knowing the initial mistuning of the structure, the perturbation has also been retrieved in terms of masses to completely validate the proposed method. This work has been performed in collaboration with the University of Michigan, Ann Arbor, MI.

4.2 Component mode mistuning (CMM) method for multi-stage structure

In this Section, the component mode mistuning (CMM) method developed by Lim [15] based on the work of Yang and Griffin [74] and Bladh [9] is reviewed and extended to the case of multi-stage structures with both mass and stiffness mistunings.

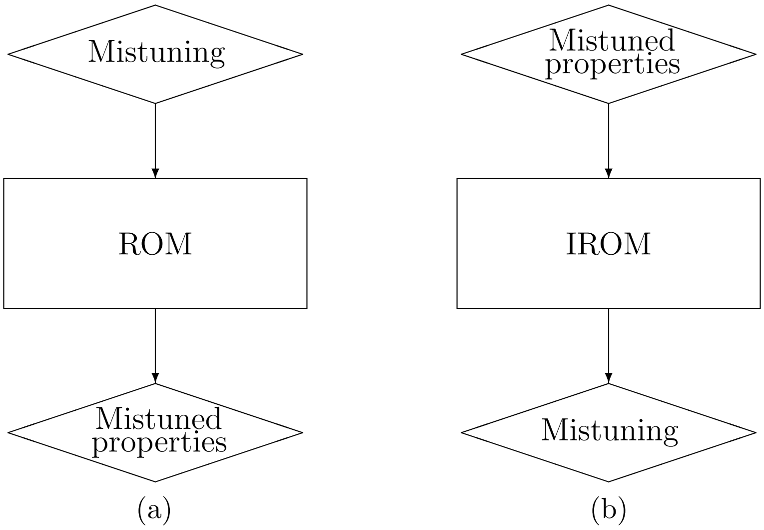

Figure 4.1: CMM: Direct problem (a) and inverse problem (b).

Most reduced order models (ROMs) are used for solving the direct problem, namely predicting the dynamics given the system parameters. ROMs based on CMM have been used in the past to obtain mistuned eigenfrequencies and the corresponding mode shapes for given mistuning patterns (as illustrated in Figure 4.1 on the left). In contrast to direct problems, identification (the inverse problem) requires distinct ROMs, also referred to as inverse reduced-order models (IROMs) [27, 123–125] which are used to identify the mistuned eigenfrequencies and mode shapes by experimental measurements of the system dynamics (as illustrated in Figure 4.1 on the right).

4.2.1 Reduced-order models (ROMs)

Consider a multi-stage system with external loads. The dynamic response of the system is governed by

$$\mathbf{M}\ddot{\mathbf{x}} + \mathbf{C}\dot{\mathbf{x}} + \mathbf{K}\mathbf{x} = \mathbf{f} \ , \tag{4.1}$$

where $\mathbf{M}$, $\mathbf{C}$ and $\mathbf{K}$ are respectively the mass, damping and stiffness matrices (dimension $ndof \times ndof$, with $ndof$ being the total number of degrees of freedom (DOF) of the multi-stage structure), $\mathbf{x}$ is the displacement vector (dimension $ndof \times 1$), and $\mathbf{f}$ is the force vector (in the physical coordinates, dimension $ndof \times 1$). The system response can be expressed in the tuned modal space as

$$\mathbf{x} = \mathbf{\Phi}\ \mathbf{p}\ , \tag{4.2}$$

where $\mathbf{\Phi}$ (dimension $ndof \times m$, with m being the number of retained mode shapes) is the matrix of tuned eigenvectors of the multi-stage system, and $\mathbf{p}$ (dimension $m \times 1$) is the vector of modal coordinates. Pre-multiplying Equation (4.1) by $\mathbf{\Phi}^T$ yields (with $\mathbf{F} = \mathbf{\Phi}^T\mathbf{f}$)

$$\mathbf{\Phi}^T\mathbf{M}\mathbf{\Phi}\ \ddot{\mathbf{p}} + \mathbf{\Phi}^T\mathbf{C}\mathbf{\Phi}\ \dot{\mathbf{p}} + \mathbf{\Phi}^T\mathbf{K}\mathbf{\Phi}\ \mathbf{p} = \mathbf{F}\ . \tag{4.3}$$

Equation (4.3) can be written in the frequency domain, considering structural damping (i.e., $\mathbf{C}\dot{\mathbf{x}} = i\gamma\ \mathbf{K}\mathbf{x}$), as

$$-\,\omega^2\mathbf{\Phi}^T\mathbf{M}\mathbf{\Phi}\ \mathbf{p} + (1+i\gamma)\,\mathbf{\Phi}^T\mathbf{K}\mathbf{\Phi}\ \mathbf{p} = \mathbf{F}\ . \tag{4.4}$$

Next, mistuning is introduced in the equation of motion. Small mistuning is considered here i.e., the perturbation of the nominal modal properties of the system is small. Due to the high modal density, this implies that the mistuned mode shapes can be expressed as a combination of tuned mode shapes in the frequency range of interest. The mistuned equation of motion can be written as

$$-\,\omega^2\mathbf{\Phi}^T\left(\mathbf{M}_0 + \mathbf{M}^\delta\right)\mathbf{\Phi}\ \mathbf{p} + (1+i\gamma)\,\mathbf{\Phi}^T\left(\mathbf{K}_0 + \mathbf{K}^\delta\right)\mathbf{\Phi}\ \mathbf{p} = \mathbf{F}\ , \tag{4.5}$$

where $\mathbf{M}_0$ and $\mathbf{K}_0$ (dimension $ndof \times ndof$) represent respectively the tuned mass and stiffness matrices, and $\mathbf{M}^\delta$ and $\mathbf{K}^\delta$ (dimension $ndof \times ndof$) represents respectively the perturbation in the mass and stiffness matrix due to mistuning ($\mathbf{M} = \mathbf{M}_0 + \mathbf{M}^\delta$ and $\mathbf{K} = \mathbf{K}_0 + \mathbf{K}^\delta$). Then, considering that the mode shapes are mass-normalized, Equation (4.5) becomes

$$-\,\omega^2\ \left[\mathbf{I} + \mathbf{\Phi}^T\mathbf{M}^\delta\mathbf{\Phi}\right]\ \mathbf{p} + (1+i\gamma)\left[\mathbf{\Lambda}_0 + \mathbf{\Phi}^T\mathbf{K}^\delta\mathbf{\Phi}\right]\mathbf{p} = \mathbf{F}\ , \tag{4.6}$$

where $\mathbf{I}$ (dimension $m \times m$) is the identity matrix, and $\mathbf{\Lambda}_0$ (dimension $m \times m$) is the stiffness matrix defined in tuned modal coordinates i.e., a diagonal matrix that contains the square eigenfrequencies of the tuned system.

Three assumptions are made in CMM:

1. Mistuning is considered to be located on the blades only and not on the disk/drum, as illustrated in Figure 4.2. This assumption is made because blade mistuning is known to have a larger impact than disk/drum mistuning. This implies that matrices $\mathbf{M}^\delta$ and $\mathbf{K}^\delta$ are non-zero only in the blade portion i.e.,

$$\mathbf{\Phi}^T\mathbf{M}^\delta\mathbf{\Phi} = \sum_{s=1}^{S}\sum_{n=1}^{N_s}{\mathbf{\Phi}_{ns}}^T\mathbf{M}^\delta_{ns}\ \mathbf{\Phi}_{ns}\ , \tag{4.7}$$

and

$$\mathbf{\Phi}^T \mathbf{K}^\delta \mathbf{\Phi} = \sum_{s=1}^{S} \sum_{n=1}^{N_s} {\mathbf{\Phi}_{ns}}^T \mathbf{K}_{ns}^\delta \ \mathbf{\Phi}_{ns} \ , \tag{4.8}$$

where S in the number of stages, N_s is the number of blades of stage s, $\mathbf{M}_{ns}^\delta$ and $\mathbf{K}_{ns}^\delta$ are respectively the mass and stiffness matrices restricted to the DOF of blade n ($n = 1, ..., N_s$) of stage s ($s = 1, ..., S$) (dimension $ndofb_{ns} \times ndofb_{ns}$ with $ndofb_{ns}$ the number of DOF of blade n of stage s), and $\mathbf{\Phi}_{ns}$ (dimension $ndofb_{ns} \times m$) is the matrix of tuned mode shapes restricted to the DOF of blade n of stage s.

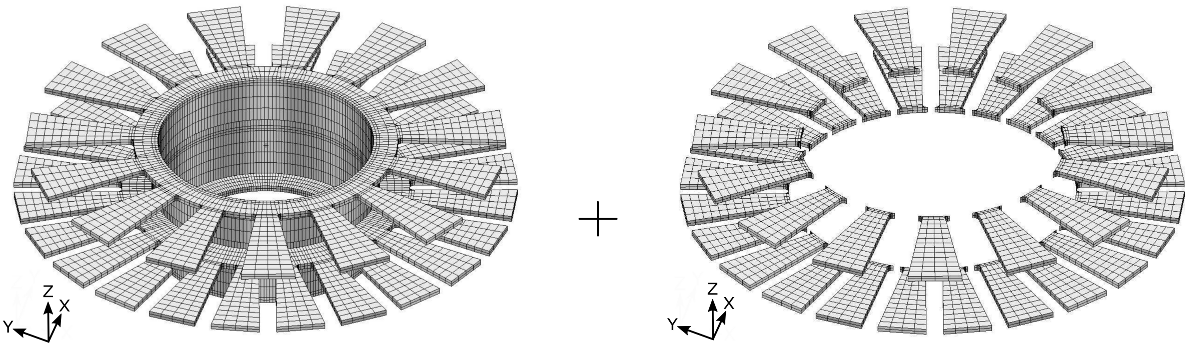

$\mathbf{M}_0, \mathbf{K}_0$ $\mathbf{M}^\delta, \mathbf{K}^\delta$

Figure 4.2: Mass and stiffness perturbations in the blade DOF.

2. The tuned mode shape matrix $\mathbf{\Phi}_{ns}$ of blade n ($n = 1, ..., N_s$) of stage s ($s = 1, ..., S$) can be written as a linear combination of cantilevered blade modes i.e.,

$$\mathbf{\Phi}_{ns} = \mathbf{\Phi}_s^{CB} \mathbf{Q}_{ns} \ , \tag{4.9}$$

where $\mathbf{\Phi}_s^{CB}$ is a matrix which contains the cantilevered blade modes for one nominal blade of stage s, and $\mathbf{Q}_{ns}$ (dimension $m \times m$) is the matrix of modal participation factors.

3. The expressions ${\mathbf{\Phi}_s^{CB}}^T \mathbf{M}_{ns}^\delta \ \mathbf{\Phi}_s^{CB}$ and ${\mathbf{\Phi}_s^{CB}}^T \mathbf{K}_{ns}^\delta \ \mathbf{\Phi}_s^{CB}$ are supposed to be diagonally dominant since mistuning is assumed to be small, which means that one tuned cantilevered blade mode is dominant. The off-diagonal terms representing the coupling between cantilevered blade modes can be neglected. The third assumption can be written as

$${\mathbf{\Phi}_s^{CB}}^T \mathbf{M}_{ns}^\delta \ \mathbf{\Phi}_s^{CB} = \mathrm{diag}_{r \in R} \left(\mu_{ns,r}^\delta \right) \ , \tag{4.10}$$

and

$$\mathbf{\Phi}_s^{CB^T}\mathbf{K}_{ns}^{\delta}\ \mathbf{\Phi}_s^{CB} = \mathrm{diag}_{r\in R}\left(\lambda_{ns,r}^{\delta}\right)\ , \tag{4.11}$$

where R is the set of retained cantilevered blade modes, $\mu_{ns,r}^{\delta} = \mathbf{\Phi}_{s,r}^{CB^T}\mathbf{M}_{ns}^{\delta}\ \mathbf{\Phi}_{s,r}^{CB}$, and $\lambda_{ns,r}^{\delta} = \mathbf{\Phi}_{s,r}^{CB^T}\mathbf{K}_{ns}^{\delta}\ \mathbf{\Phi}_{s,r}^{CB}$ is the eigenvalue deviation of the r^{th} cantilevered blade mode of blade n of stage s.

Considering these three assumptions, the term $\mathbf{\Phi}^T\mathbf{M}^{\delta}\mathbf{\Phi}$ of Equation (4.6) becomes

$$\begin{aligned}
\mathbf{\Phi}^T\mathbf{M}^{\delta}\mathbf{\Phi} &= \sum_{s=1}^{S}\sum_{n=1}^{N_s}\mathbf{\Phi}_{ns}{}^T\mathbf{M}_{ns}^{\delta}\ \mathbf{\Phi}_{ns} && (4.12)\\
&= \sum_{s=1}^{S}\sum_{n=1}^{N_s}\mathbf{Q}_{ns}{}^T\mathbf{\Phi}_s^{CB^T}\mathbf{M}_{ns}^{\delta}\mathbf{\Phi}_s^{CB}\mathbf{Q}_{ns} && (4.13)\\
&= \sum_{s=1}^{S}\sum_{n=1}^{N_s}\mathbf{Q}_{ns}{}^T\,\mathrm{diag}_{r\in R}\left(\mu_{ns,r}^{\delta}\right)\mathbf{Q}_{ns}\ , && (4.14)
\end{aligned}$$

and the term $\mathbf{\Phi}^T\mathbf{K}^{\delta}\mathbf{\Phi}$ becomes

$$\begin{aligned}
\mathbf{\Phi}^T\mathbf{K}^{\delta}\mathbf{\Phi} &= \sum_{s=1}^{S}\sum_{n=1}^{N_s}\mathbf{\Phi}_{ns}{}^T\mathbf{K}_{ns}^{\delta}\ \mathbf{\Phi}_{ns} && (4.15)\\
&= \sum_{s=1}^{S}\sum_{n=1}^{N_s}\mathbf{Q}_{ns}{}^T\mathbf{\Phi}_s^{CB^T}\mathbf{K}_{ns}^{\delta}\mathbf{\Phi}_s^{CB}\mathbf{Q}_{ns} && (4.16)\\
&= \sum_{s=1}^{S}\sum_{n=1}^{N_s}\mathbf{Q}_{ns}{}^T\,\mathrm{diag}_{r\in R}\left(\lambda_{ns,r}^{\delta}\right)\mathbf{Q}_{ns}\ . && (4.17)
\end{aligned}$$

Introducing Equations (4.14) and (4.17) in Equation (4.6), one obtains

$$\begin{aligned}
&-\omega^2\left[\mathbf{I} + \sum_{s=1}^{S}\sum_{n=1}^{N_s}\mathbf{Q}_{ns}{}^T\,\mathrm{diag}_{r\in R}\left(\mu_{ns,r}^{\delta}\right)\mathbf{Q}_{ns}\right]\mathbf{p}\\
&\qquad + (1+i\gamma)\left[\mathbf{\Lambda}_0 + \sum_{s=1}^{S}\sum_{n=1}^{N_s}\mathbf{Q}_{ns}{}^T\,\mathrm{diag}_{r\in R}\left(\lambda_{ns,r}^{\delta}\right)\mathbf{Q}_{ns}\right]\mathbf{p} = \mathbf{F}\ .
\end{aligned} \tag{4.18}$$

The computation of the modal participation factors $\mathbf{Q}_{ns}$ in Equation (4.18) is performed by rewriting Equation (4.9). First, Equation (4.9) is pre-multiplied by $\mathbf{\Phi}_s^{CB^T}\mathbf{K}_s^{CB}$, such as

$$\mathbf{\Phi}_s^{CB^T}\mathbf{K}_s^{CB}\mathbf{\Phi}_{ns} = \mathbf{\Phi}_s^{CB^T}\mathbf{K}_s^{CB}\mathbf{\Phi}_s^{CB}\mathbf{Q}_{ns}\ , \tag{4.19}$$

or

$$\mathbf{\Phi}_s^{CB^T}\mathbf{K}_s^{CB}\mathbf{\Phi}_{ns} = \mathbf{\Lambda}_s^{CB}\mathbf{Q}_{ns} \ , \tag{4.20}$$

where $\mathbf{\Lambda}_s^{CB}$ a diagonal matrix containing the squared eigenfrequencies of the cantilevered blade modes of stage s. Finally, the expression of the participation factor $\mathbf{Q}_{ns}$ can be written as

$$\mathbf{Q}_{ns} = \mathbf{\Lambda}_s^{CB^{-1}}\mathbf{\Phi}_s^{CB^T}\mathbf{K}_s^{CB}\mathbf{\Phi}_{ns} \ . \tag{4.21}$$

Using both Equations (4.18) and (4.21), the mistuned properties of the system can be computed for a given mistuning pattern. All the needed input data can be retrieved from $S+1$ finite element models: the finite element model of the tuned multi-stage structure, which enables to retrieve

- the tuned multi-stage mode shapes restricted to the blades DOF $\mathbf{\Phi}_{ns}$;
- the eigenvalues of the multi-stage tuned system in order to obtain $\mathbf{\Lambda}_0$;

and the finite element model of the blade of each stage, clamped at its basis, which enables to compute

- the eigenvalues of cantilevered blade of stage s in order to construct $\mathbf{\Lambda}_s^{CB}$;
- the cantilevered blade modes of stage s, $\mathbf{\Phi}_s^{CB}$;
- the cantilevered blade stiffness matrix of stage s, $\mathbf{K}_s^{CB}$.

4.2.2 Inverse reduced-order models (IROMs)

In this Section, the identification method for the mistuning parameters is presented. The construction of the inverse reduced-order models (IROMs) is based on the mistuned equations of motion of Section 4.2.1.

Since $\mathbf{p}$ is a complex quantity, it can be written as

$$\mathbf{p} = \mathbf{p}^R + i\ \mathbf{p}^I \ , \tag{4.22}$$

where $\mathbf{p}^R$ and $\mathbf{p}^I$ are respectively the real and imaginary parts of $\mathbf{p}$. Introducing Equation (4.22) in Equation (4.18), one obtains

$$\begin{aligned} &-\omega^2\left[\mathbf{I}+\sum_{s=1}^{S}\sum_{n=1}^{N_s}\mathbf{Q}_{ns}{}^T\,\mathrm{diag}_{r\in R}\left(\mu^{\delta}_{ns,r}\right)\mathbf{Q}_{ns}\right]\left(\mathbf{p}^R+i\ \mathbf{p}^I\right) \\ &\qquad +(1+i\gamma)\left[\mathbf{\Lambda}_0+\sum_{s=1}^{S}\sum_{n=1}^{N_s}\mathbf{Q}_{ns}{}^T\,\mathrm{diag}_{r\in R}\left(\lambda^{\delta}_{ns,r}\right)\mathbf{Q}_{ns}\right]\left(\mathbf{p}^R+i\ \mathbf{p}^I\right)=\mathbf{F}\ , \end{aligned} \tag{4.23}$$

or, developing the different terms,

$$\begin{aligned}
&-\omega^2 \mathbf{I}\left(\mathbf{p}^R + i\ \mathbf{p}^I\right) - \omega^2 \sum_{s=1}^{S}\sum_{n=1}^{N_s} \mathbf{Q}_{ns}{}^T \operatorname{diag}_{r\in R}\left(\mu^{\delta}_{ns,r}\right)\mathbf{Q}_{ns}\ \left(\mathbf{p}^R + i\ \mathbf{p}^I\right)\\
&\qquad + \mathbf{\Lambda}_0\ \left(\mathbf{p}^R + i\ \mathbf{p}^I + i\gamma\mathbf{p}^R - \gamma\mathbf{p}^I\right)\\
&\qquad + \sum_{s=1}^{S}\sum_{n=1}^{N_s} \mathbf{Q}_{ns}{}^T \operatorname{diag}_{r\in R}\left(\lambda^{\delta}_{ns,r}\right)\mathbf{Q}_{ns}\ \left(\mathbf{p}^R + i\ \mathbf{p}^I + i\gamma\mathbf{p}^R - \gamma\mathbf{p}^I\right) = \mathbf{F}\ . \qquad (4.24)
\end{aligned}$$

Stiffness mistuning

If only a perturbation in the stiffness matrix is assumed, the terms $\mu^{\delta}_{ns,r} = 0$. In this case, the mistuning of each blade can be seen as the deviation of its tuned clamped blade eigenfrequencies.

Reorganizing the terms of Equation (4.24) yields

$$\begin{aligned}
&\sum_{s=1}^{S}\sum_{n=1}^{N_s} \mathbf{Q}_{ns}{}^T \operatorname{diag}_{r\in R}\left(\lambda^{\delta}_{ns,r}\right)\mathbf{Q}_{ns}\ \left(\mathbf{p}^R + i\ \mathbf{p}^I + i\gamma\mathbf{p}^R - \gamma\mathbf{p}^I\right) =\\
&\qquad\qquad \mathbf{F} + \omega^2 \mathbf{I}\left(\mathbf{p}^R + i\ \mathbf{p}^I\right) - \mathbf{\Lambda}_0\ \left(\mathbf{p}^R + i\ \mathbf{p}^I + i\gamma\mathbf{p}^R - \gamma\mathbf{p}^I\right)\ . \qquad (4.25)
\end{aligned}$$

Equation (4.25) can be divided into two sets of equations by considering its real and imaginary parts as

$$\begin{cases}
\sum_{s=1}^{S}\sum_{n=1}^{N_s} \mathbf{Q}_{ns}{}^T \operatorname{diag}_{r\in R}\left(\lambda^{\delta}_{ns,r}\right)\mathbf{Q}_{ns}\left(\mathbf{p}^R - \gamma\mathbf{p}^I\right) = \mathbf{F} + \omega^2\mathbf{I}\mathbf{p}^R - \mathbf{\Lambda}_0\left(\mathbf{p}^R - \gamma\mathbf{p}^I\right) & (4.26)\\
\sum_{s=1}^{S}\sum_{n=1}^{N_s} \mathbf{Q}_{ns}{}^T \operatorname{diag}_{r\in R}\left(\lambda^{\delta}_{ns,r}\right)\mathbf{Q}_{ns}\left(\mathbf{p}^I + \gamma\mathbf{p}^R\right) = \omega^2\mathbf{I}\mathbf{p}^I - \mathbf{\Lambda}_0\left(\mathbf{p}^I + \gamma\mathbf{p}^R\right)\ . & (4.27)
\end{cases}$$

Both equations are linear in $\lambda^{\delta}_{ns,r}$. The number of unknowns is equal to the total number of blades of all stages $\sum_s N_s$ multiplied by the number of retained cantilevered blade modes N^{CB}. Both Equations (4.26) and (4.27) can be used to retrieve $\lambda^{\delta}_{ns,r}$. However, Equation (4.27) has the advantage that it does not involve the force vector which is difficult to compute. Therefore, Equation (4.27) will be used in the following. Moreover, it can be noted that $\mathbf{p}^I \gg \gamma\mathbf{p}^R$. Considering that m modes are measured, Equation (4.27) can be written in matrix form as

$$\begin{bmatrix} {\mathbf{Q}_{11,1}}^T\mathbf{Q}_{11,1}\ \mathbf{p}_1^I & {\mathbf{Q}_{11,2}}^T\mathbf{Q}_{11,2}\ \mathbf{p}_1^I & \cdots & {\mathbf{Q}_{N_ss,N^{CB}}}^T\mathbf{Q}_{N_ss,N^{CB}}\ \mathbf{p}_1^I \\ {\mathbf{Q}_{11,1}}^T\mathbf{Q}_{11,1}\ \mathbf{p}_2^I & {\mathbf{Q}_{11,2}}^T\mathbf{Q}_{11,2}\ \mathbf{p}_2^I & \cdots & {\mathbf{Q}_{N_ss,N^{CB}}}^T\mathbf{Q}_{N_ss,N^{CB}}\ \mathbf{p}_2^I \\ \vdots & & \cdots & \vdots \\ {\mathbf{Q}_{11,1}}^T\mathbf{Q}_{11,1}\ \mathbf{p}_m^I & {\mathbf{Q}_{11,2}}^T\mathbf{Q}_{11,2}\ \mathbf{p}_m^I & \cdots & {\mathbf{Q}_{N_ss,N^{CB}}}^T\mathbf{Q}_{N_ss,N^{CB}}\ \mathbf{p}_m^I \end{bmatrix} \begin{bmatrix} \lambda_{11,1}^{\delta} \\ \lambda_{11,2}^{\delta} \\ \vdots \\ \lambda_{N_ss,N^{CB}}^{\delta} \end{bmatrix} = \begin{bmatrix} \omega_1^2\ \mathbf{p}_1^I - \mathbf{\Lambda}_0\ \mathbf{p}_1^I \\ \omega_2^2\ \mathbf{p}_2^I - \mathbf{\Lambda}_0\ \mathbf{p}_2^I \\ \vdots \\ \omega_m^2\ \mathbf{p}_m^I - \mathbf{\Lambda}_0\ \mathbf{p}_m^I \end{bmatrix}, \tag{4.28}$$

where $\mathbf{p}_k^I$ and ω_k, with $k = 1, ..., m$, are the data related to the k^{th} measured mode, and $\mathbf{Q}_{ns,r}$ refers to the r^{th} lines of $\mathbf{Q}_{ns}$.

Mass mistuning

The same procedure is used to construct the inverse reduced order model in presence of mass mistuning. The stiffness mistuning is assumed to be known, and the mass variations are identified. Reorganizing the terms of Equation (4.24) leads to

$$\begin{aligned} -\omega^2 \sum_{s=1}^{S}\sum_{n=1}^{N_s} {\mathbf{Q}_{ns}}^T \operatorname{diag}_{r\in R}\left(\mu_{ns,r}^{\delta}\right) \mathbf{Q}_{ns}\ \left(\mathbf{p}^R + i\ \mathbf{p}^I\right) &= \mathbf{F} + \omega^2\mathbf{I}\left(\mathbf{p}^R + i\ \mathbf{p}^I\right) \\ &- \mathbf{\Lambda}_0\ \left(\mathbf{p}^R + i\ \mathbf{p}^I + i\gamma\mathbf{p}^R - \gamma\mathbf{p}^I\right) \\ &- \sum_{s=1}^{S}\sum_{n=1}^{N_s} {\mathbf{Q}_{ns}}^T \operatorname{diag}_{r\in R}\left(\lambda_{ns,r}^{\delta}\right) \mathbf{Q}_{ns}\ \left(\mathbf{p}^R + i\ \mathbf{p}^I + i\gamma\mathbf{p}^R - \gamma\mathbf{p}^I\right)\ . \end{aligned} \tag{4.29}$$

Equation (4.29) can be divided into two sets of equations by considering its real and imaginary parts as

$$\left\{ \begin{aligned} & -\omega^2 \sum_{s=1}^{S}\sum_{n=1}^{N_s} {\mathbf{Q}_{ns}}^T \operatorname{diag}_{r\in R}\left(\mu_{ns,r}^{\delta}\right) \mathbf{Q}_{ns}\ \mathbf{p}^R = \\ & \qquad \mathbf{F} + \omega^2\mathbf{I}\mathbf{p}^R - \mathbf{\Lambda}_0\left(\mathbf{p}^R - \gamma\mathbf{p}^I\right) - \sum_{n=1}^{N_s} {\mathbf{Q}_{ns}}^T \operatorname{diag}_{r\in R}\left(\lambda_{ns,r}^{\delta}\right) \mathbf{Q}_{ns}\left(\mathbf{p}^R - \gamma\mathbf{p}^I\right) \quad (4.30) \\ & -\omega^2 \sum_{s=1}^{S}\sum_{n=1}^{N_s} {\mathbf{Q}_{ns}}^T \operatorname{diag}_{r\in R}\left(\mu_{ns,r}^{\delta}\right) \mathbf{Q}_{ns}\ \mathbf{p}^I = \\ & \qquad \omega^2\mathbf{I}\mathbf{p}^I - \mathbf{\Lambda}_0\ \left(\mathbf{p}^I + \gamma\mathbf{p}^R\right) - \sum_{i=1}^{N_s} {\mathbf{Q}_{ns}}^T \operatorname{diag}_{r\in R}\left(\lambda_{ns,r}^{\delta}\right) \mathbf{Q}_{ns}\left(\mathbf{p}^I + \gamma\mathbf{p}^R\right)\ . \quad (4.31) \end{aligned} \right.$$

Both equations are linear in $\mu^{\delta}_{ns,r}$. The second set of equations (Equation (4.31)) will be used to identify the $\mu^{\delta}_{ns,r}$ since it has the advantage to not involve the force vector. Considering that m modes are measured and that $\mathbf{p}^I \gg \gamma \mathbf{p}^R$, Equation (4.31) can be written in matrix form as

$$\begin{bmatrix} \mathbf{Q}_{11,1}{}^T\mathbf{Q}_{11,1}\ \mathbf{p}_1^I & \mathbf{Q}_{11,2}{}^T\mathbf{Q}_{11,2}\ \mathbf{p}_1^I & \cdots & \mathbf{Q}_{N_s s,N^{CB}}{}^T\mathbf{Q}_{N_s s,N^{CB}}\ \mathbf{p}_1^I \\ \mathbf{Q}_{11,1}{}^T\mathbf{Q}_{11,1}\ \mathbf{p}_2^I & \mathbf{Q}_{11,2}{}^T\mathbf{Q}_{11,2}\ \mathbf{p}_2^I & \cdots & \mathbf{Q}_{N_s s,N^{CB}}{}^T\mathbf{Q}_{N_s s,N^{CB}}\ \mathbf{p}_2^I \\ \vdots & & \cdots & \vdots \\ \mathbf{Q}_{11,1}{}^T\mathbf{Q}_{11,1}\ \mathbf{p}_m^I & \mathbf{Q}_{11,2}{}^T\mathbf{Q}_{11,2}\ \mathbf{p}_m^I & \cdots & \mathbf{Q}_{N_s s,N^{CB}}{}^T\mathbf{Q}_{N_s s,N^{CB}}\ \mathbf{p}_m^I \end{bmatrix} \begin{bmatrix} -\omega^2\mu^{\delta}_{11,1} \\ -\omega^2\mu^{\delta}_{11,2} \\ \vdots \\ -\omega^2\mu^{\delta}_{N_s s,N^{CB}} \end{bmatrix}$$
$$= \begin{bmatrix} \omega_1^2\ \mathbf{p}_1^I - \mathbf{\Lambda}_0\ \mathbf{p}_1^I \\ \omega_2^2\ \mathbf{p}_2^I - \mathbf{\Lambda}_0\ \mathbf{p}_2^I \\ \vdots \\ \omega_m^2\ \mathbf{p}_m^I - \mathbf{\Lambda}_0\ \mathbf{p}_m^I \end{bmatrix} -$$
$$\begin{bmatrix} \mathbf{Q}_{11,1}{}^T\mathbf{Q}_{11,1}\ \mathbf{p}_1^I & \mathbf{Q}_{11,2}{}^T\mathbf{Q}_{11,2}\ \mathbf{p}_1^I & \cdots & \mathbf{Q}_{N_s s,N^{CB}}{}^T\mathbf{Q}_{N_s s,N^{CB}}\ \mathbf{p}_1^I \\ \mathbf{Q}_{11,1}{}^T\mathbf{Q}_{11,1}\ \mathbf{p}_2^I & \mathbf{Q}_{11,2}{}^T\mathbf{Q}_{11,2}\ \mathbf{p}_2^I & \cdots & \mathbf{Q}_{N_s s,N^{CB}}{}^T\mathbf{Q}_{N_s s,N^{CB}}\ \mathbf{p}_2^I \\ \vdots & & \cdots & \vdots \\ \mathbf{Q}_{11,1}{}^T\mathbf{Q}_{11,1}\ \mathbf{p}_m^I & \mathbf{Q}_{11,2}{}^T\mathbf{Q}_{11,2}\ \mathbf{p}_m^I & \cdots & \mathbf{Q}_{N_s s,N^{CB}}{}^T\mathbf{Q}_{N_s s,N^{CB}}\ \mathbf{p}_m^I \end{bmatrix} \begin{bmatrix} \lambda^{\delta}_{11,1} \\ \lambda^{\delta}_{11,2} \\ \vdots \\ \lambda^{\delta}_{N_s s,N^{CB}} \end{bmatrix}, \tag{4.32}$$

where $\mathbf{p}_k^I$ and ω_k, with $k = 1, ..., m$, are the data related to the k^{th} measured mode, and $\mathbf{Q}_{ns,r}$ refers to the r^{th} lines of $\mathbf{Q}_{ns}$.

4.2.3 Identification using experimental data

In the case of the direct problem, the mistuning is known as well as the excitation force. The only unknown is the $\mathbf{p}$ vector, which can be determined at each frequency ω. The mistuned FRF can be computed for each mistuning pattern.

However, in the case of the inverse problem, ω, $\mathbf{p}$ and $\mathbf{F} = \mathbf{\Phi}^T\mathbf{f}$ are known from the experimental tests, and the unknown factors are the $\lambda^{\delta}_{ns,r}$ terms. The modal coordinates $\mathbf{p}$ can be computed based on the measured physical displacements as

$$\mathbf{x}_{exp} = \mathbf{\Phi}_{exp}\mathbf{p} \ , \tag{4.33}$$

where $\mathbf{x}_{exp}$ contains the physical displacement at the measured DOF, and $\mathbf{\Phi}_{exp}$ is a matrix that contains the tuned displacements of the measured DOF. If the matrix $\mathbf{\Phi}_{exp}$ is not a square matrix (i.e., if the number of measured DOF is larger than $\sum\limits_s N_s * N^{CB}$), the modal coordinates $\mathbf{p}$ are obtained by solving a least squares problem.

4.3 Example of an academic multi-stage drum

The demonstration structure is the mono-bloc bladed structure with two stages made of aluminum (Figure 4.3(b), and the reference sector for each stage in Figure 4.3(a)). The bottom stage (stage 1) totalizes 24 blades, and the top one (stage 2) 15 blades. The mechanical properties and the dimensions of the structure are given in Table 4.1. The blades of the top stage are designed to be shorter than the blades of the bottom stage, which enables to have accessible optical measurement points on the bottom stage.

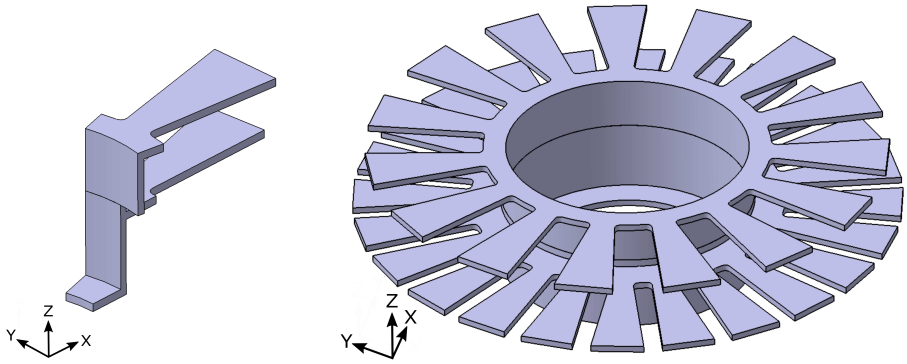

(a) (b)

Figure 4.3: Studied structure, with the reference sector of each stage (a) and the 360 degrees model (b).

	Stage 1	Stage 2
Number of sectors (N) [-]	24	15
Young's modulus [MPa]	71 000	71 000
Density [kg/m^3]	2700	2700
External diameter [mm]	420	400
Internal diameter [mm]	186	186
Thickness [mm]	5	5
Height [mm]	53	46

Table 4.1: Properties of the multi-stage academic structure.

A finite element model of the structure has been constructed in SAMCEF [120]. The multi-stage cyclic symmetric property was applied to reduce the needed computational resources following Laxalde's method [16, 110, 111]. The displacement compatibility was also applied between the interstage degrees of freedom of the bottom stage and the top stage. A numerical analysis on the mesh refining was performed and is presented in the Appendix C in order to have accurate results with a reduced computational time. The selected mesh of the reference sector of each stage is shown in Figure 4.4(a). The mesh of the bottom stage is identical to the one of the mono-stage structure (presented in Section 3.4.1). The mesh of the reference sector totalizes 8 496 degrees of freedom for the bottom stage and 5 901 degrees of freedom for the top stage. The total number of degrees of freedom is 14 091 (which is lower than $8\ 496 + 5\ 901 = 14\ 397$ because of the nodes that are interstage degrees of freedom, which are common for the two stages). As for the mono-stage structure, hexahedral volumic elements are used in the finite element model. The full recombined mesh is shown in Figure 4.4(b) with the reference sector in dark gray.

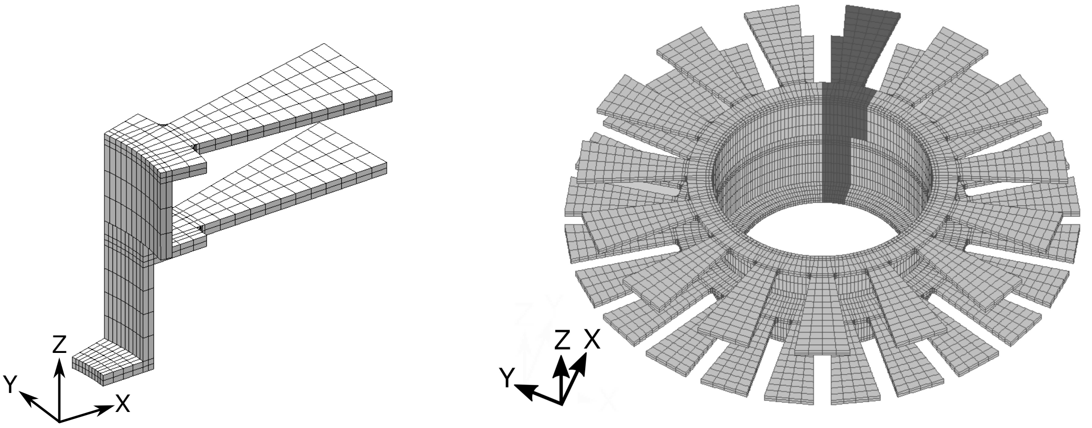

(a)

(b)

Figure 4.4: Finite element model of the reference sector of the academic structure (a) and the recombined finite element model with the reference sector in dark gray (b).

The SAFE diagram (Singh's Advanced Frequency Evaluation diagram i.e., the eigenfrequencies as a function of the number of nodal diameters, sometimes referred to as veering diagram) for each stage corresponding to the first bending (1B) modes is shown in Figure 4.5. The maximum number of nodal diameters for stage 1 (bottom stage) is $\lfloor \frac{N_1}{2} \rfloor = \lfloor \frac{24}{2} \rfloor = 12$, and the maximum number of nodal diameters for stage 2 (top stage) is $\lfloor \frac{N_2}{2} \rfloor = \lfloor \frac{15}{2} \rfloor = 7$. The range of frequencies of the 1B modes is $[258 - 324]$ Hz for stage 1, and $[282 - 304]$ Hz for stage 2. The higher increase of the frequencies with the number of nodal diameters for the first stage means that the drum has a greater participation in the mode shapes for stage 1 than for stage 2. A low participation of the drum is observed for stage 2 since the curve corresponding to the 1B mode remains relatively flat.

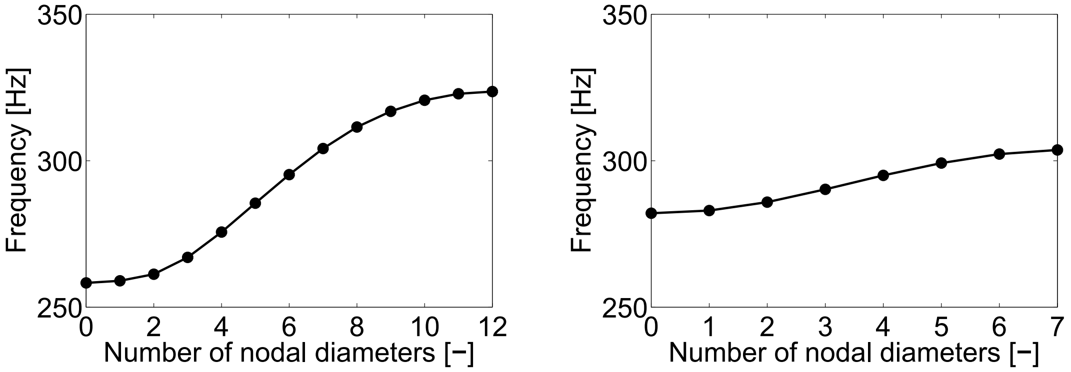

(a) Stage 1

(b) Stage 2

Figure 4.5: SAFE diagram corresponding to the 1B modes of stage 1 (a) and stage 2 (b).

4.4 Experimental stiffness mistuning identification

Experimental vibration testing has been performed in order to identify the stiffness mistuning of each blade for both stages. The measurement set-up is presented in Figure 4.6. The bottom stage is clamped at its basis with 24 fixation points (which corresponds to the number of blades of stage 1) in order to keep the cyclic symmetric property of the bottom stage. A base excitation is applied using an electrodynamic shaker. A laser is used to measure the response of the structure in the axial direction. One measurement point per blade is considered i.e., 39 measurement points (24 for stage 1 and 15 for stage 2). An accelerometer is located on the shaker table in order to measure the acceleration imposed by the shaker. The temperature is maintained constant during all the tests ($20°C$). The measurements are indeed strongly affected by changes in temperature environment. A tolerance of $0.5°C$ is kept here.

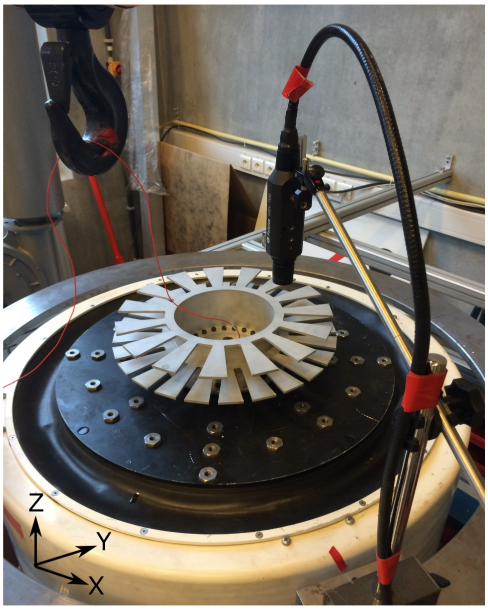

Figure 4.6: Measurement test set-up (multi-stage drum with laser measurement).

A periodic chirp is used to excite the structure in the frequency range of interest, 200 to 400 Hz (i.e., the frequency range of the 1B modes) with a resolution of 0.02 Hz. One measurement point per blade for each stage is taken at the tip of the blade.

Identification is performed using the PolyMax method [122] available in the Siemens LMS Test.Lab software [121]. The stabilization diagram is presented in Figure 4.7. At each peak corresponds a frequency and mode shape, which are given in Figure 4.8. Using the obtained experimental frequencies and mode shapes as input of the identification method, the mistuning of each blade of each stage is retrieved as explained in Section 4.2. The obtained results are presented in Figure 4.9, where it can be observed that a mistuning up to 12% is obtained for stage 1 on blade 16, and up to 9% for stage 2 on blade 13.

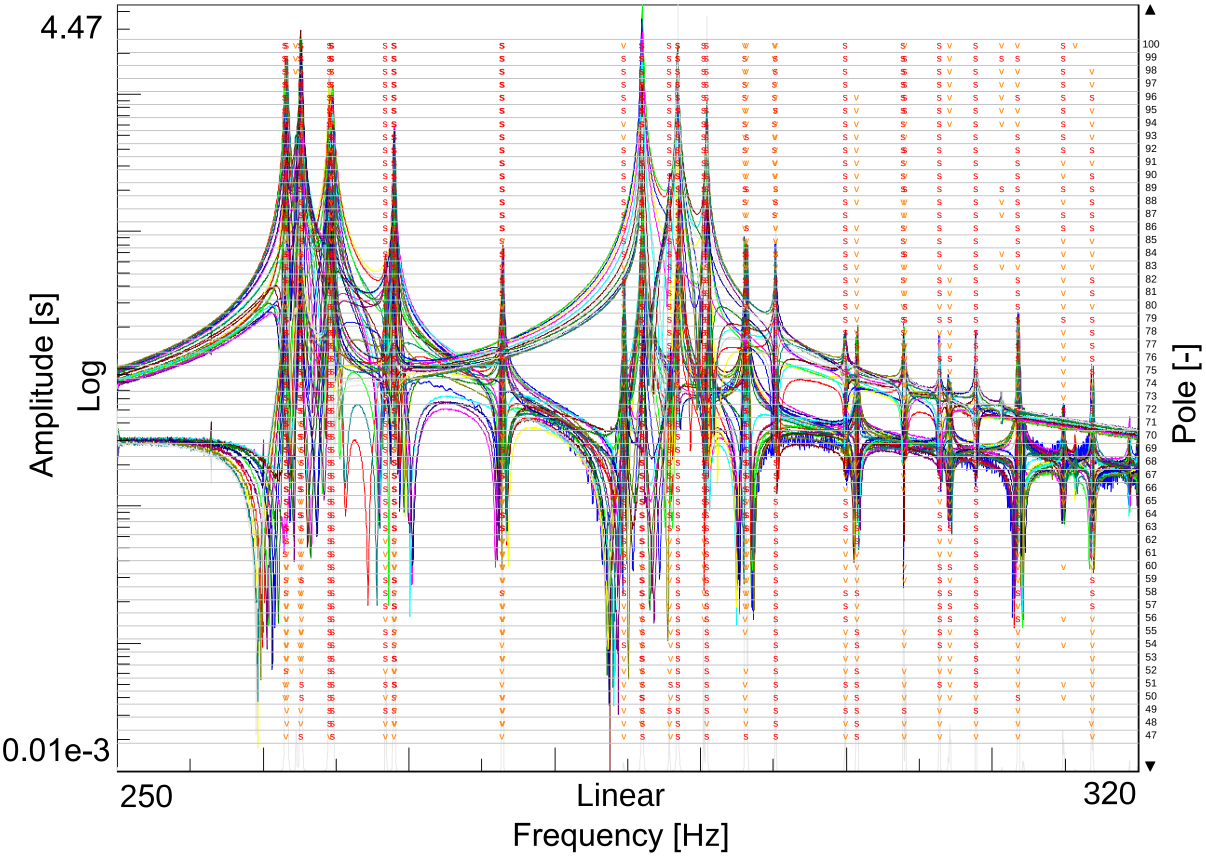

Figure 4.7: Stabilization diagram. Symbols have following meaning: o – new pole; f – stable frequency; d – stable frequency and damping; v – stable frequency and eigenvector; s – all criteria stable.

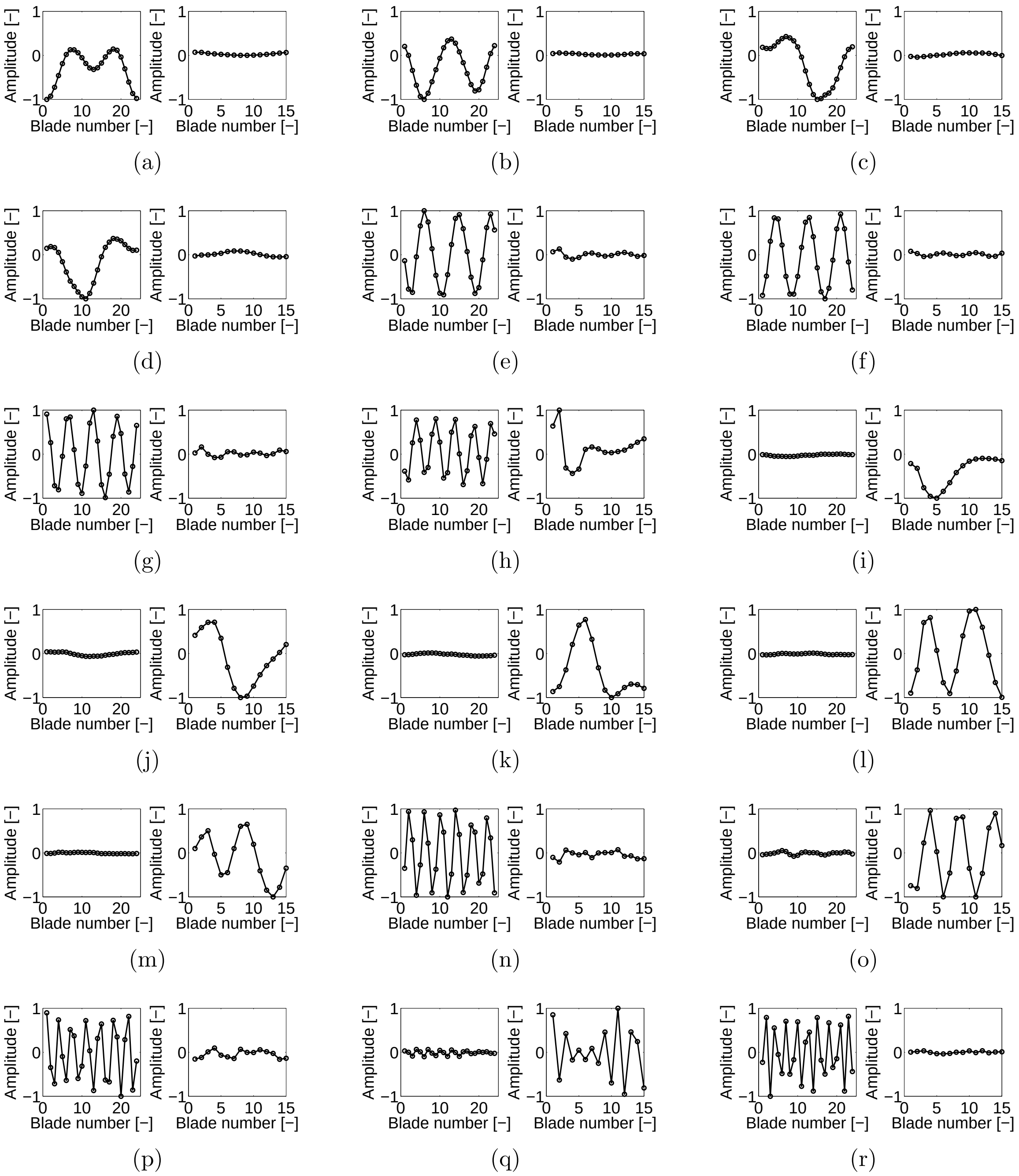

(a) (b) (c)

(d) (e) (f)

(g) (h) (i)

(j) (k) (l)

(m) (n) (o)

(p) (q) (r)

Figure 4.8: Experimental mode shapes without additional mass, stage 1 (left) and stage 2 (right).

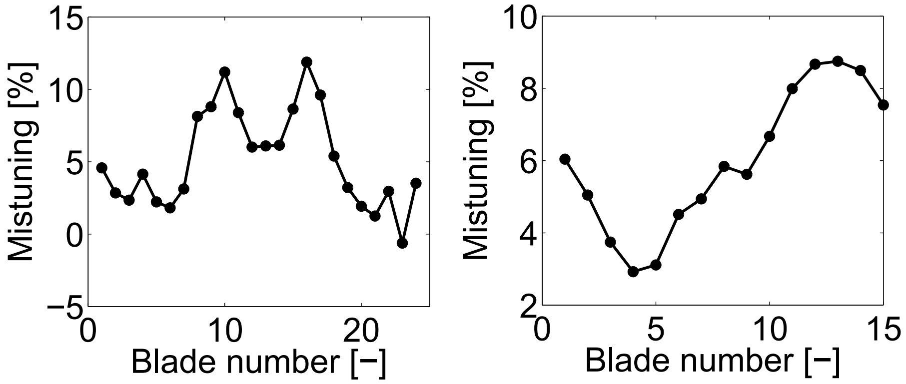

(a) Stage 1

(b) Stage 2

Figure 4.9: Experimentally identified mistuning for stage 1 (a) and stage 2 (b).

4.5 Validation of the experimental mistuning identification

In order to validate the mistuning identification method, the same test procedure is repeated, the only difference is that small lumped masses are added at the top of some blades of stage 1 and stage 2 as a controlled mistuning, as shown in Figure 4.10. Table 4.2 provides the amount and the location of the additional masses for each stage (the mass added on the bottom stage are identical to ones added in Chapter 3 for the mono-stage structure).

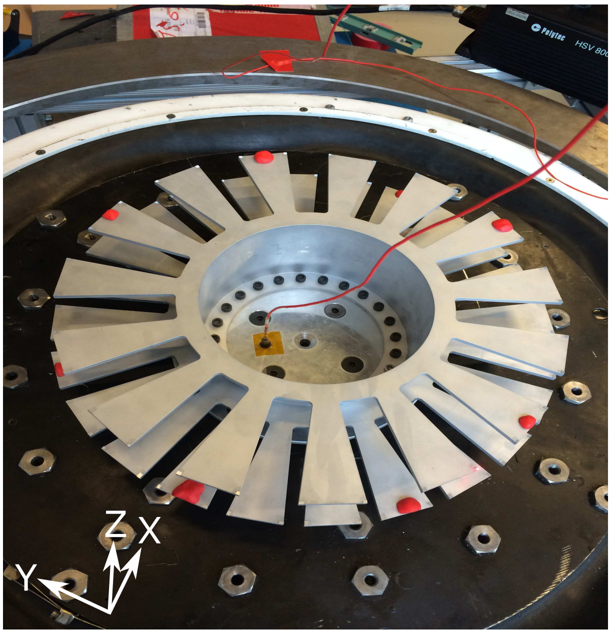

Figure 4.10: Test set-up (multi-stage bladed drum with lumped masses).

The aim of this Section is:

1. To identify the deviation in the blade eigenfrequency (i.e., the stiffness mistuning) induced by the addition of masses using the experimental data (Section 4.5.1).
2. To validate the obtained deviations in the blade eigenfrequency induced by the addition of masses using a finite element model (Section 4.5.2).
3. To identify the mass perturbation using the experimental data (Section 4.5.3).

Stage 1

Location [-]	Mass [g]
Blade 2	1.03
Blade 4	0.48
Blade 7	1.96
Blade 10	1.10
Blade 14	2.09
Blade 19	0.42

Stage 2

Location [-]	Mass [g]
Blade 1	0.51
Blade 8	0.54
Blade 11	1.11
Blade 14	1.34

Table 4.2: Location of the additional masses.

The test conditions remain identical to the ones presented in Section 4.4. The stabilization diagram obtained using the PolyMax method [122] is shown in Figure 4.11. More peaks are observed compared to the diagram without additional masses since the test structure exhibits a larger mistuning due to the addition of masses. The frequencies and mode shapes of each peak are retrieved with the PolyMax method (shown in Figure 4.12) and used in the identification method to compute the mistuning of each blade for the perturbed system.

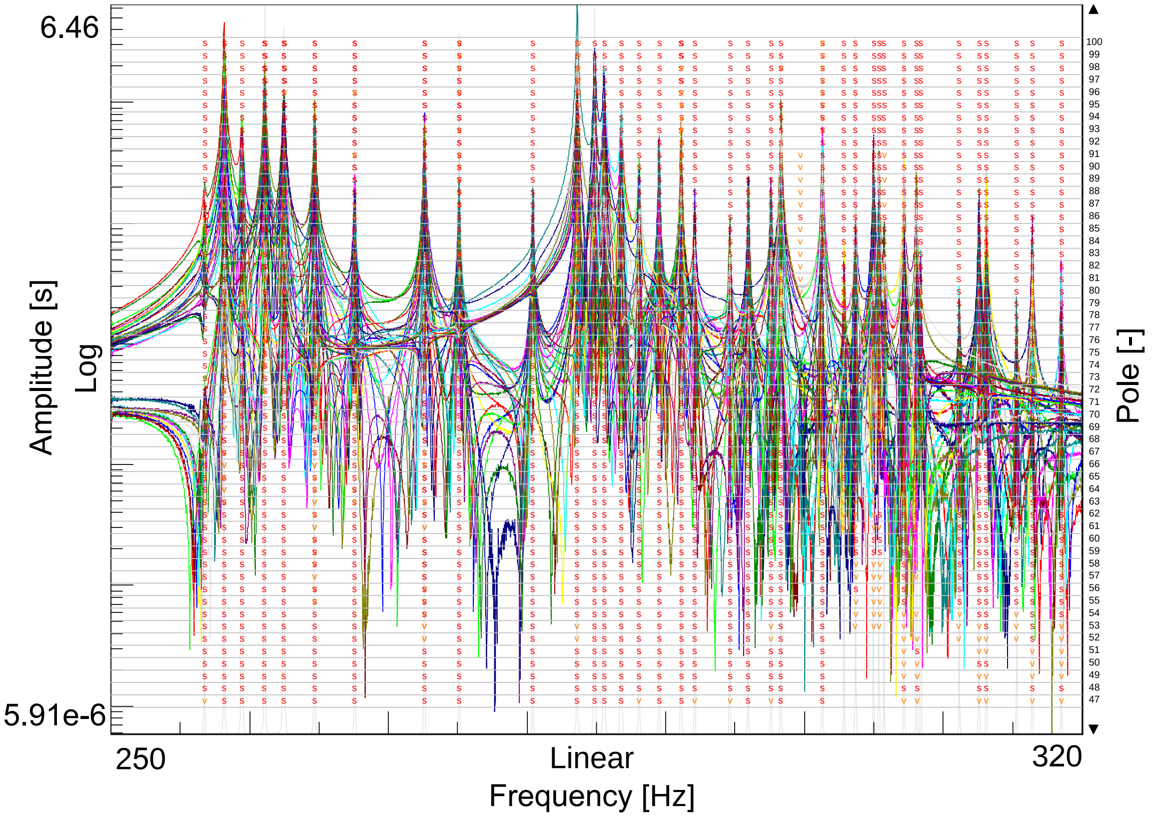

Figure 4.11: Stabilization diagram obtained with the additional masses. Symbols have following meaning: o – new pole; f – stable frequency; d – stable frequency and damping; v – stable frequency and eigenvector; s – all criteria stable.

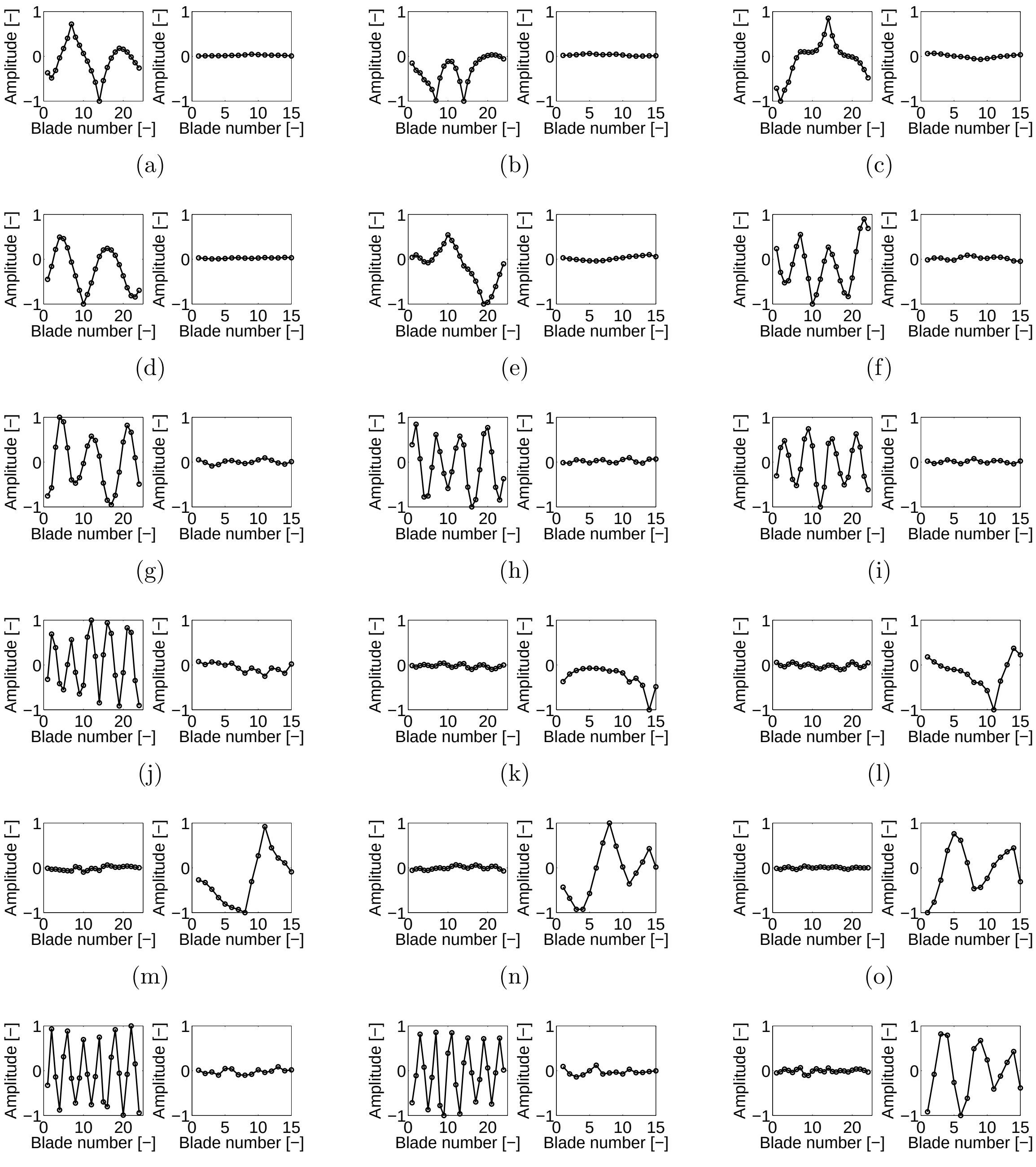

(a) (b) (c)

(d) (e) (f)

(g) (h) (i)

(j) (k) (l)

(m) (n) (o)

(p) (q) (r)

Figure 4.12: Experimental mode shapes with additional masses, stage 1 (left) and stage 2 (right).

4.5.1 Identification of the perturbed stiffness mistuning

The addition of masses on different blades can be seen as a perturbation of the eigenfrequencies, and therefore of the stiffness mistuning, of these blades. The aim of this Section is to identify the mistuning of the perturbed system.

The same procedure is applied to identify mistuning on the perturbed system i.e., the experimental eigenfrequencies and mode shapes are used to retrieved mistuning as explained in Section 4.2.2. The mistuning obtained using measurements on the perturbed structure is shown in Figure 4.13. The mistuning values obtained previously i.e., without masses, are superimposed. The mistuning values become negative for the blades where the masses are located because the addition of mass decreases their clamped blade eigenfrequencies.

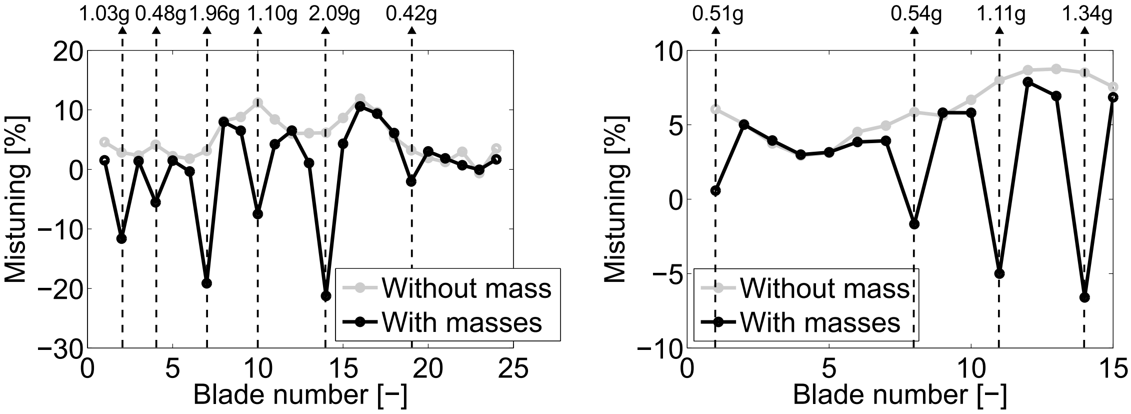

(a) Stage 1

(b) Stage 2

Figure 4.13: Comparison of mistuning obtained with the initial structure and with the structure when adding small lumped masses for stage 1(a) and stage 2 (b).

4.5.2 Validation of the identification

In order to validate the perturbed mistuning, a finite element model is constructed using the SAMCEF software [120]. The finite element model is constructed as followed:

- Since the stiffness mistuning of each blade of the non-perturbed structure has been identified in Section 4.4, a different Young's modulus is applied on each blade in the finite element model, as illustrated in Figure 4.14 (the blades have different colors in Figure 4.14, which correspond to different values of Young's modulus). Therefore, the finite element model represents the structure without masses.

- Then, small lumped masses are added in the finite element model at the same location than the experiment (black circles in Figure 4.14).

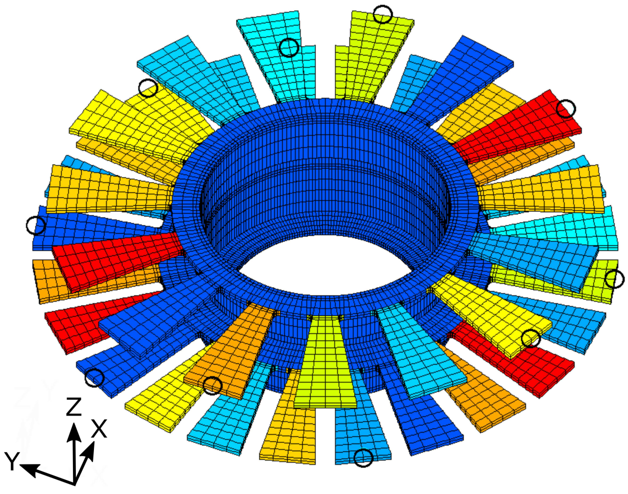

Figure 4.14: Finite element model with the identified mistuning on each blade, and small lumped masses.

Eigenfrequencies and mode shapes are computed for this finite element model, and are used as input of the identification method. Figures 4.15(a) and 4.15(b) compare the results obtained with the experimental data with additional masses (results of Section 4.5.1) and the data from the finite element model for stage 1 and stage 2 respectively. A good agreement is obtained between both results, which validates the identification method with the experimental data.

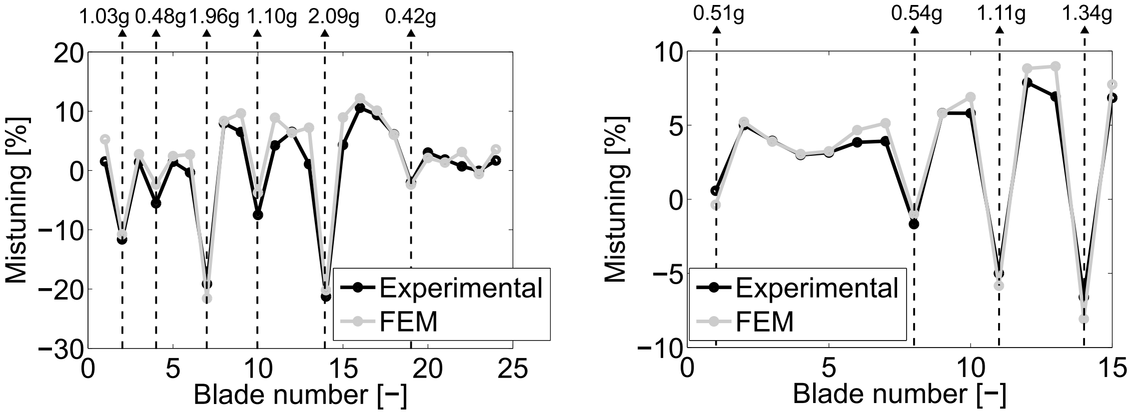

(a) Stage 1

(b) Stage 2

Figure 4.15: Comparison of mistuning obtained with the structure when adding small lumped masses, and with the finite element model for stage 1(a) and stage 2 (b).

4.5.3 Mass mistuning identification

The value of the added masses are now retrieved using Equation (4.32). The stiffness mistuning (i.e., the $\lambda^{\delta}_{ns,r}$) has been identified in Section 4.4 (measurements without masses). Using the second set of measurements (measurements with small lumped masses), the added masses can be identified by applying the developments of Section 4.2.2.

The obtained results are shown in Figure 4.16. The value of the added masses is superimposed (black curve). A good agreement is obtained between the experimental results and the masses actually added. It can be noted that the value for the blades without masses adjacent to blades where masses are added is slightly affected by the adjacent masses.

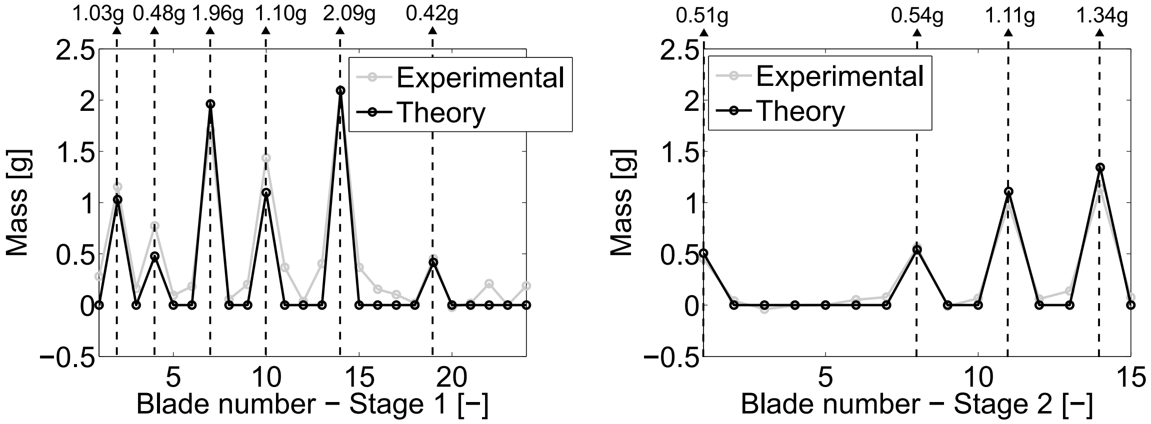

(a) Stage 1

(b) Stage 2

Figure 4.16: Mass identification for stage 1 (a) and stage 2 (b).

4.6 Sensitivity of the identification method

In order to evaluate the sensitivity of the identification method, perturbations in the input eigenfrequencies are introduced. Each frequency is perturbed independently. The perturbation on each measured frequency is defined as

$$f'_{exp} = f_{exp}\,(1+\delta) \ , \tag{4.34}$$

where f'_{exp} is the perturbed measured frequencies, f_{exp} the non-perturbed measured frequencies and δ is the perturbation which follows a normal distribution law. The error on the mistuning identified with the perturbed input data (noted $m^{\star}_{ID}$) compared to the mistuning identified with the non-perturbed input data (noted m_{ID}) is computed. The error E_{ID} is defined as

$$E_{ID} = \frac{m^{\star}_{ID} - m_{ID}}{\max\left(m_{ID}\right)} \ . \tag{4.35}$$

Figure 4.17 shows the error obtained when the perturbation in the input frequencies increases. 1000 perturbation samples are considered, with a normal distribution of the perturbation. An increase up to 2.5% is observed for a perturbation up to 1.5 Hz in the input eigenfrequencies.

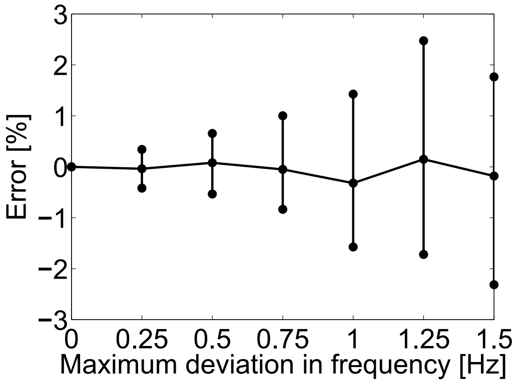

Figure 4.17: Error on the identified mistuning with noise in the input eigenfrequencies (minimum, mean and maximum values).

Then, the frequency response function (FRF) obtained for each pattern of identified values is computed. The FRF is compared with the one obtained with the initially introduced mistuning values. More particularly, the amplification factors obtained with the identified mistuning and the initially introduced mistuning are computed for an increasing perturbation. The used definition for the amplification factor, noted AF, is given by

$$AF = \frac{\max\left(\text{Mistuned forced response on each blade}\right)}{\text{mean}\left(\text{Mistuned forced response on each blade}\right)} , \tag{4.36}$$

The corresponding error on the amplification factor E_{AF} is defined as

$$E_{AF} = \frac{AF^{\star}_{ID} - AF_{ID}}{AF_{ID}} . \tag{4.37}$$

where $AF^{\star}_{ID}$ is the amplification factor obtained the mistuning identified using the perturbed eigenfrequencies, and AF_{ID} is the amplification factor obtained using the mistuning initially identify without any perturbation in the input data. Figure 4.18 shows the error on the amplification factor when the perturbation increases. The error reaches 5% for the bottom stage (stage 1), and 3% for the top stage (stage 2).

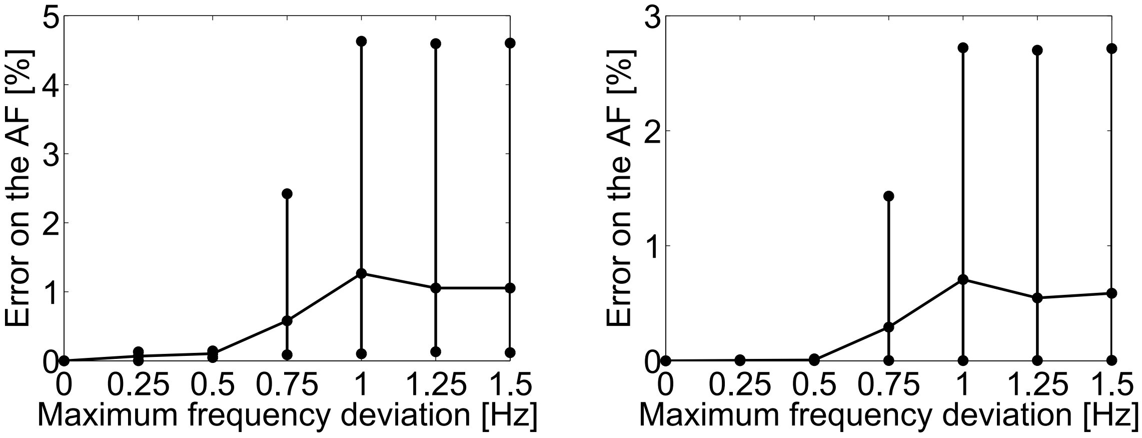

(a) Stage 1

(b) Stage 2

Figure 4.18: Error on the amplification factor (minimum, mean and maximum values) for stage 1 (a) and stage 2 (b).

4.7 Conclusion

Manufacturing of one-piece multi-stage structures significantly increases the influence of the interstage coupling that cannot be neglected anymore in the numerical models. The effects of mistuning are exacerbated due to the low damping level of the structure, to the higher disk/drum flexibility, and to coupling between the blades and the disk/drum. As a consequence it appears that multi-stage structures may present higher amplification factor than those related to single stage configuration.

Therefore, the ability of characterizing mistuning in multi-stage bladed structure is important since the dynamic behavior of the structure is strongly affected by mistuning.

An extension of the CMM identification method initially developed by Lim has been proposed in this work to treat the case of multi-stage structures. The proposed method enables to retrieve the mistuning of the blades of each stage using measurements of eigenfrequencies and mode shapes. The associated test procedure established in this work is simple to implement in practice.

Modal testing has been performed on an academic drum composed of two stages. A simple test procedure to identify mistuning in a multi-stage structure has been established and validated in this work. A base excitation was used in order to not disturb the structure by adding a contact excitation to the blades or the disk/drum. The response on each blade of each stage was measured in the axial direction with a laser vibrometer. Then, the experimental frequencies and mode shapes, retrieved from the stabilization diagram using the PolyMax method, were used as input data of the identification method. The mistuning of each blade was computed using the identification method.

Validation of the obtained mistuning has been performed by adding small lumped masses on some blades of the structure. The experimental eigenfrequencies and mode shapes of this disturbed system are used to determine the deviation in the clamped blade eigenfrequencies for each blade. This deviation has been computed with a good accuracy. In the same way, the perturbation has also been successfully retrieved in terms of masses, which completely validates the experimental identification.

A study of the sensitivity of the identification to noise in the input data has also been performed. It results that the quality of the measurements has a limited impact on the value of the identified mistuning since a linear increase of the error with noise has been observed. However, it has a larger impact on the resulting amplification factor. The results show that the error performed on the amplification factor highly increases above a limit of 0.5 Hz (i.e., 0.2 %) in this case.

Chapter 5

Geometric mistuning and model updating

Mistuning in both mono-stage and multi-stage academic blisks has been identified in Chapters 3 and 4 respectively using vibration tests. Since the structures are one-piece manufactured, the material properties can be assumed to be uniform, and there are no bounded connections between the blades and the drum. Thus, the main source of mistuning for these two structures is the geometry variations due to the manufacturing process. An optical measurement is used in this Chapter to determine the exact geometry of the two structures. A geometrical mistuning is associated to each blade. Differences are observed between the experimentally identified mistuning and the geometrical mistuning because of non-uniformities in the clamping conditions.

5.1 Introduction

Different studies have been performed in the past to retrieve the geometric mistuning of bladed structures. Two types of geometric metrology have been used: contacting touch probe (or coordinate measurement machines) and optical measurement systems (see Figures 5.1(a) and 5.1(b) respectively) [126].

Coordinate measurement machines have the advantage to provide well-ordered cross section data and spot measurements. However, the automation of the measurement process requires an expert knowledge in Computer Numerical Control (CNC) machinery. Huang et al. [128] used in their work an automated system for 3D coordinate measurement of turbine vane airfoils. A repeatability of 10 μm in the measurements was found. Garzon et al. [129] also used coordinate measurement machines to retrieve blade profiles and construct from these data the corresponding Computational Fluid Dynamic (CFD) performance models. Sinha et al. [130] used coordinate measurement machines data from a commercial rotor to study modal variations of airfoils. They measured in their work the deviation in blade alone modal response and compared it with the geometric measurements. Brown et al. [131–133] also worked on mistuning by quantifying airfoil geometry variation using contacting probe coordinate measurement machines. They show the impact of geometric variations in response prediction, in particular for higher order modes.

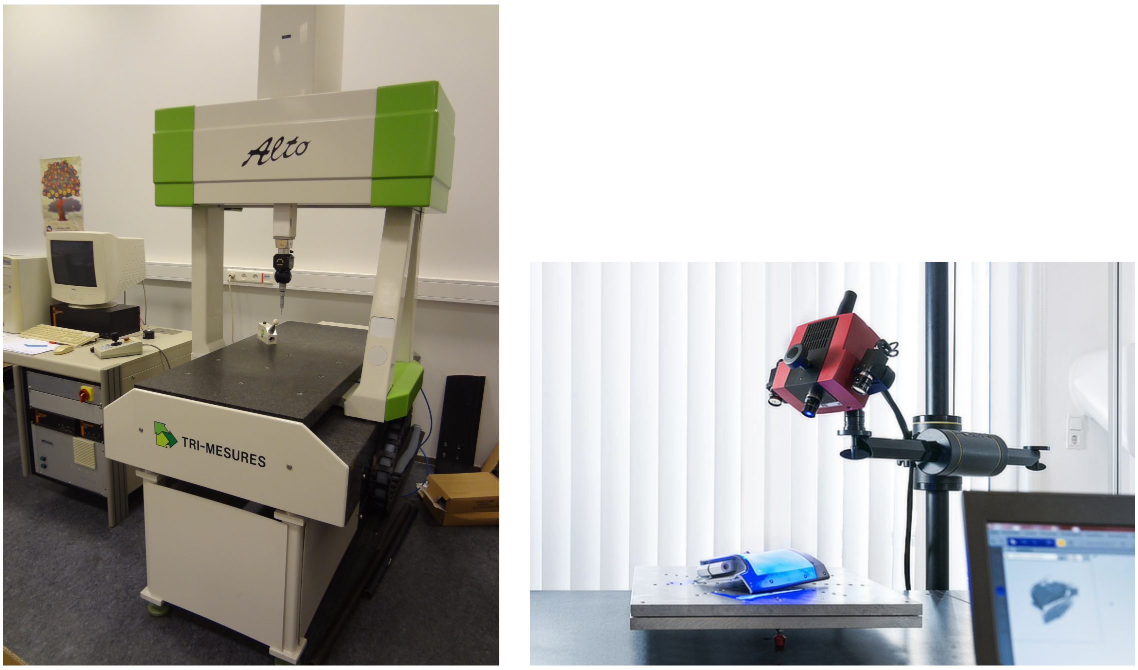

(a) (b)

Figure 5.1: Contacting touch probe (a), and optical measurement systems [127] (b).

Numerous studies have been performed using optical measurement systems [134]. The advantages of these systems are the rapidity of the process and dense measurement spots. For these reasons, the optical inspection systems are largely used and lot of works are performed to overcome their current challenges. Indeed, it remains some challenges concerning reflective surface noise, line of sight requirements, merging results from multiple scans, and unstructured data point clouds. Holtzhausen et al. [135] used in their work a 3D optical measuring and data conditioning process for turbine engine inserted airfoils. The obtain accuracy for the measurement was found to be 5 μm. The acquisition time was approximately 30 minutes per blade. Lange et al. [136] measured with the optical scanning system a large population of airfoils, and created steady CFD performance models. [126] used an optical measurement system on a blisk in order to predict the modal and mistuned response of the structure. They convert point cloud measurements to physics-based mistuning models, and quantify the impact of the geometric uncertainty on the predicted mistuned response. De Cazenove et al. [137] measured accurately the geometry of a realistic blisk and built a high-fidelity FE model of the structure. They compared the cantilevered-blade and full disk calculated eigenfrequencies with the experimental individual blade and full disk in quasi-vacuum conditions.

In this Chapter, the exact geometry of both mono-stage and multi-stage academic structures is measured by means of an optical geometry measurement system, quantifying the level of geometric mistuning. Based on these optical data, a finite element model of each structure is constructed, and a geometrical mistuning is associated to each blade.

The mistuning of each blade in both mono-stage and multi-stage academic blisks was previously identified in Chapters 3 and 4 respectively using vibration tests. The measurement of the geometry of each blade of both structures permits to quantify the relative importance of geometric mistuning compared to other sources of mistuning. In this case, since the studied bladed structures are both one-piece manufactured, there are no welded connections between the blades and the drum and the material properties can be assumed to be uniform. Thus, the main source of additional mistuning for this structure is the clamping condition which cannot be perfect in practice.

5.2 Test set-up for the optical measurement of the geometry

The geometry of the structure is measured with a 3D camera [127]. The aim of these measurements is to compare the mistuning due to changes in geometry induced by the manufacturing tolerances, with the mistuning identified using vibration tests.

An optical geometry measurement system is used to obtain the geometry of each blade of both structures. The test set-up is shown in Figure 5.2. The optical system is composed of a central Light Emitting Diode (LED) source to illuminate the structure with a regular grid pattern projection. In order to reflect the light projected by the optical device, the scanned object is powdered beforehand [126]. However, the two studied structures are made in a highly reflective material, and the white powder is not necessary here. The distorted profile of the structure is captured by two cameras on either side of the LED source and the projected shape is used to triangulate surface coordinates. A series of picture are captured and merged together using common reference points. These standard reference circles placed on the structures are shown in Figure 5.3. With the measurement system available in the Centre Spatial de Liège (CSL) [138], the geometry of the structures can be retrieved with an accuracy lower than 50 μm.

Figure 5.2: Test set-up for the optical measurement of the geometry.

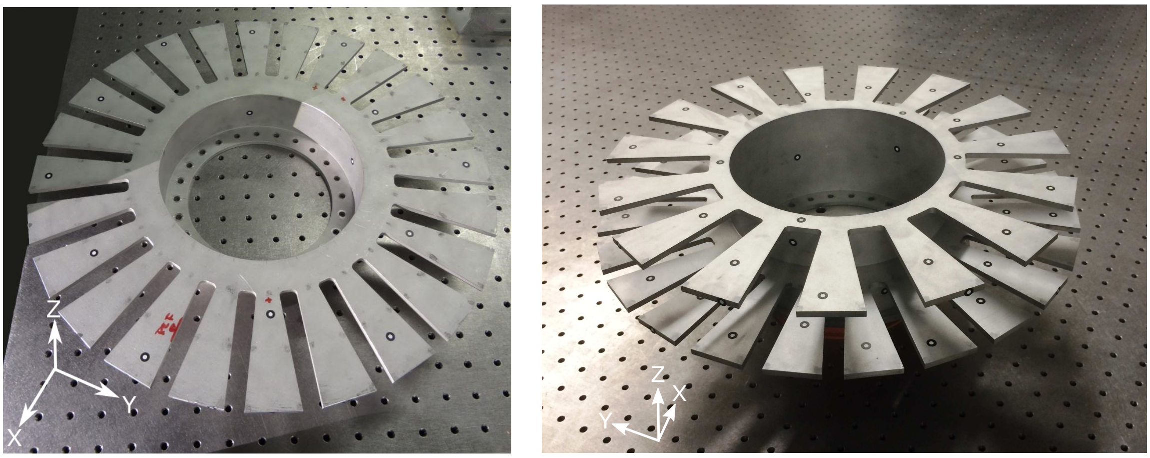

(a) Mono-stage

(b) Multi-stage

Figure 5.3: Standard reference circles placed on the mono-stage (a) and multi-stage (b) structures.

5.3 Geometry measurement

Using the experimental set-up of Section 5.2 for both academic structures, their detailed geometries are retrieved. The obtained measurements are presented in this Section.

5.3.1 Mono-stage academic structure

Figures 5.4 and 5.5 show the precise profile of respectively the upper and lower faces of the mono-stage structure. The profile is defined as the vertical deviation of the measured geometry compared to a horizontal plane at an elevation of 0 and -5 *mm* respectively for the upper and lower face i.e., the theoretical location of the upper and lower surfaces if the structure was perfectly identical to the CAD model. The upper bound (red color) represents the maximum vertical elevation of the points of the geometry compared to a theoretical plane (the plane of the reference tuned structure), and the lower bound (blue color) is the minimum value of the elevation. A positive sign represents a point at a higher vertical coordinate compared to its theoretical position, and a negative sign represents a lower vertical coordinate of the point compared to its theoretical position. The black curve on the left of the color bar shows the repartition of the elevation, between -0.08 *mm* and 0.08 *mm* for the upper surface. The middle bound (green color) represents the theoretical value. The majority of the values are between 0.02 *mm* and -0.08 *mm*. For the lower surface, the scale is between -0.08 *mm* and 0.1 *mm*. The middle bound (green color) represents the theoretical value. The majority of the values are between 0.02 *mm* and -0.08 *mm*.

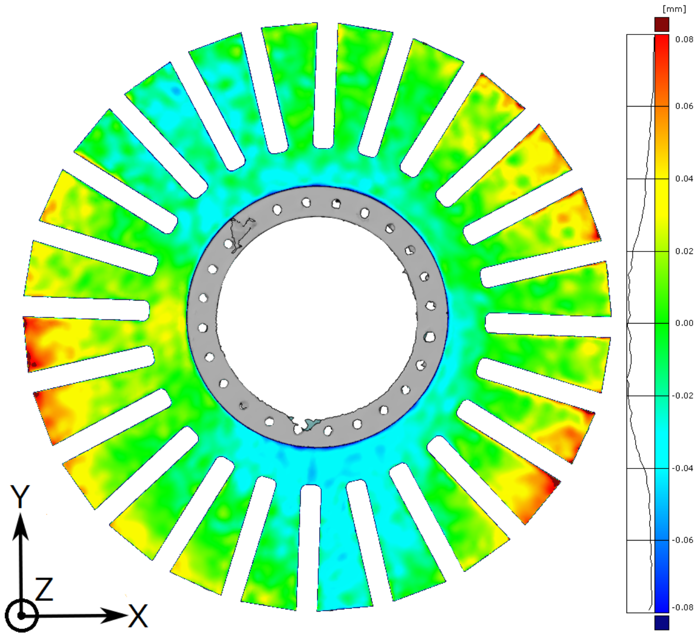

Figure 5.4: Measured profile of the upper face of the mono-stage structure.

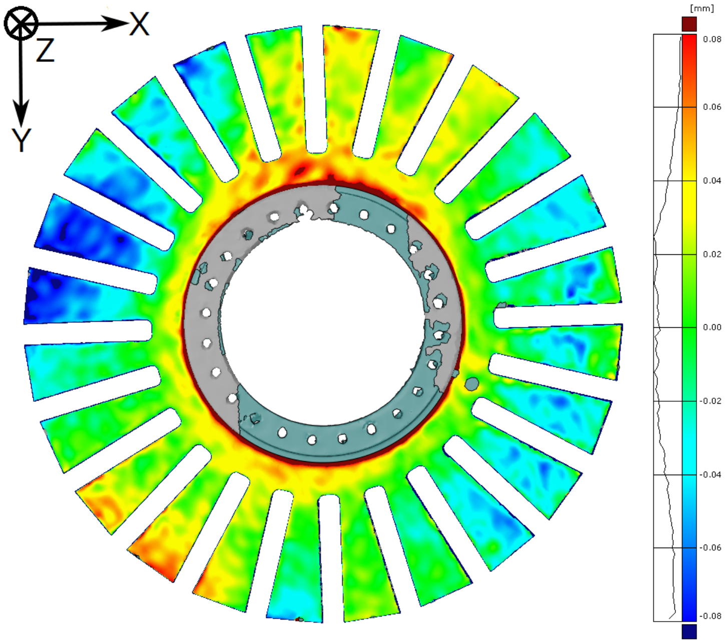

Figure 5.5: Measured profile of the lower face of the mono-stage structure.

5.3.2 Multi-stage academic structure

Figures 5.6 and 5.7 show the precise profile of respectively the upper and lower faces of the bottom stage of the multi-stage structure, and Figures 5.8 and 5.9 the precise profile of the upper and lower faces of the top stage respectively. The profile is again defined as the vertical deviation of the measured geometry compared to four horizontal planes at an elevation of 0 mm (for the upper face of stage 1), -5 mm (for the lower face of stage 1), 46 mm (for the upper face of stage 2), and 41 mm (for the lower face of stage 2). The same color scale as for the mono-stage structure is used here. These four planes correspond to the location of each face if the structure was exactly identical to the CAD model.

The deviation comparing to the nominal planes are from -0.3 mm and 0.3 mm for the four surfaces. Therefore, the manufacturing tolerances for the multi-stage structure are 3 times larger than for mono-stage structure (tolerance up to 0.1 mm). This is due to the higher complexity of the multi-stage structure from the manufacturing point of view.

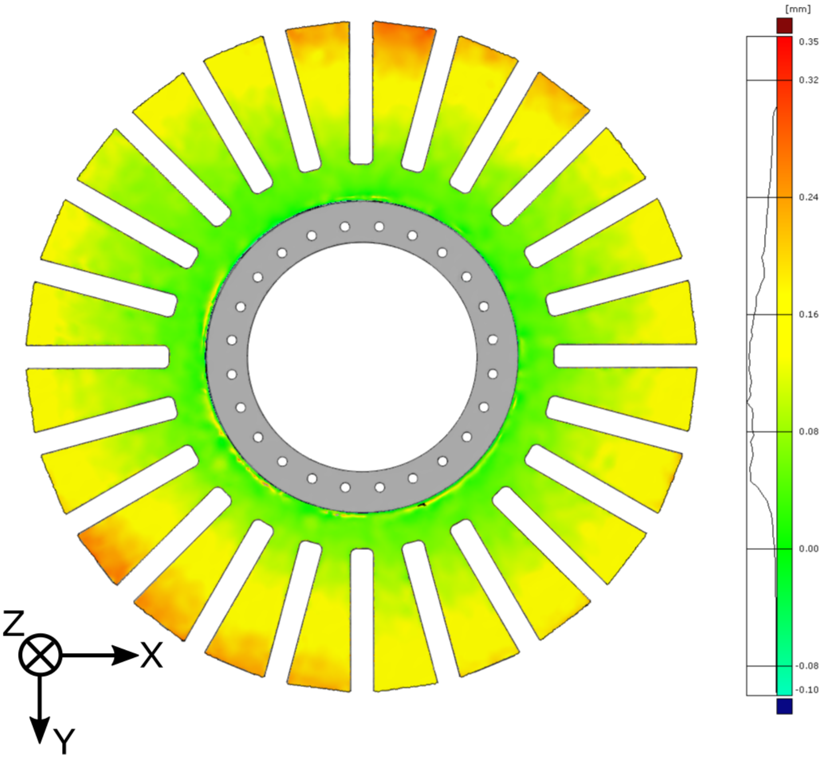

Figure 5.6: Measured profile of the upper face of the bottom stage of the multi-stage structure.

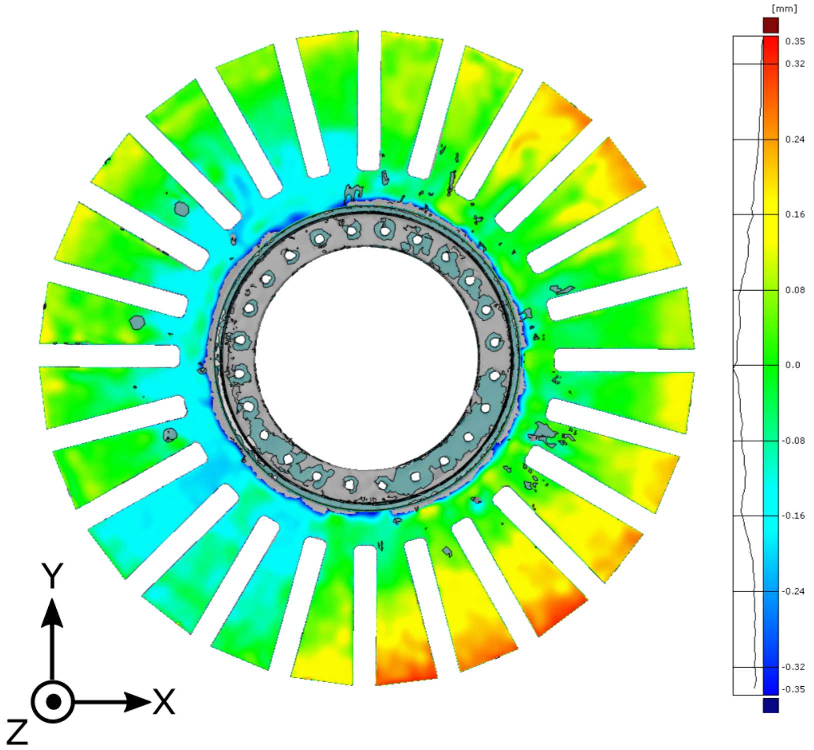

Figure 5.7: Measured profile of the lower face of the bottom stage of the multi-stage structure.

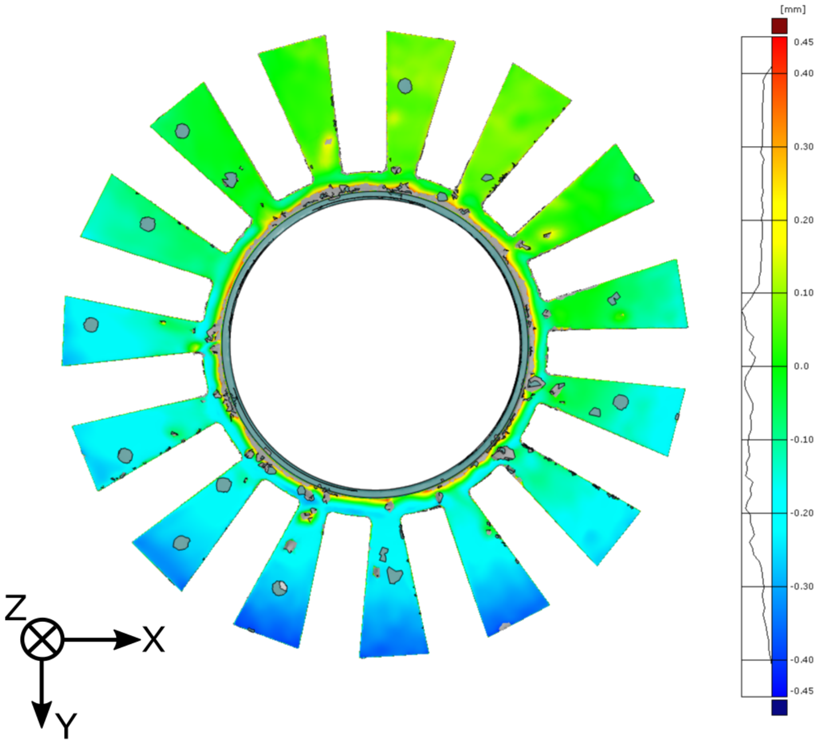

Figure 5.8: Measured profile of the upper face of the top stage of the multi-stage structure.

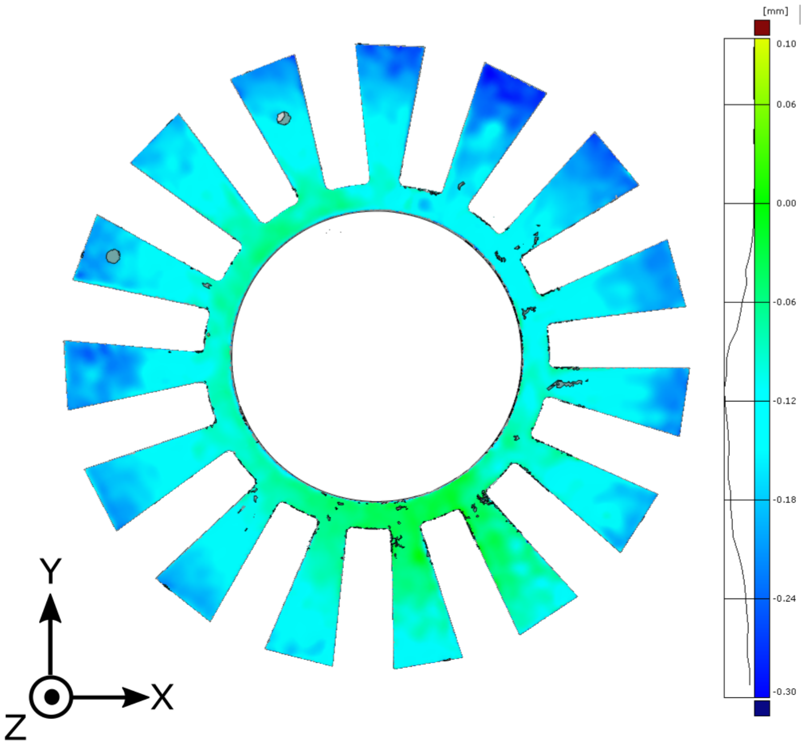

Figure 5.9: Measured profile of the lower face of the top stage of the multi-stage structure.

5.4 Construction of the finite element model

Based on the optical geometry measurements, a refined finite element model of each structure is constructed. In these finite element models, each sector has a different shape, the Young's modulus remaining uniform for all the structure. The data given by the optical geometry measurement system is a set of points of the envelope of the structure. The detailed procedure to construct the models is explained in Appendix E.

5.4.1 Mono-stage academic structure

The set of points obtained from the mono-stage academic structure is presented in Figure 5.10.

The initial tuned model (i.e., the mesh with exactly identical sectors) is first finely meshed. The number of nodes in the refined finite element model is 727 491. The aim of refining the mesh is that it enables to match all the irregularities in the shape of the structure. Next, the nodes on the skin of the refined finite element model are modified by adapting the elevation of each node to follow the profile measured by the optical system.

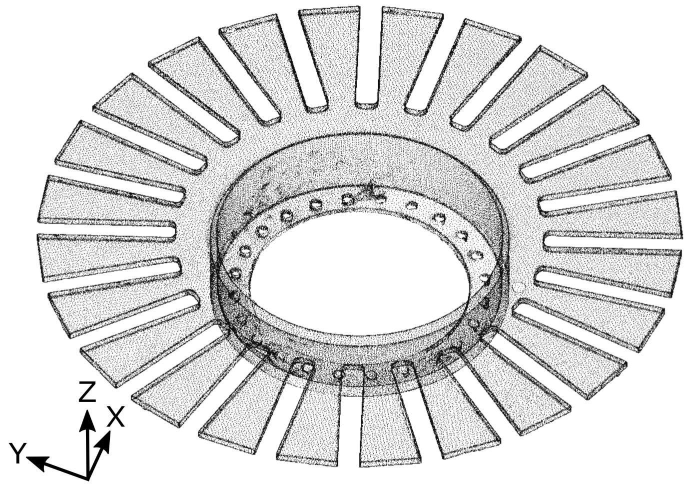

Figure 5.10: Set of points of the envelope of the mono-stage structure given by the optical measurement system.

The eigenfrequencies and the corresponding mode shapes are computed for the refined finite element model. Figure 5.11 shows the three first mode shapes (one point per sector is considered, at the tip of each blade). The mode shapes are normalized using the modal scale factor (MSF). The mode shapes obtained experimentally in Chapter 3 using laser vibrometer measurements are superimposed (black curves). Large differences are observed between both mode shapes.

The mode-shapes can be compared using the using the Modal Assurance Criterion (MAC). The MAC is a quantitative measure of the alignment between two modes, defined as

$$\mathrm{MAC}_{ij} = \frac{|\mathbf{\Phi}_{1,i}^T \mathbf{\Phi}_{2,j}|^2}{\left(\mathbf{\Phi}_{1,i}^T \mathbf{\Phi}_{1,i}\right)\left(\mathbf{\Phi}_{2,j}^T \mathbf{\Phi}_{2,j}\right)} \,, \tag{5.1}$$

where $\mathbf{\Phi}_{1,i}$ is the i^{th} mode of the set of modes $\mathbf{\Phi}_1$, and $\mathbf{\Phi}_{2,j}$ is the j^{th} mode of the set of modes $\mathbf{\Phi}_2$. A MAC value of 1 indicates fully consistent modes, and 0 indicates that the modes are not consistent [139].

Figure 5.12 shows the MAC matrix between the experimental modes used for the identification and the first eigenmodes obtained with the finite element model. The MAC number is 0.9 for the first mode, and 0.7 for the second and third modes but in a different order. Different sources can explain these differences, such as variations in the material properties, differences in the boundary conditions (in the finite element model, a perfect clamping of the structure is assumed, but this assumption is not feasible in practice), residual constraints after machining...

However, the finite element model with the accurate geometry can precisely predict the mode shapes in higher frequency ranges, as illustrated for a few modes using holographic measurements in Figures 5.13 (1T modes), 5.14 (2B modes), 5.15 (2T modes) and 5.16 (3BT modes).

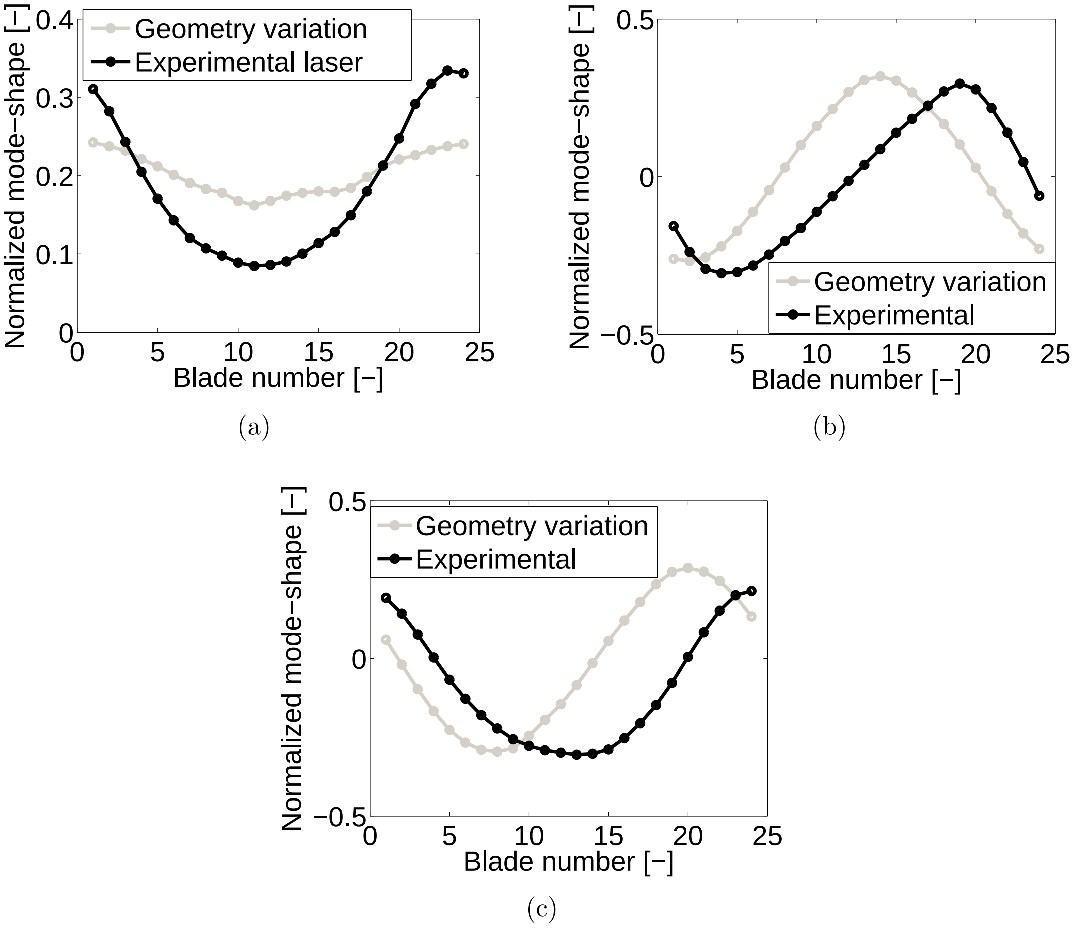

Figure 5.11: Mode shapes corresponding to the first (a), to the second (b) and to the third eigenfrequencies (c).

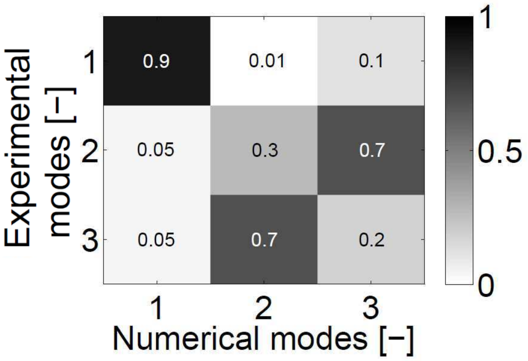

Figure 5.12: MAC matrix between the mode shapes from the geometrically mistuned finite element model and the experimental mode shapes.

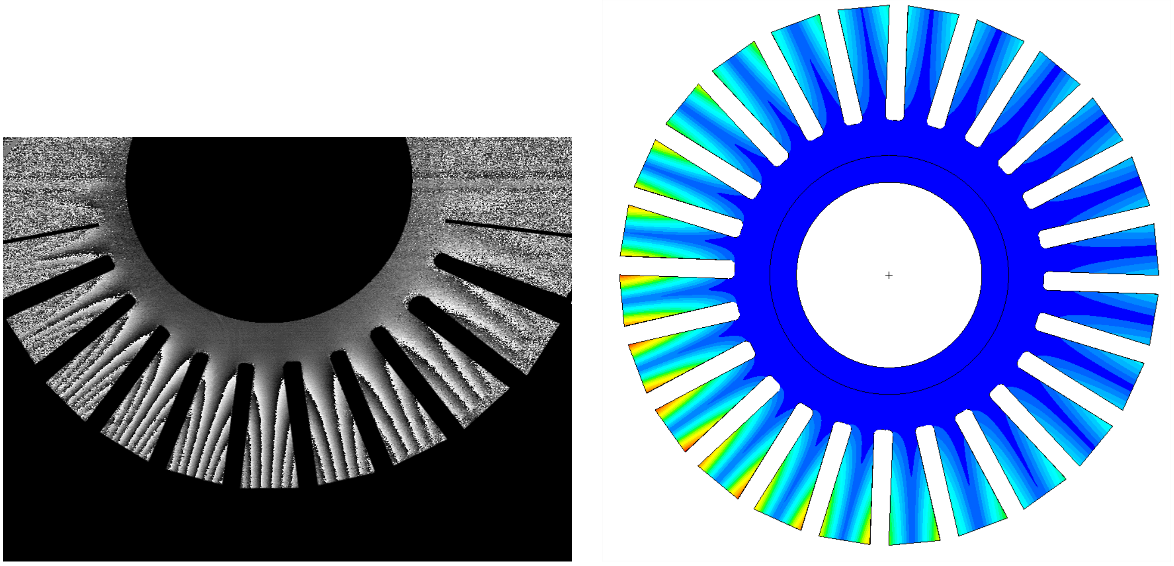

(a) Holography (b) FE model

Figure 5.13: Mode shape measured with holography at a frequency of 1950 Hz (a) and numerical mode shape at a frequency of 1951 Hz (b).

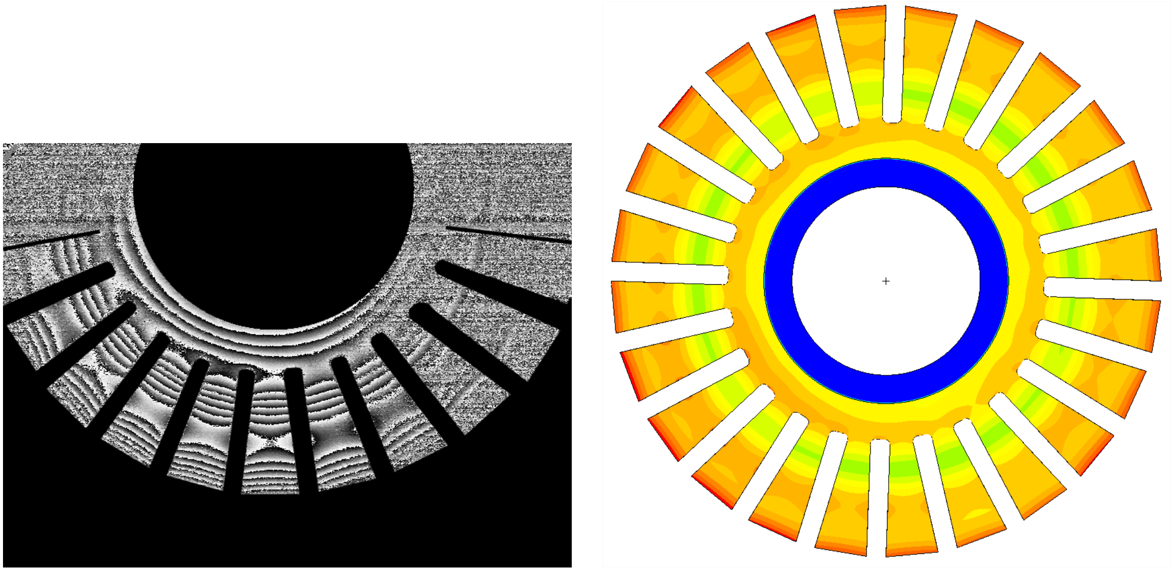

(a) Holography (b) FE model

Figure 5.14: Mode shape measured with holography at a frequency of 4100 Hz (a) and numerical mode shape at a frequency of 4061 Hz (b).

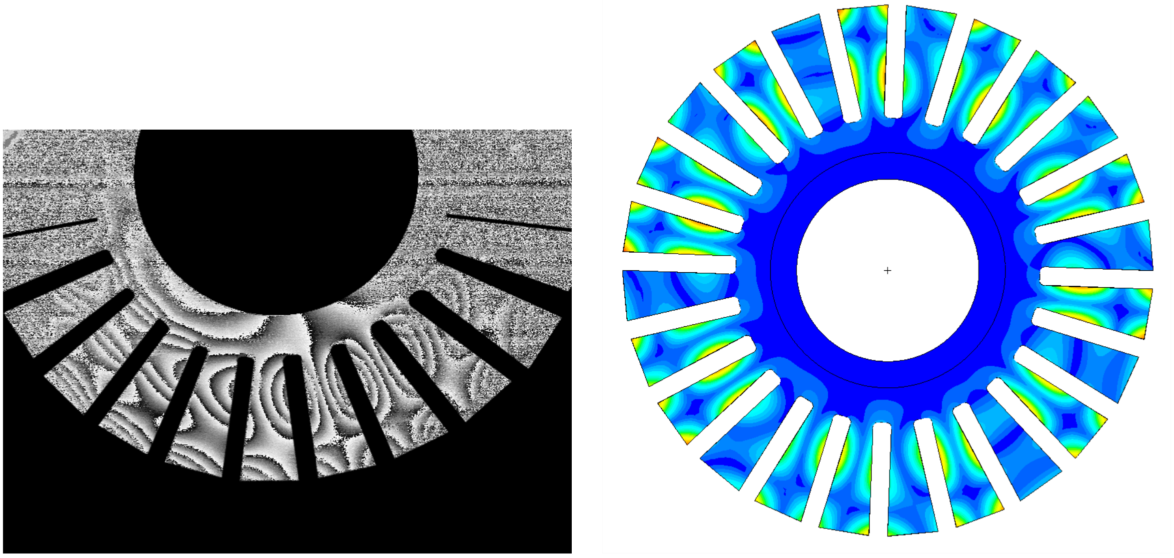

(a) Holography (b) FE model

Figure 5.15: Mode shape measured with holography at a frequency of 8283 Hz (a) and numerical mode shape at a frequency of 8283 Hz (b).

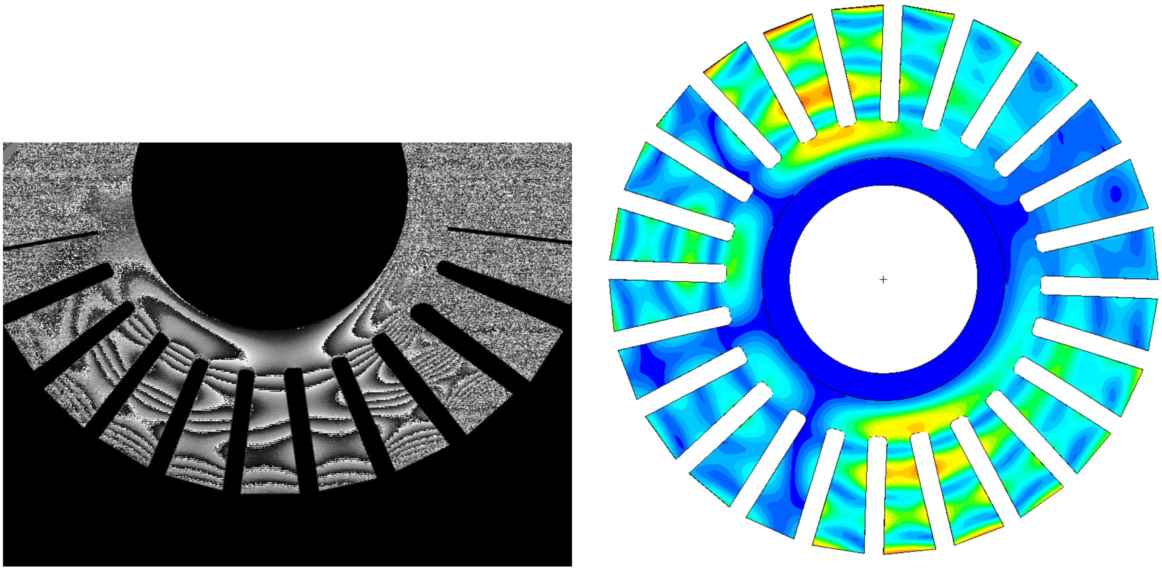

(a) Holography (b) FE model

Figure 5.16: Mode shape measured with holography at a frequency of 9300 Hz (a) and numerical mode shape at a frequency of 9407 Hz (b).

5.4.2 Multi-stage academic structure

The set of points obtained from the multi-stage academic structure is presented in Figure 5.17.

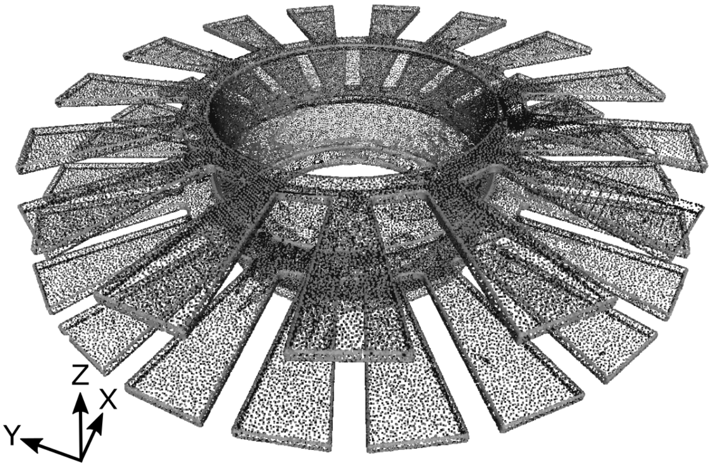

Figure 5.17: Set of points of the envelope of the multi-stage structure given by the optical measurement system.

The initial tuned model (i.e., the mesh with exactly identical sectors) is again finely meshed to be able to match all the irregularities in the shape of the structure. The number of nodes in the refined finite element model is 1 239 365. After that, the nodes on the skin of the refined finite element model are modified by adapting the elevation of each node to follow the profile measured by the optical system.

The eigenfrequencies and the corresponding mode shapes are computed for the refined finite element model. Figure 5.18 shows for each stage the first mode shape obtained experimentally in Chapter 4 using laser vibrometer measurements (black curves), normalized using the MSF. One measurement point per sector is considered, at the tip of each blade. The corresponding finite element mode shape with similar deformation is superimposed, also normalized using the MSF (gray curves). The displacements of stage 1 is shown in Figure 5.18(a), and the displacements of stage 2 in Figure 5.18(b). Large differences are again observed between both mode shapes for the first mode. Figure 5.19 gives the MAC matrix between the experimental modes used for the identification and the eigenmodes obtained with the finite element model. The MAC number is 0.5 for the first mode, and the second. Then, differences are observed between experimental and numerical results for the three following modes. For higher modes, low differences are observed.

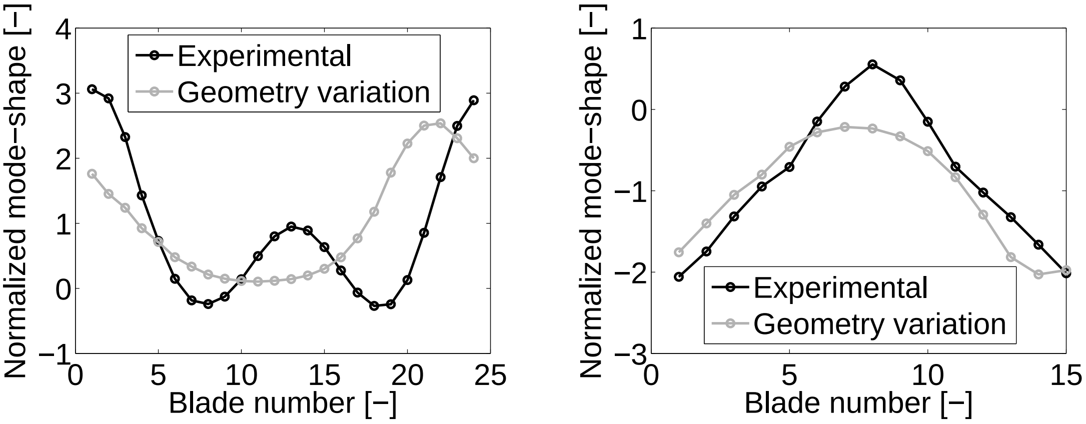

(a) Stage 1

(b) Stage 2

Figure 5.18: First experimental and numerical mode shape for stage 1 (a) and stage 2 (b).

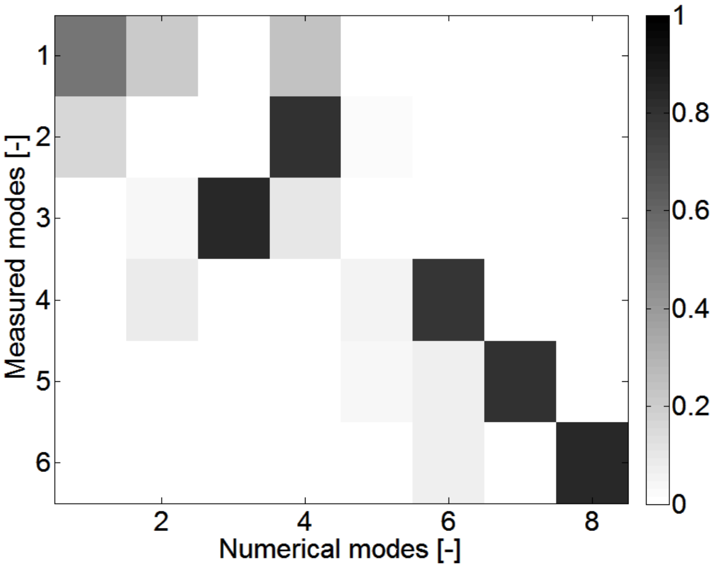

Figure 5.19: MAC matrix between the mode shapes from the geometrically mistuned multi-stage finite element model and the experimental mode shapes.

5.5 Comparison of the frequency and geometric mistuning

In order to be able to compare the geometric mistuning with the mistuning identified experimentally in Chapters 3 and 4, the clamped blade eigenfrequencies of the geometric models constructed in Section 5.4 are computed. Since the experimentally identified mistuning is actually the deviation of the clamped blade eigenfrequencies, the comparison between both mistuning is possible by this way.

5.5.1 Mono-stage academic structure

The clamped blade eigenfrequencies of the geometric model are computed. This enables to associate a geometric mistuning to each blade of the structure. The obtained geometric mistuning is compared to the mistuning identified experimentally in Figure 5.20. Differences are observed between both results.

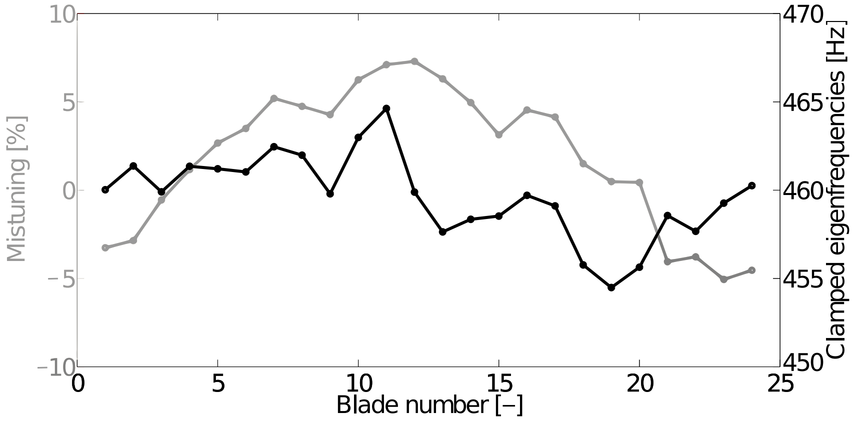

Figure 5.20: Mistuning experimentally identified (in gray) and clamped blade eigenfrequencies (in black).

Since the studied bladed drum is a one-piece structure and there are no welded connections between the blades and the drum, the material properties can be assumed to be uniform. The main remaining source of mistuning is the boundary conditions. Indeed, in the finite element model, a perfect and uniform clamping of the structure is assumed, but this assumption is not feasible in practice.

5.5.2 Multi-stage academic structure

The clamped blade eigenfrequencies of the multi-stage geometric model are computed. The obtained geometric mistuning is compared for each stage to the mistuning identified experimentally in Figure 5.21. Differences are again observed between both results. Since the structure is also one-piece manufactured, the main remaining source of mistuning is the boundary conditions as for the mono-stage structure. An update of the boundary conditions of the finite element model with the refined geometry is performed in Section 5.6.

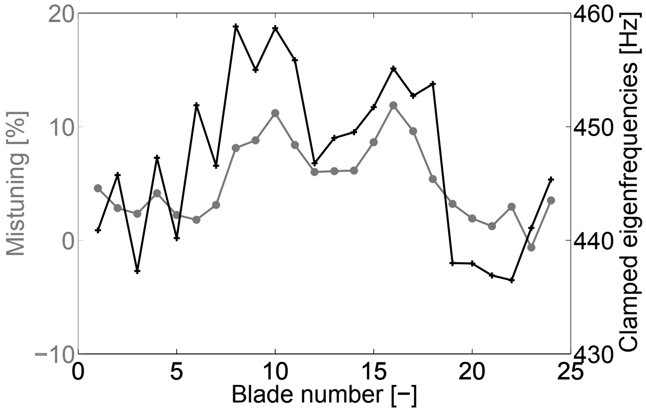

(a) Stage 1

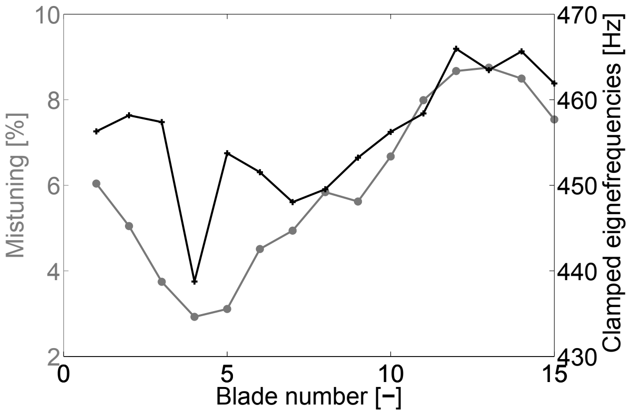

(b) Stage 2

Figure 5.21: Mistuning experimentally identified (in gray) and clamped blade eigenfrequencies (in black) for stage 1 (a) and stage 2 (b).

5.6 Update of the clamping conditions

In order to update the model, the perfect clamping condition is replaced by springs in the finite element model, as illustrated in Figure 5.22. To impose this updated boundary condition in the SAMCEF finite element software, the nodes initially clamped are duplicated. Then, springs are added between each pair of duplicated nodes. Displacements are allowed only in the axial direction (Z-axis). A finite stiffness is attributed for each spring.

The springs on the boundary condition have a different stiffness for each sector. Both mono-stage and multi-stage structures have 24 (i.e., the same number as the number of blades of the bottom stage) fixation points in the experimental set-up. Therefore, there are 24 unknown factors, named δ_n^k $(n = 1, ..., N)$, defined as

$$k_n = k_0 \left(1 + \delta_n^k\right) \ , \tag{5.2}$$

where k_0 is the initial (finite value) of the stiffness of the springs in the updating clamping conditions, and k_n is the mistuned clamping stiffness of sector n.

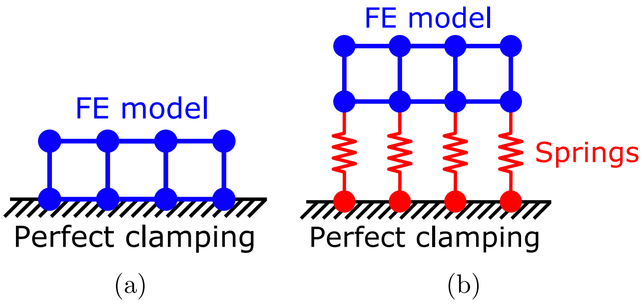

(a) (b)

Figure 5.22: Previous (a) and updated (b) boundary conditions.

The software Boss Quattro [140] is used to determine the value of the unknown factors for both finite element models. This software performs optimization process, interacting with the finite element software SAMCEF [120]. In order to reduce the computational time of the optimization, superelements (SE) of the finite element models are created. Indeed, it has been explained in Section 5.4 that the meshes of the finite element models with the precise geometry are highly refined in order to follow the profile of the structures. The nodes retained in the SE are the clamped nodes, and one node at the blade tip for each blade. 24 internal modes are also retained for the mono-stage model, and $24+15=39$ internal modes for the multi-stage model. The number of degrees of freedom and the computational time on a standard laptop are given in Table 5.1.

	DOF number [-]	Computational time
Mono-stage initial FE model	2 172 073	1 h 33 min
Mono-stage SE model	5 296	2 min
Multi-stage initial FE model	3 698 895	4 h 10 min
Multi-stage SE model	6 556	3 min

Table 5.1: Comparison between the initial finite element models and the models with superelements.

In order to construct the superelement from the finite element model, the Young's modulus has to be fixed. For this reason, the Young's modulus is not defined as an internal variable for the optimization, and the optimization is performed on the experimental mode shapes only, and not on the eigenfrequencies.

Four steps are repeated to get the value of our 24 unknown factors, as illustrated in Figure 5.23:

1. The SAMCEF input file is constructed such that the unknown factors are defined as parameters instead of giving a defined value. Then, these parameters are defined in Boss Quattro [140] as internal variables for the optimization process. They are all initialized to k_0 for the first iteration.

2. A dynamical analysis is performed with the current value of the internal variables. The current eigenfrequencies and mode shapes can be retrieved.

3. Boss Quattro [140] computes the sensibility of the eigenvectors for each variable by finite differences.

4. Boss Quattro [140] computes the updated values of the internal variables. The target function is defined here as the mean square error between the numerical and experimental deformation of the first eigenvectors. Since the Young's modulus has been fixed, no target function is added on the eigenfrequencies. Once the new values of the internal variables are computed, the process begins again from step 2 until convergence.

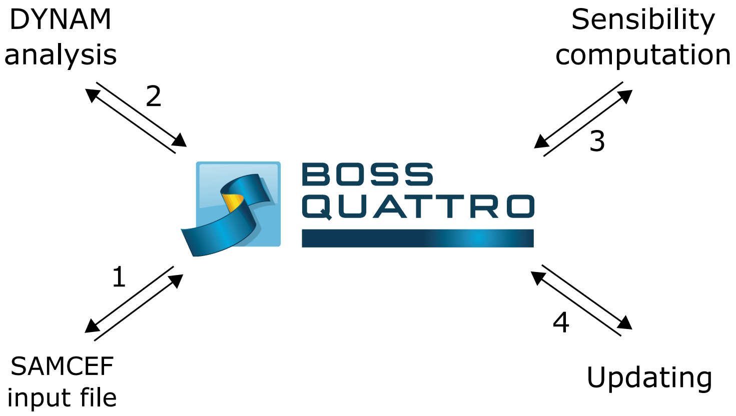

Figure 5.23: Different steps of the optimization process.

5.6.1 Mono-stage academic structure

The optimization process presented in Section 5.6 is applied for the mono-stage academic structure. Five iterations are necessary to converge.

The springs on the boundary conditions have now a different stiffness for each sector, as illustrated in Figure 5.24. Darker areas represent higher stiffness of the springs, and lighter areas represent a lower stiffness.

Figure 5.25 gives the absolute values of the geometric mistuning and the "clamping mistuning" for each blade. The geometry mistuning is defined here as the variation in the volume of the blade compared to the mean volume. Both mistunings are of the same order of magnitude but the stiffness mistuning remains larger (up to 7 %). When adding the geometric mistuning and the mistuning in the stiffnesses of the boundary conditions, the mistuning experimentally identified is retrieved.

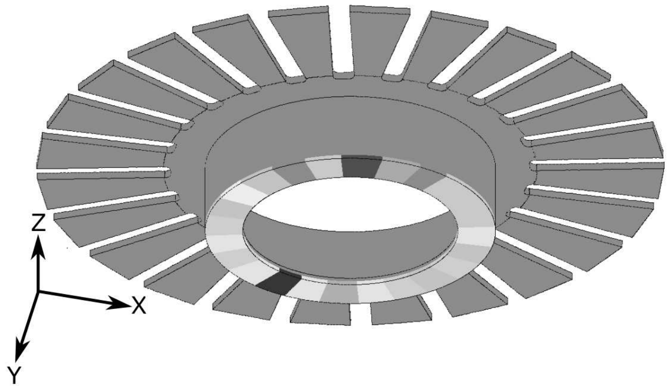

Figure 5.24: Non-uniform clamping conditions for the mono-stage structure.

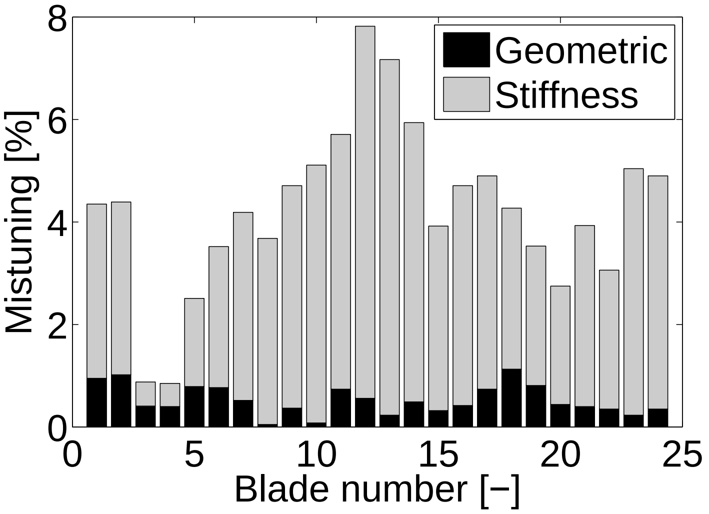

Figure 5.25: Geometric and stiffness mistuning.

The new mode shapes are given in Figure 5.26. A good correspondence is obtained for the first three modes. The MAC values between experimental and numerical mode shapes are 1 for the three considered modes.

The modification of the clamping conditions has improved the correspondence between the mode shapes of the numerical model and the experimental data. The remaining error in blade mistuning using the updated numerical mode shapes is 3 %. It can be concluded that the mistuning of blade can be determined experimentally, and this identified mistuning has two main sources: the geometry variations between the different sectors which are due to the manufacturing tolerances, and the clamping conditions which differ from the perfect clamping conditions usually used in the finite element models.

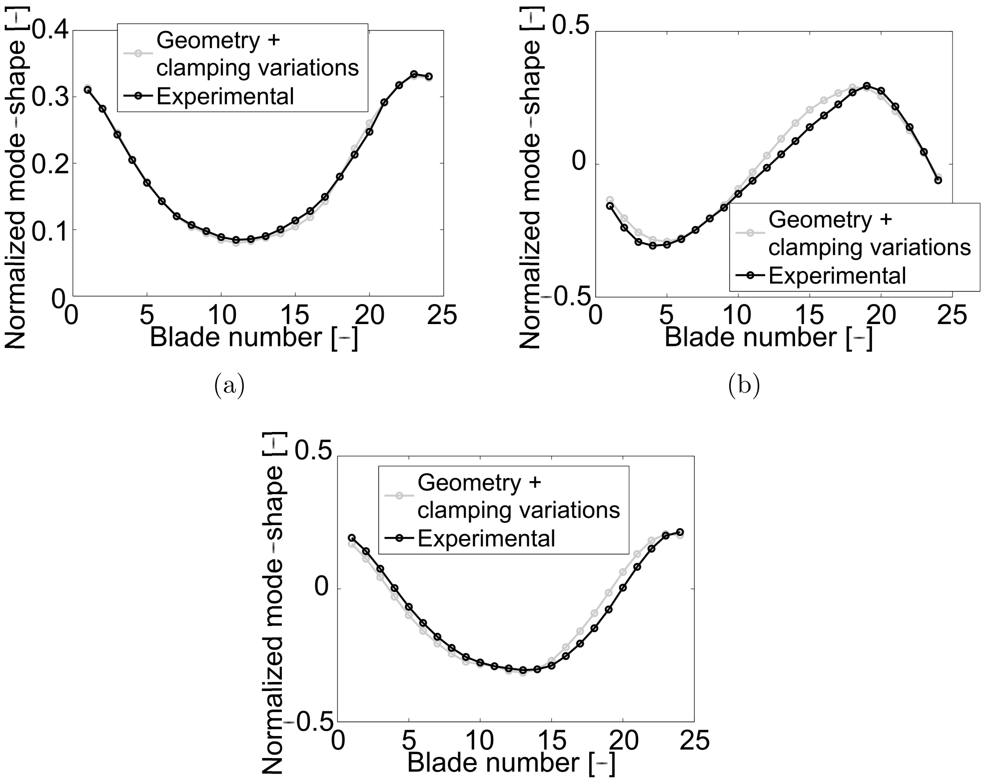

(a)

(b)

(c)

Figure 5.26: Mode shape corresponding to the first eigenfrequency (a) to the second eigenfrequency (b) and to the third eigenfrequency (c).

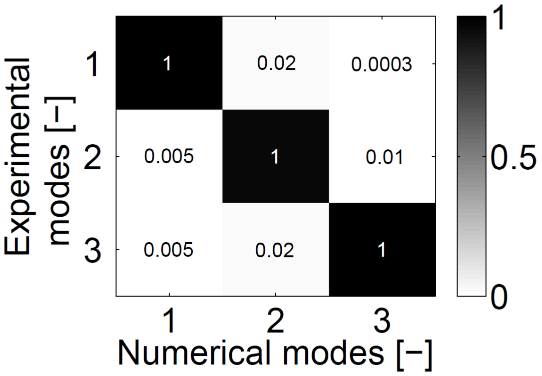

Figure 5.27: MAC matrix between the mode shapes from the geometrically mistuned finite element model and the experimental mode shapes.

5.6.2 Multi-stage academic structure

First, in order to verify that the differences between the spring stiffness of each sector is due to the clamping of the structure and not to a systematic error due to the shaker, the same ”spring stiffness mistuning” pattern than the one found for the mono-stage structure is applied as boundary conditions on the multi-stage structure. All the orientations of the ”spring stiffness mistuning” clamping conditions are tested. The retained orientation for the clamping of the numerical model is the one giving the best MAC between experimental and numerical modes shapes. Figure 5.28 compares the first experimental mode shape and the first numerical one (only the first mode shapes, corresponding to low frequencies, are affected by the boundary conditions). Since only the bottom stage responds, only the displacement of this stage is plotted in Figure 5.28. Figure 5.29 shows the MAC matrix between the experimental and numerical mode shapes. Differences are observed between both sets of mode shapes, which confirms that differences comes from mistuning in the bounded connections and not from a systematic error induced by the electrodynamic shaker.

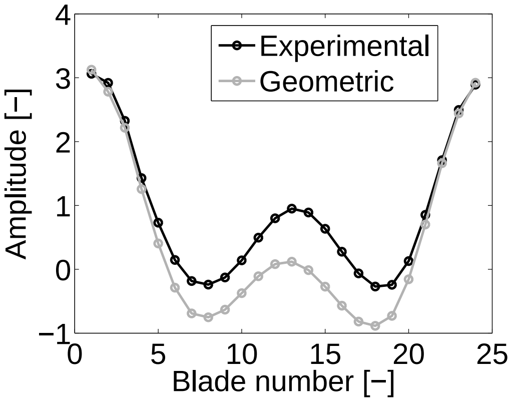

Figure 5.28: Comparison between the first experimental mode and the first numerical mode with the same clamping condition than the one found for the mono-stage structure.

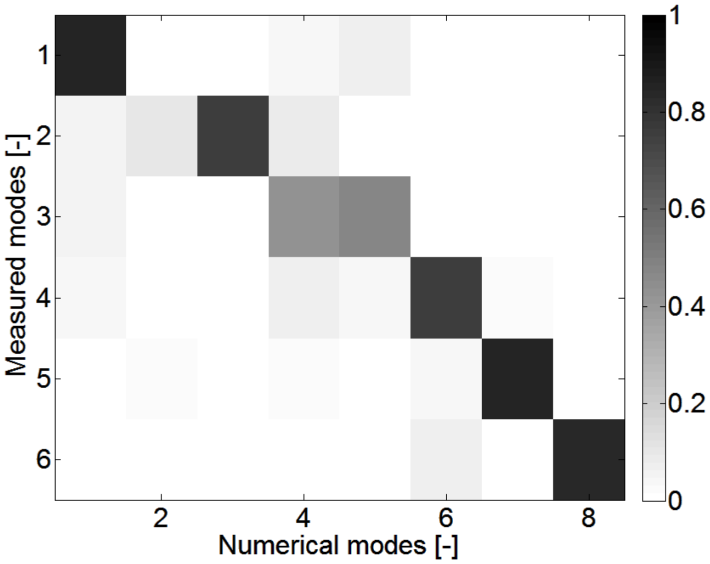

Figure 5.29: MAC matrix between the experimental modes and the numerical modes with the same clamping condition than the one found for the mono-stage structure.

Then, the optimization process presented in Section 5.6 is applied on the multi-stage model. 26 iterations are necessary to converge, which is much more than for the mono-stage model.

Figure 5.30 illustrates the obtained distribution of the spring stiffnesses. Darker areas represent a higher stiffness of the springs, and lighter areas represent a lower stiffness. Figure 5.31 gives the absolute values of the geometric mistuning and the "clamping mistuning" for each blade. The geometry mistuning is defined as the variation in the volume of the blade compared to the mean volume. The stiffness mistuning has a lower importance regarding to the geometric mistuning for the multi-stage than for the mono-stage structure (Figure 5.25).

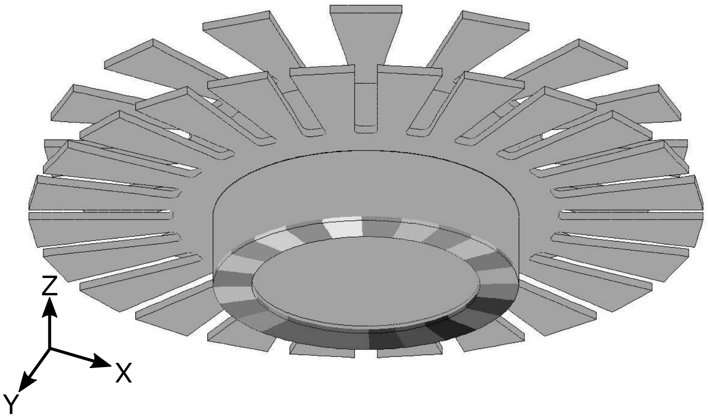

Figure 5.30: Non-uniform clamping conditions for the multi-stage structure.

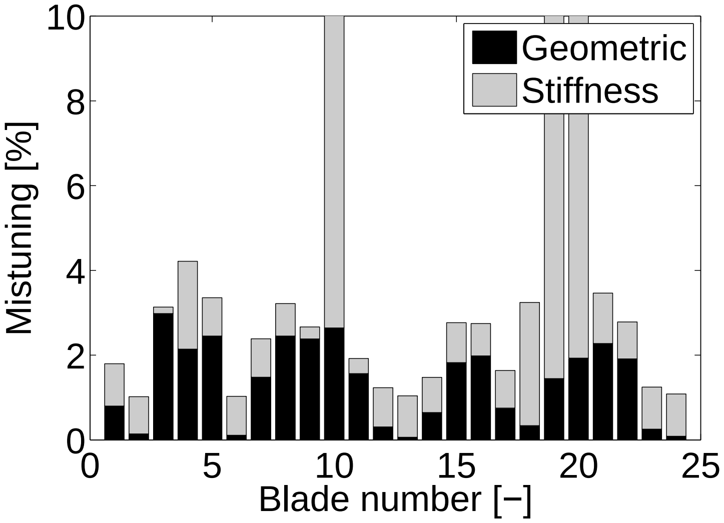

Figure 5.31: Geometric and stiffness mistuning.

The new comparison between the first experimental and numerical mode shapes is given in Figure 5.32. The displacement of the bottom stage only is shown. A good correspondence is obtained between numerical and experimental mode shapes, but some differences remain. The associated MAC matrix between the experimental and numerical modes is shown in Figure 5.33. The modification of the clamping conditions has improved the correspondence between the finite element model and the used experimental measurements for the first mode shapes, more particularly for the first eigenfrequencies. The numerical mode shapes corresponding to higher frequencies are not affected by the modification of the boundary conditions. It can be seen that the third and fifth numerical modes were not present in the experimental set of modes. This is due to the low mistuning level for these modes which practically not separate the double identical eigenfrequencies.

The obtained results enable to conclude that both geometry variations and clamping non-uniformities have to be taken into account in the finite element model to get a good correspondence of the first modes, and that both mistuning sources are of the same order of magnitude. Larger mistuning values have been obtained for the multi-stage structure than for the mono-stage one, which can be explained by the manufacturing complexity for the multi-stage bladed structure, but the stiffness mistuning due to clamping non-uniformities were lower.

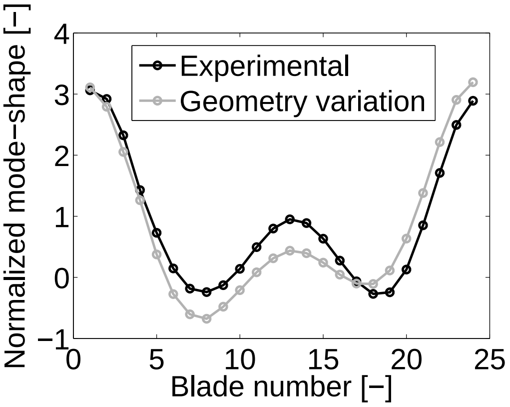

Figure 5.32: Comparison of the experimental and numerical mode shapes.

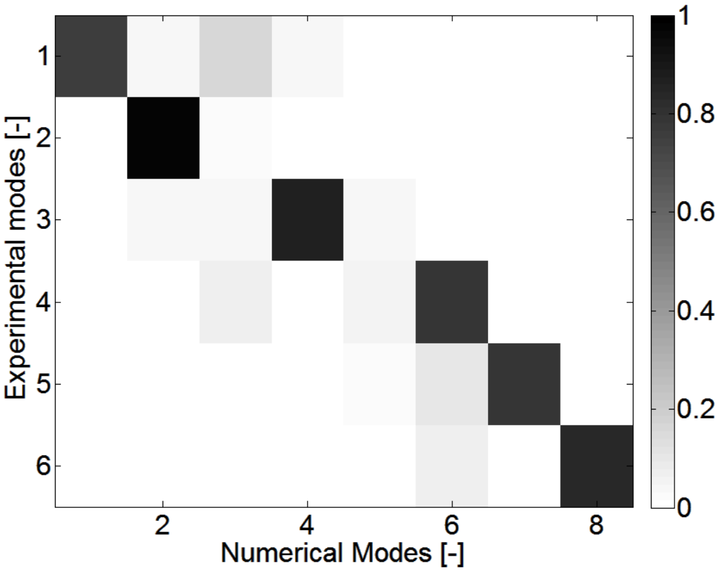

Figure 5.33: MAC matrix between the mode shapes from the geometrically mistuned multi-stage finite element model and the experimental mode shapes.

5.7 Conclusion

The main source of mistuning for both academic structures is the geometric variations of each sector due to the manufacturing tolerances. Indeed, since the bladed disks are one-piece structures, there are no welded connections between the blades and the drum and the material properties can be assumed to be uniform. An optical geometry measurement system was used to retrieve the exact profile of each blade for each structure. This enables to determine the mistuning of each blade due to variations in the geometry. Differences have been observed between the mistuning identified in Chapters 3 and 4 using vibration tests and the geometric mistuning. These differences may be attributed to non-uniformities in the clamping conditions.

Both sources of mistuning have been quantified. It was found that both geometric mistuning and clamping non-uniformities are of the same order of magnitude (1.2 and 7 % respectively for the mono-stage structure and 2.6 and 10 % for the multi-stage structure). Depending of the structure, the relative importance between the different sources of mistuning can change.

The indirect mistuning induced by clamping conditions can be reduced by modifying the test set-up to tend to the perfect clamping conditions, for example by adding a steel plate at the center of the structure. It would allow reducing the effect of the clamping conditions, but would not be representative of actual boundary conditions. In practice, connections between the blades and the disk/drum, wear during use, material non-uniformities are additional sources of indirect mistuning.

Since numerous factors induce mistuning in the structure, the experimentally identified mistuning can differ from the actual mistuning of the structure in real conditions. Consequently, this work evidences the importance of characterizing the level of mistuning induced during the manufacturing and assembly processes and the interest of using probabilistic approaches since the knowledge of the exact mistuning is illusory. Probabilistic approaches enable to evaluate the sensitivity of the amplification of the forced response with respect to small changes in the considered mistuning.

Chapter 6

Parametric and nonparametric modeling of mistuned multi-stage bladed structures

In this Chapter, probabilistic approaches are studied to evaluate the mean amplification of the forced response in mistuned structures. The nonparametric approach for uncertainties modeling is extended to handle the case of multi-stage structures. Both mono-stage and multi-stage predictions for the amplification of the forced response are compared. Then, the differences between the predicted amplification factors of the CMM parametric approach and of the nonparametric approach are compared. Finally, a combination of the two methods is proposed, incorporating the advantages of both methods to model the mistuned forced response with reduced computational time.

6.1 Introduction

Concerning blade mistuning modeling, a complete probabilistic parametric description of the uncertain parameters (boundary conditions, geometry...) is not feasible because of the large number of parameters to take into account in the model. In linear structural dynamics, random uncertainties are usually modelled using parametric models. In these parametric approaches, the uncertain parameters in the global mass, damping and stiffness matrices of the system have to be identified, and an appropriate probabilistic model has to be associated to the uncertain parameters. In the previous Chapters, a widespread parametric approach has been used to model mistuning (the CMM method, presented in Section 3.2), which considers only the Young's modulus of each blade as uncertain variable with a Gaussian distribution.

Soize [86, 141–144] developed a nonparametric probability approach for constructing a random uncertainties model of the generalized mass, damping and stiffness matrices, which does not need the identification of uncertain local parameters and consequently no mapping of the domain of the uncertain local parameters. This nonparametric model of random uncertainties uses the entropy maximization principle with the available information to construct the probabilistic model. This formulation takes into account both data and model uncertainties whereas the parametric approach considers only parametric uncertainties. Capiez and Soize [87] have adapted the proposed nonparametric probability approach in the case of cyclic symmetric structures.

In this Chapter, the nonparametric approach of Capiez and Soize [87] is extended to the case of multi-stage structures. Then, the prediction in terms of amplification of the forced response as a function of the mistuning level is compared for the parametric and nonparametric approaches. The mean value and the dispersion of the predicted amplification factor for a large number of samples are compared for each approach.

A new combination of the two modeling techniques of mistuned bladed disks is also proposed in this Chapter, incorporating the advantages of both methods to model more precisely the mistuned response of bladed disks with reduced computational time. The reduced-order modeling technique based on cyclic symmetry is combined with the nonparametric approach for modeling uncertainties in order to introduce the uncertainties directly in the modal space of the blades of the structure in order to reduce the computational time.

Finally, the influence of the number of harmonics retained for the construction of the ROMs on the predicted amplification factor is analyzed. Since the tuned mode shapes used to construct the ROMs are computed for the reference sector for each number of nodal diameters, a reduction of the number of considered harmonics decreases the computational time.

6.2 Nonparametric modeling of mistuned multi-stage structure

The extension of the nonparametric modeling method for multi-stage structure and for forced response computation is developed in this Section.

6.2.1 Mean (tuned) reduced model

The nonparametric probability method is constructed on the basis of a mean reduced model i.e., the tuned model of the studied structure. The construction of the mono-stage mean model is first presented, according to the formulation of Capiez [87]. The mode matrix is also constructed to retrieve the physical displacements from the generalized coordinates. Then, the mean model is extended for multi-stage structures.

Mono-stage structure

The system is split into the contribution of the disk and the contribution of the N blades. Since the mistuning is assumed to be statistically independent from blade to blade, the nonparametric probability models of random uncertainties for each blade are independent.

Consider Σ_n the coupling interface between the blade n ($n \in [0, N-1]$) and the disk, as illustrated in Figure 6.1. It is assumed that the blades are only coupled by the disk.

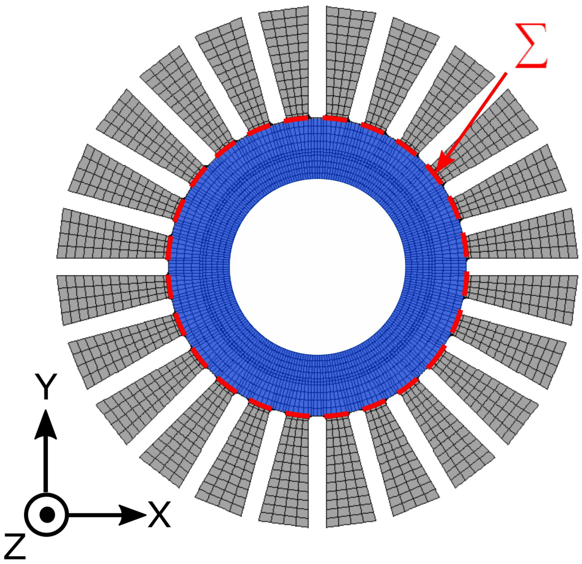

Figure 6.1: Division of the mono-stage structure in blades, disk and blade/disk interfaces.

For the disk, the block decomposition with respect to the internal (subscript i) and with respect to the coupling interface degrees of freedom (the coupling interface Σ_n of all blades are grouped using the subscript Σ) yields

$$\mathbf{A}^d = \begin{bmatrix} \mathbf{A}^d_{ii} & \mathbf{A}^d_{i\Sigma} \\ \mathbf{A}^d_{\Sigma i} & \mathbf{A}^d_{\Sigma\Sigma} \end{bmatrix} , \tag{6.1}$$

where $\mathbf{A}$ can refer to the mass, damping or stiffness matrices ($\mathbf{M}$, $\mathbf{C}$ or $\mathbf{K}$ respectively).

In order to reduce the size of the matrices, the Craig-Bampton decomposition method [64] is used. The internal degrees of freedom of the disk are condensed (the subscript i denotes the eventual remaining non-condensed nodes and the subscript Σ refers to the blade/disk interface nodes) and a given number of fixed coupling interface modes is retained (subscript I). The reduced matrices can be expressed as

$$\mathbf{A}^d_{red} = \begin{bmatrix} \mathbf{A}^d_{ii} & \mathbf{A}^d_{i\Sigma} & \mathbf{A}^d_{iI} \\ \mathbf{A}^d_{\Sigma i} & \mathbf{A}^d_{\Sigma\Sigma} & \mathbf{A}^d_{\Sigma I} \\ \mathbf{A}^d_{Ii} & \mathbf{A}^d_{I\Sigma} & \mu^d {\omega^d_I}^2 \end{bmatrix} . \tag{6.2}$$

Then, each blade n is also reduced using the Craig-Bampton decomposition method in the same way, with a given number of fixed coupling interface modes. Its block decomposition with respect to the generalized coordinates and the coupling interface degrees of freedom can be written as

$$\mathbf{A}^n_{red} = \begin{bmatrix} \mathbf{A}^n_{ii} & \mathbf{A}^n_{i\Sigma} & \mathbf{A}^n_{iI} \\ \mathbf{A}^n_{\Sigma i} & \mathbf{A}^n_{\Sigma\Sigma} & \mathbf{A}^n_{\Sigma I} \\ \mathbf{A}^n_{Ii} & \mathbf{A}^n_{I\Sigma} & \mu^n {\omega^n_I}^2 \end{bmatrix} . \tag{6.3}$$

The reduced matrix of each blade n can be determined from the reference blade (blade 1) by a rotation around the disk axis:

$$\mathbf{A}^n_{red} = \mathbf{O}^{nT}\mathbf{A}^1_{red}\,\mathbf{O}^n \;, \qquad n = 2, ..., N \;, \tag{6.4}$$

where $\mathbf{O}^n$ is a square matrix given by

$$\mathbf{O}^n = \begin{bmatrix} \ddots & & \\ & \mathbf{R}^{nT} & \mathbf{0} \\ & & \ddots \\ & \mathbf{0} & \mathbf{I} \end{bmatrix} , \tag{6.5}$$

in which $\mathbf{R}^n$ is the rotation matrix for an angle of $\frac{2\pi(n-1)}{N}$.

Then, the mode matrix of each blade n can be computed by rotation of the mode matrix of blade 1, such as

$$\mathbf{\Psi}^n = \mathbf{L}^n\;\mathbf{\Phi}^1\;\mathbf{O}^n \;, \tag{6.6}$$

with

$$\mathbf{L}^n = \begin{bmatrix} \ddots & & \mathbf{0} \\ & \mathbf{R}^n & \\ \mathbf{0} & & \ddots \end{bmatrix} . \tag{6.7}$$

The mean reduced matrix model of the bladed disk is then obtained by assembling the contribution of the disk and the blades (the superscript b groups all the blades of the structure):

$$\begin{bmatrix} \mathbf{A}^d_{ii} & \mathbf{0} & \mathbf{A}^d_{i\Sigma} & \mathbf{A}^d_{iI} & \mathbf{0} \\ \mathbf{0} & \mathbf{A}^b_{ii} & \mathbf{A}^b_{i\Sigma} & \mathbf{0} & \mathbf{A}^b_{iI} \\ \mathbf{A}^d_{\Sigma i} & \mathbf{A}^b_{\Sigma i} & (\mathbf{A}^d_{\Sigma\Sigma} + \mathbf{A}^b_{\Sigma\Sigma}) & \mathbf{A}^d_{\Sigma I} & \mathbf{A}^b_{\Sigma I} \\ \mathbf{A}^d_{Ii} & \mathbf{0} & \mathbf{A}^d_{I\Sigma} & \mu^d {\omega^d_I}^2 & \mathbf{0} \\ \mathbf{0} & \mathbf{A}^b_{Ii} & \mathbf{A}^b_{I\Sigma} & \mathbf{0} & \mu^b {\omega^b_I}^2 \end{bmatrix} , \tag{6.8}$$

and the assembled mode matrix is given by

$$\mathbf{\Psi} = \begin{bmatrix} \mathbf{I} & \mathbf{0} & \mathbf{0} & \mathbf{0} & \mathbf{0} \\ \mathbf{0} & \mathbf{I} & \mathbf{0} & \mathbf{0} & \mathbf{0} \\ \mathbf{0} & \mathbf{0} & \mathbf{I} & \mathbf{0} & \mathbf{0} \\ \mathbf{\Psi}^d_i & \mathbf{0} & \mathbf{\Psi}^d_\Sigma & \mathbf{\Psi}^d_I & \mathbf{0} \\ \mathbf{0} & \mathbf{\Psi}^b_i & \mathbf{\Psi}^b_\Sigma & \mathbf{0} & \mathbf{\Psi}^b_I \end{bmatrix} . \tag{6.9}$$

Multi-stage structure

In the case of multi-stage structures, the mean reduced matrix model is constructed in the same way. The system is split into the contribution of the disk and the contribution of the N_s blades of each stage s. The nonparametric probability models of random uncertainties for each blade are independent.

Consider Σ_{ns} the coupling interface between the blade n ($n \in [1, N_s]$) of stage s ($s \in [1, S]$) and the disk, as illustrated in Figure 6.2. All blades are only coupled by the disk.

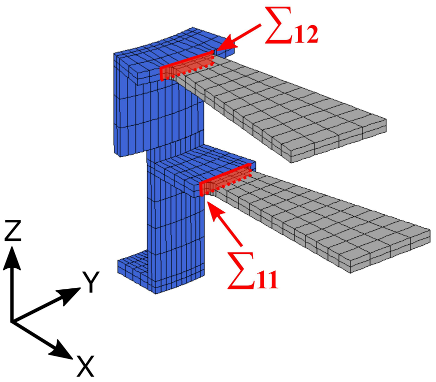

Figure 6.2: Division of the multi-stage structure in blades, disk and blade/disk interfaces for the reference sector of each stage.

For the disk, the block decomposition with respect to the internal degrees of freedom (subscript i denotes the possible remaining non-condensed nodes) and with respect to the coupling interface degrees of freedom (subscript Σ_s, with $s = 1, ..., N_s$) yields ($\mathbf{A}$ can refer to $\mathbf{M}$, $\mathbf{C}$ or $\mathbf{K}$)

$$\mathbf{A}^d = \left[\begin{array}{c|ccc} \mathbf{A}^d_{ii} & \mathbf{A}^d_{i\Sigma_1} & \cdots & \mathbf{A}^d_{i\Sigma_S} \\ \hline \mathbf{A}^d_{\Sigma_1 i} & \mathbf{A}^d_{\Sigma_1\Sigma_1} & & \mathbf{0} \\ \vdots & & \ddots & \\ \mathbf{A}^d_{\Sigma_S i} & \mathbf{0} & & \mathbf{A}^d_{\Sigma_S\Sigma_S} \end{array}\right] . \tag{6.10}$$

The model is reduced using the Craig-Bampton decomposition method [64] in order to reduce the size of the matrices. The internal degrees of freedom of the disk are condensed and a given number of fixed coupling interface modes are retained. The reduced matrices can be expressed as

$$\mathbf{A}^d_{red} = \left[\begin{array}{c|ccc|c} \mathbf{A}^d_{ii} & \mathbf{A}^d_{i\Sigma_1} & \cdots & \mathbf{A}^d_{i\Sigma_S} & \mathbf{A}^d_{iI} \\ \hline \mathbf{A}^d_{\Sigma_1 i} & \mathbf{A}^d_{\Sigma_1\Sigma_1} & & \mathbf{0} & \mathbf{A}^d_{\Sigma_1 I} \\ \vdots & & \ddots & & \vdots \\ \mathbf{A}^d_{\Sigma_S i} & \mathbf{0} & & \mathbf{A}^d_{\Sigma_S\Sigma_S} & \mathbf{A}^d_{\Sigma_S I} \\ \hline \mathbf{A}^d_{Ii} & \mathbf{A}^d_{I\Sigma_1} & \cdots & \mathbf{A}^d_{I\Sigma_S} & \mu^d \omega_I^{d2} \end{array}\right] . \tag{6.11}$$

Then, each blade n of each stage s is also reduced using the Craig-Bampton decomposition method with a given number of fixed coupling interface modes. Its block decomposition with respect to the generalized coordinates and the coupling interface degrees of freedom writes:

$$\mathbf{A}_{red}^{ns} = \left[\begin{array}{c|c|c} \mathbf{A}_{ii}^{ns} & \mathbf{A}_{i\Sigma}^{ns} & \mathbf{A}_{iI}^{ns} \\ \hline \mathbf{A}_{\Sigma_s i}^{ns} & \mathbf{A}_{\Sigma_s\Sigma_s}^{ns} & \mathbf{A}_{\Sigma_s i}^{ns} \\ \hline \mathbf{A}_{Ii}^{ns} & \mathbf{A}_{I\Sigma_s}^{ns} & \mu^{ns}\omega_I^{ns2} \end{array}\right] . \tag{6.12}$$

The reduced matrix of each blade n can be determined from the reference blade (blade 1) by a rotation around the disk axis:

$$\mathbf{A}_{red}^{ns} = \mathbf{O}^{nsT}\mathbf{A}_{red}^{1s}\,\mathbf{O}^{ns} \ , \qquad n = 2, ..., N_s \ , \tag{6.13}$$

where $\mathbf{O}^{ns}$ is a square matrix given by

$$\mathbf{O}^{ns} = \begin{bmatrix} \ddots & & \\ & \mathbf{R}^{nsT} & \mathbf{0} \\ & & \ddots \\ & \mathbf{0} & \mathbf{I} \end{bmatrix} , \tag{6.14}$$

in which $\mathbf{R}^{ns}$ is the rotation matrix for an angle of $\frac{2\pi(n-1)}{N_s}$.

Then, the mode matrix of each blade n of each stage s can be computed by rotation of the mode matrix of blade 1 of each stage s, such as

$$\mathbf{\Psi}^{ns} = \mathbf{L}^{ns}\ \mathbf{\Phi}^{1s}\ \mathbf{O}^{ns} \ , \tag{6.15}$$

with

$$\mathbf{L}^{ns} = \begin{bmatrix} \ddots & & \mathbf{0} \\ & \mathbf{R}^{ns} & \\ \mathbf{0} & & \ddots \end{bmatrix} . \tag{6.16}$$

The mean reduced matrix model of the bladed disk is then obtained by assembling the contribution of the disk and the blades of each stage (the superscript b_s groups all the blades of stage s):

$$\left[\begin{array}{c|ccc|ccc|c|ccc}
\mathbf{A}^{d}_{ii} & \mathbf{0} & \cdots & \mathbf{0} & \mathbf{A}^{d}_{i\Sigma_1} & \cdots & \mathbf{A}^{d}_{i\Sigma_S} & \mathbf{A}^{d}_{iI} & \mathbf{0} & \cdots & \mathbf{0} \\
\hline
\mathbf{0} & \mathbf{A}^{b_1}_{ii} & & \mathbf{0} & \mathbf{A}^{b_1}_{i\Sigma_1} & & \mathbf{0} & \mathbf{0} & \mathbf{A}^{b_1}_{iI} & & \mathbf{0} \\
\vdots & & \ddots & & & \ddots & & \vdots & & \ddots & \\
\mathbf{0} & \mathbf{0} & & \mathbf{A}^{b_2}_{ii} & \mathbf{0} & & \mathbf{A}^{b_S}_{i\Sigma_S} & \mathbf{0} & \mathbf{0} & & \mathbf{A}^{b_2}_{iI} \\
\hline
\mathbf{A}^{d}_{\Sigma_1 i} & \mathbf{A}^{b_1}_{\Sigma_1 i} & & \mathbf{0} & \begin{matrix}(\mathbf{A}^{d}_{\Sigma_1\Sigma_1}+\\ \mathbf{A}^{b_1}_{\Sigma_1\Sigma_1})\end{matrix} & & \mathbf{0} & \mathbf{A}^{d}_{\Sigma_1 I} & \mathbf{A}^{b_1}_{\Sigma_1 I} & & \mathbf{0} \\
\vdots & & \ddots & & & \ddots & & \vdots & & \ddots & \\
\mathbf{A}^{d}_{\Sigma_S i} & \mathbf{0} & & \mathbf{A}^{b_S}_{\Sigma_S i} & \mathbf{0} & & \begin{matrix}(\mathbf{A}^{d}_{\Sigma_S\Sigma_S}+\\ \mathbf{A}^{b_S}_{\Sigma_S\Sigma_S})\end{matrix} & \mathbf{A}^{d}_{\Sigma_S I} & \mathbf{0} & & \mathbf{A}^{b_S}_{\Sigma_S I} \\
\hline
\mathbf{A}^{d}_{Ii} & \mathbf{0} & \cdots & \mathbf{0} & \mathbf{A}^{d}_{I\Sigma_1} & \cdots & \mathbf{A}^{d}_{I\Sigma_S} & \mu^{d}\omega_I^{d2} & \mathbf{0} & \cdots & \mathbf{0} \\
\hline
\mathbf{0} & \mathbf{A}^{b_1}_{Ii} & & \mathbf{0} & \mathbf{A}^{b_1}_{I\Sigma_1} & & \mathbf{0} & \mathbf{0} & \mu^{b_1}{\omega_I^{b_1}}^2 & & \mathbf{0} \\
\vdots & & \ddots & & & \ddots & & \vdots & & \ddots & \\
\mathbf{0} & \mathbf{0} & & \mathbf{A}^{b_S}_{Ii} & \mathbf{0} & & \mathbf{A}^{b_S}_{I\Sigma_S} & \mathbf{0} & \mathbf{0} & & \mu^{b_S}{\omega_I^{b_S}}^2
\end{array}\right], \tag{6.17}$$

and the assembled mode matrix is given by

$$\mathbf{\Psi} = \left[\begin{array}{c|ccc|ccc|c|ccc}
\mathbf{I} & \mathbf{0} & \cdots & \mathbf{0} & \mathbf{0} & \cdots & \mathbf{0} & \mathbf{0} & \mathbf{0} & \cdots & \mathbf{0} \\
\hline
\mathbf{0} & \mathbf{I} & & \mathbf{0} & \mathbf{0} & \cdots & \mathbf{0} & \mathbf{0} & \mathbf{0} & \cdots & \mathbf{0} \\
\vdots & & \ddots & & & \ddots & & \vdots & & \ddots & \\
\mathbf{0} & \mathbf{0} & & \mathbf{I} & \mathbf{0} & \cdots & \mathbf{0} & \mathbf{0} & \mathbf{0} & \cdots & \mathbf{0} \\
\hline
\mathbf{0} & \mathbf{0} & \cdots & \mathbf{0} & \mathbf{I} & & \mathbf{0} & \mathbf{0} & \mathbf{0} & \cdots & \mathbf{0} \\
\vdots & & \ddots & & & \ddots & & \vdots & & \ddots & \\
\mathbf{0} & \mathbf{0} & \cdots & \mathbf{0} & \mathbf{0} & & \mathbf{I} & \mathbf{0} & \mathbf{0} & \cdots & \mathbf{0} \\
\hline
\mathbf{\Psi}^{d}_{i} & \mathbf{0} & \cdots & \mathbf{0} & \mathbf{\Psi}^{d}_{\Sigma_1} & \cdots & \mathbf{\Psi}^{d}_{\Sigma_S} & \mathbf{\Psi}^{d}_{I} & \mathbf{0} & \cdots & \mathbf{0} \\
\hline
\mathbf{0} & \mathbf{\Psi}^{b_1}_{i} & & \mathbf{0} & \mathbf{\Psi}^{b_1}_{\Sigma_1} & & \mathbf{0} & \mathbf{0} & \mathbf{\Psi}^{b_1}_{I} & & \mathbf{0} \\
\vdots & & \ddots & & & \ddots & & \vdots & & \ddots & \\
\mathbf{0} & \mathbf{0} & & \mathbf{\Psi}^{b_S}_{i} & & \mathbf{0} & \mathbf{\Psi}^{b_S}_{\Sigma_S} & \mathbf{0} & \mathbf{0} & & \mathbf{\Psi}^{b_S}_{I}
\end{array}\right] . \tag{6.18}$$

6.2.2 Nonparametric model of random uncertainties for blade mistuning

The nonparametric probabilistic approach consists in modeling the reduced structural matrix for blade n of stage s as the random matrix $\mathbf{A}^{ns\,\prime}_{red}$ ($\mathbf{A}$ can refer to $\mathbf{M}$, $\mathbf{C}$ and $\mathbf{K}$). Since the random uncertainties are supposed statistically independent from blade to blade, random matrices $\mathbf{A}^{1,s\,\prime}_{red}$,...,$\mathbf{A}^{N_s,s\prime}_{red}$ are independent. The random matrices are constructed using the mathematical developments of Soize and Capiez [87] i.e.,

$$\mathbf{A}^{ns\,\prime}_{red} = \mathbf{L}^{nsT}_{A}\mathbf{G}^{ns}_{A}\mathbf{L}^{ns}_{A}, \qquad \mathbf{A} = \{\mathbf{M}, \mathbf{C}, \mathbf{K}\}\,, \tag{6.19}$$

in which $\mathbf{L}_A^{ns}$ ($\mathbf{A} = \{\mathbf{M}, \mathbf{C}, \mathbf{K}\}$) are upper triangular real matrices such that

$$\mathbf{A}_{red}^{ns} = \mathbf{L}_A^{nsT}\,\mathbf{L}_A^{ns}, \qquad \mathbf{A} = \{\mathbf{M}, \mathbf{C}, \mathbf{K}\}\,, \tag{6.20}$$

and $\mathbf{G}_A^{ns}$ is the random positive-definite symmetric matrix.

The random matrix $\mathbf{G}_A^{ns}$ can be written as

$$\mathbf{G}_A^{ns} = \mathbf{L}_G^{nsT}\mathbf{L}_G^{ns}\ , \tag{6.21}$$

where $\mathbf{L}_G^{ns}$ is a real upper triangular random matrix such that:

1. The elements $\mathbf{L}_{G_{jj'}}^{ns}$ with $j \leq j'$ are independent;
2. for $j < j'$, real-valued random variable $\mathbf{L}_{G_{jj'}}^{ns}$ can be written as $\mathbf{L}_{G_{jj'}}^{ns} = \sigma_n U_{jj'}$ in which $\sigma_n = \delta\,(n+1)^{\frac{N_A}{2}}$, δ is the mistuning dispersion parameter, N_A is the size of $\mathbf{A}_{red}^{ns}$, and $U_{jj'}$ is a real-valued Gaussian random variable with zero mean and variance equal to 1.
3. For $j = j'$, positive-valued random variable $\mathbf{L}_{G_{jj}}^{ns}$ can be written as $\mathbf{L}_{G_{jj}}^{ns} = \sigma_n\sqrt{2V_j}$ where V_j is a positive-valued gamma random variable whose probability density function $p_{V_j}(v)$ with respect to dv is written as

$$p_{V_j}(v) = \mathbb{1}_{\mathbb{R}^+}\frac{1}{\Gamma\left(\frac{N_A+1}{2\delta^2} + \frac{1-j}{2}\right)}v^{\frac{N_A+1}{2\delta^2} - \frac{1+j}{2}}e^{-v}\ . \tag{6.22}$$

6.2.3 Forced response computation

In order to apply an excitation on the structure and to compute the forced response, the force vector $\mathbf{f}$ is projected in the basis of the reduced matrix as

$$\mathbf{\Psi}^T\mathbf{f}\ . \tag{6.23}$$

Then, the physical displacement $\mathbf{x}$ of the structure can be retrieved from the generalised coordinates by the inverse projection.

6.3 Application on a two-stage academic structure

The theoretical developments are applied on a two-stage academic blisk. To compare the results between the mono-stage and multi-stage analyses, the bottom stage (stage 1) and top stage (stage 2) are also considered independently. The material and geometrical properties are given for each stage in Table 6.1.

The three structures are clamped at their basis, as can be seen in Figure 6.3. One excitation point per blade is considered, as illustrated in Figure 6.4.

	Stage 1	Stage 2
Number of sectors (N) [-]	24	15
Young's modulus [MPa]	71 000	71 000
Density [kg/m^3]	2700	2700
External diameter [mm]	420	400
Internal diameter [mm]	186	186
Thickness [mm]	5	5
Height [mm]	53	46
Blade length [mm]	86	86
Blade width [mm]	40	45

Table 6.1: Material and geometric properties of the multi-stage academic structure.

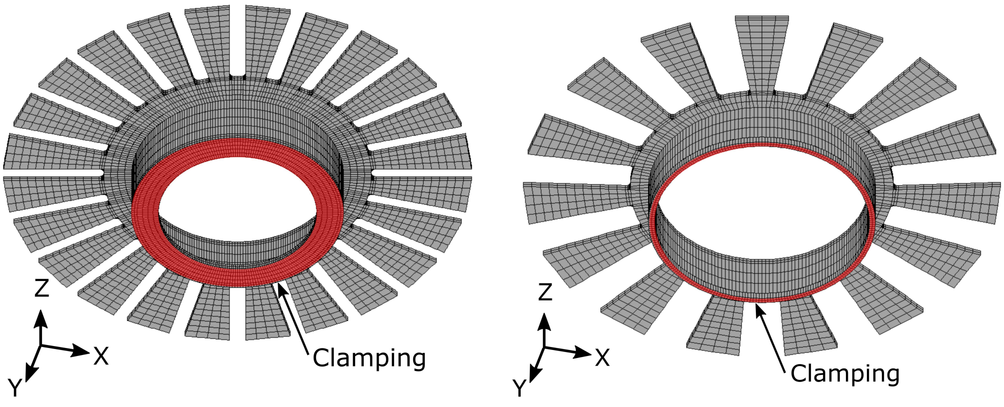

(a) Mono-stage - Stage 1 (b) Mono-stage - Stage 2

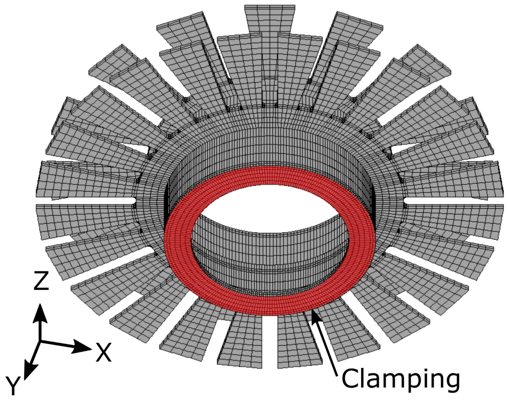

(c) Multi-stage

Figure 6.3: Finite element model of stage 1 (a), of stage 2 (b), and of the multi-stage structure (c) with their clamping degrees of freedom.

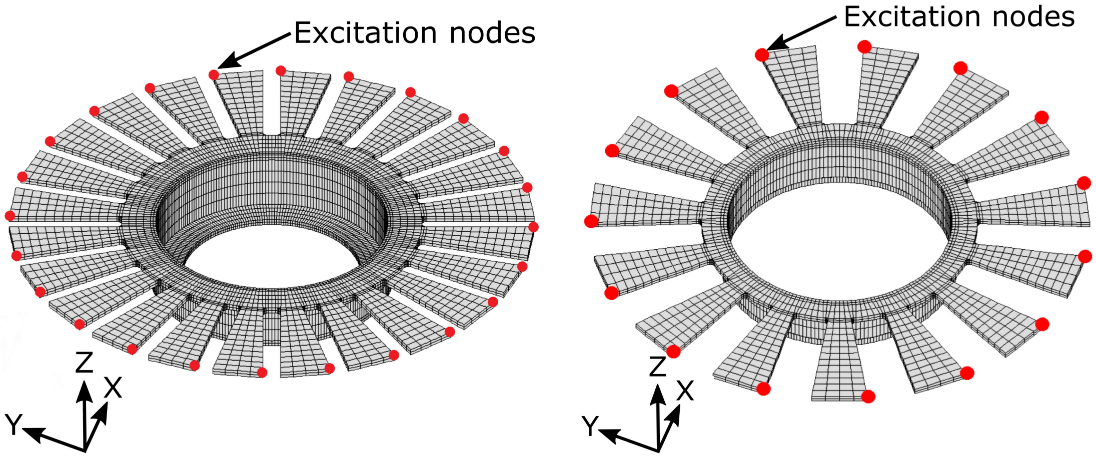

(a) Mono-stage - Stage 1 (b) Mono-stage - Stage 2

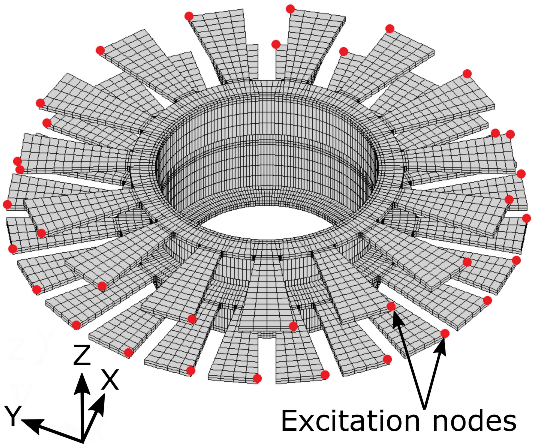

(c) Multi-stage

Figure 6.4: Excitation nodes for the finite element model of stage 1 (a), of stage 2 (b), and of the multi-stage structure (c).

The frequency range considered here is $[100 - 800]$ Hz, such that the $1B$ modes are excited, and the chosen engine order of excitation is 5. Figure 6.5 shows the mean amplification factor obtained for different mistuning percentages, for the bottom and top stages of the multi-stage structure, and for the two mono-stage structures. 500 samples are considered for each case. An increase of the amplification factor is observed in the multi-stage analysis comparing to the mono-stage cases, especially for the top stage. The corresponding relative errors are shown in Figure 6.6. The errors first increase with the mistuning dispersion parameter and then stabilize. Errors up to 11 % are obtained for stage 1, and up to 33 % are found for stage 2. The errors are higher for stage 2, which means that these stage is more affected by the change of boundary conditions.

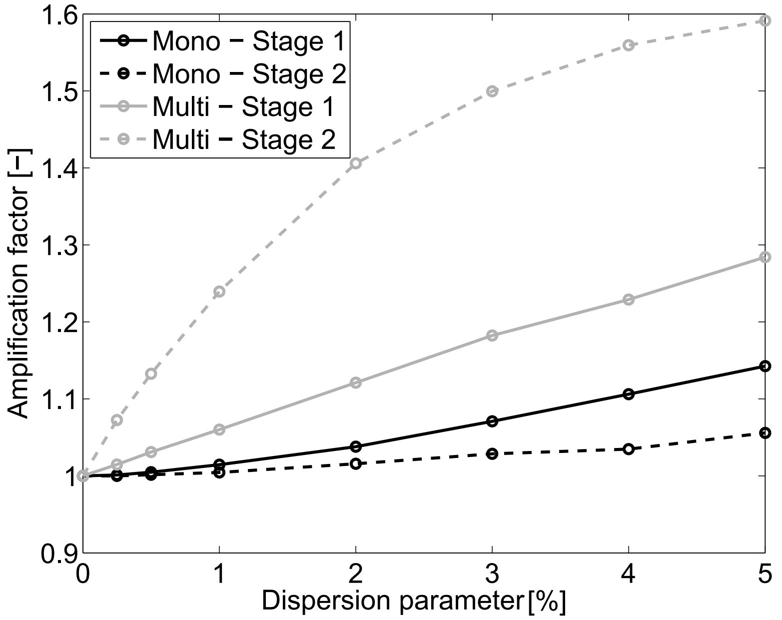

Figure 6.5: Amplification factor.

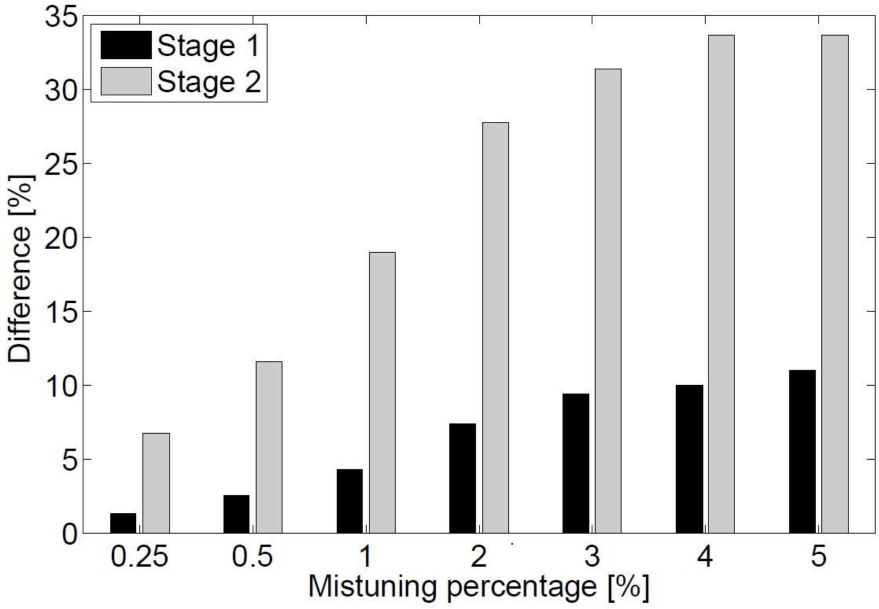

Figure 6.6: Error between the mono-stage and multi-stage amplification factor.

Figure 6.7 shows the probability density function (PDF) of the amplification factor for all considered cases. The mean amplification factor increases with mistuning percentages, as well as the standard deviation. For the second stage of the multi-stage model (Figure 6.7(d)), larger amplification factors and dispersions are observed.

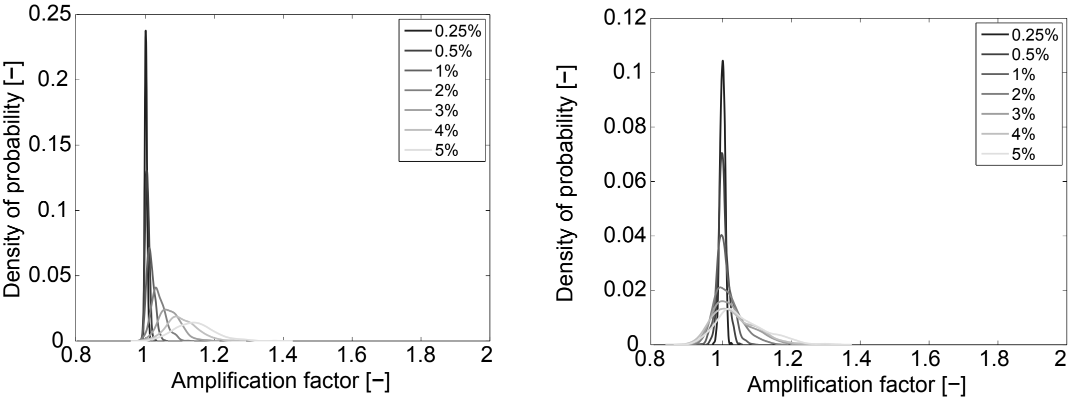

(a) Mono-stage - Stage 1

(b) Mono-stage - Stage 2

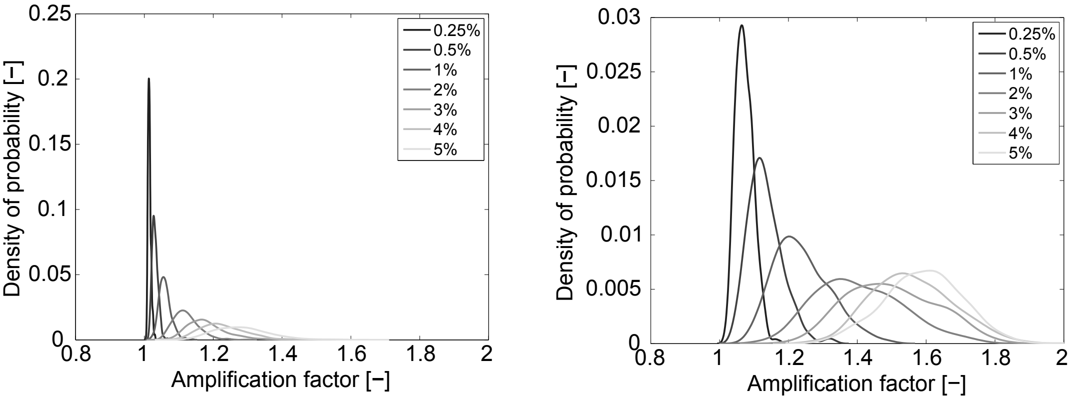

(c) Multi-stage - Stage 1

(d) Multi-stage - Stage 2

Figure 6.7: Density of probability functions of the amplification factor.

6.4 Proposed approach

The approach proposed here is a combination of the two modeling techniques. The CMM reduced-order modeling technique based on cyclic symmetry formulation (method used in Chapters 3, 4 and 7) is combined with the nonparametric approach for modeling uncertainties in order to introduce them in the modal space of the blades in order to reduce the computational time. The approach allows to incorporate:

1. The advantages of reduced-order modeling techniques based on modal synthesis i.e., reduced computational costs.
2. The nonparametric approach, which allows considering the coupling between blade modes neglected in the parametric approach.

The principle of the proposed approach is to separate the global structural matrices defined in the modal space (for example the reduced stiffness matrix $\mathbf{K}_r$, since in the majority of the reduced order model, the stiffness matrix only is perturbed) into two contributions, thanks to a Craig-Bampton modal synthesis [64] method for the blades:

$$\mathbf{K}_r = \mathbf{K}_r^0 + \sum_{s=1}^{S}\sum_{n=1}^{N_s} {\mathbf{Q}_{ns}}^T \boldsymbol{\Lambda}_{ns}\mathbf{Q}_{ns} \ . \tag{6.24}$$

The first term $\mathbf{K}_r^0$ in Equation (6.24) takes into account the contribution of the disk and the static modes of the blades. The second term represents the contribution of the internal vibration modes of the blades (the matrix $\mathbf{\Lambda}_{ns}$ contains the modal stiffnesses of the retained internal vibration modes of each blade), which are projected in the modal space of the whole system by means of the projection matrix $\mathbf{Q}_{ns}$ ($\mathbf{Q}_{ns}$ is the modal participation factors of blade n of stage s, as seen in Chapter 4).

The mistuned model is then simply written as

$$\mathbf{K}_r' = \mathbf{K}_r^0 + \sum_{s=1}^{S} \sum_{n=1}^{N_s} {\mathbf{Q}_{ns}}^T \mathbf{\Lambda}_{ns}' \mathbf{Q}_{ns} \ , \tag{6.25}$$

in which $\mathbf{\Lambda}_{ns}'$ is a random matrix based on the mean matrix $\mathbf{\Lambda}_{ns}$ of eigenvalues. The uncertainties are thus introduced in the modal space of the blades using the probability model for symmetric positive definite real random matrices proposed by Soize [86] and applied by Capiez and al. [87] to cyclic symmetric structures.

The two approaches can be summarised as follows:

Capiez method:

1. Construction of the mean model ($\mathbf{A} \ = \ \{\mathbf{K}, \mathbf{C}, \mathbf{M}\}$):

$$\begin{bmatrix} \mathbf{A}^d_{ii} & \mathbf{0} & \mathbf{A}^d_{i\Sigma} & \mathbf{A}^d_{iI} & \mathbf{0} \\ \mathbf{0} & \mathbf{A}^b_{ii} & \mathbf{A}^b_{i\Sigma} & \mathbf{0} & \mathbf{A}^b_{iI} \\ \mathbf{A}^d_{\Sigma i} & \mathbf{A}^b_{\Sigma i} & \mathbf{A}^d_{\Sigma\Sigma} + \mathbf{A}^b_{\Sigma\Sigma} & \mathbf{A}^d_{\Sigma I} & \mathbf{A}^b_{\Sigma I} \\ \mathbf{A}^d_{Ii} & \mathbf{0} & \mathbf{A}^d_{I\Sigma} & \mu^d {\omega^d_I}^2 & \mathbf{0} \\ \mathbf{0} & \mathbf{A}^b_{Ii} & \mathbf{A}^b_{I\Sigma} & \mathbf{0} & \mu^b {\omega^b_I}^2 \end{bmatrix} \ ;$$

2. Nonparametric perturbation of the stiffness matrix;

3. Projection of the matrices in the modal space:

$$\mathbf{\Phi}^T \left(\mathbf{K}' + i\omega\mathbf{C} - \omega^2\mathbf{M}\right) \mathbf{\Phi} \ \mathbf{p} = \mathbf{F} \ ,$$

   or

$$\left(\mathbf{K}_r' + i\omega\mathbf{C}_r - \omega^2\mathbf{M}_r\right) \mathbf{p} = \mathbf{F} \ .$$

Proposed approach:

1. Construction of the reduced structural matrices;

2. Computation of the modal participation factors $\mathbf{Q}_{ns}$;

3. Nonparametric perturbation of the reduced stiffness matrix:

$$\mathbf{K}_r' = \mathbf{K}_r^0 + \sum_{s=1}^{S} \sum_{n=1}^{N_s} {\mathbf{Q}_{ns}}^T \mathbf{\Lambda}_{ns}' \mathbf{Q}_{ns} \ .$$

Concerning Capiez's nonparametric approach, the construction of the mean model (point 1) requires a 360° finite element model of the disk for the assembly of the structural matrices. The number of nodes of the whole disk rapidly increases with the number of sectors and the mesh refinement. Thus the computational resources to retrieve the disk structural matrices increases too (the size of the matrices is equal to the sum the number of retained nodes in the disk and the blades, the blades/disk interface nodes, and the number of retained internal vibration modes for the disk and the blades). After that, concerning the point 3, this projection is performed for each sample. This requires high computational time when the dimension of the structural matrices and of the $\mathbf{\Phi}$ matrix increases.

In the case of the proposed approach, the structural matrices are directly computed in the modal space, from the finite element model of one reference sector. This drastically reduces the computation time of the mean model. Moreover, the modal participation factors are computed only once, based on the tuned finite element model. The uncertainties are then introduced in the modal space of the blades (the size of the disturbed matrix is N times the number of retained cantilevered blade modes).

Therefore, considering a perturbation restricted to the blades internal vibration modes, the proposed approach enables to reduce the size of all the contributing matrices compared to Capiez's method. Figures 6.8(a) and 6.8(b) illustrate the size of the matrices respectively for the nonparametric approach and the proposed approach. The part of the matrix in dark gray shows the element in which the uncertainties are introduced. It illustrates that the size of the matrices involved in the nonparametric approach is much larger than in the proposed approach.

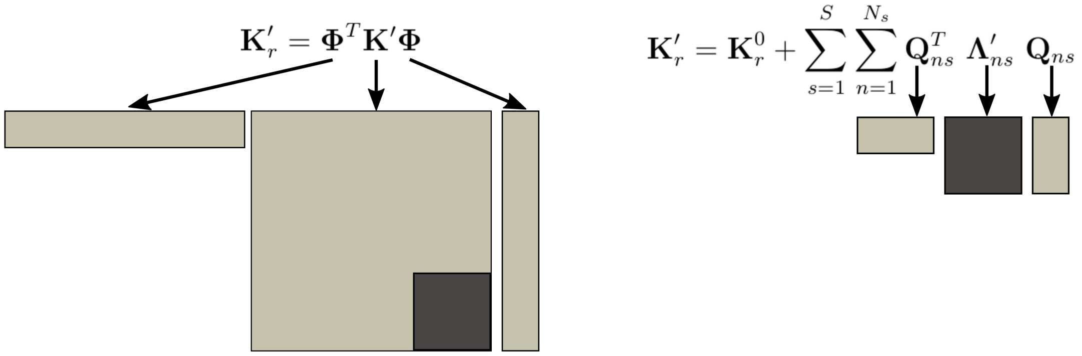

(a) Nonparametric approach

(b) Proposed approach

Figure 6.8: Comparison of the size of the involve matrices in the nonparametric approach (a) and in the proposed approach (b). The dark areas refer to the perturbed elements.

This drastic reduction of size in the involved matrices is performed using an additional assumption comparing to the classic nonparametric approach. The modal participation factors are computed only once as in the parametric approach, which adds the assumption that the mistuned mode shapes can be written as a linear combination of the tuned mode shapes. Therefore, for a structure or a frequency range with moderate coupling, the same results than the ones obtained with the nonparametric approach with highly reduced computational time. However, in the case of high coupling, the results of the proposed approach tend to the one of the parametric approach due to the additional assumption.

6.5 Comparison with the CMM parametric approach

In this Section, the CMM parametric approach used in Chapters 3 and 4 is compared with the nonparametric approach and the proposed approach in terms of the forced response amplification prediction.

For the CMM parametric approach, Capiez [104] shows that the dispersion indicator W^s_{param} is defined as

$$W^s_{param} = \mathcal{E}\{\|\mathbf{K}^{s\prime}_r - \mathbf{K}^s_r\|^2\} \ , \tag{6.26}$$

where $\mathbf{K}^s_r$ is the reduced stiffness matrix of stage s, $\mathbf{K}^{s\prime}_r$ is the perturbed reduced stiffness matrix of stage s and $\mathcal{E}$ referred to the expected value. Taking into account the symmetry property of the matrix $\mathbf{K}^s_r$, one obtains

$$W^s_{param} = \delta^s_{param} \ \mathrm{tr}\left(\mathbf{K}^{s2}_r\right) \ , \tag{6.27}$$

where δ^s_{param} is the dispersion parameter of stage s in the parametric approach and tr means the trace of the matrix.

In the same way, the dispersion indicator for the nonparametric approach $W^s_{nonparam}$ is defined as [104]

$$W^s_{nonparam} = \mathcal{E}\{\|{\mathbf{K}^s_{red}}' - \mathbf{K}^s_{red}\|^2\} \ , \tag{6.28}$$

which can be expressed as (see the mathematical developments available in [104])

$$W^s_{nonparam} = \frac{\left(\delta^s_{nonparam}\right)^2}{\sqrt{\tilde{m}^K + 1}} \left(\mathrm{tr}\left({\mathbf{K}^s_{red}}^2\right) + \mathrm{tr}\left(\mathbf{K}^s_{red}\right)^2\right) \ , \tag{6.29}$$

where $\tilde{m}^K$ is the rank of the matrix $\mathbf{K}^s_{red}$ and $\delta^s_{nonparam}$ is the dispersion parameter of stage s in the nonparametric approach.

Both probabilistic approaches can be compared equalizing the two dispersion indicators i.e.,

$$W^s_{param} = W^s_{nonparam} \ , \tag{6.30}$$

or, using Equations (6.27) and (6.29),

$$\delta_{param} = \frac{\left(\delta_{nonparam}\right)^2}{\sqrt{\tilde{m}^K + 1}} \left(1 + \frac{\mathrm{tr}\left(\mathbf{K}^s_{red}\right)^2}{\mathrm{tr}\left({\mathbf{K}^s_{red}}^2\right)}\right) \ . \tag{6.31}$$

Figure 6.9 gives the correspondence between both dispersion parameters for the academic structure, for the two stages.

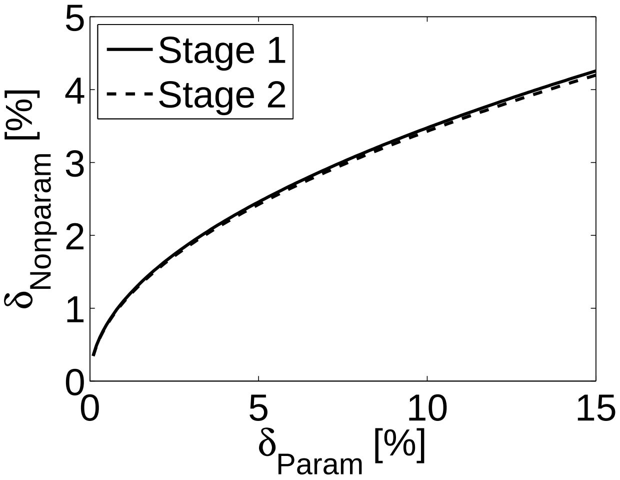

Figure 6.9: Correspondence between the dispersion parametric for the parametric and nonparametric approaches for the academic structure.

Figure 6.10 gives, for 0.5 and 5 % of mistuning (the corresponding dispersion parameters or the nonparametric approach can be found using the correspondance curve in Figure 6.9), the probability density of the amplification factor for the nonparametric approach, the proposed approach, and the parametric approach. 500 mistuning samples are considered for each case. Table 6.2 gives the obtained means and standard deviations for all cases. The three methods give globally the same mean amplification factor. It can be seen that for the parametric approach, the results are more centered on the mean value than for the nonparametric method. The distribution is also more symmetric in parametric approach. The proposed approach gives intermediate results, but closer to the nonparametric method.

	Nonparametric approach	Proposed approach	Parametric approach
0.5 %			
Mean	1.19	1.20	1.15
Standard deviation	0.062	0.062	0.073
5 %			
Mean	1.61	1.61	1.65
Standard deviation	0.11	0.13	0.14

Table 6.2: Comparison between the parametric and nonparametric results.

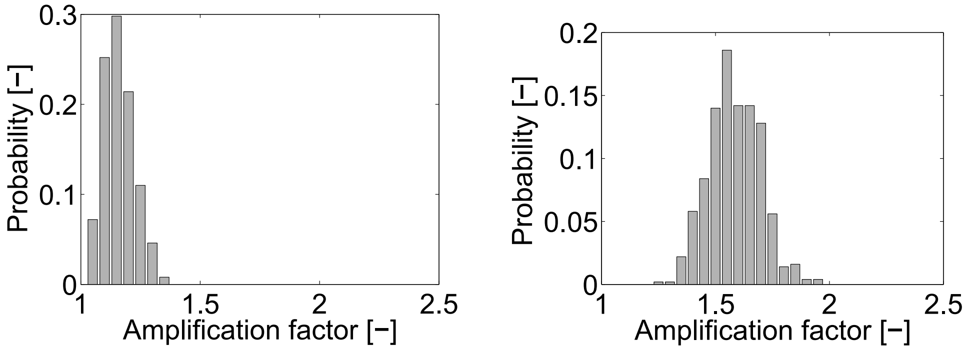

(a) 0.5 %

(b) 5 %

Nonparametric approach

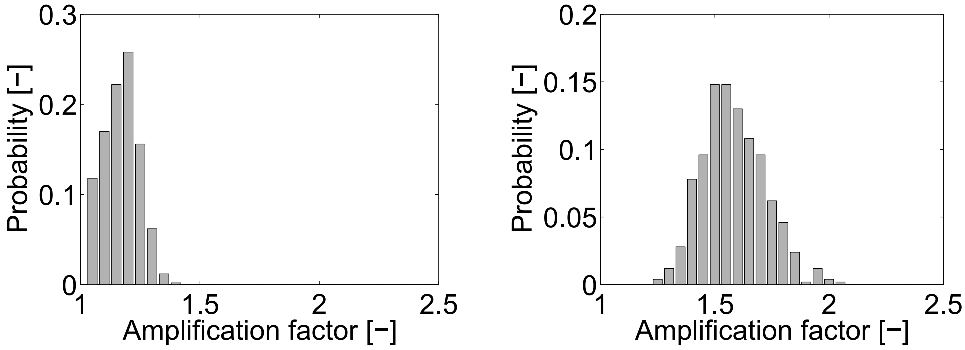

(c) 0.5 %

(d) 5 %

Proposed approach

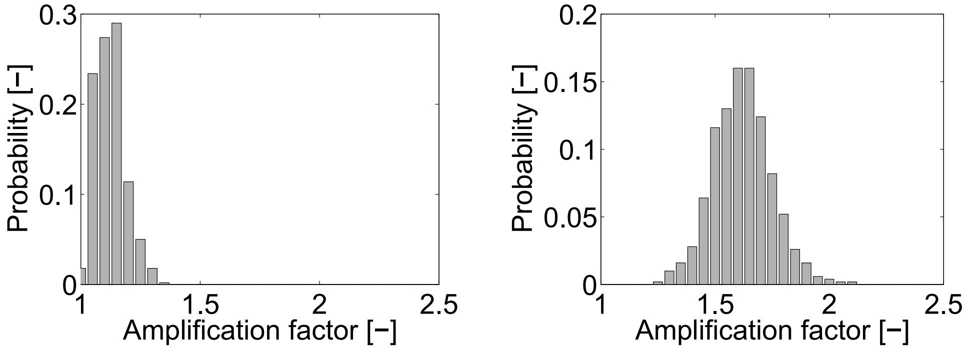

(e) 0.5 %

(f) 5 %

Parametric approach

Figure 6.10: Amplification factor obtained using the nonparametric approach ((a) for 0.5 % of mistuning and (b) for 5 % of mistuning), using the proposed approach ((c) for 0.5 % of mistuning and (d) for 5 % of mistuning), and using the parametric approach ((e) for 0.5 % of mistuning and (f) for 5 % of mistuning).

6.6 Influence of the number of retained harmonics

The influence of the number of retained harmonics in the construction of reduced order models is discussed in this Section. Indeed, to construct the reduced order model and to perform statistical analyses on the amplification factor, the tuned mode shapes have to be computed using the finite element model. In order to reduce the computational time, the cyclic symmetry property is applied in the finite element model. In this case, the computation is performed for each harmonic. Knowing the deformation of the reference sector and the number of nodal diameters of the mode, the deformation can be retrieved for the 360° structure.

In the case of an industrial structure, the number of possible different numbers of nodal diameters is large ($\frac{N}{2}+1$ for an even number of blades N, and $\frac{N-1}{2}+1$ for N odd) because of the high number of blades. Therefore, doing the computations for a minimum numbers of harmonics is a high gain in CPU time.

In this study, the multi-stage academic structure is considered. An engine order of 2 is considered for the excitation. An increasing number of harmonics is considered in the reduced order model. The first case contains only the harmonics corresponding to the engine order of the excitation. Then, the direct adjacent harmonics are progressively added, as shown in Table 6.3.

Number of additional harmonics [-]	Retained harmonics [-]
0	2
1	$[1-3]$
2	$[0-4]$
3	$[0-5]$
4	$[0-6]$
5	$[0-7]$
6	$[0-8]$

Table 6.3: Retained harmonics.

Figure 6.11 shows the error on the obtained amplification factor when considering an increasing number of harmonics, for different mistuning levels. 10 samples are considered for each case. The CMM reduced order modeling technique is used here. The reference amplification factor is the one obtained when considering all harmonics in the model. The error decreases when the number of considered harmonics increases. For 5 harmonics and more, the obtained amplification factor is identical to the reference case. The error is also more important for higher mistuning levels. This is due to the higher harmonic content of mistuned mode shapes.

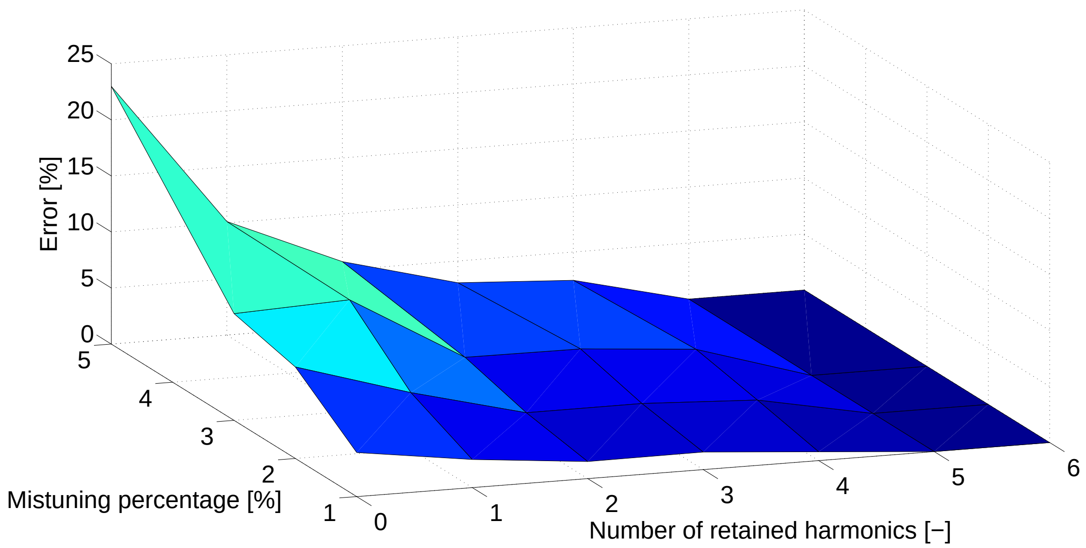

Figure 6.11: Influence of the number of retained harmonics for different amount of mistuning.

6.7 Conclusion

The nonparametric probabilistic approach has the advantage to model both data and model uncertainties while parametric approaches only take into account data uncertainties. The nonparametric approach has been extended to handle multi-stage structures. The extended method has been applied on a two-stage academic structure.

To compare the predicted amplification factor with a mono-stage model and with a multi-stage analysis, the two computations have been performed. An increase up to 33 % of the predicted amplification factor has been observed for the top stage. Therefore, taking into account stages separately instead of both stages together for the studied structure has a high impact on the predicted amplification factor. A more detailed analysis of the influence of the multi-stage coupling will be performed in the next Chapter, in order to determine when multi-stage approaches are necessary.

Comparing to the parametric CMM approach, the size of the model and the computational times are higher when using the nonparametric approach due to the larger size of the involved matrices. Therefore, a new combination of the two modeling methods has been proposed in order to take the advantages of both methods with reduced computational times. To obtain a drastic size reduction of the used structural matrices, the assumption of the parametric method is retained i.e., mistuned mode shapes can be written as a linear combination of the tuned mode shapes, and the uncertainties are directly introduced in the modal space of the blades.

The three methods (the CMM, nonparametric and proposed approaches) have been applied and compared on a two-stage one-piece academic structure. For a structure or a frequency range with moderate coupling, the same amplification factors than the nonparametric approach are obtained. For a highly coupled case, the results of the proposed approach tend to the ones of the parametric approach due to the additional assumption.

The influence of the number of harmonics retained for the construction of the reduced order model has been also evaluated. Indeed, the tuned mode shapes used to construct the ROMs are computed for the reference sector for each number of nodal diameters. Reducing the number of considered harmonics reduces the computational time. The analysis has been performed on a two-stage academic blisk. It has been shown that considering the harmonics $[EO-5, EO+5]$ in the reduced order models leads to the same predicted amplification factor than the case with all harmonics. However, the analysis should be performed on other structures to generalize the obtained results.

Chapter 7

Influence of multi-stage coupling

In this Chapter, a characterization of the interstage coupling in multi-stage bladed structures is performed. More particularly, the effect of the drum flexibility is evaluated. The difference between the results obtained with a mono-stage and with a multi-stage analysis is compared in terms of frequencies and mode shapes. The difference between both analyses is shown to be related to the strain energy localized in the drum, which was computed for different interstage coupling values. This enables to establish a criterion to determine, depending on the localization of the energy in the structure, when a multi-stage finite element analysis is necessary instead of only computing the different mono-stage models separately based on equivalent parameters. Numerical analyses are first performed on a lumped mass model and then applied on a two-stage bladed drum.

7.1 Introduction

So far, most of the existing studies on mistuning analysis have focused on single stage structures. However, the development of one-piece multi-stage structures has significantly increased the influence of the interstage coupling that cannot be neglected anymore in the numerical models. As a consequence it appears that multi-stage structures may present higher amplification factor than those related to single stage configuration.

While a large amount of researches has been performed on single stage structure, the literature on multi-stage structure is limited. Sinha [92] constructed a mistuned lumped mass model and performed Monte Carlo simulations to get the global behavior of the system. Bladh [2] evaluates the importance of interstage coupling by a study of sensitivity to blade mistuning. Bladh's paper suggests that multi-stage analyses may be required when excitations are expected to fall in or near eigenfrequency veering regions [145–147] or when the sensitivity to blade mistuning is to be accounted for. Avalos and Mignolet [107] extended Whitehead's analytical formula to multi-stage assemblies. Their works lead to a new upper limit for the maximum amplification of blade response due to mistuning. However, this paper mentions that a larger amplification factor can be observed in some situations, which is due to a significant transfer of energy between stages induced by a combination of multiple modes. Song [108] developed a new reduced order modeling technique for multi-stage systems and unified it with the component mode mistuning (CMM) method to efficiently treat mistuning in multi-stage systems. The approach was then used for the identification of mistuning in multi-stage structures [26] and for structural health monitoring [119]. Laxalde [25, 111] proposed a method similar in concept to

Song [26], in which the CMM method developed by Lim [15] has been coupled to multi-stage cyclic modeling. The method was applied for modal analysis and forced response calculations for multi-stage industrial bladed disks. Additionally, recent works on multi-stage effects induced by modeling the coupling between flexible shafts and rotors were performed [148–153]. Based upon these developments, D'Souza et al. [154, 155] proposed an identification methodology relying on a statistical characterization of mistuning in multi-stage structures. They showed that the characterization of multi-stage mistuning can only be assessed by considering a multi-stage approach.

In this Chapter, the effect of the drum flexibility in multi-stage structures is evaluated. The strain energy located in the drum and in the blades is computed for different values of the drum stiffness. This enables to establish a criterion based on equivalent parameters to determine, depending on the localization of the energy in the structure, when a multi-stage finite element analysis is necessary instead of only computing the different mono-stage models separately. Numerical analyses are performed on a two-stage bladed drum. The results are first computed for the tuned case. Then, the effect of mistuning on the obtained results is analyzed. A reduced order model based on the component mode mistuning (CMM) method is used to retrieve the frequency response function for the mono-stage and multi-stage models, and the corresponding amplification factors. The resulting error on the amplification factor is also computed for different mistuning levels.

7.2 Analysis of the influence of the interstage structure on a lumped mass model

In order to evaluate the influence of the interstage structure in multi-stage structures, an equivalent lumped mass model is constructed. Each blade is represented by a mass m_b^s, with s the stage number, and each sector of the disk of stage s by a mass m_d^s. Each blade of stage s is connected to the corresponding disk sector by a stiffness k_b^s. Each disk sector is connected to the adjacent one by a stiffness k_d^s and clamped through a stiffness k_{cl}^s. The two-stage lumped mass model is shown in Figure 7.1. The stiffness between the sectors of two different stages (springs in gray in Figure 7.1) is assumed to be proportional to the contact area between sectors of both stages.

The mass matrix of the considered system is given by

$$\mathbf{M} = \begin{bmatrix} \mathbf{M}^{(1)} & \mathbf{0} \\ \mathbf{0} & \mathbf{M}^{(2)} \end{bmatrix}, \tag{7.1}$$

with (for $s = 1, ..., S$)

$$\mathbf{M}^{(s)} = \left[\begin{array}{ccc|ccc} m_b^s & & \mathbf{0} & & & \\ & \ddots & & & \mathbf{0} & \\ \mathbf{0} & & m_b^s & & & \\ \hline & & & m_d^s & & \mathbf{0} \\ & \mathbf{0} & & & \ddots & \\ & & & \mathbf{0} & & m_d^s \end{array}\right], \tag{7.2}$$

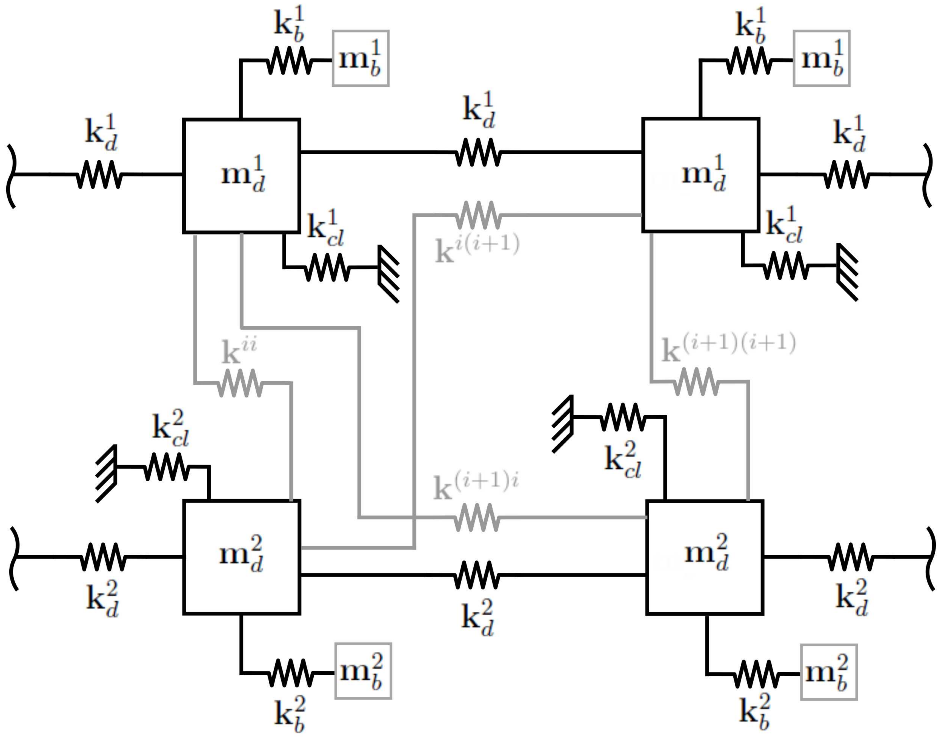

Figure 7.1: Two-stage lumped mass model.

and the corresponding stiffness matrix is given by

$$\mathbf{K} = \left[\begin{array}{cc} \mathbf{K}^{(1)} & \mathbf{K}^{(12)} \\ \mathbf{K}^{(21)} & \mathbf{K}^{(2)} \end{array} \right] , \tag{7.3}$$

with (for $s = 1, ..., S$)

$$\mathbf{K}^{(s)} = \left[\begin{array}{ccc|cccccc} k_b^s & & \mathbf{0} & -k_b^s & & & & & \mathbf{0} \\ & \ddots & & & & \ddots & & & \\ \mathbf{0} & & k_b^s & \mathbf{0} & & & & & -k_b^s \\ \hline -k_b^s & & \mathbf{0} & K_d^{1s} & -k_d^s & & \mathbf{0} & & -k_d^s \\ & & & -k_d^s & K_d^{2s} & -k_d^s & & \mathbf{0} & \\ & \ddots & & \mathbf{0} & \ddots & \ddots & \ddots & & \mathbf{0} \\ & & & & & & & & \\ & & & & \mathbf{0} & & -k_d^s & K_d^{(N_s-1)s} & -k_d^s \\ \mathbf{0} & & -k_b^1 & -k_d^s & & \mathbf{0} & & -k_d^s & K_d^{N_s s} \end{array} \right] , \tag{7.4}$$

where

$$K_d^{ns} = k_b^s + 2k_d^s + \sum_{i=1}^{N_s} k^{ni} + k_{cl}^s \ , \tag{7.5}$$

and

$$\mathbf{K}^{(12)} = \left(\mathbf{K}^{(21)}\right)^T = \left[\begin{array}{ccc|cccc} & \mathbf{0} & & & \mathbf{0} & & \\ \hline \mathbf{0} & \dots & \mathbf{0} & -k^{11} & -k^{12} & \dots & -k^{N_2 1} \\ \mathbf{0} & \dots & \mathbf{0} & -k^{21} & -k^{22} & \dots & -k^{N_2 2} \\ \vdots & & \vdots & \vdots & \vdots & & \vdots \\ \mathbf{0} & \dots & \mathbf{0} & -k^{1N_1} & -k^{2N_1} & \dots & -k^{N_2 N_1} \end{array}\right] . \tag{7.6}$$

The equation of motion of the undamped system is written as

$$\mathbf{M}\ddot{\mathbf{x}} + \mathbf{K}\mathbf{x} = \mathbf{f} \ , \tag{7.7}$$

where $\mathbf{x}$ is the displacement vector for all degrees of freedom of the system, and $\mathbf{f}$ the external forces vector. The eigenfrequencies and mode shapes can be retrieved by solving the corresponding eigenvalue problem.

Figure 7.2 shows the distribution of the energy in the blades and the disk of each stage for different interstage coupling values. The parameters related to the blades given in Table 7.1 remain constant, while the stiffnesses of the disks and between stages progressively increase. It can be seen that, for low stiffness values, the coupling between stages is important. In Figure 7.2(a), both stages participate together in the mode shapes. The percentage of energy in the disk degrees of freedom is important. The coupling between stages progressively decreases in Figures 7.2(b) and 7.2(c). In Figure 7.2(d), the two-stage are uncoupled and the mode shapes are localized in stage 1 or stage 2 separately. The disk participation becomes negligible.

m_b^1	m_b^2	k_b^1	k_b^2	m_d^1	m_d^2	$k_d^1 = k_{cl}^1$	$k_d^2 = k_{cl}^2$
0.6 kg	0.5 kg	10^5 N/m	10^5 N/m	1.2 kg	1 kg	varies	varies

Table 7.1: Used lumped mass parameters.

Figure 7.3 shows the evolution of the maximum energy in the disk as a function of the coupling stiffness. For high interstage coupling (Figures 7.2(a) and 7.2(b) for example), a high percentage of the energy is contained in the drum. For low interstage coupling (Figure 7.2(d) for example), a low percentage of energy is localized in the drum. A threshold between coupled stages and uncoupled stages can be defined by observing the value of the energy percentage localized in the disk. Above the threshold value of energy percentage in the drum, coupling between stages occurs and a multi-stage analysis becomes necessary.

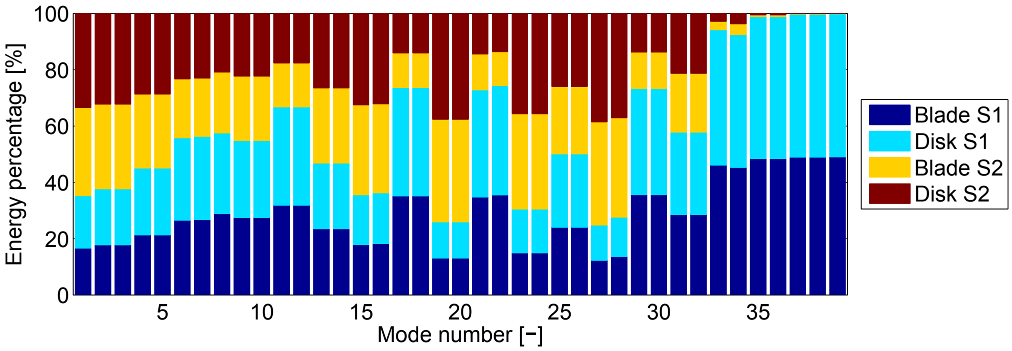

(a) $k_c = 10^4$ N/m

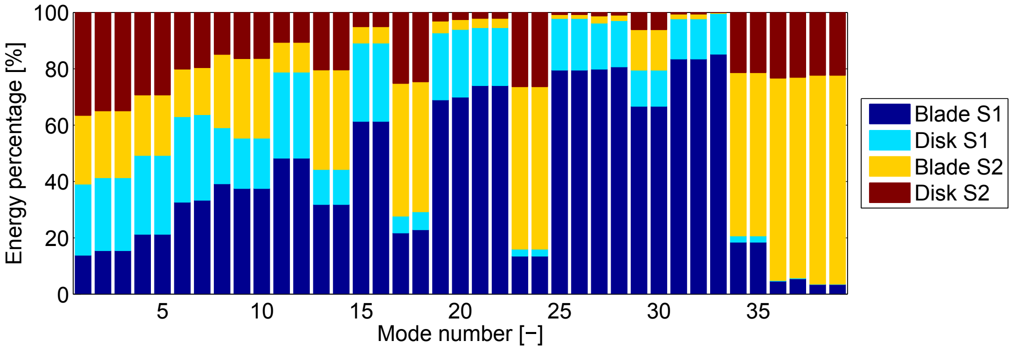

(b) $k_c = 10^5$ N/m

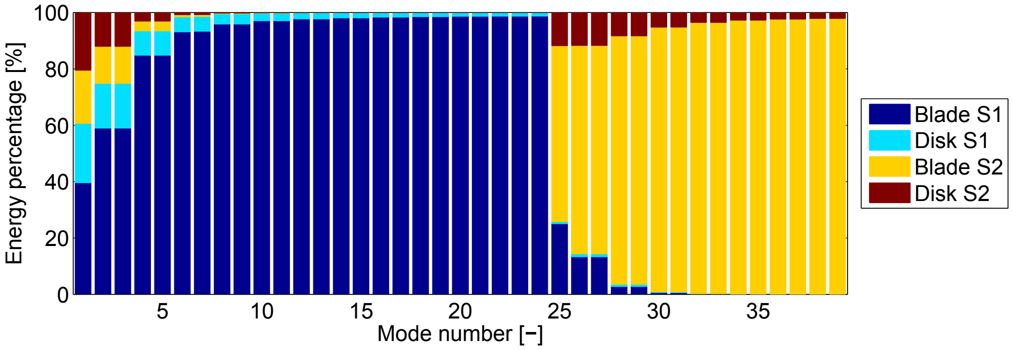

(c) $k_c = 10^6$ N/m

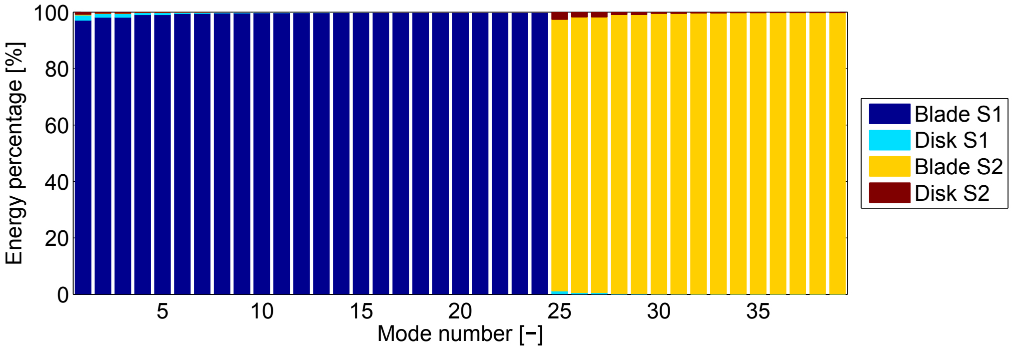

(d) $k_c = 10^7$ N/m

Figure 7.2: Distribution of the energy in the disk and blades of each stage for each mode ($k_d^1 = k_d^2$).

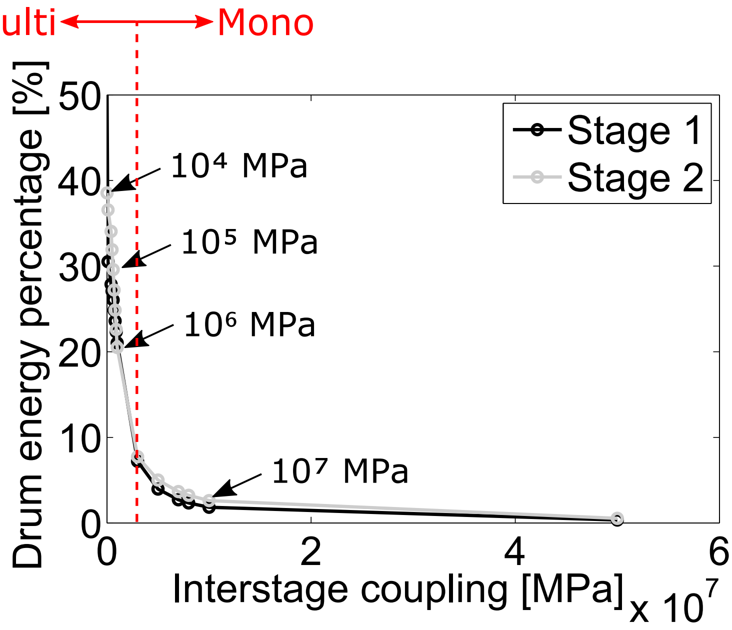

Figure 7.3: Evolution of the energy percentage localized in the disk for each stage as a function of the coupling stiffness in the dynamic case.

The same analysis is repeated in the static case. A unit force is considered on each blade, and no force on the disk degrees of freedom. Figure 7.4 shows the evolution of the energy percentage localized in the drum as a function of the interstage coupling stiffness. The same lumped mass parameters as for the dynamic analysis are considered. The same behavior is observed, and the same threshold of energy percentage in the drum can be considered to distinguish coupled and uncoupled system. The fact that dynamical and statical analyses give the same threshold enables to develop an analytical solution for the energy percentage localized in the drum using the equivalent parameters of the model.

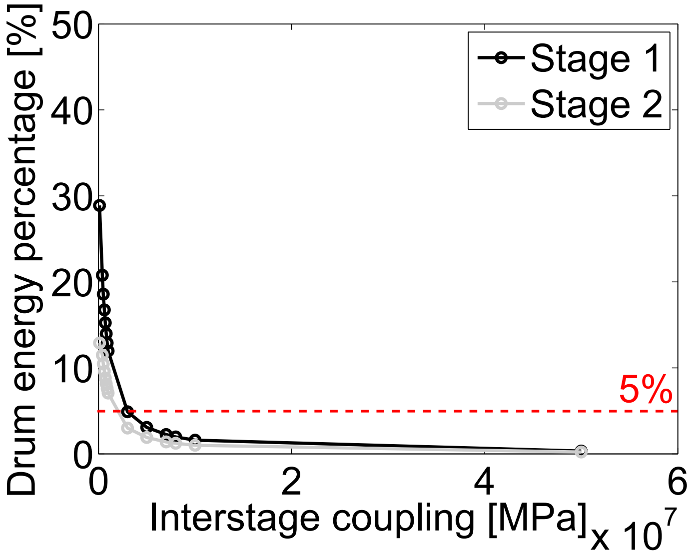

Figure 7.4: Evolution of the energy percentage localized in the disk for each stage as a function of the coupling stiffness in the static case.

The static equilibrium condition is given by

$$\mathbf{K}\mathbf{x} = \mathbf{f} \ , \tag{7.8}$$

where $\mathbf{x}$ is the physical displacement vector of all degrees of freedom, and $\mathbf{f}$ is the external force vector. A unit force is applied on each blade degrees of freedom of each stage, and no force on the disk degrees of freedom. Taking into account Equation (7.8) and the expression of the stiffness matrix given in Equation (7.3) leads to

$$k_b^s x_b^{ns} - k_b^s x_d^{ns} = 1 \ , \tag{7.9}$$

for $n = 1, ..., N_s$ and $s = 1, ..., S$, and

$$-\, k_b^s x_b^{ns} + K_d^{ns} x_d^{ns} - k_d^s \left(x_d^{(n-1)s} + x_d^{(n+1)s} \right) - \sum_{i=1}^{N_s} k^{ni} x_d^{is'} = 0 \ , \tag{7.10}$$

for $n = 1, ..., N_s$ and $s = 1, ..., S$ and where s' refers to the connected stage ($s' = 2$ for stage 1 and $s' = 1$ for stage 2). Equations (7.9) and (7.10) form a set of $2 \sum_s N_s$ linear equations with $2 \sum_s N_s$ unknown factors.

The displacement of the blades and the disk can be expressed as

$$x_b^{ns} = \frac{1}{k_b^s} + \frac{(N_1 + N_2)\, k_c + N_2 k_{cl}^s}{k_c \left(N_1 k_{cl}^1 + N_2 k_{cl}^2 \right) + N_2 k_{cl}^1 k_{cl}^2} \ , \tag{7.11}$$

for $n = 1, ..., N_s$ and $s = 1, ..., S$, and

$$x_d^s = \frac{(N_1 + N_2)\, k_c + N_2 k_{cl}^s}{k_c \left(N_1 k_{cl}^1 + N_2 k_{cl}^2 \right) + N_2 k_{cl}^1 k_{cl}^2} \ , \tag{7.12}$$

for $s = 1, ..., S$.

Then, an analytical expression can be found for the energy ratio localized in the disk and in the blade for each stage

$$\frac{E_b^s}{E_b^s + E_d^s} = \frac{1}{1 + \frac{k_b^s k_d^s A^2}{\left(A k_b^s + B \right)^2}} \ , \tag{7.13}$$

and

$$\frac{E_d^s}{E_b^s + E_d^s} = \frac{1}{1 + \frac{\left(A k_b^s + B \right)^2}{k_b^s k_d^s A^2}} \ . \tag{7.14}$$

with

$$\begin{cases} A = (N_1 + N_2)\,k_c + N_2 k_{cl}^s & (7.15) \\ B = k_c\left(N_1 k_{cl}^1 + N_2 k_{cl}^2\right) + N_2 k_{cl}^1 k_{cl}^2\;. & (7.16) \end{cases}$$

Figure 7.5 shows the evolution of the ratio proposed in Equation (7.14) for different values of coupling stiffness. The same lumped mass parameters are considered. Using this simplified formula, a ratio value above 5 % leads to coupling between stages and a multi-stage analysis is necessary. Under 5 % of energy localized in the disk, the two stages are uncoupled.

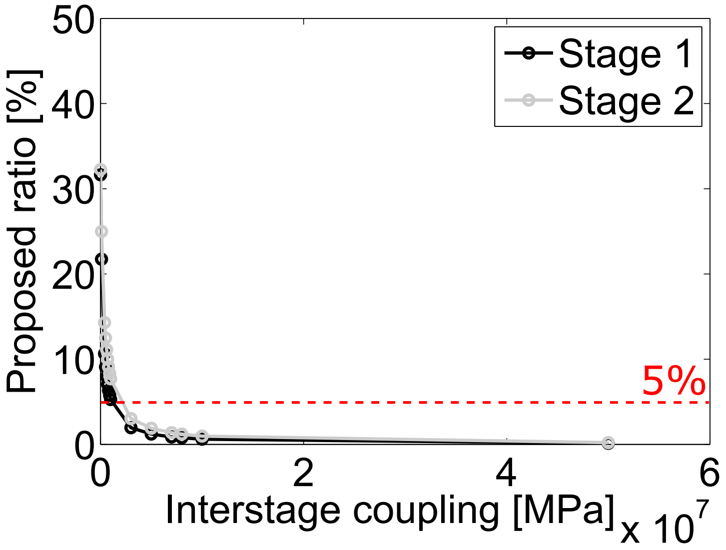

Figure 7.5: Evolution of the proposed ratio as a function of the coupling stiffness.

If only one stage is clamped (i.e., $k_{cl}^1 = k_{cl}$, and $k_{cl}^2 = 0$), the displacement of the blades of stage 1 and 2 is given by

$$x_b^{n1} = \frac{(N_1 + N_2)}{N_1 k_{cl}} + \frac{1}{k_b^1} \qquad \text{and} \qquad x_b^{n2} = \frac{(N_1 + N_2)}{N_1 k_{cl}} + \frac{1}{k_b^2} + \frac{N_2}{N_1 k_c}\;, \tag{7.17}$$

and the displacement of the disk of both stages by

$$x_d^1 = \frac{(N_1 + N_2)}{N_1 k_{cl}} \qquad \text{and} \qquad x_d^2 = \frac{(N_1 + N_2)}{N_1 k_{cl}} + \frac{N_2}{N_1 k_c}\;. \tag{7.18}$$

The energy distribution between the blades and the disk can be written as

$$\frac{E_b^1}{E_b^1+E_d^1} = \frac{1}{1+\frac{(N_1+N_2)^2 k_d^1 k_b^1}{\left((N_1+N_2)k_b^1+N_1 k_{cl}\right)^2}}\ , \tag{7.19}$$

$$\frac{E_b^2}{E_b^2+E_d^2} = \frac{1}{1+\frac{k_b^2 k_d^2 ((N_1+N_2)k_c+N_2 k_{cl})^2}{\left((N_1+N_2)k_b^2 k_c+N_2 k_b^2 k_{cl}+N_1 k_c k_{cl}\right)^2}}\ , \tag{7.20}$$

$$\frac{E_d^1}{E_b^1+E_d^1} = \frac{1}{1+\frac{\left((N_1+N_2)k_b^1+N_1 k_{cl}\right)^2}{(N_1+N_2)^2 k_d^1 k_b^1}}\ , \tag{7.21}$$

$$\frac{E_d^2}{E_b^2+E_d^2} = \frac{1}{1+\frac{\left((N_1+N_2)k_b^2 k_c+N_2 k_b^2 k_{cl}+N_1 k_c k_{cl}\right)^2}{k_b^2 k_d^2 ((N_1+N_2)k_c+N_2 k_{cl})^2}}\ . \tag{7.22}$$

Figure 7.6 shows the evolution of the four ratios of Equations (7.19), (7.20), (7.21) and (7.22). The same lumped mass parameters are used, except for k_e^1 which is set to 0. The same conclusions than before (i.e., a ratio above 5 % leads to coupling between stages) can be done for these clamping conditions.

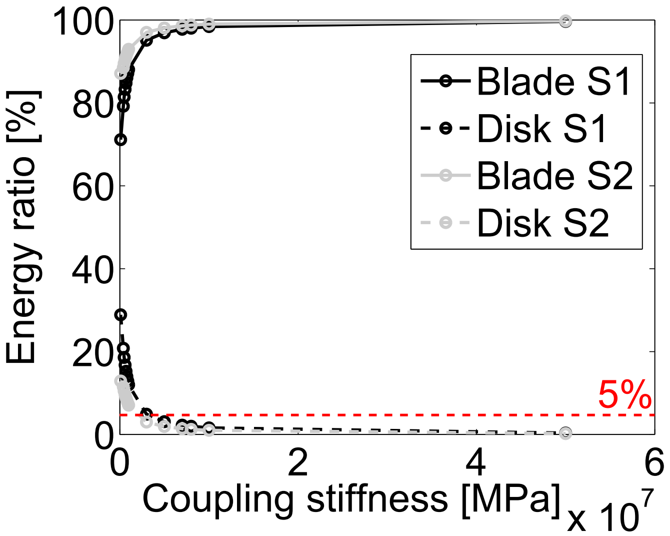

Figure 7.6: Evolution of the energy distribution as a function of the coupling stiffness k_c (k_d also varies proportionality to k_c).

7.3 Application on an academic structure

The developments performed on the lumped mass model are applied on an academic bladed structure composed of two-stages. A dynamical analysis of the two independent stages is made in order to compare the mono-stage results with the multi-stage ones, and to verify that the criterion based on a localization of the energy in the drum is applicable for a real structure. The bottom stage (stage 1) is shown in Figure 7.7(a), the top stage (stage 2) in Figure 7.7(b), and the multi-stage structure in Figure 7.7(c). The first stage totalizes 24 blades, and the second one 15 blades. The structures are made of aluminum. The material and geometric properties are given in Table 7.2 for each stage.

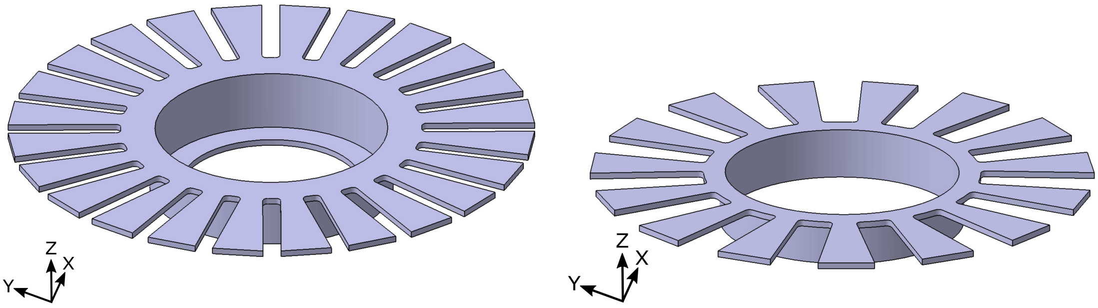

(a) Mono-stage - Stage 1

(b) Mono-stage - Stage 2

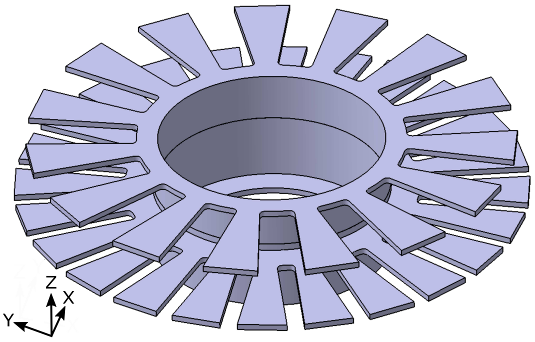

(c) Multi-stage

Figure 7.7: CAD of stage 1 (a), of stage 2 (b), and of the multi-stage structure (c).

	Stage 1	Stage 2
Number of sectors (N) [-]	24	15
Young's modulus [MPa]	71 000	71 000
Density [kg/m^3]	2700	2700
External diameter [mm]	420	400
Internal diameter [mm]	186	186
Thickness [mm]	5	5
Height [mm]	53	46
Blade length [mm]	86	86
Blade width [mm]	40	45

Table 7.2: Material and geometric properties of each stage of the academic structures.

7.3.1 Comparison of the dynamical properties between the mono-stage and multi-stage academic structures

The dynamical behavior of each stage of the academic structure is compared to their behavior in the multi-stage assembly. The boundary conditions are chosen to be representative of the test conditions. For the first stage, two finite element (FE) models are used:

- The first stage is considered alone, clamped at its basis (as illustrated in Figure 7.8(a) on the left).
- The first stage in the two-stages structure, which is clamped at its basis (as illustrated in Figure 7.8(a) on the right).

For the second stage, also two FE models are considered:

- The second stage alone, clamped at its basis (as illustrated in Figure 7.8(b) on the left).
- The second stage in the two-stages assembly, the structure is clamped at its basis (as illustrated in Figure 7.8(b) on the right).

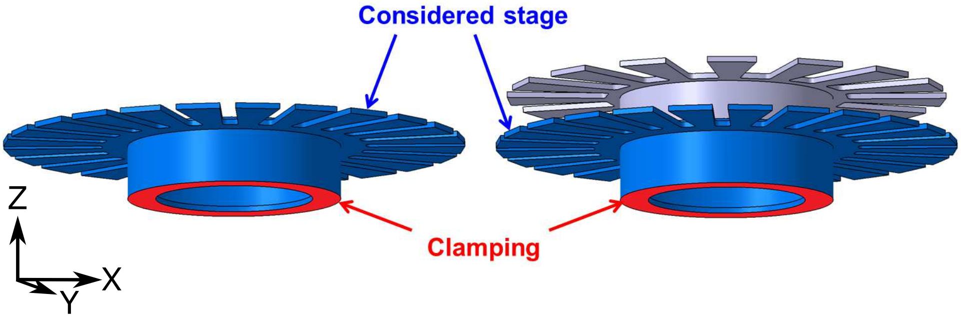

(a) Stage 1

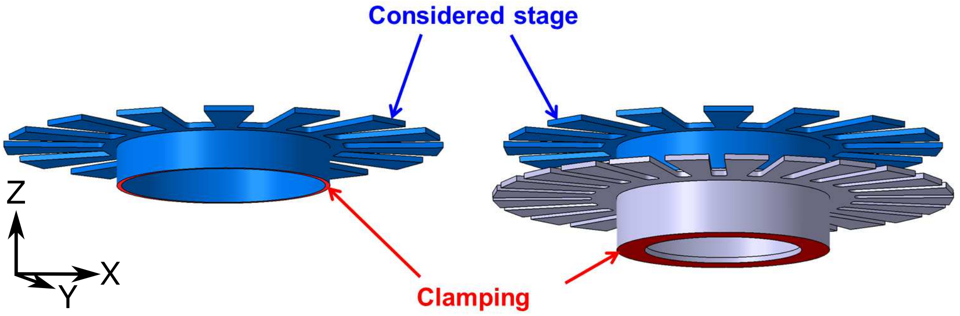

(b) Stage 2

Figure 7.8: Comparison between the mono-stage model of stage 1 (a) and stage 2 (b) with the model of one stage in the multi-stage assembly.

Frequency comparison

Based on the cyclic symmetric finite element model, the SAFE diagram (Singh's Advanced Frequency Evaluation diagram i.e., the eigenfrequencies in function of the number of nodal diameters) of the each structure is constructed. The maximum number of nodal diameters is equal to $\lfloor \frac{N_1}{2} \rfloor = 12$ for the bottom stage, and to $\lfloor \frac{N_2}{2} \rfloor = 7$ for the top stage.

For the multi-stage structure, since the two stages have different numbers of blades, the spatial aliasing has to be taken into account. Figure 7.9 shows the compatible harmonics for this combination of number of blades.

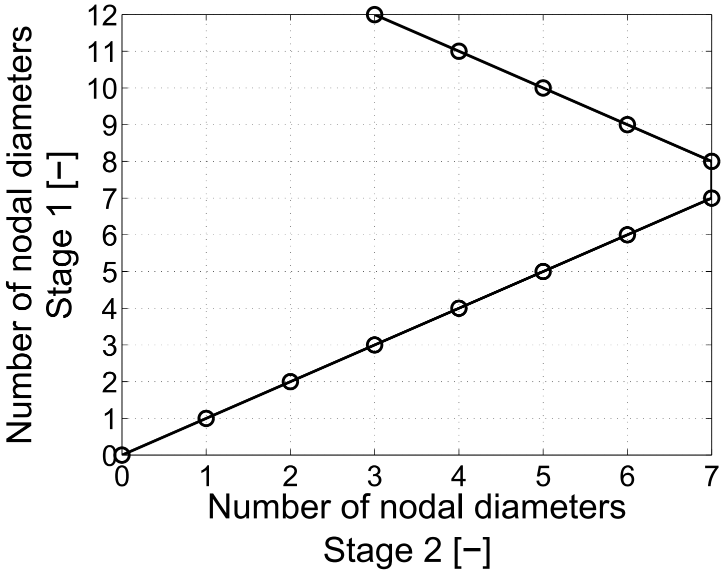

Figure 7.9: Compatible harmonics for stage 1 and 2.

The eigenfrequencies in the frequency range $[0 - 7000]$ Hz are computed for each structure and for each nodal diameter. A classification on the mode shapes of each eigenmodes has been performed. Different symbols are used in order to distinguish the type of mode shape, such as bending modes (1B, 2B...), torsion modes (1T, 2T...), plane bending modes...

The eigenfrequencies of the mono-stage and multi-stage models are compared. The SAFE diagrams of both models are first superimposed. Then, the relative differences are computed. Figure 7.10(a) superimposes:

- the frequencies of stage 1 clamped at its basis (black solid lines);
- the frequencies of the multi-stage structure corresponding to the mode shapes where only stage 1 responds and to the mode shapes where both stages participate (black dotted lines).

Figure 7.10(b) superimposes:

- the frequencies of stage 2 clamped at its basis (black solid lines);
- the frequencies of the multi-stage structure corresponding to the mode shapes where only stage 2 responds and to the mode shapes where both stages participate (black dotted lines).

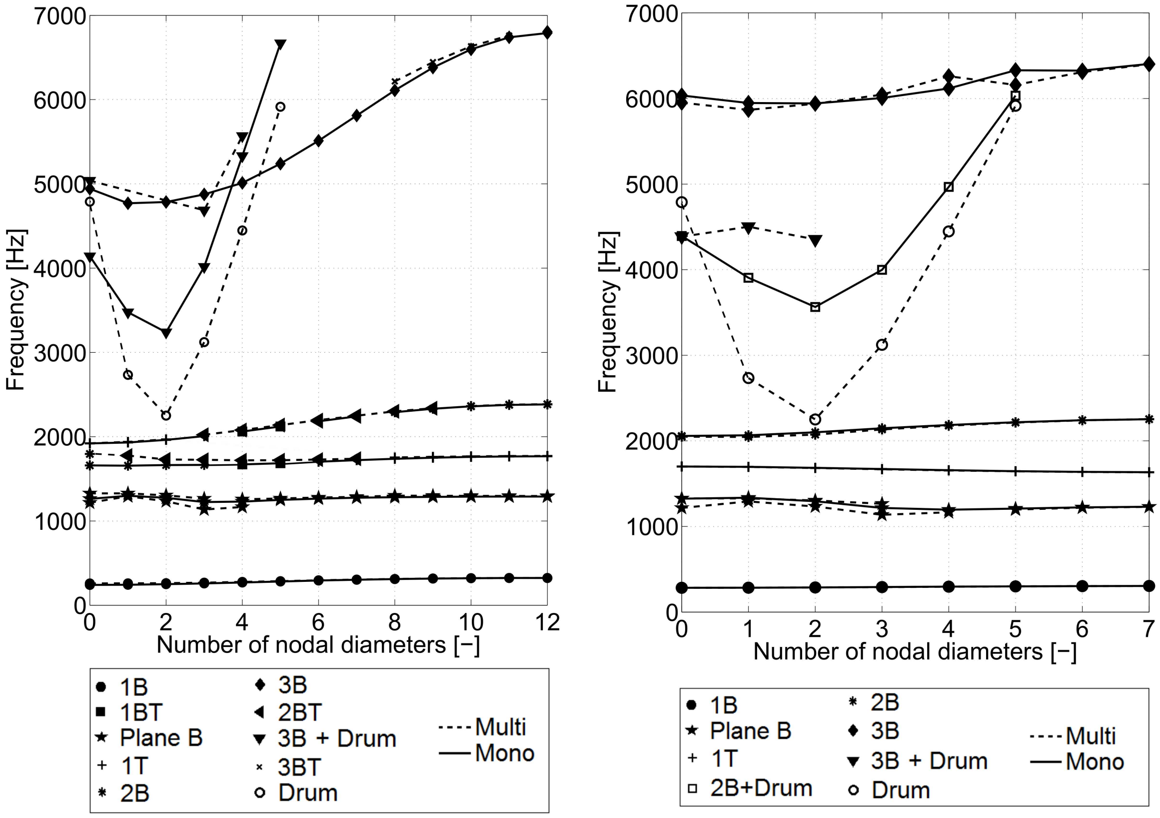

(a) Stage 1

(b) Stage 2

Figure 7.10: Comparison between the SAFE diagram of stage 1 (a) and stage 2 (b) with the corresponding eigenfrequencies obtained in the multi-stage analysis.

In Figure 7.10(a), the first mode family, represented by the • symbol, corresponds to the 1B modes of the bottom stage for both mono-stage and multi-stage models. The mode shape for the reference sector of the mono-stage model is shown in Figure 7.11(a) for the mono-stage model and in Figure 7.13(a) for the multi-stage model. The difference in frequencies between both models is small for all numbers of nodal diameters, decreasing when the number of nodal diameters increases (7 % for the 1B mode with 0 nodal diameters, and no difference for the 1B mode with 12 nodal diameters). This is due to a higher percentage of strain deformation in the drum for low numbers of nodal diameters. No coupling between the stages is observed for this mode family. The second mode family is the plane bending mode family, represented by the ★ symbol. The corresponding mode shape is shown in Figure 7.11(b) for the mono-stage model. For the multi-stage model, at low numbers of nodal diameters (0 to 4 nodal diameters), both stages participate in the mode shape (Figure 7.13(c)). At higher number of nodal diameters, only the bottom stage participates (mode shape shown in Figure 7.13(d)). Larger differences in frequency between the mono-stage and multi-stage models are observed for low numbers of nodal diameters (5 % for the plane bending mode with 0 nodal diameters) than for high numbers of nodal diameters (0.4 % of difference for the plane bending mode with 12 nodal diameters). In the frequency range $[1500 - 2500]$ Hz, the frequency curves of the mono-stage and multi-stage models practically superimpose but the mode shapes are different. For the mono-stage model, at a frequency around 1500 Hz, 2B modes, represented by the $*$ symbol, appear first from 0 to 3 nodal diameters (mode shape shown in Figure 7.11(c)), followed by 1BT modes from 4 to 5 nodal diameters represented by the ■ symbol (mode shape shown in Figure 7.11(e)), and 1T modes from 6 to 12 nodal diameters referred by the + symbol (mode shape shown in Figure 7.11(d)). At a frequency of 2000 Hz, 1T modes appear (0 to 4 nodal diameters), then 1BT (5 to 6 nodal diameters) and 2B modes (8 to 12 nodal diameters) follow. For the multi-stage model, the mode shapes are different. At a frequency around 1500 Hz, 2B modes appear first with the 0 nodal diameter (mode shape shown in Figure 7.13(h)), followed by 2BT modes from 1 to 7 nodal diameters (represented by the ◀ symbol, mode shapes in Figure 7.13(i)), and 1T modes from 8 to 12 nodal diameters (mode shape shown in Figure 7.13(f)). At a frequency of 2000 Hz, 1T modes appear from 0 to 3 nodal diameters, then 2BT from 4 to 9 nodal diameters, and 2B modes follow from 10 to 12 nodal diameters. Then, at higher frequencies, for the mono-stage structure at low number of nodal diameters, a 3B mode family with drum participation follows (mode shape shown in Figure 7.11(f)), referred by the ▼ symbol. A high increase of the eigenfrequency is observed for these modes due to the participation of the drum in the modal deformation. For the multi-stage model, drum modes are also observed (○ symbol, mode shape shown in Figure 7.13(k)). Large differences in frequencies are observed for these modes. The last observed family, referred by the ⧫ symbol, corresponds to the third bending modes in the mono-stage model (mode shapes in Figure 7.11(g)). For the multi-stage model, 3B modes with drum participation are first observed (mode shape shown in Figure 7.13(l)), then the 3BT modes with the participation of the bottom stage only is observed from 8 to 11 nodal diameters (represented by the × symbol, mode shape in Figure 7.13(o)), and finally a 3B mode is present again for 12 nodal diameters (mode shape shown in Figure 7.13(n)).

In Figure 7.10(b), the first family, represented by the • symbol, corresponds to the first bending modes of the top stage (mode shape of the reference sector shown in Figure 7.12(a) for the mono-stage structure, and in Figure 7.13(b) for the multi-stage one). For the 1B modes, the difference in frequencies between the mono-stage and multi-stage models is small for all numbers of nodal diameters, decreasing when the number of nodal diameters increases (7 % for the 1B mode with 0 nodal diameters, and 0.3 % for the 1B mode with 7 nodal diameters). This is due to a higher percentage of strain deformation in the drum for low numbers of nodal diameters. The second mode family (mode shape shown in Figure 7.12(b) and represented by the ★ symbol) corresponds to the plane bending modes. In the multi-stage model, for low number of nodal diameters (0 to 4 nodal diameters), two modes are observed, where both stages participate (mode shape shown in Figure 7.13(c)). Then, for higher numbers of nodal diameters, mode shapes with the participation of the top stage only are observed (mode shapes shown in Figure 7.13(e)) and the difference in frequencies between the mono-stage and multi-stage model decreases (0.4 % for the mode with 7 nodal diameters). The third and fourth ones are respectively the torsion modes, represented by the + symbol, (mode shapes in Figure 7.12(c) for the mono-stage model and in Figure 7.13(g) for the multi-stage model) and the second bending mode family, referred represented by the $*$ symbol, (mode shapes in Figure 7.12(d) for the mono-stage model and in Figure 7.13(j) for the multi-stage model). For the 1T modes and 2B modes, the difference in frequencies remains small for all numbers of nodal diameters, decreasing again when the number of nodal diameters increases (respectively 6 % and 8 % for the 1T and 2B mode with 0 nodal diameters, and respectively 1.6 % and 1.9 % for the 1T and 1B mode with 7 nodal diameters). Slightly higher differences are obtained for the 1T and 2B modes than for the 1B and plane bending modes. These first four families draw quite horizontal lines in the SAFE diagram, which means that these modes are blade modes. For the mono-stage model, the next family is the second bending modes family with drum participation (mode shapes in Figure 7.12(e) and represented by the □ symbol). High variations in frequency are observed for this family for the different nodal diameters. This is due to the drum participation in the mode shapes. For the multi-stage model, drum modes are also observed (represented by the ○ symbol, mode shape shown in Figure 7.13(k)). 3B modes of the top stage with drum participation (represented by the ▼ symbol and mode shape shown in Figure 7.13(m)) are also observed. High frequency variations are also observed for the different numbers of nodal diameters. Larger differences between the frequencies of the mono-stage and multi-stage models are observed (4 to 44 % of difference). Finally, the last observed family, represented by the ♦ symbol, corresponds to the third bending modes (mode shapes in Figure 7.12(f) for the mono-stage structure and in Figure 7.13(p) for the multi-stage structure). Low differences are observed between both models (differences up to 4.5 % are observed).

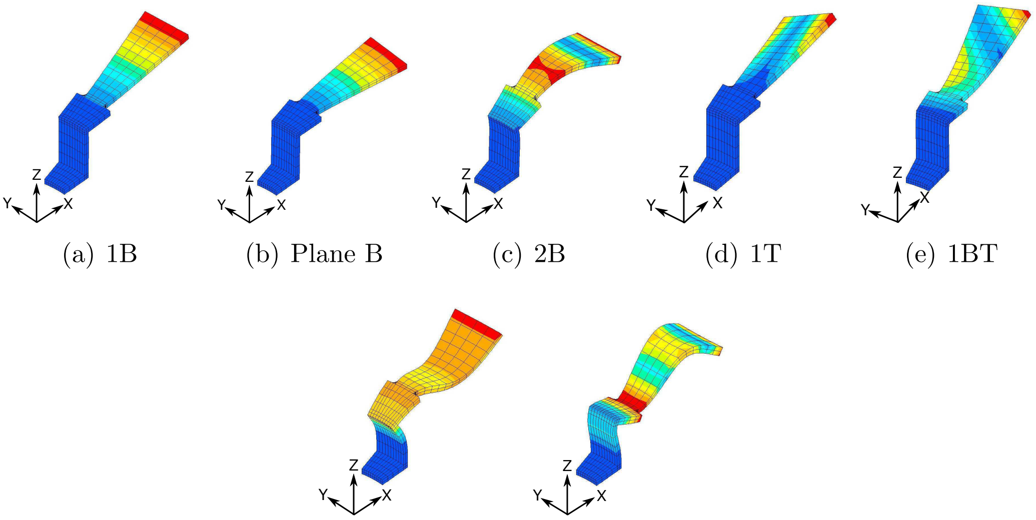

(a) 1B (b) Plane B (c) 2B (d) 1T (e) 1BT

(f) 2B + drum (g) 3B

Figure 7.11: Mode shapes of the mono-stage academic structure of stage 1 for the reference sector.

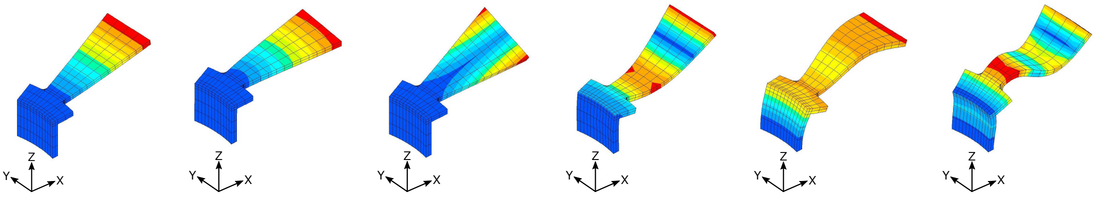

(a) 1B (b) Plane B (c) 1T (d) 2B (e) 2B + drum (f) 3B

Figure 7.12: Mode shapes of the mono-stage structure of stage 2 for the reference sector.

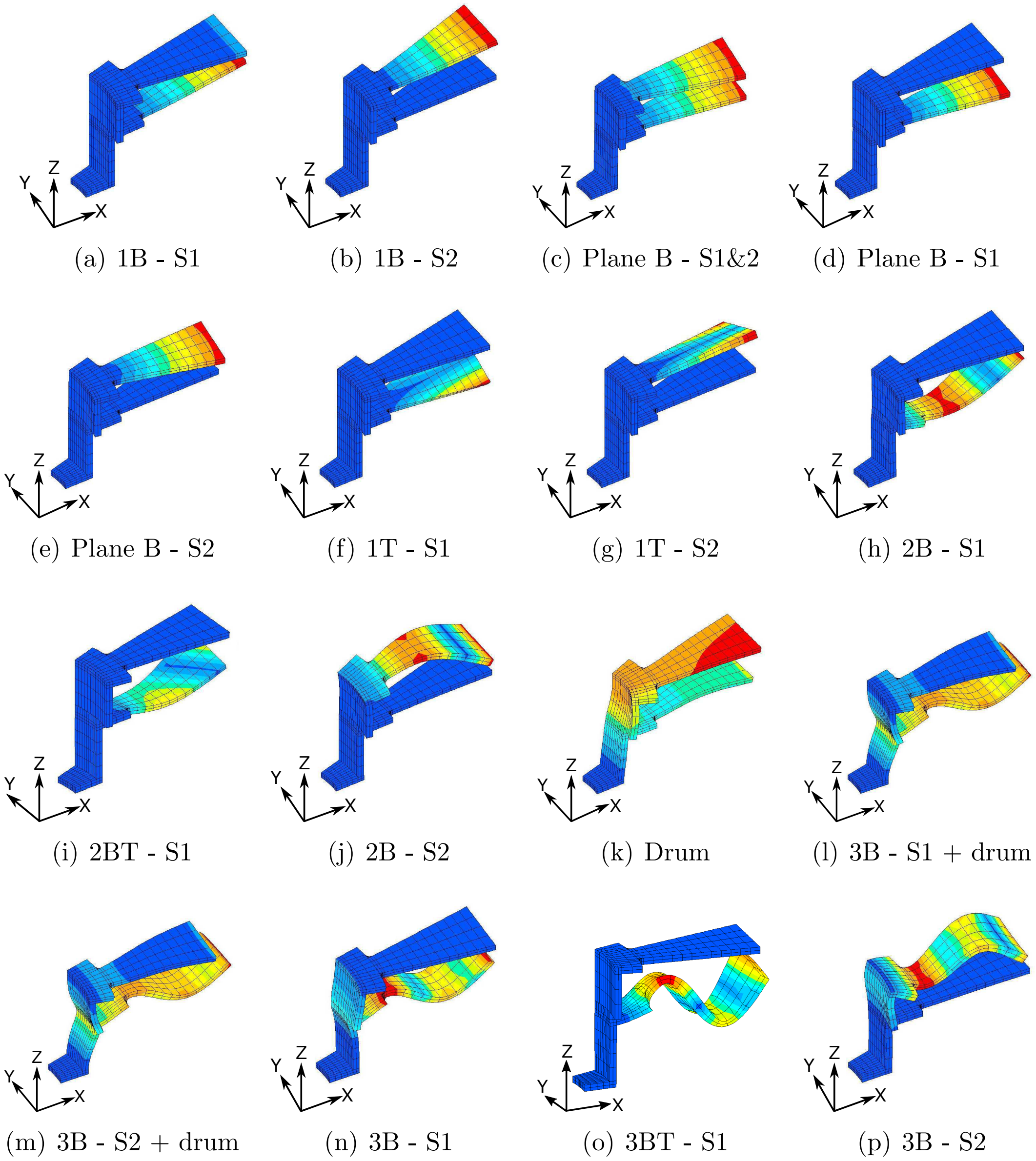

(a) 1B - S1 (b) 1B - S2 (c) Plane B - S1&2 (d) Plane B - S1

(e) Plane B - S2 (f) 1T - S1 (g) 1T - S2 (h) 2B - S1

(i) 2BT - S1 (j) 2B - S2 (k) Drum (l) 3B - S1 + drum

(m) 3B - S2 + drum (n) 3B - S1 (o) 3BT - S1 (p) 3B - S2

Figure 7.13: Mode shapes of the multi-stage structure for the reference sector of each stage.

The comparison between the frequencies of the mono-stage and multi-stage model is summarized in Table 7.3.

	Stage 1	Stage 2
0 nodal diameter	9 %	7 %
$\frac{N}{2}$ nodal diameters	0.2 %	0.4 %
Drum modes	58 %	44 %

Table 7.3: Summary of the comparison between the frequencies of the mono-stage and multi-stage model.

Since the most important differences are obtained for modes with high energy in the drum, the difference is plotted as a function of the energy in the drum for each mode. Figure 7.14 gives the obtained differences on the eigenfrequencies between the mono-stage and multi-stage structures for both stages as a function of the energy in the drum. Only the frequencies of the modes with similar mode shapes (MAC > 0.7, the MAC criterion is defined in the Section just below) are compared. An increase of the difference in frequencies with the drum energy percentage is observed. The gray dotted line on the graphs is the identity line ($x = y$). It can be seen that all modes have globally a lower difference than the percent of energy in the drum.

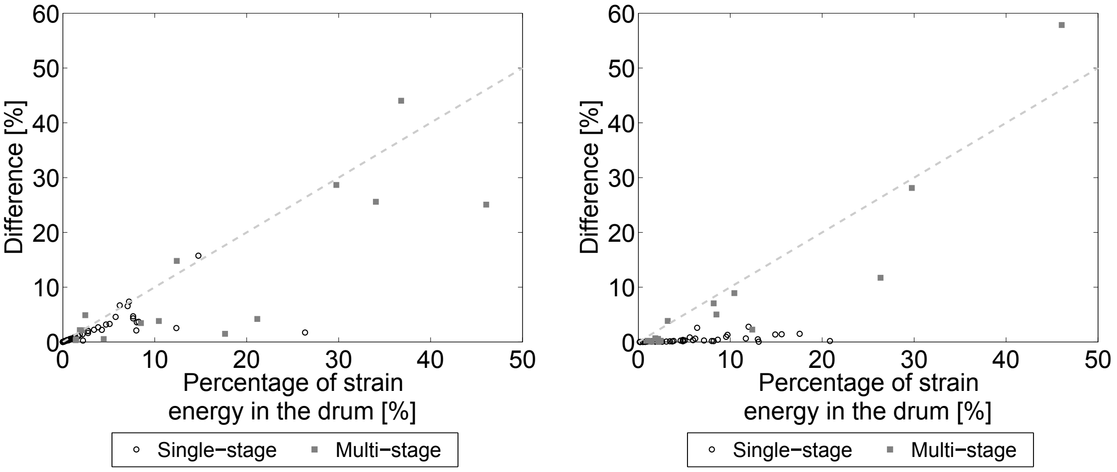

(a) Stage 1

(b) Stage 2

Figure 7.14: Difference between the frequencies of the mono-stage model of stage 1 (a) and stage 2 (b) with the frequencies for which the stage participates in the multi-stage model.

Modes comparison

The mode shapes corresponding to frequencies plotted in the SAFE diagram are compared using the Modal Assurance Criterion (MAC) [139] in Figure 7.15. Both MAC matrices obtained when comparing the modes of the mono-stage and the multi-stage models are not exactly diagonal. First, there are more mode shapes involving the considering stage for the multi-stage model than for the mono-stage model. Then, mode shapes differ for the mono-stage and multi-stage model since low MAC numbers are observed for some modes (mainly multi-stages modes i.e., mode shapes for which both stages participate).

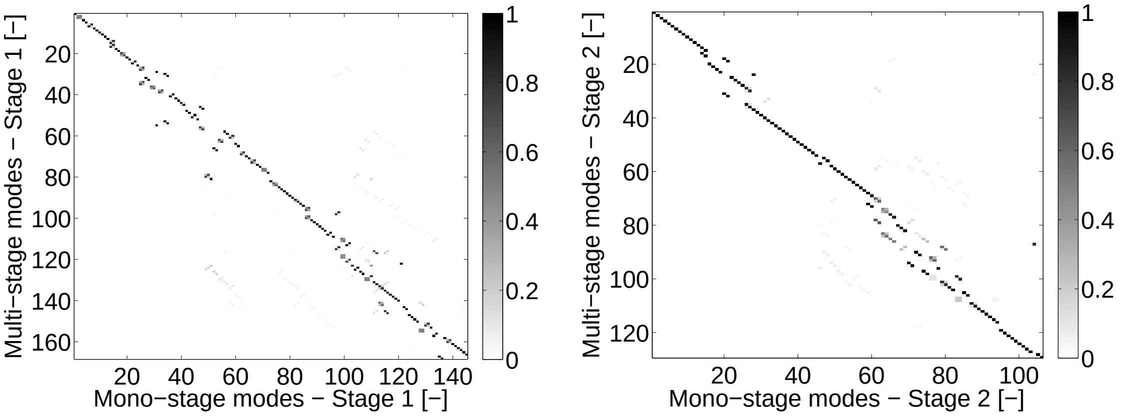

(a) Stage 1

(b) Stage 2

Figure 7.15: MAC matrix between the modes of the mono-stage model of stage 1 (a) and stage 2 (b) with the modes obtained with the multi-stage analysis.

Since the most important differences are due to high energy in the drum, the difference is calculated as a function of the energy in the drum for each mode. Figure 7.16 gives the difference on the maximum MAC values for each multi-stage modes with all mono-stage modes as a function of the energy in the drum. Different symbols are used to distinguish single-stage modes ($\circ$) and multi-stage modes (■). It can be seen that multi-stage modes have more energy in the drum part. However, no correlation between the mode shape difference and the drum energy is observed.

In Figure 7.16(a), all MAC values are higher than 0.5. A large number of mono-stage modes have a MAC number of 1. However, it remains mono-stage modes with lower MAC numbers. Concerning multi-stage modes, the majority has low MAC numbers. In Figure 7.16(b), all mono-stage modes tend to have a MAC of 1. However, even if higher MAC values are obtained for single-stage modes (MAC $\in [0.85-1]$) than for multi-stage modes (MAC $\in [0-1]$), no clear correlation between the mode shape difference and the drum energy is observed. Therefore, the mono-stage model does not correctly represent the dynamic behavior of the multi-stage structure, even for mono-stage mode shapes, and a multi-stage analysis can be necessary.

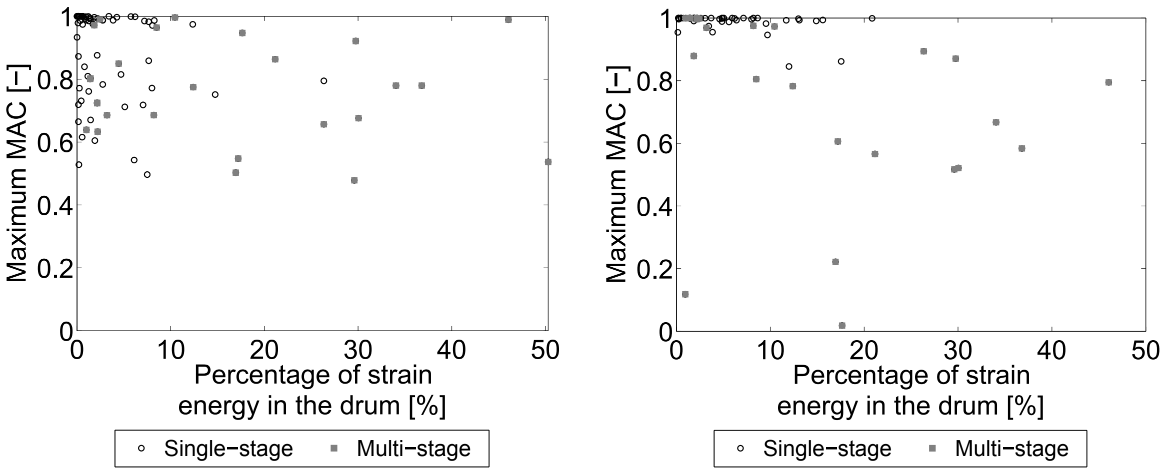

(a) Stage 1

(b) Stage 2

Figure 7.16: Maximum MAC values for each multi-stage modes for which the considered stage participates with all modes of the mono-stage model of stage 1 (a) and stage 2 (b).

7.3.2 Influence of the drum stiffness and coupling criterion in the academic structure

In this Section, the influence of the drum stiffness is evaluated in order to understand the coupling effect. The drum flexibility depends on the geometry of the structure, on the material properties, on the boundary conditions... In order to artificially modify the drum flexibility, different values of the Young's modulus are considered for the drum. A softer drum leads to higher coupling between stages, and a stiffer drum gives lower interstage coupling. This can be shown by computing the strain energy in the different parts of the drum for different values of the Young's modulus of the drum. In order to compute the participation of the drum and the blades in the mode shapes for each mode, the structure is divided in six parts: the blades for each stage, the axial part of the drum for each stage, and the radial part of the drum for each stage. Figure 7.17 shows the different groups on the reference sector. In this study, the Young's modulus of the radial and axial parts of the drum is modified.

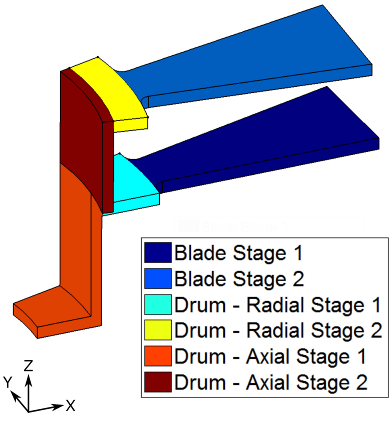

Figure 7.17: Division of the structure in six parts (the blades, the axial part of the drum, and the radial part of the drum, for each stage).

Figure 7.18 shows the maximum energy in the vertical part of the drum as a function of the value of the drum Young's modulus for two cases: the 1B mode family (uncoupled family), and the 3B modes with drum participation family (coupled family). For the second family, a high percentage of energy is localized in the drum of stage 2. Two modes from this family are shown in Figure 7.19. It can be observed that the localization of the energy in the drum of stage 2 allows exchanges of energy between both stages.

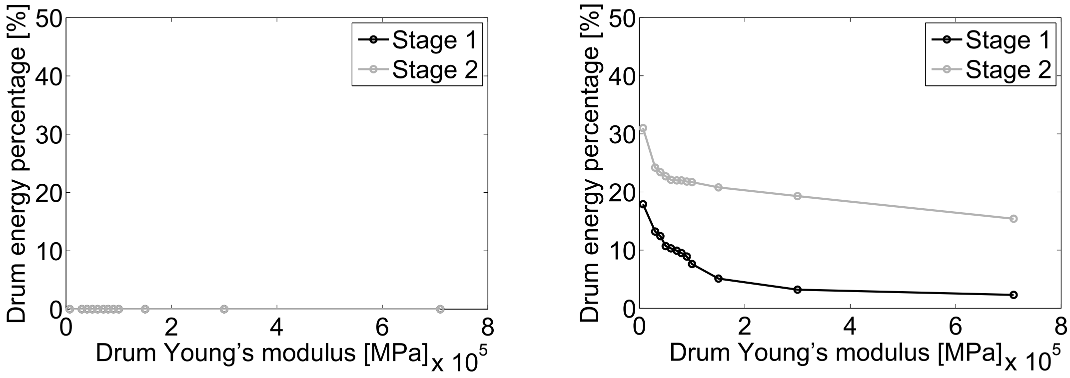

(a) Uncoupled family (b) Coupled family

Figure 7.18: Maximum energy in the drum for stage 1 and stage 2 as a function of the drum Young's modulus for the 1B mode family (a) and for the 3B modes with drum participation family (b).

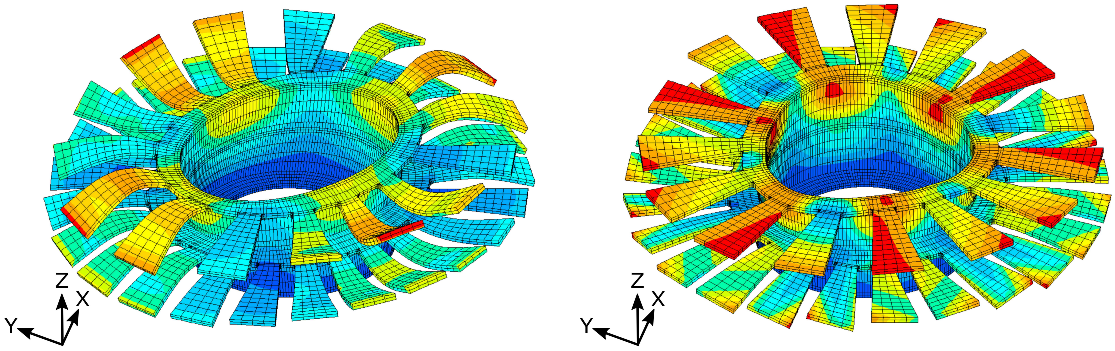

(a) 2ND (b) 3ND

Figure 7.19: Coupled modes with 2 nodal diameters (a) and with 3 nodal diameters (b).

To obtain the equivalent parameters of the first family, one node is retained on each blade, and one other on each drum sector. The two nodes are shown in Figure 7.20 for the reference sector. The Guyan condensation method [156] is used to obtain the equivalent parameters of the model. Only the axial direction is retained. The obtained mass and stiffness matrices are both circulant and of size $2N \times 2N$ for each stage. The equivalent parameters can be easily obtained from these matrices. For the other families, the equivalent parameters are computed such that the eigenfrequencies of the lumped mass model correspond to the considered mode family.

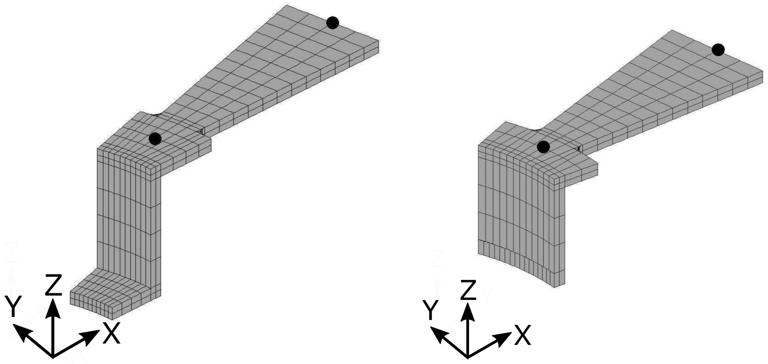

(a) Stage 1 (b) Stage 2

Figure 7.20: Nodes retained in the equivalent lumped mass model for the reference sector of stage 1 (a) and stage 2 (b).

The evolution of the equivalent parameters with the drum Young's modulus can be followed. Each case takes only a reduced computational time (more than 80 % of time reduction for the proposed example). More particularly, Figure 7.21 shows the evolution of the ratio given in Equation (7.14) using the equivalent parameters corresponding to each considered family. The same conclusion about the coupling between stages can be done following the evolution of the proposed ratio (ratio lower than 5 % in Figure 7.21(a) and higher than 5 % in Figure 7.21(b)).

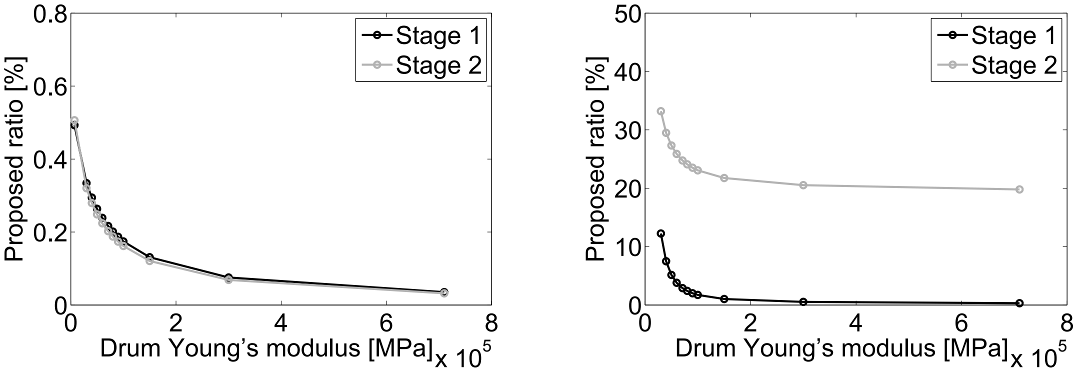

(a) Uncoupled family (b) Coupled family

Figure 7.21: Evolution of the proposed ratio for the 1B mode family (a) and for the 3B modes with drum participation family (b).

7.4 Difference on the mono- and multi-stage amplification factor with the drum stiffness

In the previous Sections, only the tuned finite element models were considered. The effect of the drum stiffness on the amplification factor is evaluated here. The difference between the predicted amplification factor using the mono-stage or the multi-stage model is evaluated for different mistuning level and for different values of drum stiffness. The definition of the amplification factor used here is given by

$$AF = \frac{\max\left(\text{Response of the mistuned system}\right)}{\max\left(\text{Response of the tuned system}\right)} \ . \tag{7.23}$$

The component mode mistuning (CMM) method has been used to reduce the size of the system and compute the mistuned forced response. The theoretical developments of CMM can be found in Sections 3.2 and 4.2.

Figures 7.22 and 7.23 shows the mean amplification factor of the mono-stage model of stage 1 and 2 respectively as a function of the mistuning percentage and the drum stiffness. For a very soft drum, mistuning has almost no effect on the system dynamics. The same phenomena is observed for a very stiff drum. For intermediate values of drum Young's modulus ($E \in]7.1\ 10^3 - 7.1\ 10^6[$ MPa), amplification factors until 2.5 are observed. A higher amplification factor is obtained for stage 1 than for stage 2.

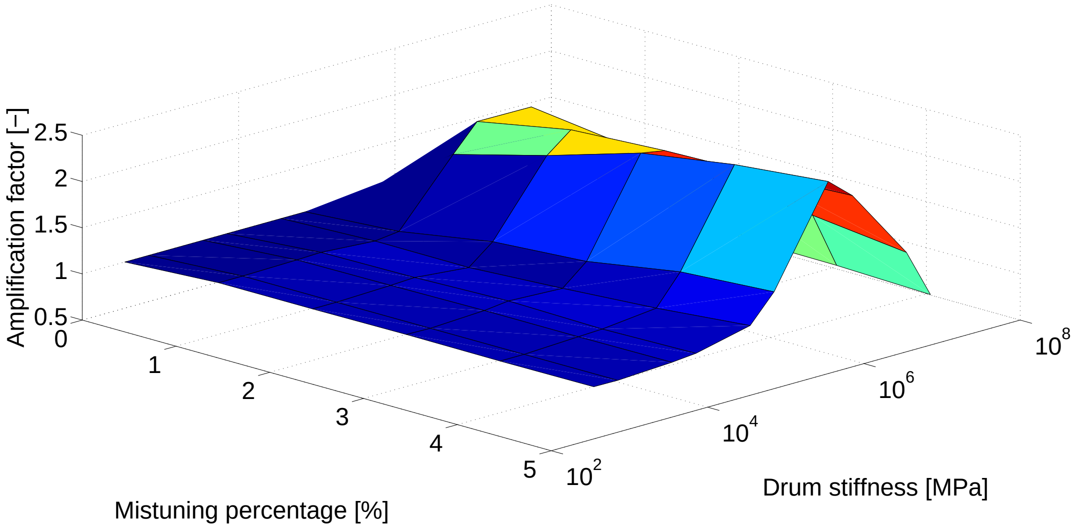

Figure 7.22: Mean amplification factor of the mono-stage model of stage 1 as a function of the mistuning percentage and the drum stiffness.

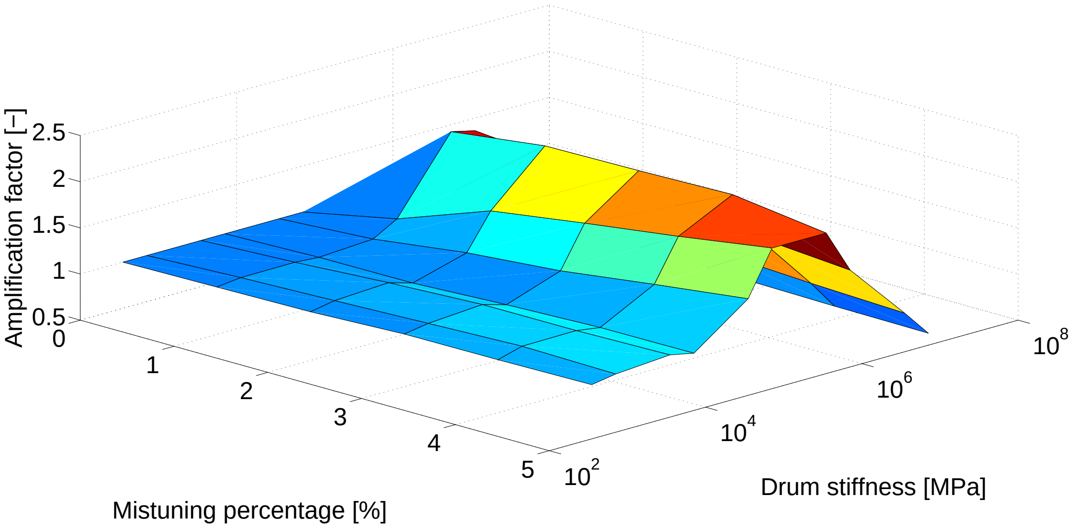

Figure 7.23: Mean amplification factor of the mono-stage model of stage 2 as a function of the mistuning percentage and the drum stiffness.

Figure 7.24 shows the mean amplification factor for each stage of the multi-stage model as a function of the mistuning percentage and the drum stiffness. Monte Carlo simulations are performed for each case. The global behavior of the amplification factor remains the same as for both mono-stage models (Figures 7.22 and 7.23). However, stage 2 is found to have a higher amplification factor than stage 1, which is the contrary results than for the mono-stage analysis.

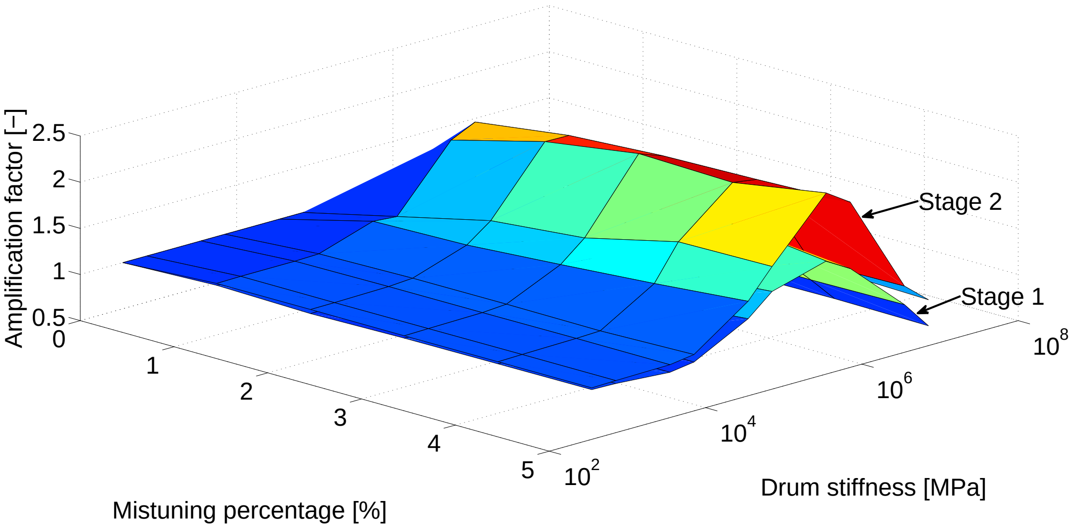

Figure 7.24: Mean amplification factor for stage 1 and 2 of the multi-stage model as a function of the mistuning percentage and the drum stiffness.

Figures 7.25 and 7.26 shows the relative difference on the mean amplification factor of respectively stage 1 and stage 2 between the mono-stage and multi-stage model as a function of the mistuning percentage and the drum stiffness. For stage 1, the amplification factor was overestimated or underestimated by the mono-stage analysis. For stage 2, the amplification factor was underestimated.

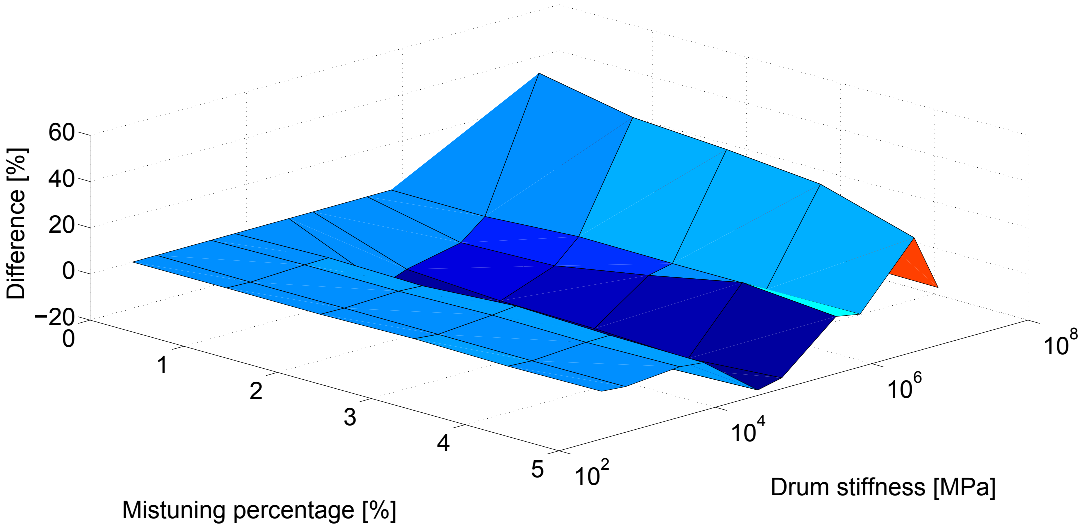

Figure 7.25: Difference on the mean amplification factor of stage 1 between the mono-stage and multi-stage model as a function of the mistuning percentage and the drum stiffness.

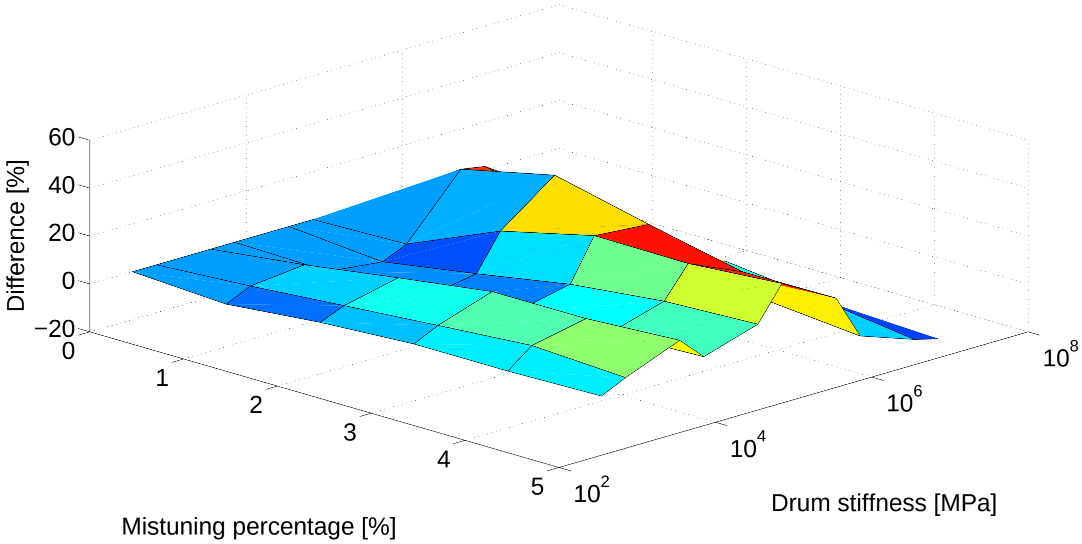

Figure 7.26: Difference on the mean amplification factor of stage 2 between the mono-stage and multi-stage model as a function of the mistuning percentage and the drum stiffness.

7.5 Conclusion

The aim of this Chapter is to evaluate in which cases a multi-stage analysis is necessary, a mono-stage study leading to high differences. For this, the mode shapes and eigenfrequencies have been compared in both mono-stage and multi-stage conditions to evaluate the difference when considering mono-stage analysis instead of the complete assembly.

A lumped mass model with two stages has been first used to evaluate the interstage coupling influence. An analytical solution has been developed for the static case to evaluate the amount of coupling for different drum flexibilities.

Then, a two-stage academic structure has been studied. The comparison between the frequencies of the mono-stage and multi-stage model shows higher differences for low nodal diameters modes than for high nodal diameters modes. This is due to lower drum flexibility when both stages are considered. For drum modes, high differences are obtained. More particularly, a linear increase of the frequency difference between the mono-stage and multi-stage model with the percentage of energy localized in the drum has been obtained. However, no correlation between the MAC values and the percentage of energy localized in the drum were noticed. Then, the Young's modulus of the drum has been varied to evaluate the influence of the interstage coupling. The number of multi-stage modes decreases when the drum Young's modulus increases, as well as the percentage of energy localized in the drum. The difference in frequencies between the mono-stage and multi-stage model has been shown to be proportional to the percentage of energy in the drum. The approach based on equivalent lumped mass model has been applied on the academic structure to obtain the evolution of the percentage of energy in the drum (i.e., the interstage coupling) with reduced computational resources. The use of equivalent parameters enables to found the limit between a weak coupling (a mono-stage analysis leading to low differences) and a high coupling (multi-stage analysis necessary) with a high reduction of computational time. If the proposed ratio has a value higher than 5 %, a multi-stage analysis is necessary.

Finally, the amplification factor has been computed for different values of drum stiffness for different mistuning percentages. For a very soft or a very stiff drum, mistuning has practically no effect on the system dynamics. For intermediate values of drum Young's modulus, differences are observed between mono-stage and multi-stage structures, and a multi-stage analysis is necessary.

For industrial applications, the aerodynamical effects have to be taken into account to obtain an accurate quantitative value of the actual amplification factor. In the next Chapter, the effect of the aerodynamical damping on the predicted amplification is studied in detail.

Chapter 8

Aerodynamic coupling

In this Chapter, the influence of the aerodynamic coupling on the forced response is evaluated. Both structural and aerodynamic coupling are considered here. The influence on the predicted amplification factor when neglecting the structural or the aerodynamic coupling term is analyzed for different values of drum Young's modulus. The sensibility of the frequency response to noise in the aerodynamic coefficients is also evaluated.

8.1 Introduction

The different blades in a bladed disk are structurally coupled through the disk, the drum or the shrouds depending on the configuration of the considered bladed structure, but also aerodynamically coupled. In the previous Chapters, only the structural coupling has been taken into account in the models. In the majority of research works, only structural coupling has been considered. However, it has been shown that both coupling mechanisms influence the stability and maximum blade resonance determination [43,45,56,61,157–164].

The first mistuning studies that take into account the aerodynamic coupling were based on low fidelity structural models. Then, more advanced mistuning models were developed [7–9, 13, 74, 165–170]. Pierre et al. [171, 172] performed detailed studies on mode localization for mistuned bladed structures. Other models incorporated unsteady aerodynamic coefficients, but these are rare in the literature. Seinturier et al. [173] have performed a flutter analysis on a mistuned fan with both structural and aerodynamic coupling. De Cazenove et al. [174] performed for a geometrically mistuned bladed disk a sensitivity analysis of uncertain parameters in terms of their influence on the forced response level with aeromechanical coupling.

Kielb et al. [175, 176] proposed an approach to take into account both structural and aerodynamic couplings. A reduced order model (ROM) is used to model the structural coupling, and an unsteady CFD code is used to model the aerodynamic coupling. The used reduced order model is the FMM theory, initially developed for structures with very stiff disks [13] and later generalized for more flexible system [18]. Blade coupling forces are adding using the cascade aerodynamic theory [56].

In this Chapter, the same approach than Kielb et al. [175] is followed. The used reduced order technique is the component mode mistuning (CMM) method, as the method used in Chapters 3, 4 and 7. A study of relative importance of the structural and aerodynamic couplings is performed for different values of drum stiffness. The error on the frequency response functions (FRF) is analyzed. The sensibility of the obtained FRFs to noise in the aerodynamic coefficients is also analyzed.

8.2 Single blade flutter

Aeroelasticity is the study of the interaction of inertial, structural and aerodynamic forces. The interaction between these three forces can cause several undesirable phenomena, such as flutter, but also limit cycle oscillations, divergence, vortex shedding, buffeting, or galloping. The notations of this Section follows the formulation of the course of Pr. Dimitriadis (University of Liège) [177]. In order to avoid flutter, aeroelastic designs are performed.

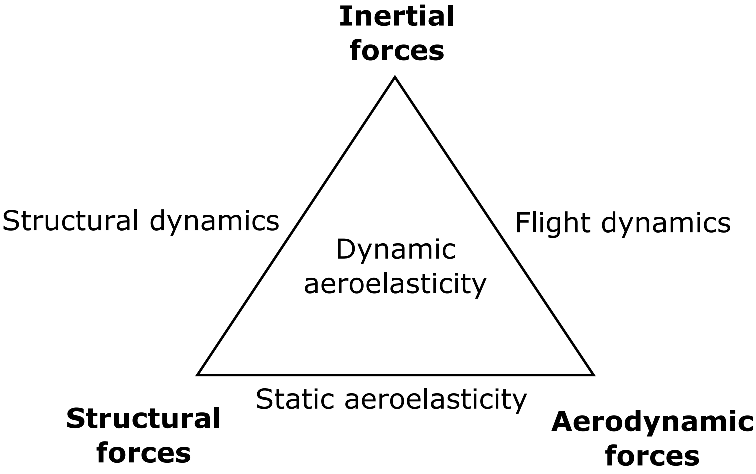

Figure 8.1: Aeroelasticity [177].

To understand the flutter phenomenon, a two degrees of freedom system is constructed, as illustrated in Figure 8.2. α is the pitch degree of freedom and h the plunge degree of freedom. K_α denotes the pitch spring stiffness, K_h the plunge spring stiffness, and I_α is the mass moment of inertia of the blade. x_f is the position of the fluxural axis (pivot), and x_c is the position of the center of mass. In order to further simplify the model, a flat plate airfoil is considered i.e., without any thickness or camber. This simple model permits to demonstrate most aeroelastic phenomena.

The aerodynamic force acting on the blade is the lift $l\left(t\right)$ and it is placed on the quarter chord $\frac{c}{4}$ (aerodynamic center). There is also an aerodynamic moment $m\left(t\right)$ acting around the flexural axis. These two external loads are illustrated in Figure 8.3.

Apart from the circulatory lift and moment, the air exerts another force on the airfoil. The wing is forcing a mass of air around it to move. The air reacts and this force, known as the added mass effect, causes both lift and moment contributions, noted $p\left(t\right)$ and $r\left(t\right)$ respectively. It can be seen as the effort required to move a cylinder of air with a mass equals to $\pi\rho\frac{c^2}{4}$. This force causes both lift and moment contributions.

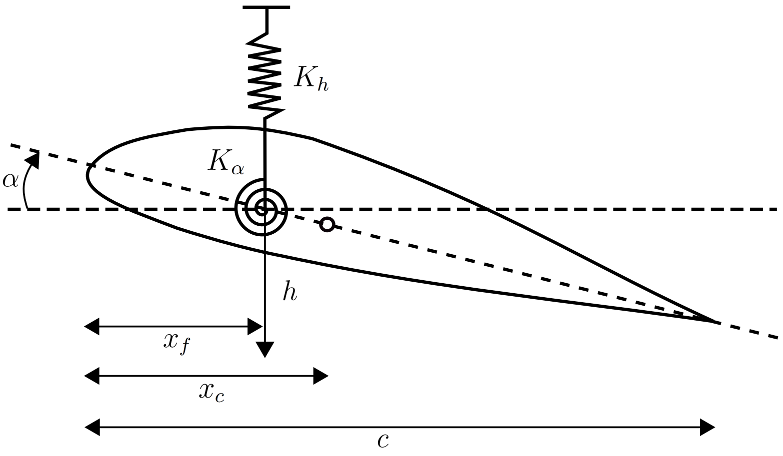

Figure 8.2: Flutter two degrees of freedom system [177].

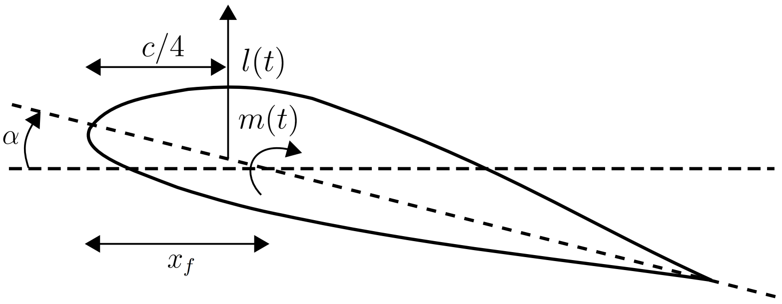

Figure 8.3: Lift and moment [177].

The equations of motion of the two degrees of freedom model can be written as

$$\begin{pmatrix} m & S_a \\ S_a & I_\alpha \end{pmatrix} + \begin{Bmatrix} \ddot{h} \\ \ddot{\alpha} \end{Bmatrix} + \begin{pmatrix} K_h & 0 \\ 0 & K_\alpha \end{pmatrix} \begin{Bmatrix} h \\ \alpha \end{Bmatrix} = \begin{Bmatrix} -l\,(t) + p\,(t) \\ m\,(t) + r\,(t) \end{Bmatrix} . \tag{8.1}$$

The detailed expressions and developments of the terms $l\,(t)$, $m\,(t)$, $p\,(t)$ and $t\,(t)$ can be found in the reference [177]. Replacing these four terms by their expressions in Equation (8.1), ones obtains the following large expression

$$\begin{aligned} &\underbrace{\begin{pmatrix} m & S_a \\ S_a & I_\alpha \end{pmatrix}}_{\mathbf{A}} \underbrace{\begin{Bmatrix} \ddot{h} \\ \ddot{\alpha} \end{Bmatrix}}_{\ddot{\mathbf{q}}} + \rho\pi\frac{c^2}{4} \underbrace{\begin{pmatrix} 1 & \left(\frac{c}{2}-x_f\right) \\ \left(\frac{c}{2}-x_f\right) & \left(\frac{c}{2}-x_f\right)^2+\frac{c^2}{24} \end{pmatrix}}_{\mathbf{B}} \underbrace{\begin{Bmatrix} \ddot{h} \\ \ddot{\alpha} \end{Bmatrix}}_{\ddot{\mathbf{q}}} + \\ &\rho U c\pi \underbrace{\begin{pmatrix} 1 & \left(\frac{3c}{4}-x_f\right)+\frac{c}{4} \\ -ec & \left(\frac{c}{2}-x_f\right)^2+\left(\frac{3c}{4}-x_f\right)\frac{c}{4} \end{pmatrix}}_{\mathbf{D}} \underbrace{\begin{Bmatrix} \dot{h} \\ \dot{\alpha} \end{Bmatrix}}_{\dot{\mathbf{q}}} + \\ &\underbrace{\begin{pmatrix} K_h & 0 \\ 0 & K_\alpha \end{pmatrix}}_{\mathbf{E}} \underbrace{\begin{Bmatrix} h \\ \alpha \end{Bmatrix}}_{\mathbf{q}} + \rho U^2 c\pi \underbrace{\begin{pmatrix} 0 & 1 \\ 0 & -ec \end{pmatrix}}_{\mathbf{F}} \underbrace{\begin{Bmatrix} h \\ \alpha \end{Bmatrix}}_{\mathbf{q}} = \begin{Bmatrix} 0 \\ 0 \end{Bmatrix} . \end{aligned} \tag{8.2}$$

These are the full equations of motion for the pitch-plunge airfoil with quasi-steady aerodynamics. These equations of motion are linear ordinary differential equations of second order. Equation (8.2) is of the form

$$\left(\mathbf{A} + \rho\pi\frac{c^2}{4}\mathbf{B}\right)\ddot{\mathbf{q}} + \left(\mathbf{C} + \rho U c\pi\mathbf{D}\right)\dot{\mathbf{q}} + \left(\mathbf{E} + \rho U^2 c\pi\mathbf{F}\right)\mathbf{q} = \mathbf{0}\ , \tag{8.3}$$

when posing

$$\mathbf{q} = \left\{\begin{array}{c} h \\ \alpha \end{array}\right\}\ , \tag{8.4}$$

with mass, damping and stiffness matrices for both aerodynamic and structural contributions.

Then, the equations of motion can be assembled as

$$\left\{\begin{array}{c} \ddot{\mathbf{q}} \\ \dot{\mathbf{q}} \end{array}\right\}\left(\begin{array}{cc} -\mathbf{M}^{-1}\left(\mathbf{C} + \rho U c\pi\mathbf{D}\right) & -\mathbf{M}^{-1}\left(\mathbf{E} + \rho U^2 c\pi\mathbf{F}\right) \\ \mathbf{I} & \mathbf{0} \end{array}\right)\left\{\begin{array}{c} \dot{\mathbf{q}} \\ \mathbf{q} \end{array}\right\}\ , \tag{8.5}$$

where $\mathbf{M} = \mathbf{A} + \pi\rho\frac{c^2}{4}\mathbf{B}$. In this way, the equations of motion are now first order equations, with the form

$$\dot{\mathbf{z}} = \mathbf{Q}\mathbf{z}\ , \tag{8.6}$$

with

$$\mathbf{z} = \left\{\begin{array}{c} \dot{\mathbf{q}} \\ \mathbf{q} \end{array}\right\}\ . \tag{8.7}$$

This equation can be solved by considering a sinusoidal motion i.e.,

$$\mathbf{z} = \mathbf{z}_0 e^{\lambda t}\ , \tag{8.8}$$

where λ are the eigenvalues of the system and can be obtained from the characteristic polynomial

$$a_4\lambda^4 + a_3\lambda^3 + a_2\lambda^2 + a_1\lambda + a_0\ . \tag{8.9}$$

The absolute value of the obtained eigenvalues are the natural frequencies i.e., $\omega_n = |\lambda|$. The damping ratios are defined as $\zeta = -\frac{\Re(\lambda)}{\omega_n}$. The damping ratios give the amount of damping present in each vibration mode. Both natural frequencies and damping ratios are functions of the airspeed and of the air density.

The equations of motion can be solved for each airspeed U. An example is shown in Figure 8.4. As the airspeed increases, the two natural frequencies approach each other (Figure 8.4(a)). One of the damping ratios increases while the other first increases and then decreases (Figure 8.4(b)). The critical damping ratio becomes zero and then negative, and the instability occurs. This phenomenon is called flutter and the zero damping speed is the flutter speed [177].

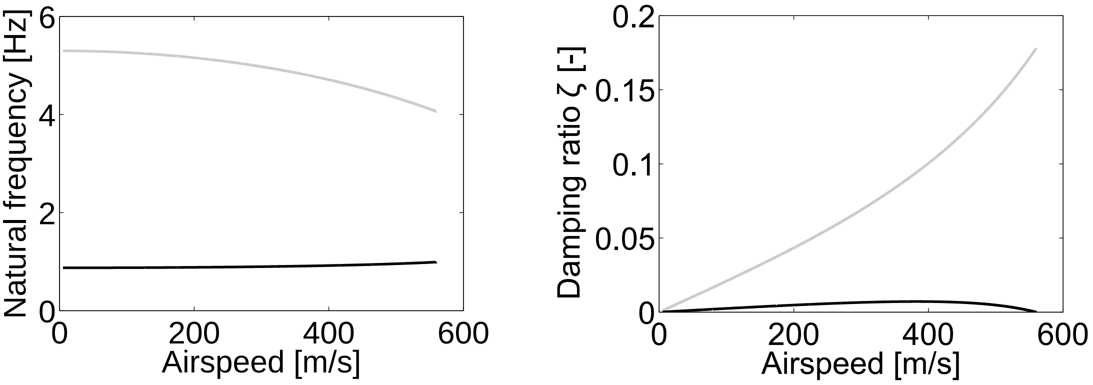

(a) (b)

Figure 8.4: Eigenfrequencies (a) and damping ratio (b) as a function of airspeed.

8.3 Multi-airfoils (cascade) flutter

Turbomachines contain a succession of bladed disks. In a bladed disk, the blades are no more isolated, but are submitted to the influence of their neighbored blades, as illustrated in Figure 8.5 [178–181]. The reference blade is named here blade 0, the direct neighboured blades are named blade +1 and −1, the next blades are named +2 and −2, etc. This convention is the one used in the field of aeroelasticity in turbomachinery. The notations of this Section follows the formulation of the course of Pr. Kielb (Duke University) [181].

A traveling wave seen by blade n, w_n, is the sum of the contribution of all blades, as

$$w_n = \sum_{k=-\frac{N}{2}}^{\frac{N}{2}} W_k \; e^{jk\Delta_n} \ , \tag{8.10}$$

where Δ_n is inter-blade phase angle (i.e., $\Delta_n = \phi_n - \phi_{n-1}$ with ϕ_n the angular position of blade n, and ϕ_{n-1} the angular position of blade $n-1$) which is constant for a tuned system, and W_k is the influence coefficient of blade k. W_k can be written as

$$W_k = \bar{W}_k e^{j\phi_k} \ , \tag{8.11}$$

Figure 8.5: Cascade of blades [56, 181].

where ϕ_k is the phase of blade k. The contribution of two k^{th} conjugate pair is

$$\Re\left(\bar{W}_{+k}\ e^{j\phi_{+k}}\ e^{jk\Delta_n} + \bar{W}_{-k}\ e^{j\phi_{-k}}\ e^{-jk\Delta_n}\right) = \bar{S_k^R} \sin\left(k\Delta_n + \phi_k^R\right) \ , \tag{8.12}$$

with

$$\bar{S_k^R} = \sqrt{\bar{W}_{+k}^2 + 2\bar{W}_{+k}\bar{W}_{-k}\cos\left(\phi_{+k} + \phi_{-k}\right) + \bar{W}_{-k}^2} \ , \tag{8.13}$$

and for the particular case when $k = 0$,

$$\bar{S_0^R} = \bar{W}_0 \cos\left(\phi_0\right) \ . \tag{8.14}$$

Then, the damping coefficient Ξ can be computed for each angle α as followed:

$$\Xi_\alpha = \frac{-w}{\pi q c^2 \alpha^2} \ . \tag{8.15}$$

It can be shown [181–183] that the two dominant terms are $\bar{S_0^R}$ and $\bar{S_1^R}$. Figure 8.6 shows the damping coefficient as a function of the angular position taking into account these two terms. A stability parameter is defined as

$$\hat{S} = \bar{S}_0^R - \bar{S}_1^R \ . \tag{8.16}$$

If $\hat{S} > 0$, the system is stable. If $\hat{S} < 0$, the system is unstable.

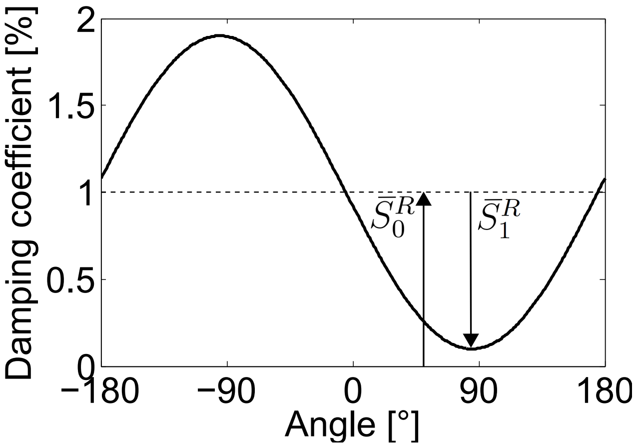

Figure 8.6: Damping coefficient [181].

8.4 Aerodynamic model

In this Section, the equation of motion are derived for a mistuned bladed disk to take into account both aerodynamic and structural coupling between the blades.

The mistuned equation of motion has been developed in the Chapters 3 and 4. CMM equations are reviewed in Chapter 3, and they have been generalized to multi-stage structure with both mass and stiffness mistuning in Chapter 4.

The generalized mistuned equation of motion (Equation (4.18)) is reminded here:

$$-\omega^2\left[\mathbf{I}+\sum_{s=1}^{S}\sum_{n=1}^{N_s}\mathbf{Q}_{ns}{}^T\,\mathrm{diag}_{r\in R}\left(\mu^{\delta}_{ns,r}\right)\mathbf{Q}_{ns}\right]\mathbf{p} + (1+i\gamma)\left[\mathbf{\Lambda}_0+\sum_{s=1}^{S}\sum_{n=1}^{N_s}\mathbf{Q}_{ns}{}^T\,\mathrm{diag}_{r\in R}\left(\lambda^{\delta}_{ns,r}\right)\mathbf{Q}_{ns}\right]\mathbf{p}=\mathbf{F}\ , \quad (8.17)$$

where

- $\mathbf{I}$ is the identity matrix;
- S is the number of stages;
- N_s is the number of blade of stage s;
- $\mathbf{Q}_{ns}$ is the modal participation factor of blade n ($n = 1, ..., N_s$) of stage s ($s = 1, ..., S$);
- $\mu^{\delta}_{ns,r} = \mathbf{\Phi}^{CB^T}_{s,r}\mathbf{M}^{\delta}_{ns}\ \mathbf{\Phi}^{CB}_{s,r}$, where $\mathbf{\Phi}^{CB}_{s,r}$ is the r^{th} clamped blade eigenvector of stage s and $\mathbf{M}^{\delta}_{ns}$ is the mass perturbation matrix of blade n of stage s;
- $\lambda^{\delta}_{ns,r} = \mathbf{\Phi}^{CB^T}_{s,r}\mathbf{K}^{\delta}_{ns}\ \mathbf{\Phi}^{CB}_{s,r}$ is the eigenvalue deviation of the r^{th} cantilevered blade mode of blade n of stage s, where $\mathbf{\Phi}^{CB}_{s,r}$ is the r^{th} clamped blade eigenvector of stage s and $\mathbf{K}^{\delta}_{ns}$ is the stiffness perturbation matrix of blade n of stage s;

- γ is the damping coefficient (a structural damping is considered);
- $\mathbf{\Lambda}_0$ is the stiffness matrix defined in tuned modal coordinates i.e., a diagonal matrix that contains the square eigenfrequencies of the tuned system;
- $\mathbf{p}$ is vector of modal coordinates;
- $\mathbf{F}$ is the modal forced vector.

Posing

$$\Delta\hat{\mathbf{M}} = \sum_{s=1}^{S}\sum_{n=1}^{N_s} \mathbf{Q}_{ns}{}^{T} \operatorname{diag}_{r\in R}\left(\mu^{\delta}_{ns,r}\right) \mathbf{Q}_{ns} \ , \tag{8.18}$$

and

$$\Delta\hat{\mathbf{K}} = (1+i\gamma)\sum_{s=1}^{S}\sum_{n=1}^{N_s} \mathbf{Q}_{ns}{}^{T} \operatorname{diag}_{r\in R}\left(\lambda^{\delta}_{ns,r}\right) \mathbf{Q}_{ns} \ , \tag{8.19}$$

the formulation of Equation (8.17) can be simplified as

$$-\omega^2\left[\mathbf{I}+\Delta\hat{\mathbf{M}}\right]\mathbf{p} + \left[(1+i\gamma)\,\mathbf{\Lambda}_0 + \Delta\hat{\mathbf{K}}\right]\mathbf{p} = \mathbf{F} \ . \tag{8.20}$$

The forced vector in Equation (8.20) can be decomposed as

$$\mathbf{F} = \mathbf{F}^m + \mathbf{F}^w \ , \tag{8.21}$$

where $\mathbf{F}^m$ is the aerodynamic modal force due to blade motion, and $\mathbf{F}^w$ is the external excitation modal force (such as wake passing). The blade modal forces $\mathbf{F}^m$ and $\mathbf{F}^w$ can be written as [56]

$$\mathbf{F}^m = \mathbf{A}^m \ \mathbf{p} \ , \tag{8.22}$$

with

$$\mathbf{A}^m = \begin{bmatrix} a_1 & & & \\ & a_2 & & \\ & & \ddots & \\ & & & a_{\sum N_s} \end{bmatrix} \ , \tag{8.23}$$

and

$$\mathbf{F}^{w} = \begin{bmatrix} w_1 \\ w_2 \\ \vdots \\ w_N \end{bmatrix} . \tag{8.24}$$

The terms a_r ($r = 1, ..., \sum N_s$) in the aerodynamic matrix $\mathbf{A}^m$ can be determined from any unsteady aerodynamic theory including the latest 3D, viscous, multistage codes. The detailed computation of the aerodynamic coefficient can be found in [175]. The coefficients a_r can also be retrieved analytically for an isolated family of modes (i.e., the frequency range of the considered family is separated from those of other families), if the strain energy is mainly located in the blades, and if the mode shapes are not significantly changed by mistuning comparing to the tuned case. The theoretical developments are given in [175].

In the same way, w_r are complex modal force coefficients, resulting from an external aerodynamic excitation, such as wake passing. To simplify the model, it is assumed that the mistuned frequencies are small perturbations of the tuned blade frequencies and that the blade mode shape is unchanged. The aerodynamic coefficients are treated as being independent of blade mistuning.

Then, a mistuning matrix $\hat{\mathbf{A}}$ is defined as [184]

$$\hat{\mathbf{A}} = \Delta\hat{\mathbf{K}} - \mathbf{\Lambda}_0 \, \Delta\hat{\mathbf{M}} . \tag{8.25}$$

Introducing the mistuning matrix $\hat{\mathbf{A}}$ and Equation (8.22) in Equation (8.20), one obtains

$$\left[-\omega^2 \mathbf{I} + (1 + i\gamma) \, \mathbf{\Lambda}_0 + \hat{\mathbf{A}}\right] \mathbf{p} = \mathbf{A}^m \, \mathbf{p} + \mathbf{F}^w . \tag{8.26}$$

Based on Equation (8.26), the flutter eigenvalue problem can be written as

$$\left[(1 + i\gamma) \, \mathbf{\Lambda}_0 + \hat{\mathbf{A}} - \mathbf{A}^m - \omega^2 \mathbf{I}\right] \mathbf{p} = \mathbf{0} . \tag{8.27}$$

The solution of the forced response problem is

$$\mathbf{p} = \left[(1 + i\gamma) \, \mathbf{\Lambda}_0 + \hat{\mathbf{A}} - \mathbf{A}^m - \omega^2 \mathbf{I}\right]^{-1} \mathbf{F}^w . \tag{8.28}$$

8.5 Studied structure

The considered structure is a mono-stage academic blisk. The structure totalizes 24 blades. The considered family of modes is the first one i.e., the first bending (1B) mode of the blade.

The aerodynamic modal forces are computed using a CFD code. The value of the forces used in this study are obtained from computations performed at Duke University by the Professor Kielb. These values are obtained for a structure with a similar number of blades and a similar SAFE diagram in terms of frequencies. The real and imaginary parts of the aerodynamic modal forces are shown in Figure 8.7 for each number of nodal diameters. The corresponding influence coefficients of the aerodynamic modal forces are given in Figure 8.8.

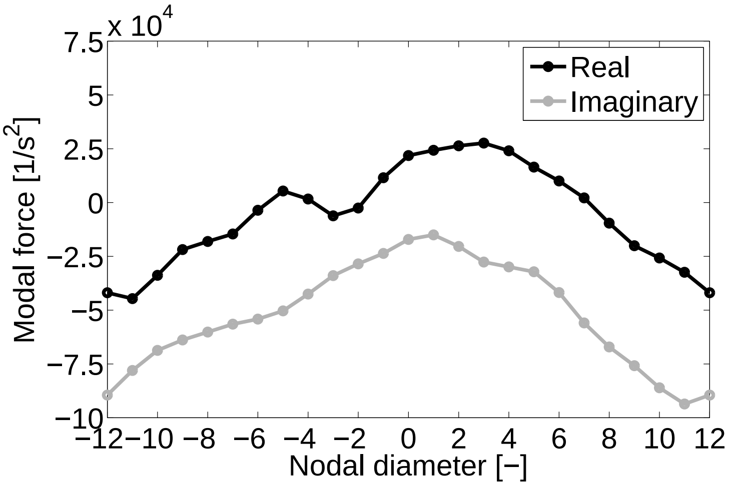

Figure 8.7: Unsteady aerodynamic modal forces.

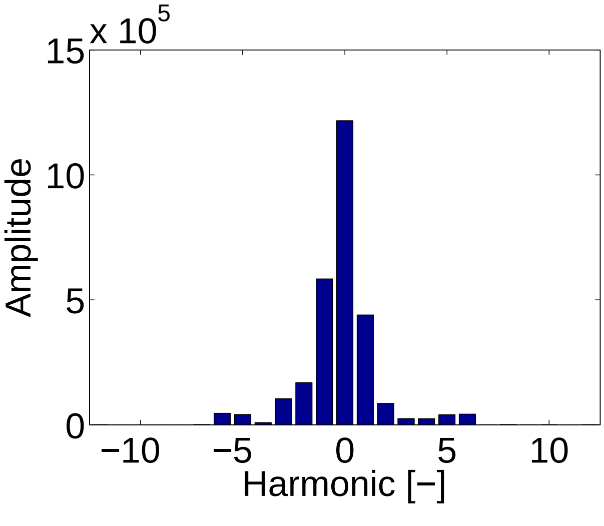

Figure 8.8: Influence coefficient of the unsteady aerodynamic modal forces.

8.6 Structural and aerodynamic coupling

In this Section, the relative importance of the structural and the aerodynamic coupling is evaluated as a function of the drum stiffness.

In order to measure this relative importance, three frequency spread parameters are defined:

- The aerodynamic frequency spread Δf_a is defined as

$$\Delta f_a = \frac{f^a_{max} - f^a_{min}}{f^a_{mean}} \ , \tag{8.29}$$

  where f^a_{max}, f^a_{min} and f^a_{mean} are respectively the maximum, minimum and mean frequencies when only the aerodynamic coupling is considered.

- The structural frequency spread Δf_s is defined as

$$\Delta f_s = \frac{f^s_{max} - f^s_{min}}{f^s_{mean}} \ . \tag{8.30}$$

  where f^s_{max}, f^s_{min} and f^s_{mean} are respectively the maximum, minimum and mean frequencies when only the structural coupling is considered.

- The relative frequency spread between the structural and aerodynamic coupling C is defined as

$$C = \frac{\Delta f_a}{\Delta f_a + \Delta f_s} \ . \tag{8.31}$$

Different values of Young's modulus are used for the drum in order to assess the influence of the drum flexibility on the frequency response function (FRF). The aim is to evaluate the error performed when considering only the structural coupling or only the aerodynamic coupling comparing to the solution with both coupling terms. Therefore, the relative importance of the structural and aerodynamic coupling with the drum flexibility is shown in this Section. For each value of the Young's modulus, the corresponding Δf_s and Δf_a are evaluated by computing the aeroelastic eigenvalues respectively when considering only the structural coupling and only the aerodynamic coupling.

Table 8.1 gives the obtained frequency spread parameters Δf_s, Δf_a and C for different values of Young's modulus. The considered range of variation for the Young's modulus is chosen extremely large to get extreme cases i.e., a very stiff drum ($C \to 100$ %) and a very soft drum ($C \to 0$ %). Figure 8.9 shows graphically the evolution of C with the drum Young's modulus.

Drum stiffness [MPa]	Δf_a [%]	Δf_s [%]	C [%]
30 000	42.7	0.57	1.3
71 000	28.4	0.57	2.0
300 000	10.3	0.57	5.2
710 000	4.8	0.57	10.5
3 000 000	1.2	0.57	31.9
7 100 000	0.5	0.57	52.3
30 000 000	0.1	0.57	82.1
71 000 000	0.05	0.57	91.6
7 100 000 000	0.0	0.57	99.6
71 000 000 000	0.0	0.57	99.6

Table 8.1: Frequency spread parameters.

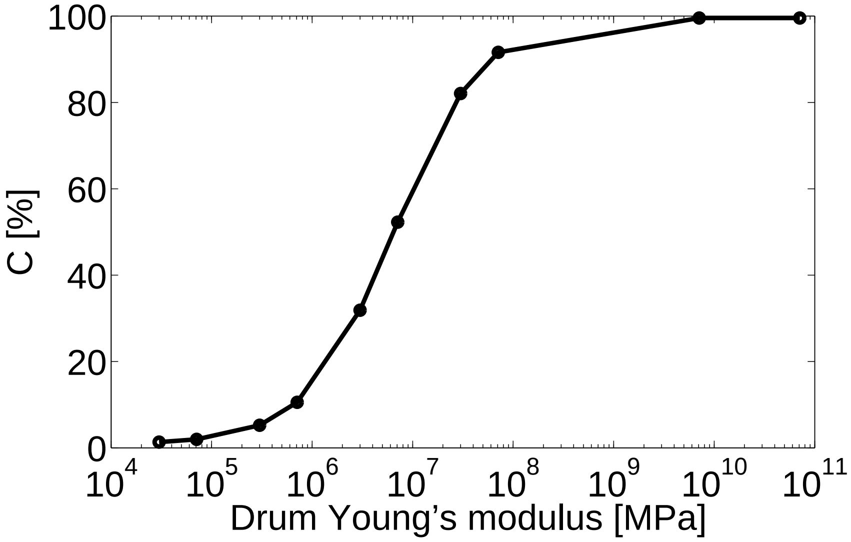

Figure 8.9: Correspondence between the drum Young's modulus and the C value.

A forced excitation is applied on the structure to compute the FRF. The chosen excitation has one excitation per blade at the right corner of the blade tip, and follows an engine order of 5. A mistuning of 1 % is considered. 20 samples are generated using Monte Carlo simulations. The maximum of the FRFs obtained with the different Young's modulus are shown in Figure 8.10. The FRFs obtained on each blade when considering only the structural coupling, only the aerodynamic coupling, and both coupling terms are superimposed on each graph.

Errors can be computed for each value of Young's modulus. More particularly, the error when considering only the structural coupling compared to the results with both structural and aerodynamic coupling terms is computed, as well as the error when considered only the aerodynamic coupling comparing to the case with both structural and aerodynamic coupling terms.

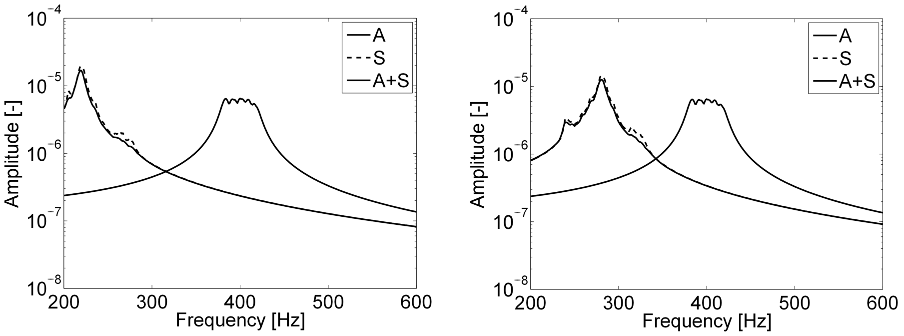

(a) $E = 3\ 10^4$ MPa - $C = 1$ %
(b) $E = 7.1\ 10^4$ MPa - $C = 2$ %

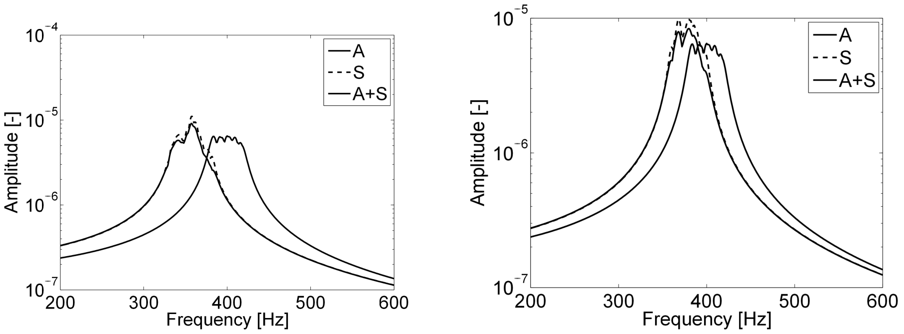

(c) $E = 3\ 10^5$ MPa - $C = 5$ %
(d) $E = 7.1\ 10^5$ MPa - $C = 11$ %

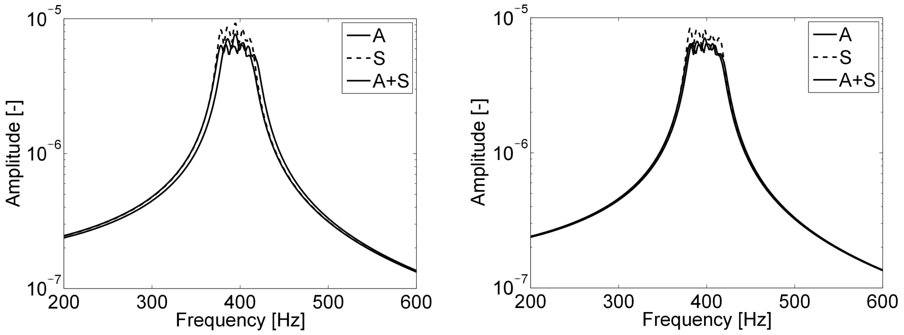

(e) $E = 3\ 10^6$ MPa - $C = 32$ %
(f) $E = 7.1\ 10^6$ MPa - $C = 52$ %

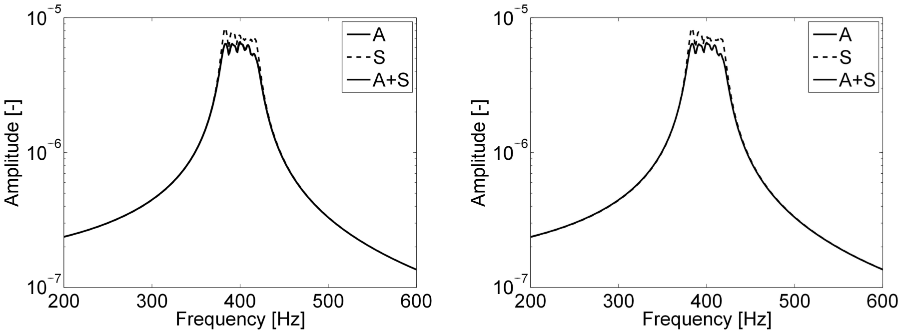

(g) $E = 3\ 10^7$ MPa - $C = 82$ %
(h) $E = 7.1\ 10^7$ MPa - $C = 92$ %

Figure 8.10: Comparison between the FRF with only aerodynamic coupling (A), with only structural coupling (S), and with both structural and aerodynamic coupling (A+S) for different values of the drum Young's modulus.

The first used error definition is based on the maximum response of each blade, such as

$$E^s = \sqrt{\frac{1}{N}\sum_{n=1}^{N}\left(e_n^s\right)^2} \qquad \text{and} \qquad E^a = \sqrt{\frac{1}{N}\sum_{n=1}^{N}\left(e_n^a\right)^2}\ , \tag{8.32}$$

with

$$e_n^s = \text{abs}\left(\max\left(\mathbf{x}_n^s\right) - \max\left(\mathbf{x}_n^b\right)\right) \qquad \text{and} \qquad e_n^a = \text{abs}\left(\max\left(\mathbf{x}_n^a\right) - \max\left(\mathbf{x}_n^b\right)\right)\ , \tag{8.33}$$

where E^s and E^a are the global error respectively for the structural coupling only and aerodynamic coupling only case, N is the total number of blades of the structure, $\mathbf{x}_n^s$ and $\mathbf{x}_n^a$ are respectively the response of blade n ($n = 1, ..., N$) for the structural coupling only or aerodynamic coupling only case, and $\mathbf{x}_n^b$ is the response of blade n when both coupling terms are considered. The obtained results for this first definition of the error are presented in Figure 8.11. Three mistuning levels are considered: 1, 3 and 5 %. 20 samples are considered and the mean error is plotted.

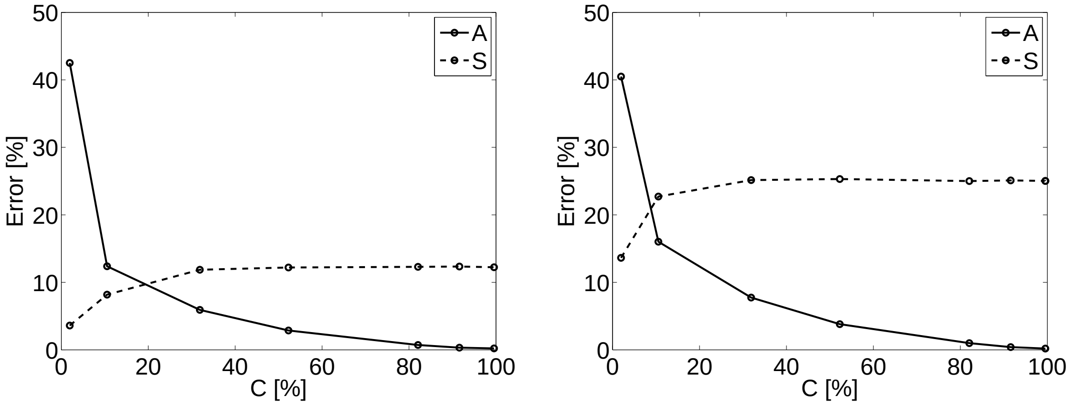

(a) 1 %

(b) 3 %

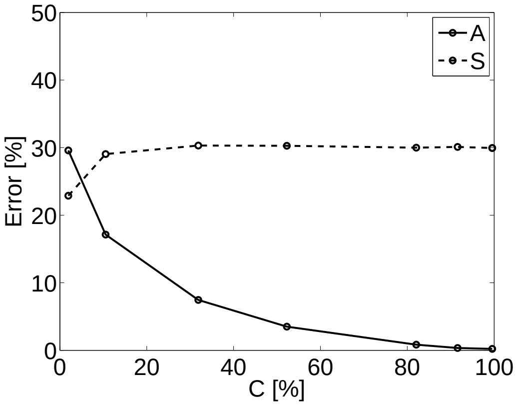

(c) 5 %

Figure 8.11: Evolution of the first definition of the error with C for 1 % (a), 3 % (b) and 5 % (c) of mistuning.

It can be seen in Figure 8.11 that for a soft drum ($C \to 0$ %), the error when considering only structural coupling decreases. For a very stiff drum ($C \to 100$ %), only the aerodynamic coupling term can be taken into account in the model, since the corresponding error tends to 0. For intermediate values of C, the two error lines cross at $C = 20$ % for 1 % of mistuning, at $C = 10$ % for 3 % of mistuning and at $C = 6$ % for 5 % of mistuning (these values are included in Table 8.2). For C lower than these thresholds (thresholds which decrease with the mistuning percentage), the structural coupling is dominant, and for C higher than these thresholds, the aerodynamic coupling is dominant.

However, this definition has the drawback that, since it is based only on the amplitude, a global frequency shift of the FRF cannot be perceived. Therefore, a second definition is established, taking into account errors due to frequency shift. The second definition is written as

$$E^s = \sqrt{\frac{1}{N}\sum_{n=1}^{N}\left(e_n^s\right)^2} \qquad \text{and} \qquad E^a = \sqrt{\frac{1}{N}\sum_{n=1}^{N}\left(e_n^a\right)^2} \;, \tag{8.34}$$

with

$$e_n^s = \sum_{\omega} \mathbf{x}_n^b\left(\omega\right) \; \text{abs}\left(\max\left(\mathbf{x}_n^s\left(\omega\right)\right) - \max\left(\mathbf{x}_n^b\left(\omega\right)\right)\right) \;, \tag{8.35}$$

and

$$e_n^a = \sum_{\omega} \mathbf{x}_n^b\left(\omega\right) \; \text{abs}\left(\max\left(\mathbf{x}_n^a\left(\omega\right)\right) - \max\left(\mathbf{x}_n^b\left(\omega\right)\right)\right) \;, \tag{8.36}$$

where ω is the frequency.

Figure 8.12 shows the error obtained with the second definition. Three mistuning levels are again considered (1, 3 and 5 %), with 20 samples. The same behavior is observed than previously with first definition i.e., the structural coupling is dominant for low C values and the aerodynamic coupling is dominant for high C values. The difference comparing to the first definition is that the crossing between both curves occurs at higher C values: at $C = 72$ % for 1 % of mistuning, at $C = 67$ % for 3 % of mistuning and at $C = 64$ % for 5 % of mistuning (these values are also included in Table 8.2 for this second definition). Since the second definition takes into account the frequency shift between both curves by weighting the error by the amplitude of the FRF, it better reflects the error between both curves.

Mistuning [%]	Definition 1 [−]	Definition 2 [−]
1	20	72
3	10	67
5	6	64

Table 8.2: Intersection between the curves of the errors with only structural or aerodynamic coupling terms.

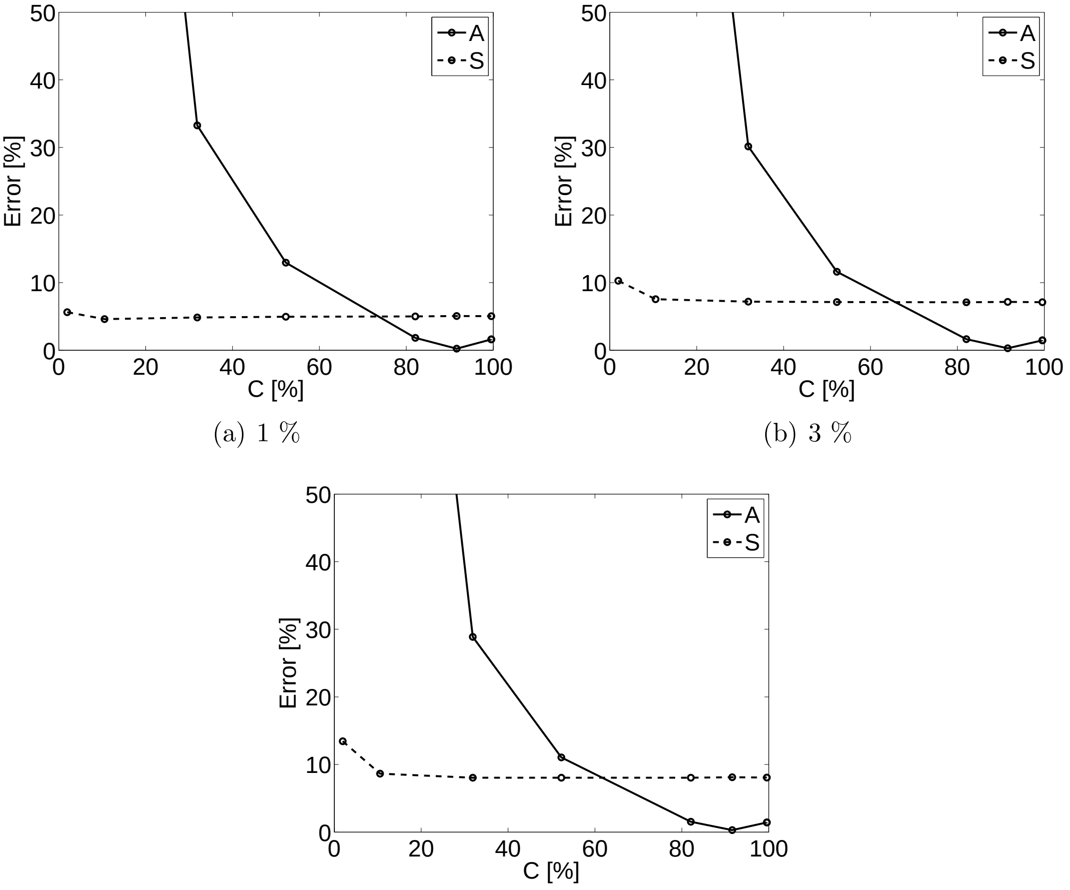

(a) 1 %

(b) 3 %

(c) 5 %

Figure 8.12: Evolution of the second definition of the error with C for 1 % (a), 3 % (b) and 5 % (c) of mistuning.

8.7 Influence of errors in the aerodynamic coefficients

The aerodynamic coefficients used in the aerodynamic matrix $\mathbf{A}^m$ (Equation 8.23) are obtained from a CFD computation, which requires a high CPU time. During the design process of the blades, CFD computations have to be performed for each change in blade geometry. Since these multiple analyses require high computation times and resources, an evaluation of the sensibility of the FRF to noise in the aerodynamic coefficients is performed here.

Figure 8.13 shows the evolution of the error on the FRF (definition of the error in Equation 8.32) for different C values with an increasing noise in the aerodynamic coefficients. The academic blisk with 1 % of mistuning is considered. An increase of the error on the FRF with the noise percentage is observed, and the system is more sensitive to noise for low C values. For $C < 10$ %, an error of 50 % in the aerodynamic coefficients leads to 5 % of error on the FRF. For $C > 10$ %, 10.5 % of error on the FRF is obtained for an error of 50 % in the aerodynamic coefficients.

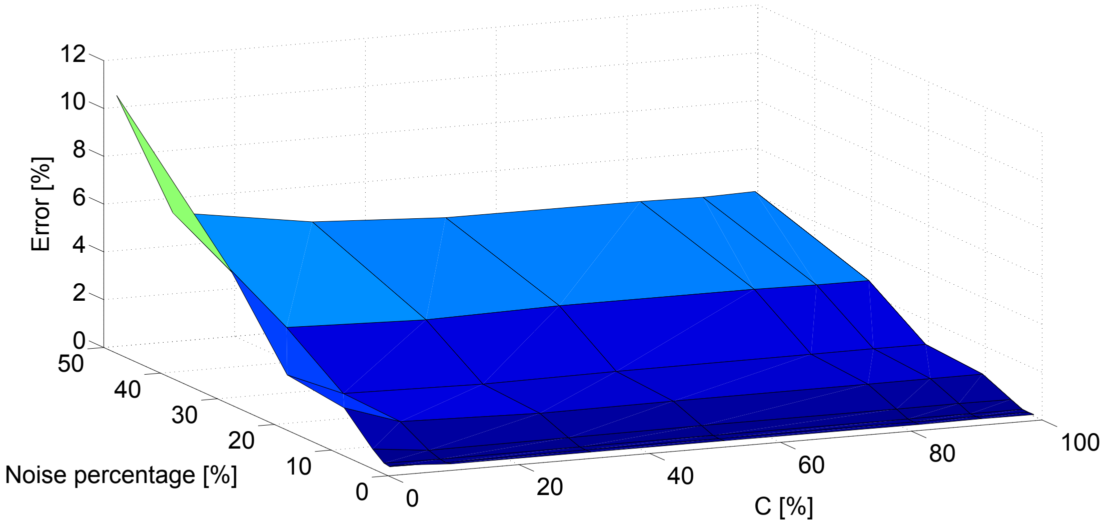

Figure 8.13: Evolution of the error on the FRF for different C values with an increasing noise in the aerodynamic coefficients.

8.8 Conclusion

In addition to the structural coupling, the bladed disks are submitted in service to aerodynamical effects. The aerodynamics adds damping due to the airflow traveling through the engine. The influence of the structural and aerodynamic damping terms has been analyzed here in terms of the error on the forced response. Numerical analyses have been performed on an academic blisk. Different drum stiffnesses have been studied to evaluate the relative influence of both damping terms in each case.

The numerical results demonstrate that the structural coupling term can be neglected for a very stiff structure, and the aerodynamic coupling term can be neglected for a very soft drum. For intermediate values, both coupling terms have to be taken into account in the model. For the studied value, the nominal value of Young's modulus corresponds to a case where both coupling terms have to be taken into account. Therefore, to compute a precise quantitative value for the amplification factor of the forced response, the aerodynamic damping cannot be neglected in the analysis.

The sensibility of the obtained frequency response functions to noise in the aerodynamic coefficients is performed. The CFD models used to obtain these coefficients require high computational times, and in the design process, different models have to be launched because of blade geometry modifications. The analysis shows a higher sensibility for low drum stiffness.

Chapter 9

Conclusions and perspectives

Manufacturing of one-piece multi-stage structures significantly increases the influence of the interstage coupling that cannot be neglected anymore in the numerical models. The effects of mistuning are exacerbated due to the low damping level of the structure, to the higher drum flexibility, and to coupling between the blades and the drum. As a consequence it appears that multi-stage structures may present higher amplification factors than those related to single stage configuration. Therefore, the ability of characterizing mistuning in multi-stage bladed structures is important since the dynamic behavior of the structure is strongly affected by mistuning.

9.1 Contributions of the thesis

Two aspects have been investigated in this work: experimental identification of mistuning in multi-stage structures, and numerical analysis and developments to reduce computational times for multi-stage systems of bladed disks.

9.1.1 Experimental identification of mistuning in multi-stage structure

An experimental validation and extension of the CMM mistuning identification method has been proposed in the thesis. A testing procedure has been developed, using a base excitation and one measurement point per blade with a laser vibrometer. The experimental tests have been conducted on mock-up mono-stage and two-stage academic bladed structures. The validation of the test procedure and of the obtained identified mistuning for the two structures has been performed by adding mass perturbations on some blades of the structures. Both stiffness and mass perturbations have been successfully retrieved.

The experimentally identified mistuning has been compared for both mono-stage and multi-stage structures with their variations in blades geometry. An optical geometry measurement system was used to retrieve the exact profile of each blade for each structure. It has been demonstrated that the resulting differences between the geometrical and the experimentally identified mistunings were due to non-uniformities in the clamping conditions.

On one hand, the geometry measurement has the advantage to provide an accurate description of the geometry of the entire structure. The feasibility and the rapidity of the measurements depend on the geometry complexity of the studied structure. The obtained geometrical characteristics are independent of the frequency range of interest. The optical measurement technique is well adapted in the case of blisk, with an homogeneity of the material properties. The drawback of the method is that these measurements cannot get the stiffness induced by the connections between the blades and the drum, which introduce additional mistuning. Moreover, non-homogeneities in the material properties cannot be detected. On the other hand, the identification of mistuning using vibration measurements is performed in a specific frequency range, and the required measurement time increases with the number of blades. But this method has the advantage to take into account mistuning induced by the connections between the blades and the drum. Both mass and stiffness non-uniformities can be treated. The mistuned reduced order model associated to the measured mistuning requires low computational times.

Numerous factors, such as connections between the blades and the drum, wear during use, or clamping conditions, introduce in practice additional mistuning in the structure. The actual mistuning of the structure in real conditions differ from the one experimentally identified in the lab. This work evidences the importance of characterizing the level of mistuning induced during the manufacturing and assembly processes and the interest of using probabilistic approaches since the knowledge of the exact mistuning is illusory. Probabilistic approaches enable to evaluate the sensitivity of the amplification of the forced response with respect to small changes in the considered mistuning.

9.1.2 Numerical analyses and developments

The CMM reduced order modeling method is widely used to predict the amplification of the forced response in mistuned bladed disks. The nonparametric modeling technique differs from the parametric CMM method by the definition of the introduced mistuning. The nonparametric probabilistic approach has the advantage to model both data and model uncertainties while parametric approaches only take into account data uncertainties. The nonparametric approach has been extended in the thesis to compute forced response analysis in multi-stage structures. A combination of these two modeling techniques has also been proposed to take the advantages of both methods with reduced computational times. The three methods have been applied and compared on a two-stage one-piece academic structure. The proposed approach has shown intermediate results between the nonparametric and the parametric approach.

Multi-stage analyses for industrial structures require high computational times and resources. In the industry, mono-stage analyses are still performed. A study of the influence of considering a mono-stage or a multi-stage analysis on the predicted amplification factor results has been conducted. It has been shown that the difference between both analyses was proportional to the energy localized in the drum for the considered modes in the frequency range of interest. An analytical analysis has been performed on a lumped mass model with two stages. The energy localized in the drum can be computed using equivalent parameters. The proposed approach for quantifying the need of a multi-stage approach has been applied on an academic structure. Then, an analysis of the number of required harmonics has been conducted to further reduce the needed computation times and resources. The results have shown that considering five harmonics around the engine order lead to accurate results in terms of amplification factor prediction.

In service, the bladed disks are submitted to aerodynamical effects in addition to the structural coupling, which adds damping due to the airflow traveling through the engine. An analysis of the relative importance of the aerodynamic and structural coupling has also been conducted. It has been shown that the aerodynamic coupling term is dominant for a very stiff structure, while the structural coupling term is dominant for a very soft drum. For intermediate stiffness values, both coupling terms have to be taken into account in the model. The nominal value of Young's modulus for the studied academic structure corresponds to a case where both coupling terms have to be taken into account. Therefore, to predict accurate amplification factors, this additional aerodynamic term cannot be neglected. Because of the high computational times of CFD analyses, a sensitivity analysis of the frequency response function with aerodynamic coefficients variation has been performed. The analysis shows a higher sensibility for low drum stiffness.

9.2 Perspectives

Some perspectives are suggested for future works:

- The proposed identification method and testing procedure was applied in the framework of this thesis in a low frequency range. The perspective of the work is to apply the mistuning identification method in a higher frequency range, with more coupling involved between the different stages and highly localized modes. A higher number of measurement points would be required. The fixation system should be adapted to avoid introducing additional mistuning.

- In the case of blisks, the structural damping is extremely low. A base excitation is well adapted for these structures because a large number of modes can be detected in the stabilization diagram. For structures with higher damping, another excitation system can be used to study modes with high numbers of nodal diameters.

- The experimental tests have been conducted on a two-stage academic structure. Future works would be to apply to same testing procedure on industrial structures, and possibly with more than two stages.

- The proposed approach to determine when multi-stage models are necessary (i.e., mono-stage analyses lead to large errors) has been applied in this work on an academic structure. The approach should nevertheless be applied on different structures to be fully validated. Moreover, no rotational speed has been considered in this analysis. The impact of the gyroscopic effect on the obtained conclusions can be further studied.

- In the thesis, the influence of mistuning in multi-stage systems of bladed disks has been analyzed in terms of amplification factors. A perspective would be to analyze the influence of mistuning in terms of constraints in the blades.

- The analysis of the aerodynamic effects on the predicted forced response and amplification factor can be extended for multi-stage structures.

Appendix A

Design and presentation of the studied structures

Two academic structures with a simplified geometry have been designed in order to perform numerical and experimental analyses in the thesis. The first structure is a mono-stage structure, and the second one a two-stage structure. The bottom stage of the two-stage structure is identical to the mono-stage structure. Both are mono-bloc structures.

A.1 Introduction

As the first step of this work, two one-piece academic bladed structures have been designed in order to perform numerical and experimental analyses. Since one of the final aim of the thesis is the identification of mistuning in multi-stage and mono-bloc structures, the design of a two-stage structure has been first performed, taking into account several constraints. For example, these two structures have a simplified geometry to better understand the experimental results. Moreover, in order to compare the behavior of a mono-stage and multi-stage structure, the mono-stage stage structure has been built as identical to the bottom stage of the two-stage structure. Both structures are mono-bloc. The different criteria for the design of these academic structures are presented. Then, a detailed presentation of both mono-stage and multi-stage structures is given. More particularly, the geometric and material characteristics of each structure are described. Both finite element models done using the software SAMCEF [120] are presented, and their vibration properties are detailed.

A.2 Design of the academic bladed structures

The aim of this work is to perform numerical analysis and experimental validation on one-piece structures. First, the tests will be performed on a mono-stage bladed structure, and then on a two-stage structure. In order to observe the effect of the addition of a second stage, the bottom stage of the two-stage structure and the mono-stage structure are identical.

Since one of the final aim of the thesis is the identification of mistuning in multi-stage structure, the design of a two-stage structure has been first performed, taking into account several constraints. The mono-stage structure is the first stage of the selected multi-stage design. The different criteria that have been taken into account for the design of the multi-stage structure are:

- A simple structure from the manufacturing point of view → the geometry of the blade is chosen to be in the same horizontal plane, without any angle of attack. The dimension of the structure is limited by the maximal size allowed in the machines available in the lab workshop.

- Frequencies lower than 2500 Hz for the first mode families in order to simplify the experimental tests → to reduce the eigenfrequencies of the system, the blades are designed to be larger at their tip, which increases their mass and decreases the eigenfrequencies.

- The presence of veering zones in order to reproduce the behavior of an industrial structure → a thin thickness of the drum and the blades is considered to increase the coupling between the blade and the participation of the drum.

- Simple boundary conditions that respect the cyclic symmetry property of the structures → the structure is clamped by its basis. A 360° clamping is considered in the finite element model, and in the experimental set-up, the structure is clamped using the same number of fixation points than the number of sectors of the bottom stage.

- A simple access to measure the response of the structure using a vibrometer laser (non-contacting measurement method) → the blades of the bottom stage are longer than the blades of the top stage, and the top stage is the one that contains the less number of blades.

- An easy way to control the mistuning on the structure → small masses can be easily added on each blade to simulate intentional mistuning in the structure.

- The cost → the chosen material is aluminium (commercially available grade).

The CAD of the finally selected design of both mono-stage and multi-stage structures are presented in Figures A.1(a) and A.1(b).

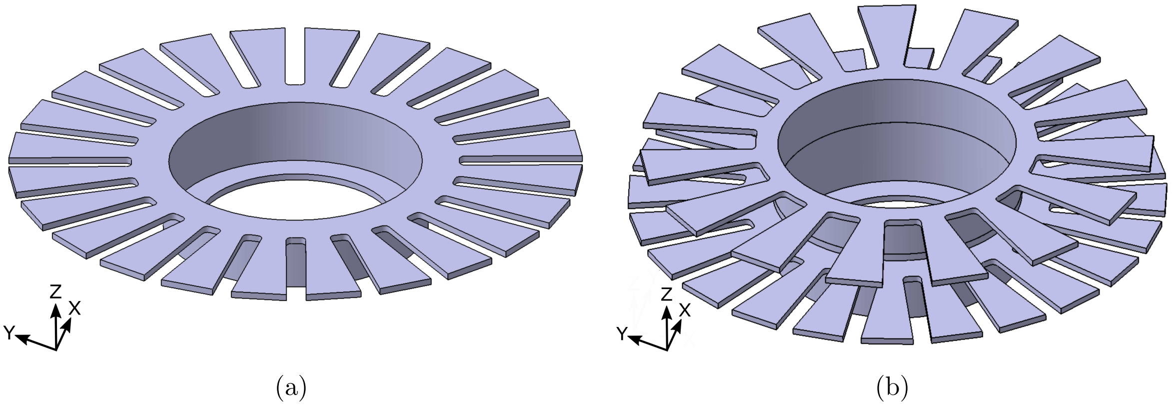

(a)

(b)

Figure A.1: CAD of the mono-stage (a) and multi-stage (b) academic bladed structure.

The material and geometric properties are given in Table A.1 for both stages. The detailed geometry is given in the Appendix B.

	Stage 1	Stage 2
Number of sectors (N) [-]	24	15
Young's modulus [MPa]	71 000	71 000
Density [kg/m^3]	2700	2700
External diameter [mm]	420	400
Internal diameter [mm]	186	186
Thickness [mm]	5	5
Height [mm]	53	46
Blade length [mm]	86	86
Blade width [mm]	40	45

Table A.1: Material and geometric properties of the multi-stage academic structure.

A.3 Presentation of the mono-stage academic structure

In this Section, the mono-stage academic structure is presented. The finite element model of the structure is described, and the dynamical characteristics are given using the SAFE diagram and the repartition of the strain energy in the different parts of the structure for each mode. The clamped blade eigenfrequencies are also computed.

A.3.1 Construction of the finite element model

A finite element model of the tuned structure has been constructed using the FE software SAMCEF [120]. The cyclic symmetry property has been applied to reduce the computational time and resources. In order to apply the cyclic symmetric property, the SAMCEF command is

```
.ZYG GROUP "NODESLEFTSURFACE" "FACESRIGHTSURFACE"
     NS 24 AXE Z WAVE (/NWAVE)
```

where `24` stands for the number of sectors, `Z` for the axis of symmetry (axial direction), `(/NWAVE)` is the considered number of nodal diameters, `NODESLEFTSURFACE` is the set of nodes on the left boundary, and `FACESRIGHTSURFACE` is the set of faces on the right boundary.

An analysis on the mesh refining can be found in the Appendix C, in order to get accurate modal properties with reduced computational times. The reference sector of the selected mesh is shown in Figure A.2(a). The mesh totalizes 8 496 degrees of freedom for the reference sector and is made of hexahedral volumic elements. Then, a recombined mesh (360°) is shown in Figure A.2(b), with the reference sector in dark gray. This 360° finite element model will be used for some validations when introducing a different mistuning for each blade, which breaks the cyclic symmetric property of the structure.

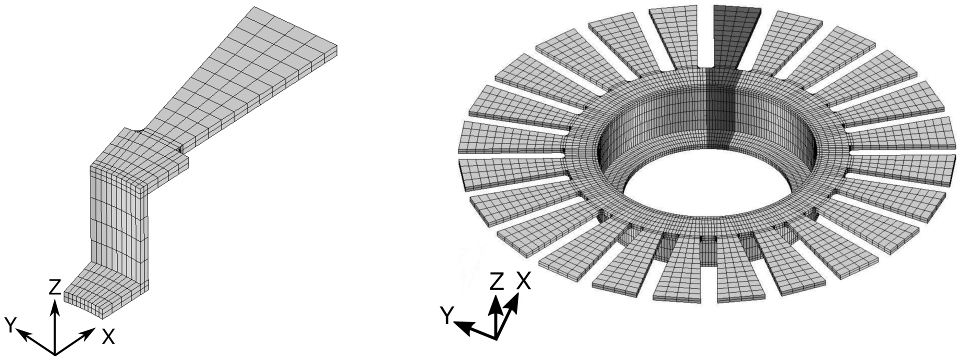

(a) (b)

Figure A.2: Finite element model of the reference sector of the academic structure (a) and the recombined finite element model with the reference sector in dark gray (b).

A.3.2 SAFE diagram

Based on the cyclic symmetric finite element model, the SAFE diagram (Singh's Advanced Frequency Evaluation diagram i.e., the eigenfrequencies in function of the number of nodal diameters) of the mono-stage structure is constructed, as shown in Figure A.3. The maximum number of nodal diameters is $\frac{N}{2} = 12$. The 5 first eigenfrequencies for each number of nodal diameters are plotted to get a good knowledge of the complete behavior of the tuned structure at low frequencies and for all nodal diameters. The information about the expected dynamic behavior of the structure enables to guide the experimental tests which are then performed to identify mistuning in the structure. A classification on the mode shapes of each eigenmodes has been performed. Different symbols are used in order to distinguish the type of mode shape, such as bending modes (1B, 2B...), torsion modes (1T, 2T...), plane bending modes...

The two first families of modes are well separated. The first family (● symbol) corresponds to the 1B modes, and the second one to the plane bending modes (★ symbol). These two curves are relatively horizontal since these modes are blade modes (no participation of the drum). Then, for low numbers of nodal diameters, 2B modes ($*$ symbol) appear and 1T modes (+ symbol) follow at higher frequencies. For large numbers of nodal diameters, it is the opposite, 2B modes have higher frequencies than 1T modes. Between 2 and 6 nodal diameters, a transition appears where 1BT modes (× symbol) respond. The curves are again quite horizontal since these modes are blade modes. Then, 2B modes with drum participation appear from 0 to 5 nodal diameters (▼ symbol). Finally, 3B modes (♦ symbol) are observed.

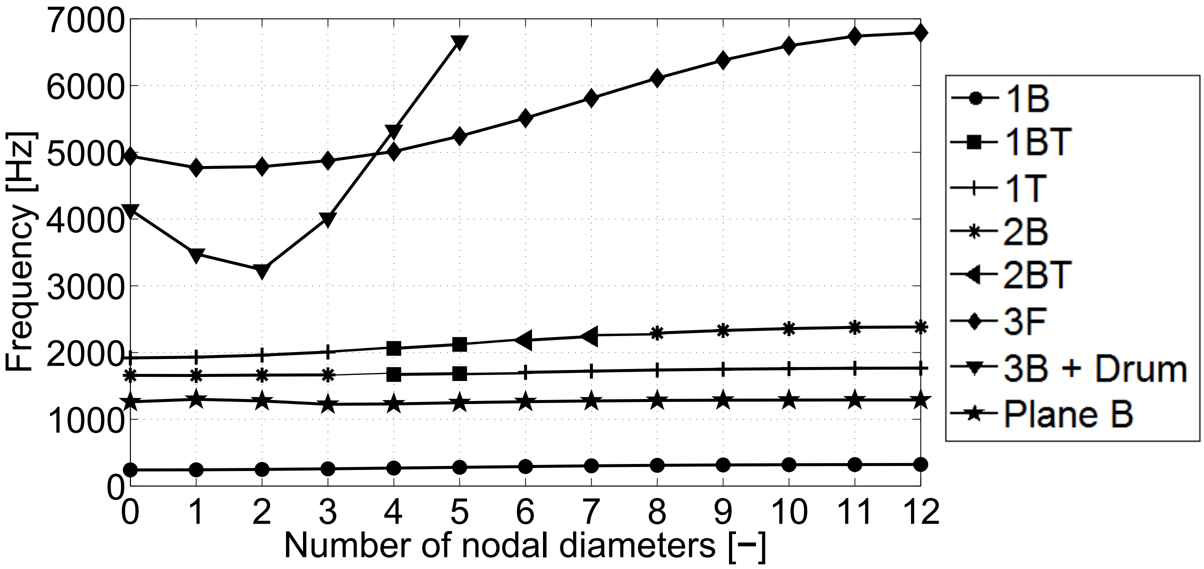

Figure A.3: SAFE diagram of the mono-stage academic structure.

A.3.3 Deformation energy for each mode shapes

In order to assess the participation of the drum and the blades in the mode shapes for an increasing number of nodal diameters, the repartition of the strain energy in the different parts of the structure is evaluated. For this, the structure is divided in three parts: the blades, the horizontal part of the drum, and the vertical part of the drum. These three groups are shown in Figure A.4.

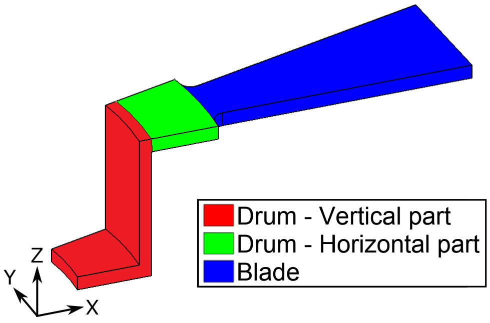

Figure A.4: Division of the structure in three parts (the blades, the horizontal part of the drum, and the vertical part of the drum) to compute the energy percentage in each part.

The energy for each group can be retrieved from the finite element software SAMCEF [120] using the command line `.ALGO ENEIMP 3` .

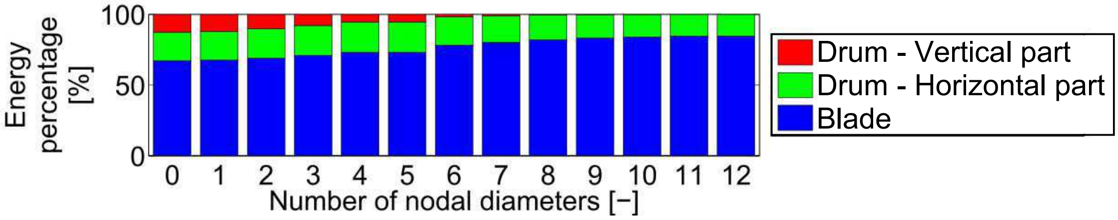

(a) 1B modes

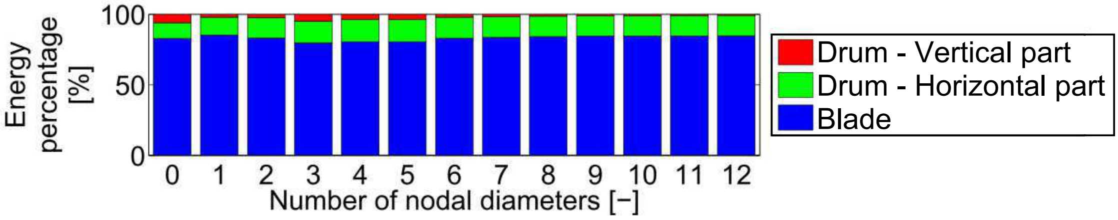

(b) Plane B modes

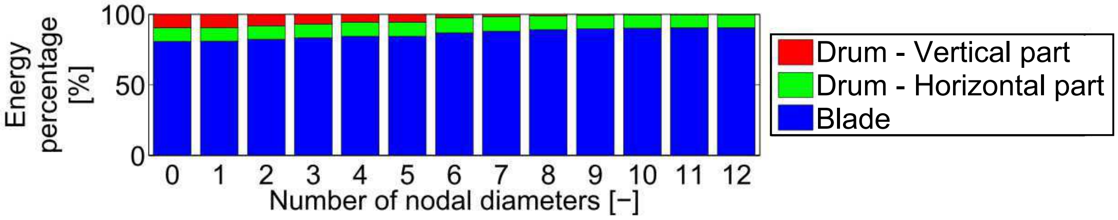

(c) 1BT - 1T modes

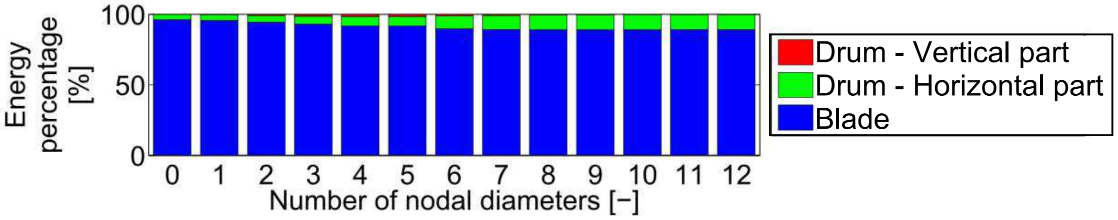

(d) 1T - 2B modes

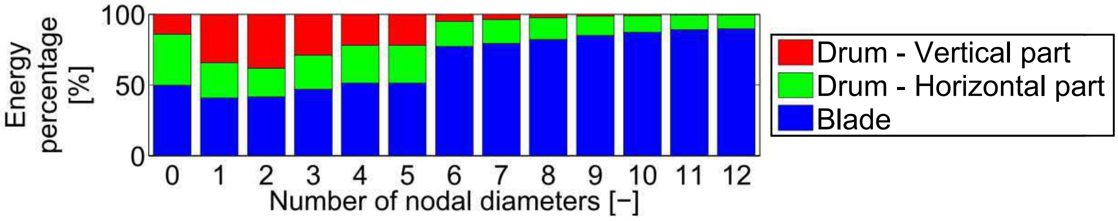

(e) 2B + Drum - 3B modes

Figure A.5: Energy percentage in the blade, the horizontal part of the drum, and the vertical part of the drum for each mode.

Figure A.5 shows the percentage of strain energy in each part, for the modes families of the SAFE diagram (Figure A.3). For the first mode family (i.e., the 1B modes), the vertical part of the drum participates for a low number of nodal diameters, but its contribution tends to 0% when the number of nodal diameters increases. The horizontal part of the drum participates in the mode shapes for all numbers of nodal diameters (the contribution of the horizontal part of the drum for high numbers of nodal diameters will enable to explain why, in Section A.3.4, the eigenfrequencies of our structure are lower than the clamped blade eigenfrequencies). The same global behavior is observed for the second and the third families. The fourth family has no contribution of the vertical part of the drum, and a low contribution of the horizontal part of the drum. Finally, concerning the fifth family of modes, a high contribution of the vertical part of the drum is observed from 0 to 5 nodal diameters. Table A.2 summarizes the participation of each part for different numbers of diameters.

	$0-1$ ND	$2-5$ ND	$6-12$ ND
Blade	×	×	×
Drum horizontal part	×	×	×
Drum vertical part		×	

Table A.2: Participation of the three parts of the structure for different numbers of diameters (ND).

A.3.4 Clamped blade properties

The clamped blade eigenfrequencies are computed. This information will be useful in the thesis since the mistuning of each blade will be defined as the deviation of the clamped blade eigenfrequencies. The clamped blade eigenfrequencies are obtained by clamping the degrees of freedom (DOF) of the drum, as shown in Figure A.6. These clamped blade eigenvectors are useful to apply the identification method in the following Sections. The first mode, at a frequency of 403 Hz, is the 1B mode (Figure A.7(a)). The second mode, corresponding to a frequency of 1560 Hz, is the plane bending mode (Figure A.7(b)). Then, the third mode, at a frequency of 2060 Hz, is the 1T mode (Figure A.7(c)). The fourth mode is a 2B mode with a frequency of 2980 Hz (Figure A.7(d)).

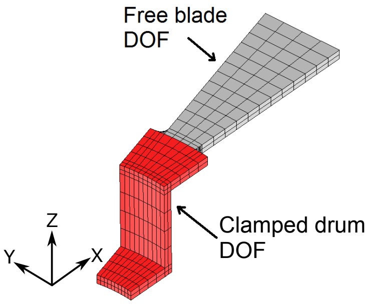

Figure A.6: Clamped sector.

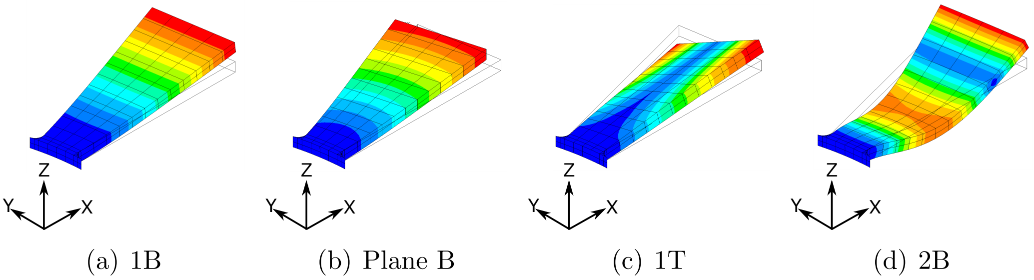

(a) 1B (b) Plane B (c) 1T (d) 2B

Figure A.7: Blade alone 1B mode - 403 Hz (a), Blade alone plane bending mode - 1560 Hz (b), Blade alone 1T mode - 2060 Hz (c), Blade alone 2B mode - 2980 Hz (d).

The clamped blade eigenfrequencies are added on the SAFE diagram in Figure A.8. Theoretically, the eigenfrequencies of the system tend to the clamped blade eigenfrequencies when the number of nodal diameters increases. This is due to the stiffening of the drum for high numbers of nodal diameters modes. Since the drum becomes stiffer, the participation of the drum in the mode shape decreases and the mode shape tend to a mode shape with only blade participation. It can be seen in Figure A.8 that the eigenfrequencies remain lower than the clamped blade eigenfrequencies. This can be explain by the low stiffness of the drum due to its thinness (5 mm thick), which enables a participation of the drum even for a high number of nodal diameters.

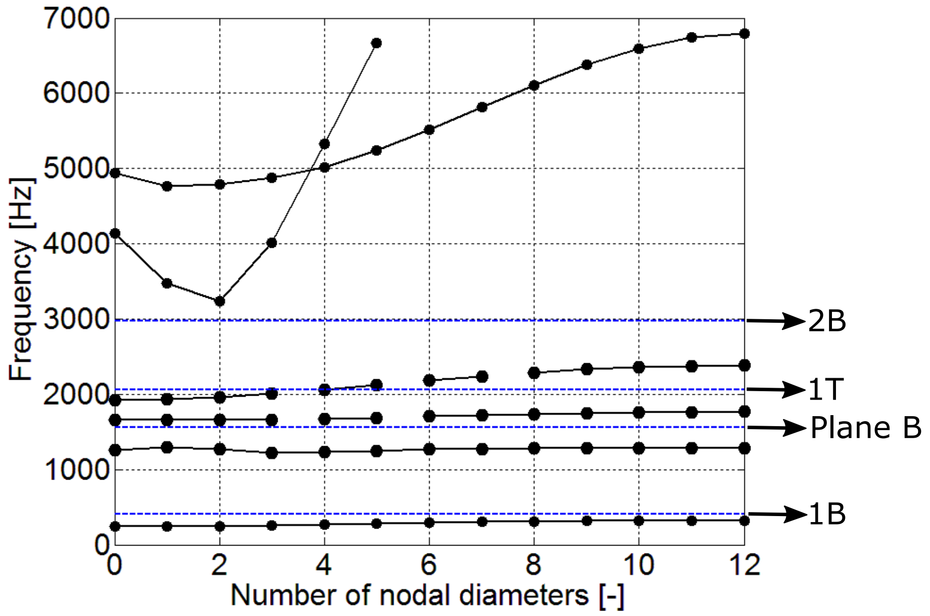

Figure A.8: Clamped blade eigenfrequencies superimposed on the SAFE diagram.

A.4 Presentation of the multi-stage academic structure

In this Section, the multi-stage academic structure is presented. The finite element model of the structure is described, and the dynamical characteristics are given using the SAFE diagram and the repartition of the strain energy in the different part of the structure for each mode. The clamped blade eigenfrequencies are also computed.

A.4.1 Construction of the finite element model

As for the mono-stage structure, a finite element model has been constructed in SAMCEF [120]. The multi-stage cyclic symmetric property was applied to reduce the needed computational resources following Laxalde's method [16,110,111]. The displacement compatibility was also applied between the interstage degrees of freedom of the bottom stage and the top stage. In the SAMCEF finite element software, these two conditions are applied using the following commands

```
.AEL GROUP "ESTAGE1" STAGE 1 SECT 24 L 1
.AEL GROUP "ESTAGE2" STAGE 2 SECT 15 L 1
.ISD AXE Z
     WAVE (/NWAVE) (/NWAVE) MULTIC 1
     GROUP "NODESCONTACTSTAGE1" "FACESCONTACTSTAGE2" ATT 22
.ALGO MULTIC 1
.SYC
```

where `ESTAGE1` and `ESTAGE2` are respectively the set of elements of stage 1 and stage 2, 24 and 15 stand for the number of sectors of stage 1 and stage 2, `Z` is the axis of symmetry (axial direction), `(/NWAVE)` is the considered number of nodal diameters, `NODESCONTACTSTAGE1` is the set of nodes of the contact area between stage 1 and 2 and which belong to stage 1, and `FACESCONTACTSTAGE2` is the set of faces of the contact area between stage 1 and 2 and which belong to stage 2. The `MULTIC 1` command enables to take into account the spatial aliasing, as explained in Section 2.10.4. The `.SYC` command defines automatic boundary conditions to take into account the cyclic symmetry property of the single sector finite element model.

A numerical analysis on the mesh refining was performed and is presented in the Appendix C in order to have accurate results with a reduced computational time. The selected mesh of the reference sector of each stage is shown in Figure A.9(a). The mesh of the bottom stage is identical to the one of the mono-stage structure (presented in Section A.3). The mesh of the reference sector totalizes 8 496 degrees of freedom for the bottom stage and 5 901 degrees of freedom for the top stage. The total number of degrees of freedom is 14 091 (which is lower than 8 496 + 5 901 = 14 397 because of the nodes that are interstage degrees of freedom that are common for the two stages). As for the mono-stage structure, hexahedral volumic elements are used in the finite element model. The full recombined mesh is shown in Figure A.9(b) with the reference sector in dark gray.

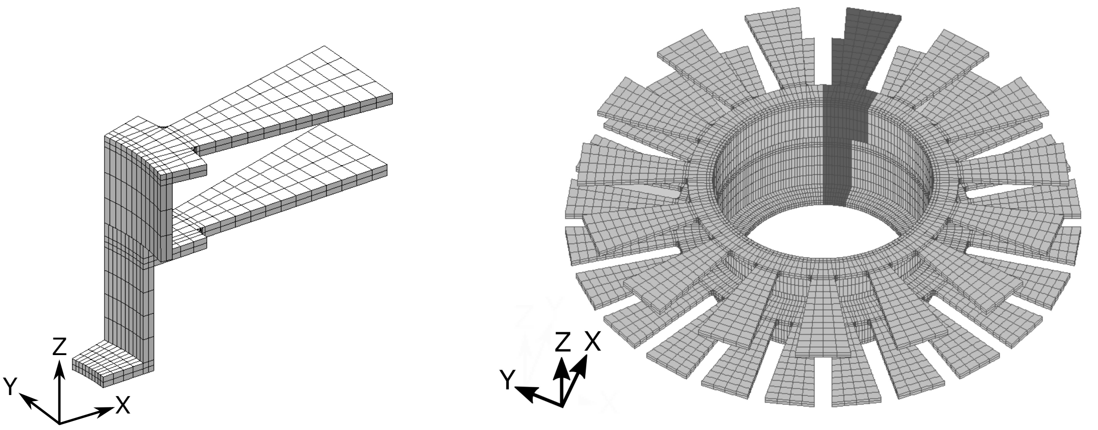

(a) (b)

Figure A.9: Finite element model of the reference sector of the academic structure (a) and the recombined finite element model with the reference sector in dark gray (b).

A.4.2 SAFE diagram

Since the two stages have different numbers of blades, the spatial aliasing has to be taken into account. The maximal number of nodal diameters for stage 1 is equal to $\lfloor \frac{N_1}{2} \rfloor = \lfloor \frac{24}{2} \rfloor = 12$ and the maximal number of nodal diameters for stage 2 is equal to $\lfloor \frac{N_2}{2} \rfloor = \lfloor \frac{25}{2} \rfloor = 7$. Figure A.10 shows the compatible harmonics for this combination of number of blades.

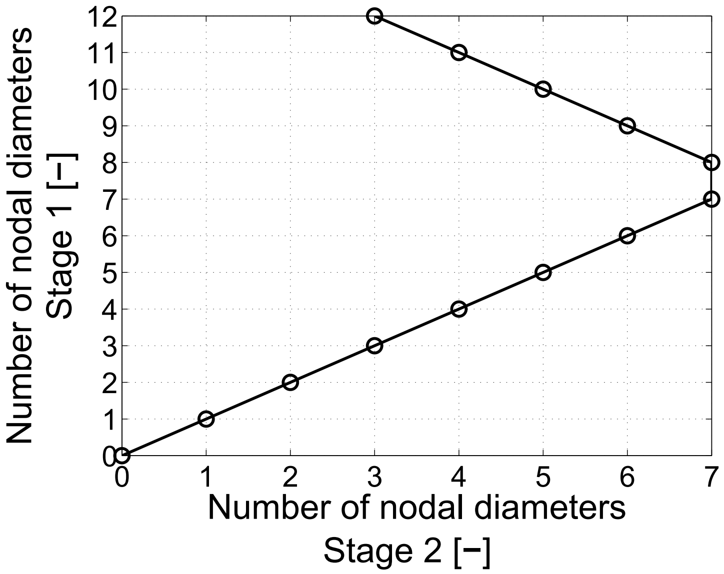

Figure A.10: Compatible harmonics for stage 1 and 2.

Based on the cyclic symmetric finite element model, the SAFE diagram of the structure can be constructed (Figure A.11). The information about the dynamic properties of the studied structure enables to prepare the experimental tests which will be performed in Chapter 4 to identify mistuning in the multi-stage bladed structure.

The different mode shapes are classified in four categories, where different parts of the structure participate in the mode shape:

- Only the bottom stage participates in the mode shape (represented in blue in Figure A.11).
- Only the top stage participates (represented in red in Figure A.11).
- Both stages participate (represented in green in Figure A.11);
- The drum participates mainly (represented in black in Figure A.11).

Different symbols are also used to distinguish the different types of mode shapes such as the bending modes (1B, 2B...), the torsion modes (1T, 2T...), the plane bending modes...

The two first families of modes, around 250 Hz, are the 1B modes families (• symbol). These families are well separated from the others. First bending modes of the bottom stage alone are present, and then first bending modes of the blades of the top stage. No coupling between the stages is observed for these two families of modes.

Then, around 1250 Hz, the next type of modes is plane bending mode (★ symbol). For low number of nodal diameters (0 to 4 nodal diameters), two modes are observed, where both stages participate. Then, for higher numbers of nodal diameters, mode shapes for which only one stage participates are present. The plane bending modes are also two well separated families.

At higher frequencies, around 2000 Hz, different types of blade modes appear. 1T modes with the only participation of the bottom stage are observed (+ symbol), and 1T modes with the only participation of the top stage. In the same frequency range, 2B modes of each stage are observed ($*$ symbol). For the bottom stage, the 2B mode with 0 nodal diameter divides in two 2BT modes (◄ symbol). For 10 to 12 nodal diameters, 2B modes with the participation of the bottom stage are observed again. For the top stage, 2B modes are observed from 0 to 7 nodal diameters, with a frequency that increases with the number of nodal diameters.

Then, drum modes are observed ($\circ$ symbol). For the drum modes, a high variation of frequency is observed for the different numbers of nodal diameters.

Finally, at higher frequencies, 3B modes (▼ symbol), with the participation of the bottom stage and the drum, and with the participation of the top stage and the drum, are observed. Finally, 3B modes are present. For the bottom stage, 3B modes are first observed from 0 to 7 nodal diameters, then the 3BT modes with the participation of the bottom stage only are observed from 8 to 11 nodal diameters (× symbol), and finally a 3B mode is present again for 12 nodal diameters. For the top stage, 3B modes are observed from 0 to 7 nodal diameters.

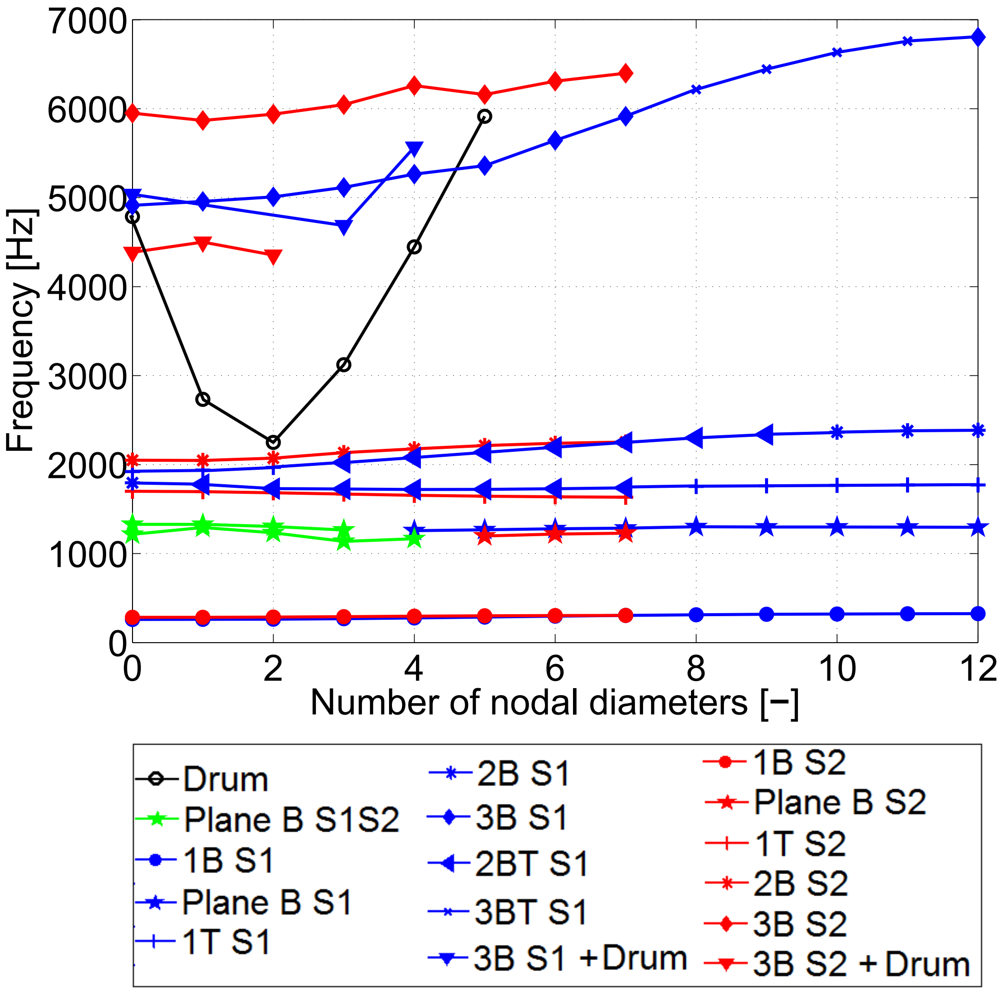

Figure A.11: SAFE diagram of the multi-stage structure.

A.4.3 Deformation energy for each mode shape

In order to show the participation of the drum and the blades in the mode shapes for each modes, the structure is divided in six parts: the blades for each stage, the horizontal part of the drum for each stage, and the vertical part of the drum for each stage. Figure A.12 shows the different groups on the reference sector.

Figures A.13, A.14 and A.15 show the percentage of energy in each part of the structure for each family of modes. These values have been computed using the SAMCEF [120] finite element software. They are classified by family of modes and sorted by increasing frequencies.

The two first family of modes are the 1B mode for each stage (Figures A.13(a) for stage 1 and A.13(b) for stage 2). The maximum number of nodal diameters is $\lfloor \frac{N_1}{2} \rfloor = \lfloor \frac{24}{2} \rfloor = 12$ for stage 1 and $\lfloor \frac{N_2}{2} \rfloor = \lfloor \frac{15}{2} \rfloor = 7$ for stage 2. The 1B modes of stage 1 present a high participation of the corresponding blade and of the horizontal part of the drum for this stage. The same repartition of energy is observed respectively for stage 2. The third and fourth modes (Figures A.13(c) and A.13(d)) correspond to plane bending mode, with

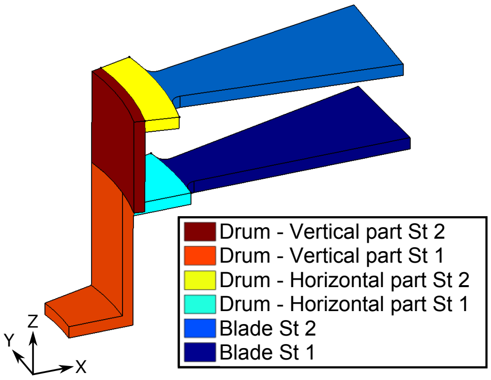

Figure A.12: Division of the structure in six parts (the blades, the horizontal part of the drum, and the vertical part of the drum, for each stage) to compute the energy percentage in each part.

participation of both stages for a low number of nodal diameters. When the number of nodal diameters increases, the third mode becomes a plane bending mode of stage 2 only, and the fourth mode becomes a plane bending mode of stage 1 only. Then, the 1T mode of stage 2 (Figure A.14(a)) shows a high participation of the blades of stage 2 for each number of nodal diameters. The 2B modes of stage 1, followed by 2BT modes (Figure A.14(b)) also presents a high participation of the blades of stage 1 for each number of nodal diameters, as well as the 1T mode of stage 1 (Figure A.14(c)). The second set of 2BT modes of stage 1 follows (Figure A.14(d)). The last family in this frequency range is the 2B modes of the top stage (Figure A.14(e)). At higher frequencies, the participation of the drum in the mode shapes becomes more important. Figures A.15(a), A.15(b) and A.15(d) correspond respectively to 3B modes of stage 2 with the participation of the drum, to drum modes, and to 3B modes of stage 1 with the participation of the drum. Finally, the two last families are 3B modes of stage 1 (Figure A.15(c)) and 3B modes of stage 2 (Figure A.15(e)).

A smooth evolution of the repartition of the strain energy is observed in the different parts of structure when the number of nodal diameters increases. For the majority of the mode families, at low numbers of nodal diameters, the blades of one or both stages have the main contribution in the strain energy, and the participation of the blades of one stage becomes dominant at high number of nodal diameters. For the drum modes, the participation of the drum is the main contribution but limited to 55 % maximum, the rest of the energy is shared into the blades of both stages.

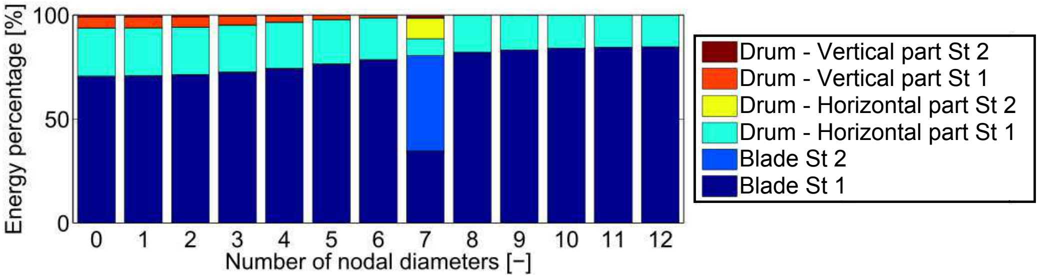

(a) 1B modes - Stage 1

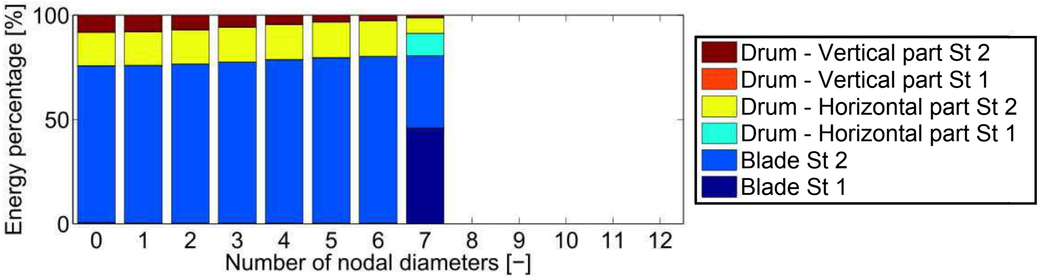

(b) 1B modes - Stage 2

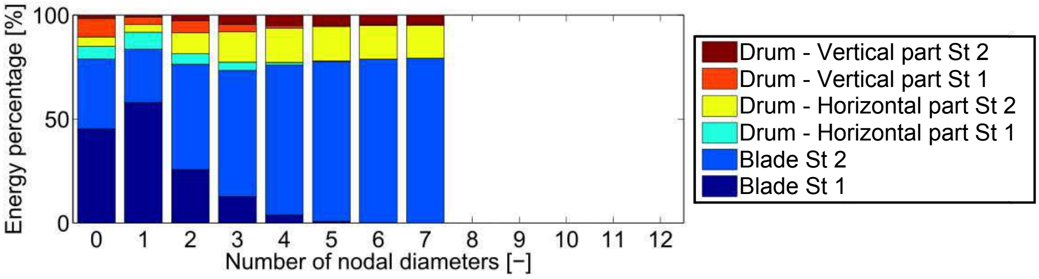

(c) Plane B modes - Stage 2

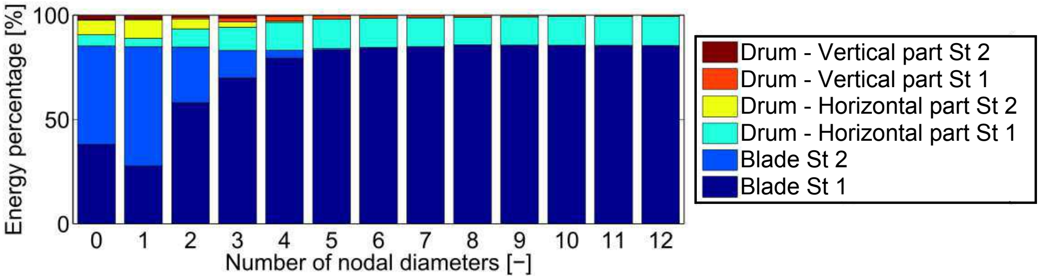

(d) Plane B modes - Stage 1

Figure A.13: Energy percentage in the blade of each stage, in the horizontal part of the drum of each stage, and the vertical part of the drum of each stage for each mode (1B and plane bending modes).

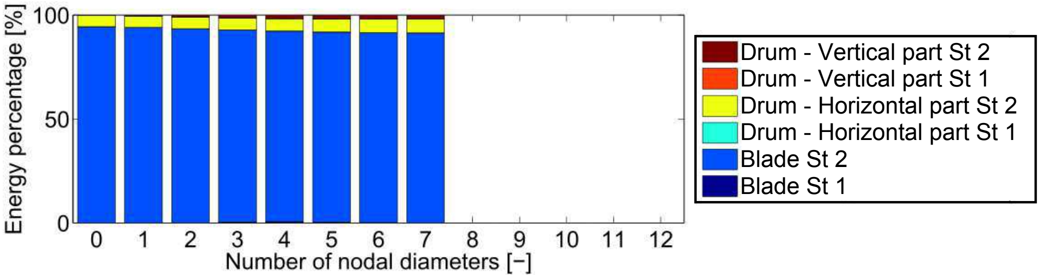

(a) 1T modes - Stage 2

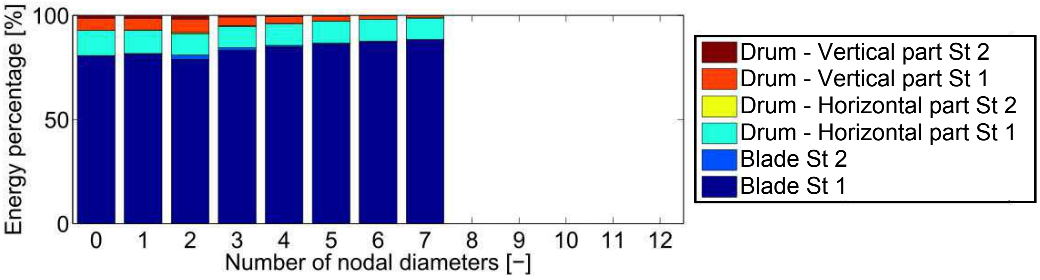

(b) 2B-2BT modes - Stage 1

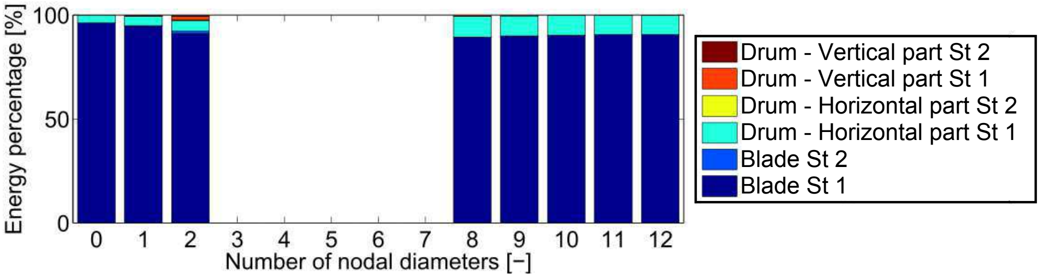

(c) 1T modes - Stage 1

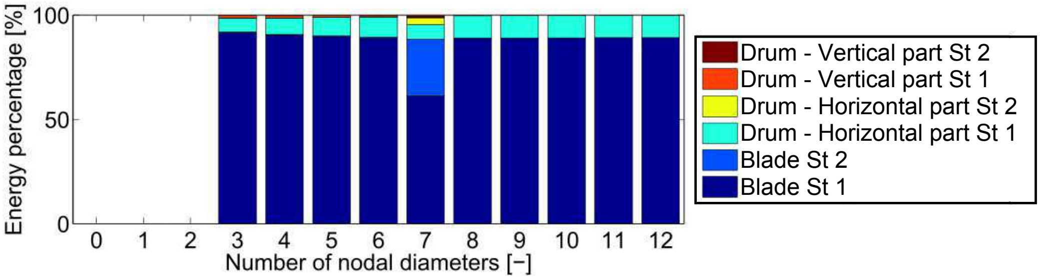

(d) 2BT modes - Stage 1

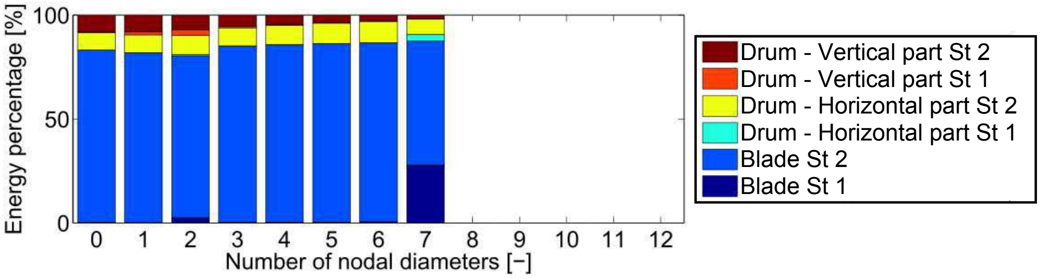

(e) 2B modes - Stage 2

Figure A.14: Energy percentage in the blade of each stage, in the horizontal part of the drum of each stage, and the vertical part of the drum of each stage for each mode (1T, 2B and 2BT modes).

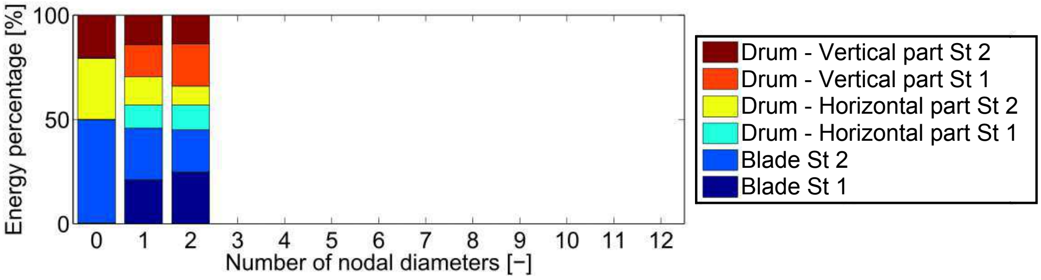

(a) 2B modes and drum - Stage 2

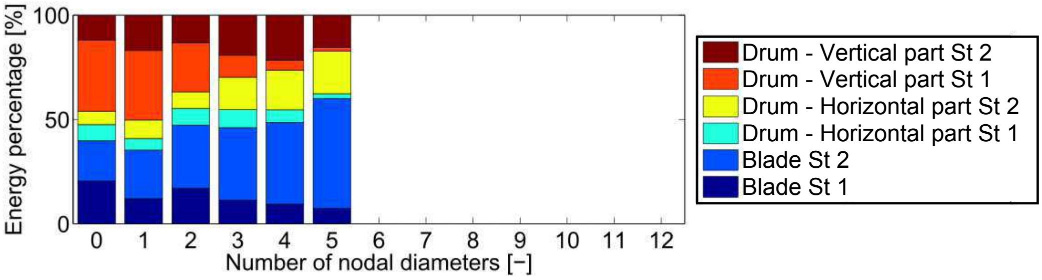

(b) Drum modes

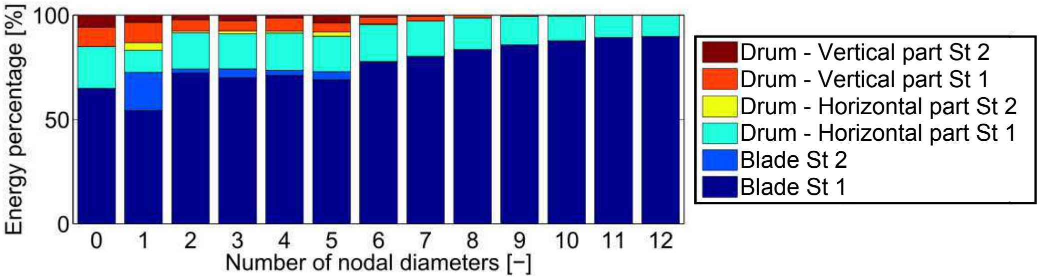

(c) 3B modes - Stage 1

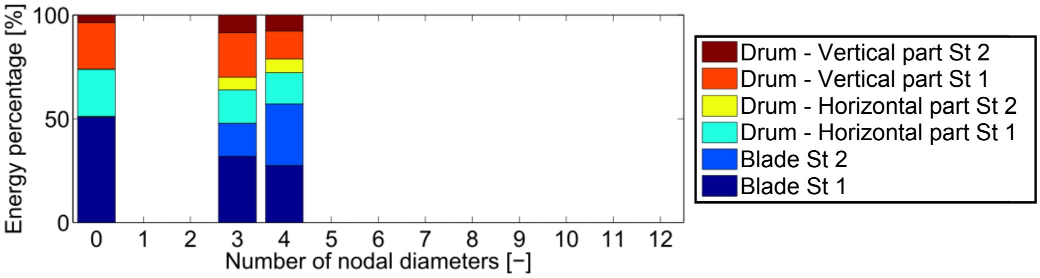

(d) 3B modes and drum - Stage 1

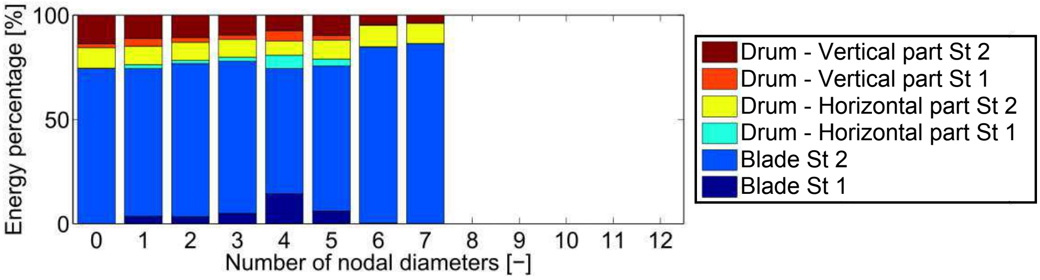

(e) 3B modes - Stage 2

Figure A.15: Energy percentage in the blade of each stage, in the horizontal part of the drum of each stage, and the vertical part of the drum of each stage for each mode (2B, drum, 3B modes).

A.4.4 Clamped blade properties

As for the mono-stage structure, the clamped blade eigenfrequencies can be computed. The clamping conditions are shown in Figure A.16. Table A.3 gives the four first eigenfrequencies of the clamped blade for both stages. The first mode for both stages is the 1B modes. The second one is the plane bending mode. Then, the thirst mode is the 1T mode. Finally, the fourth mode is the 2B mode. The mode shapes are for both stages similar to the one presented in the mono-stage Section (Figure A.7).

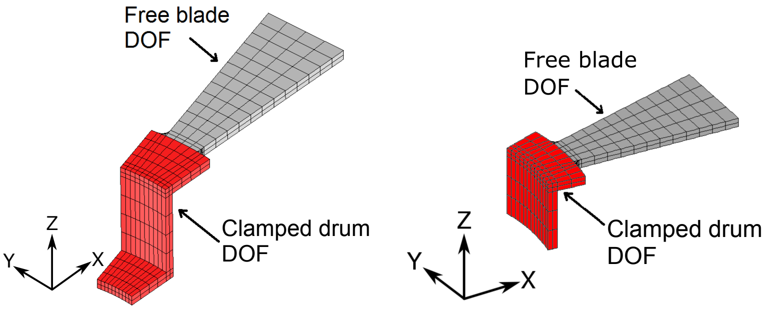

(a) (b)

Figure A.16: Clamping sector for stage 1 (a) and stage 2 (b).

Stage 1 [Hz]	Stage 2 [Hz]
403	401
1560	1641
2060	1875
2980	2985

Table A.3: First clamped blade eigenfrequencies for each stage.

The clamped blade eigenfrequencies of each stage can be added on the SAFE diagram (Figure A.17). As for the mono-stage structure, the clamped blade eigenfrequencies are higher than the system eigenfrequencies, even for the modes with high numbers of nodal diameters. This can be also explained by the drum flexibility, which enables a participation of the drum in the mode shapes even for a high number of nodal diameters.

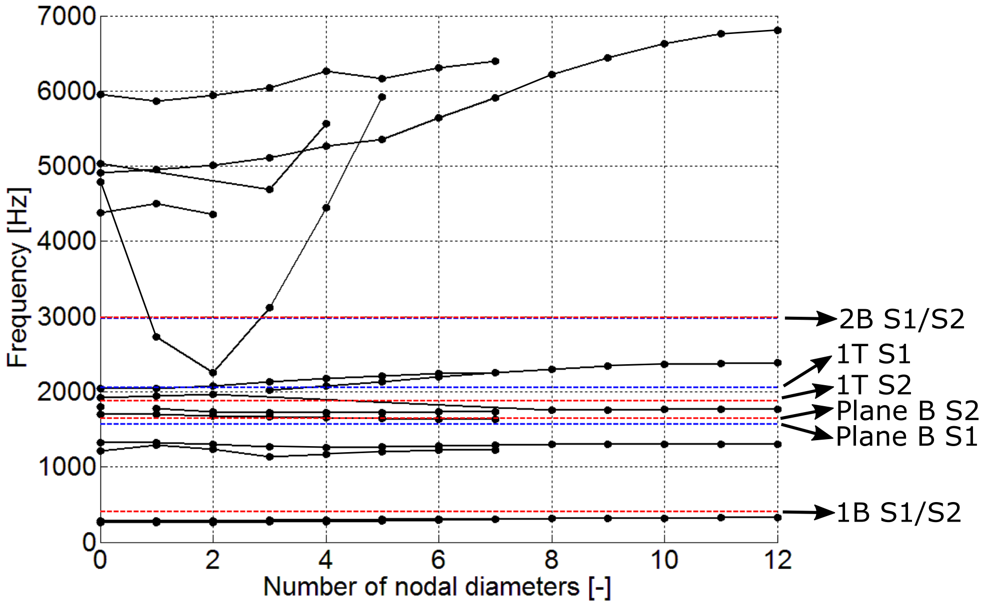

Figure A.17: Clamped blade eigenfrequencies of each stage superimposed to the SAFE diagram.

Appendix B

Drawing of the academic structures

Figure B.1 gives the drawing of the mono-stage academic structure, and Figure B.2 gives the drawing of the multi-stage academic structure.

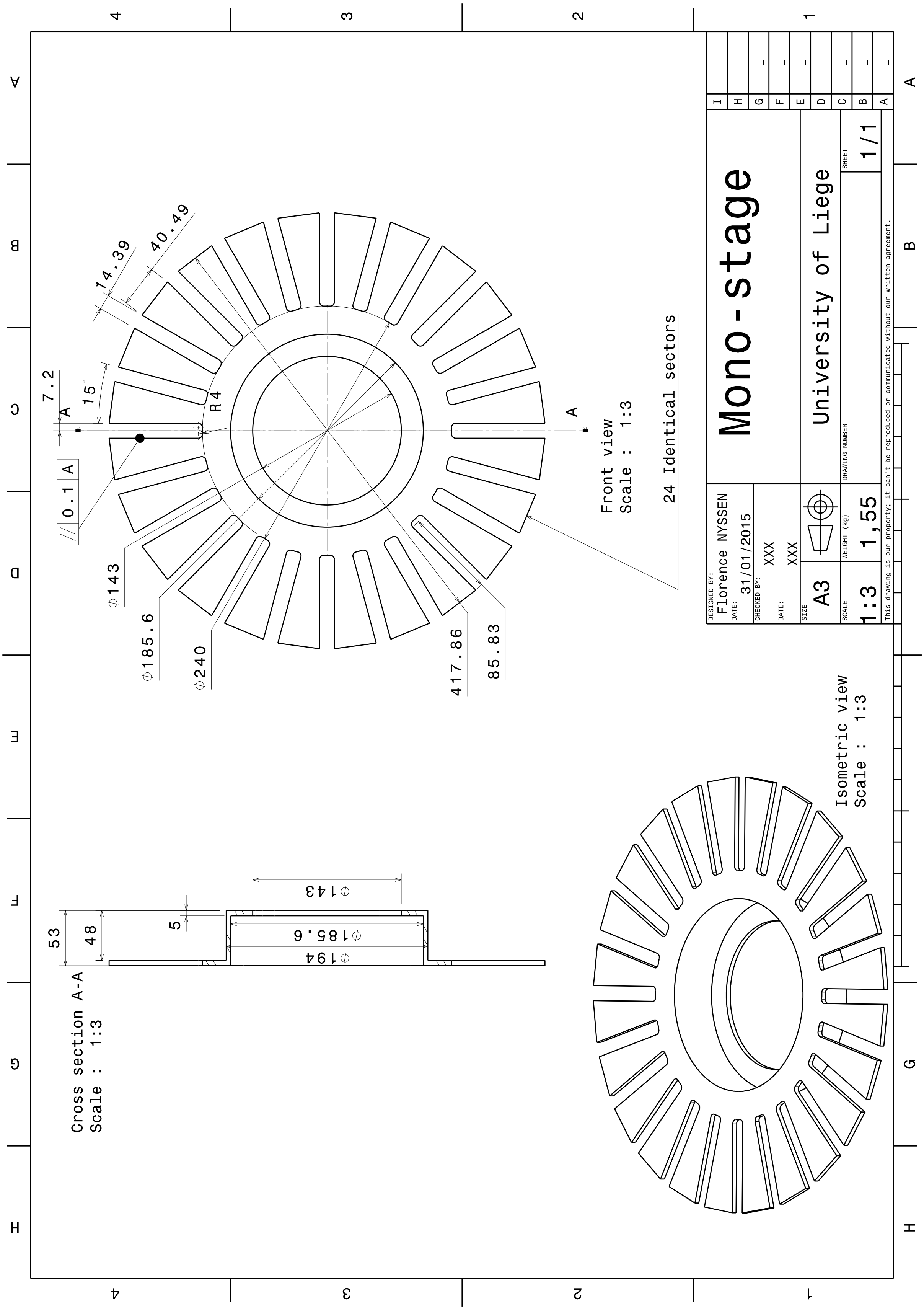

Figure B.1: Drawing of the mono-stage academic bladed structure.

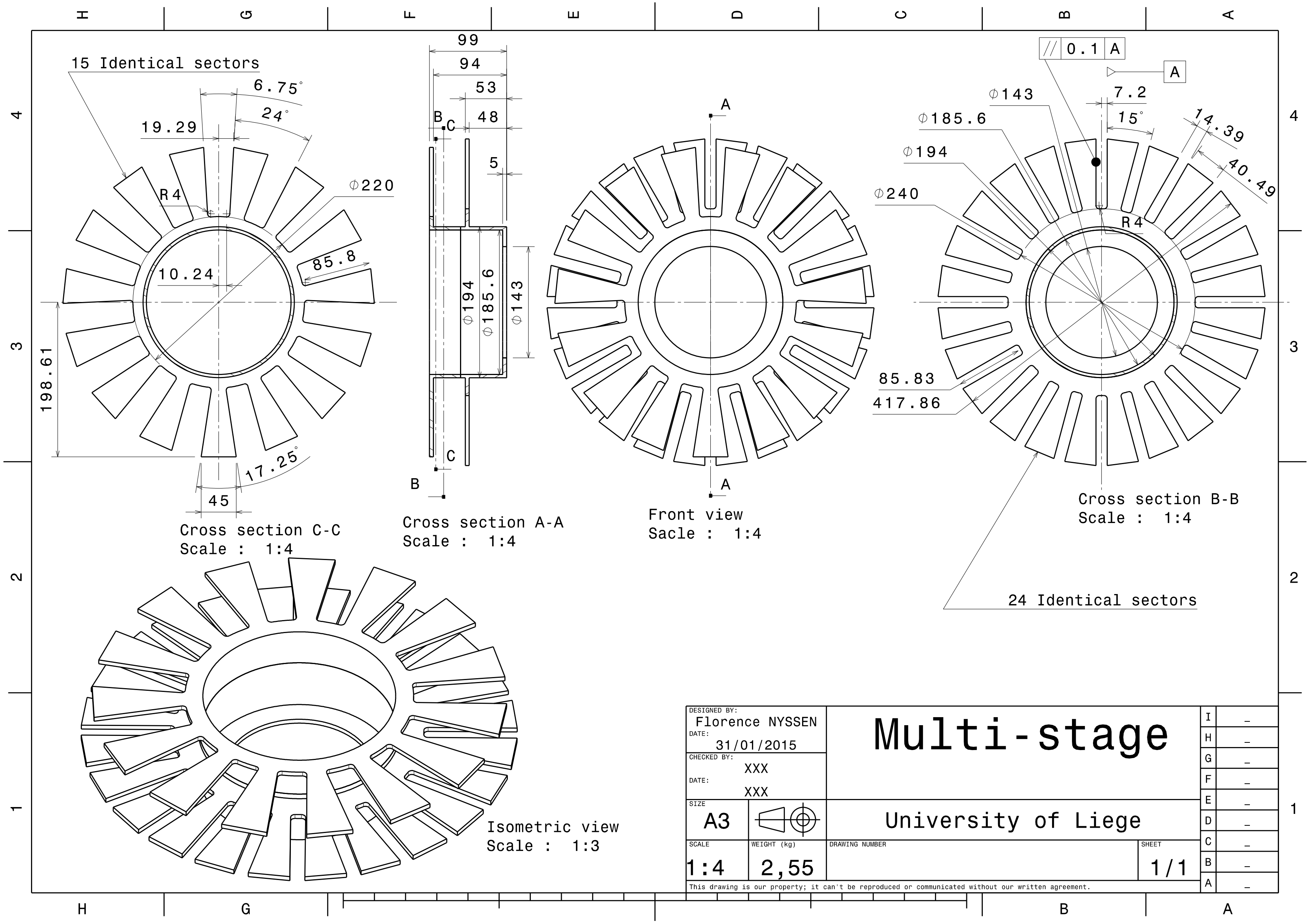

Figure B.2: Drawing of the multi-stage academic bladed structure.

Appendix C

Comparison of finite element models with different refining

C.1 Mono-stage academic structure

Two meshes are compared for the mono-stage academic structure. A refined mesh is shown in Figure C.1(a) (reference sector) and C.1(b) (recombined 360° mesh). The mesh used in the thesis is presented in Figure C.1(c) (reference sector) and C.1(d) (recombined 360° mesh). Table C.1 compares the characteristics of each finite element model.

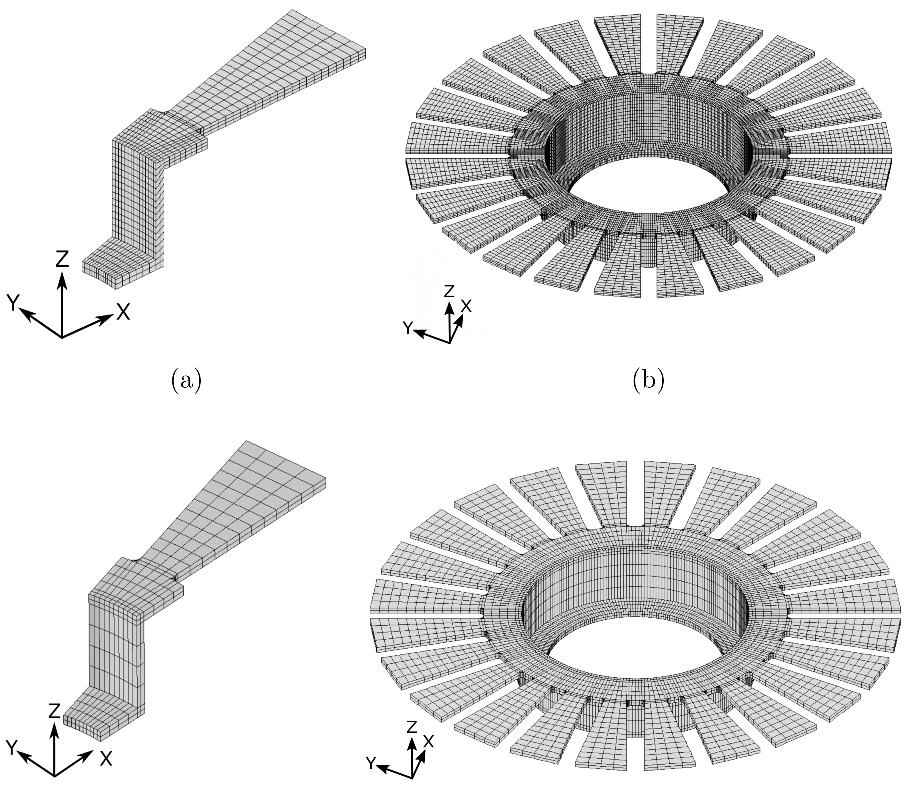

(a) (b) (c) (d)

Figure C.1: Refined mono-stage sector (a), refined mono-stage 360° model (b), mono-stage sector (c), mono-stage 360° model (d).

	Refined mono-stage sector	Refined mono-stage 360°	Mono-stage sector	Mono-stage 360°
Number of nodes	8 127	188 592	2 899	66 384
Number of DOF	24 018	537 696	8 496	184 752
CPU time	24 s	15 min	2 s	4 min

Table C.1: Characteristics of the different meshes of the mono-stage academic structure.

Figure C.2 compares the eigenfrequencies obtained for each finite element model. Figure C.3 gives the error between the eigenfrequencies of each finite element model (the reference is the frequencies of the refined 360° finite element model). Errors lower than 0.3 % are obtained between the refined and coarse meshes. However, there is a huge difference in the computational time of the two models. Therefore, the coarse mesh is used in the thesis.

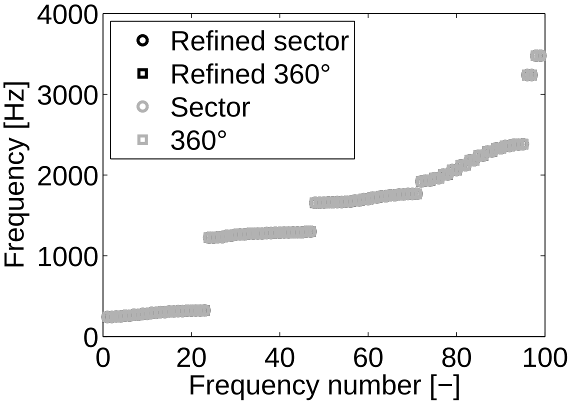

Figure C.2: Comparison between the eigenfrequencies of each mono-stage finite element model.

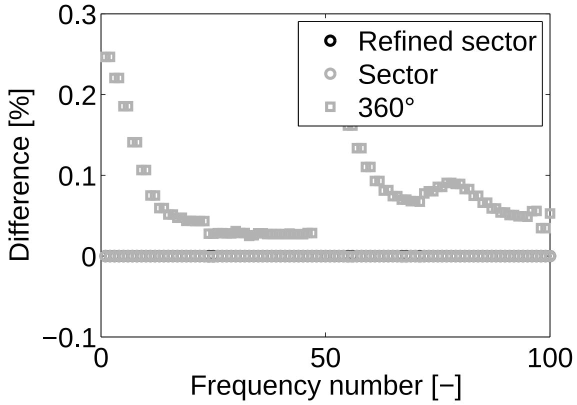

Figure C.3: Difference between the eigenfrequencies of each finite element model (the reference is the frequencies of the refined 360° mono-stage finite element model).

C.2 Multi-stage academic structure

Two meshes are compared for the multi-stage academic structure. A refined mesh is shown in Figure C.4(a) (reference sectors) and C.4(b) (recombined 360° mesh). The mesh used in the thesis is presented in Figure C.4(c) (reference sectors) and C.4(d) (recombined 360° mesh). Table C.2 compares the characteristics of each finite element model.

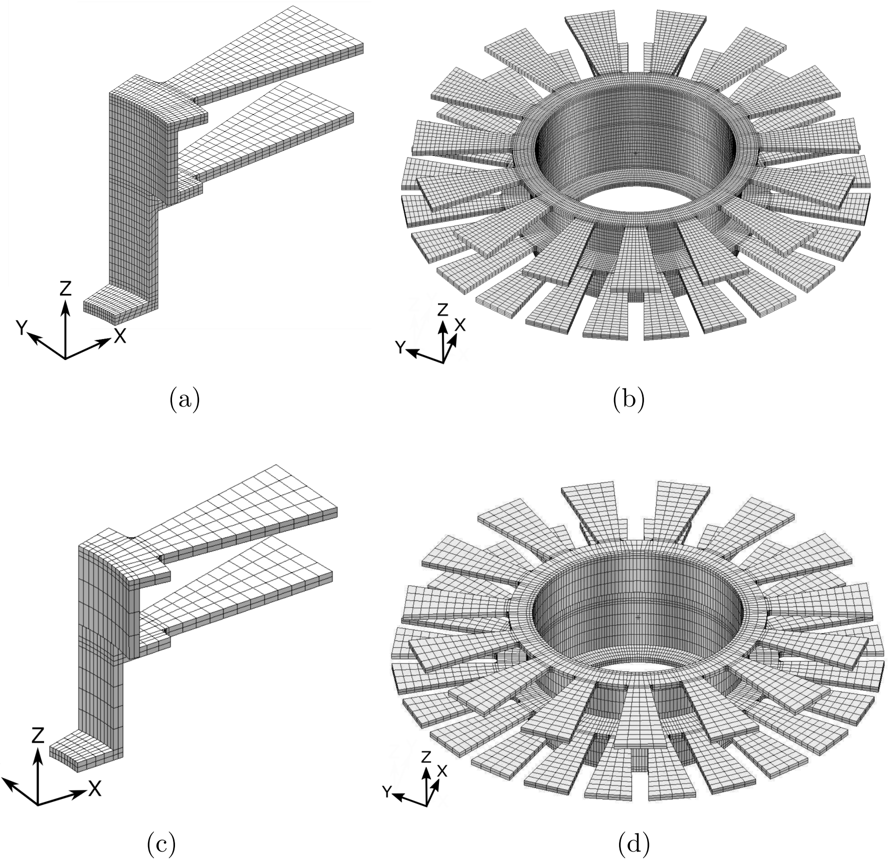

(a) (b)

(c) (d)

Figure C.4: Refined multi-stage sector (a), refined multi-stage 360° model (b), multi-stage sector (c), multi-stage 360° model (d).

	Refined multi-stage sector	Refined multi-stage 360°	Multi-stage sector	Multi-stage 360°
Number of nodes	17 347	402 447	11 654	97 659
Number of DOF	52 041	1 176 021	44 718	282 897
CPU time	50 s	45 min	38 s	13 min

Table C.2: Characteristics of the different meshes of the multi-stage academic structure.

Figure C.5 compares the eigenfrequencies obtained for each finite element model. Figure C.6 gives the error between the eigenfrequencies of each finite element model (the reference is the frequencies of the refined 360° finite element model). Errors lower than 0.6 % are obtained between the refined and coarse meshes, but there is a huge difference in the computational time of the two models. Therefore, the coarse mesh is used in the thesis.

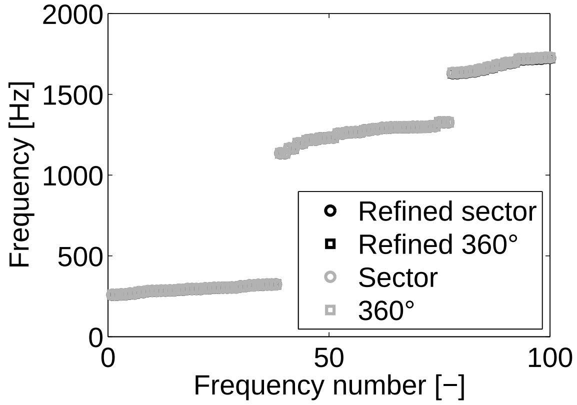

Figure C.5: Comparison between the eigenfrequencies of each multi-stage finite element model.

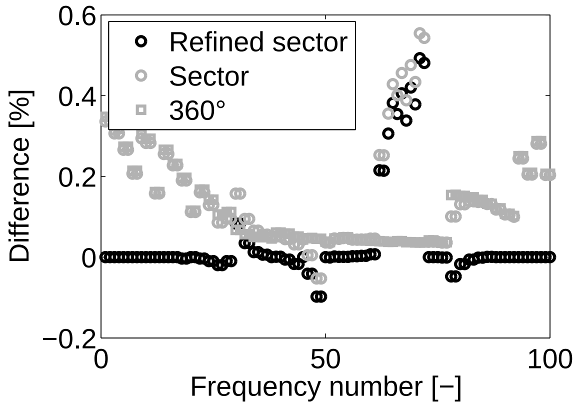

Figure C.6: Difference between the eigenfrequencies of each multi-stage finite element model (the reference is the frequencies of the refined 360° finite element model).

Appendix D

Influence of the microaccelerometer on the measurements

Measurements with a microaccelerometer and with a laser have been performed to get the influence of the microaccelerometer on the measurements. The use of a microaccelerometer is indeed easier, but it can have an impact on the measurements.

The tests performed using microaccelerometers are presented here. The results will be compared to the ones obtained in the thesis with a laser vibrometer (non-contacting measurement technique) in order to see the influence of the presence of the accelerometer in the identification process.

D.1 Measurements using microaccelerometers

In this Section, measurements have been performed using a microaccelerometer. The test set-up and the results are presented below.

D.1.1 Test set-up

The academic structure and the test set-up are presented on Figure D.1. The structure is clamped by its basis with 24 fixation points in order to keep the cyclic symmetric property: the academic structure has 24 sectors and one fixation point in the center of each sector has been considered. A base excitation is applied with an electrodynamic shaker in the axial direction (Z-axis). A microaccelerometer is used to measure the response of the structure. An accelerometer measures the acceleration of the shaker in order to get the force injected by the shaker. The used acquisition system is LMS Test.Lab [121]. The test is performed at constant temperature ($20°C$).

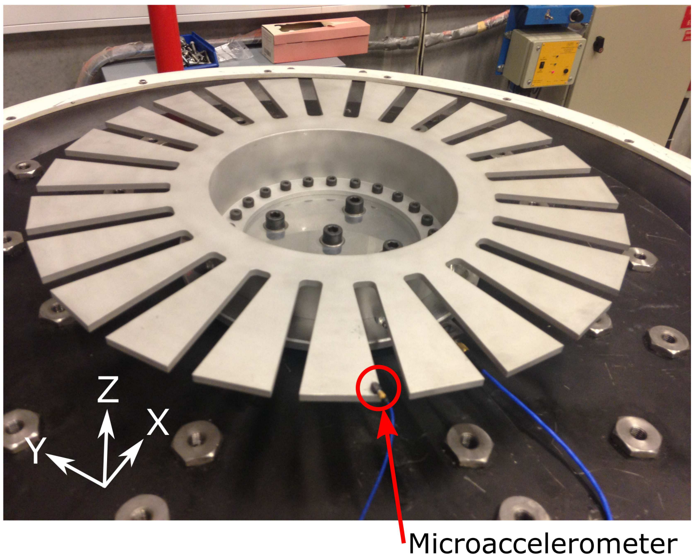

Figure D.1: Academic structure and test set-up.

Five measurement points are considered on each blade: two points at each extremity corners (blade tip), two points on each side of the blade at mid-cord, and one point on the basis of the blade (Figure D.2). The measured direction is the same as the direction of the excitation i.e., along the axis of revolution of the structure.

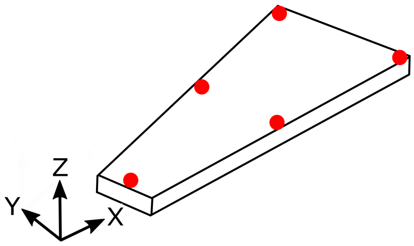

Figure D.2: Location of the measurement points on the blade.

A periodic chirp from 0 to 3200 Hz excites the structure, with a resolution of 0.04 Hz. This large frequency range enables to get the global behavior of the structure. Then, the results will focus in the frequency range of the 1B modes. The frequency resolution is limited by the acquisition system.

D.1.2 Stabilization diagram

The obtained Frequency Response Functions (FRF) for all measurement points are presented in Figure D.3. The first group of peaks of resonance (around 240 Hz) covers the 1B modes. The deformation of two blades are shown in Figure D.4(a) (the deformed blades are in green and the undeformed configuration is in grey). The plane bending modes are not measured since the measurements are performed in the axial direction. The second group (around 1200 Hz) covers 1T modes. The deformation is shown in Figure D.4(b). Then, around 1800 Hz, 2B modes (deformation in Figure D.4(d)) respond. In the same frequency range, 1BT modes respond (deformation in Figure D.4(c)). Finally, 3B modes are present. The deformation for two blades is shown in Figure D.4(e).

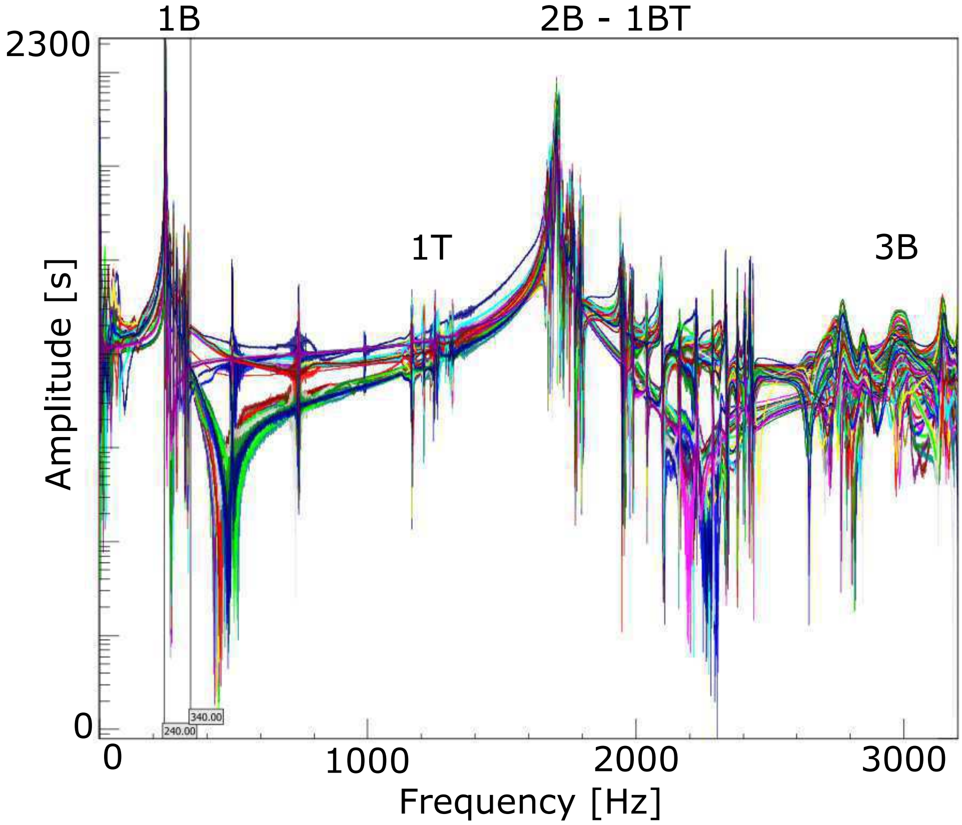

Figure D.3: FRF for all measurement points.

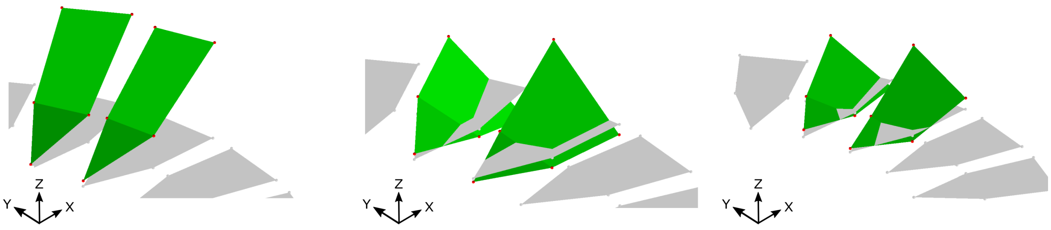

(a) 1B (b) 1T (c) 1BT

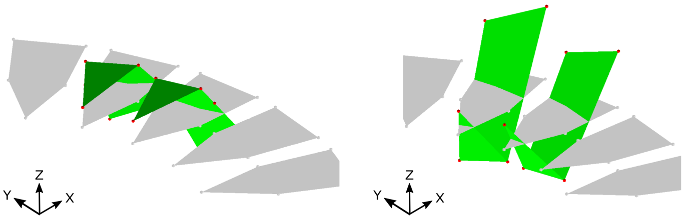

(d) 2B (e) 3B

Figure D.4: Deformation of each type of mode shapes.

Using these data, the Young's modulus of the finite element model is updated to 72 340 MPa.

We will focus here on the 1B modes. The 1B modes have their frequencies between 240 and 340 Hz. Figure D.5 shows the stabilization diagram [185] restricted to the range of frequency of the 1B modes. Symbols in the stabilization diagram have following meaning: o corresponds to a new pole, f to a stable frequency, d to a stable frequency and damping, v to a stable frequency and eigenvector, and s to all criteria stable. Physical poles are readily visible in the diagram since stabilized poles form a vertical line.

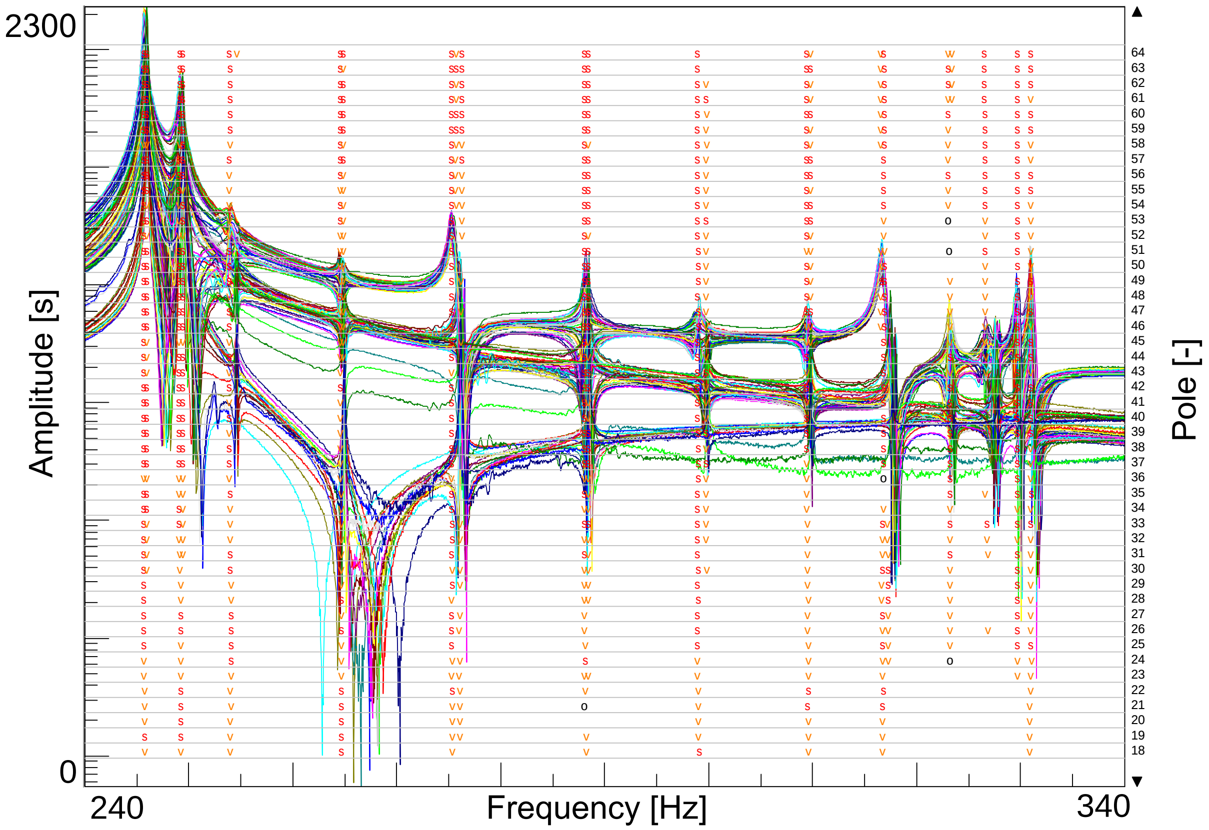

Figure D.5: Stabilization diagram: 1B modes. Symbols have following meaning: o – new pole; f – stable frequency; d – stable frequency and damping; v – stable frequency and eigenvector; s – all criteria stable.

D.1.3 Frequencies and mode shapes

The frequencies and mode shapes corresponding to each peak can be extracted from the stabilization diagram. The frequencies of the peaks between 240 and 340 Hz are given in Table D.1. Some peaks divide in two stabilized poles when the order increases. This separation is due to the mistuning of the structure, but also to the presence of the microaccelerometers.

Frequency [Hz]	Main harmonic [-]
245.7 - 245.9	0
249.1 - 249.4	1
253.9	2
264.6 - 264.9	3
275.3 -276.3	4
288.1 - 288.4	5
299.0 - 299.7	6
309.4 - 309.8	7
316.86	8
323.0	9
326.5	10
329.7	11
330.9	12

Table D.1: Characteristics of the studied structure.

Indeed, when further zooming on the first peak (the 0 nodal diameter mode), four groups of peaks can be distinguished, with four corresponding stabilized poles, as can be seen in Figure D.6. The two first groups contain the curves related to the measurement points at the top of the blades (Figure D.7(a) for the left point and D.7(b) for the right one), and the third group corresponds to the measurement points at the middle of the blades (Figure D.7(c)), and the fourth group to the measurement points at the bottom of the blades (Figure D.7(d)). The frequency of each group is 245.67 Hz, 245.74 Hz, 245.94 Hz and 245.98 Hz respectively. This corresponds to a variation of frequency of maximum 0.13%. The lower peaks correspond to the measurement point at the extremity of the blade since the impact of the additional mass (the weight of the accelerometer) is higher.

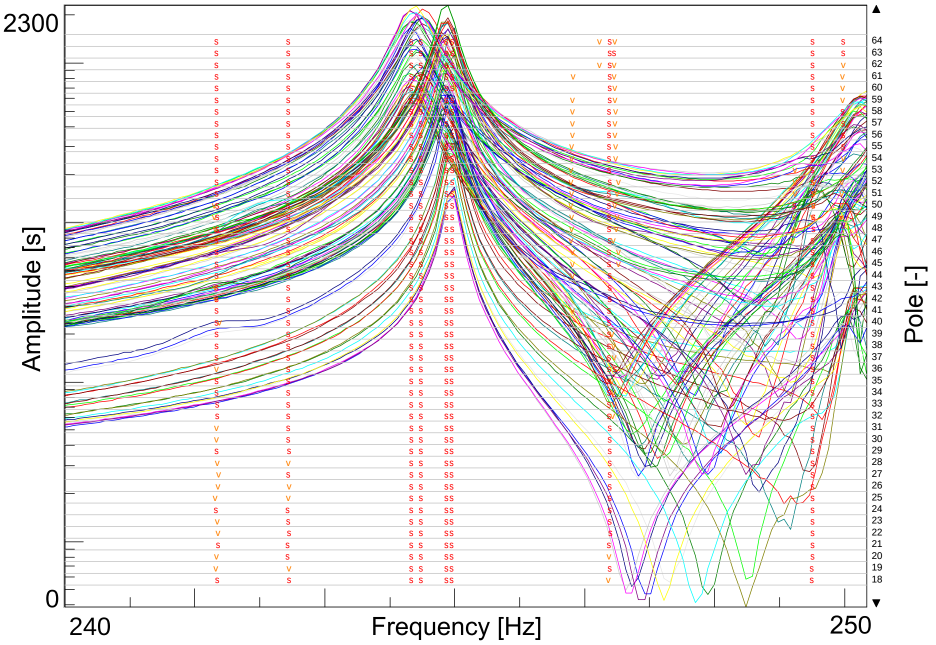

Figure D.6: Stabilization diagram: zoom on the 0 nodal diameter mode.

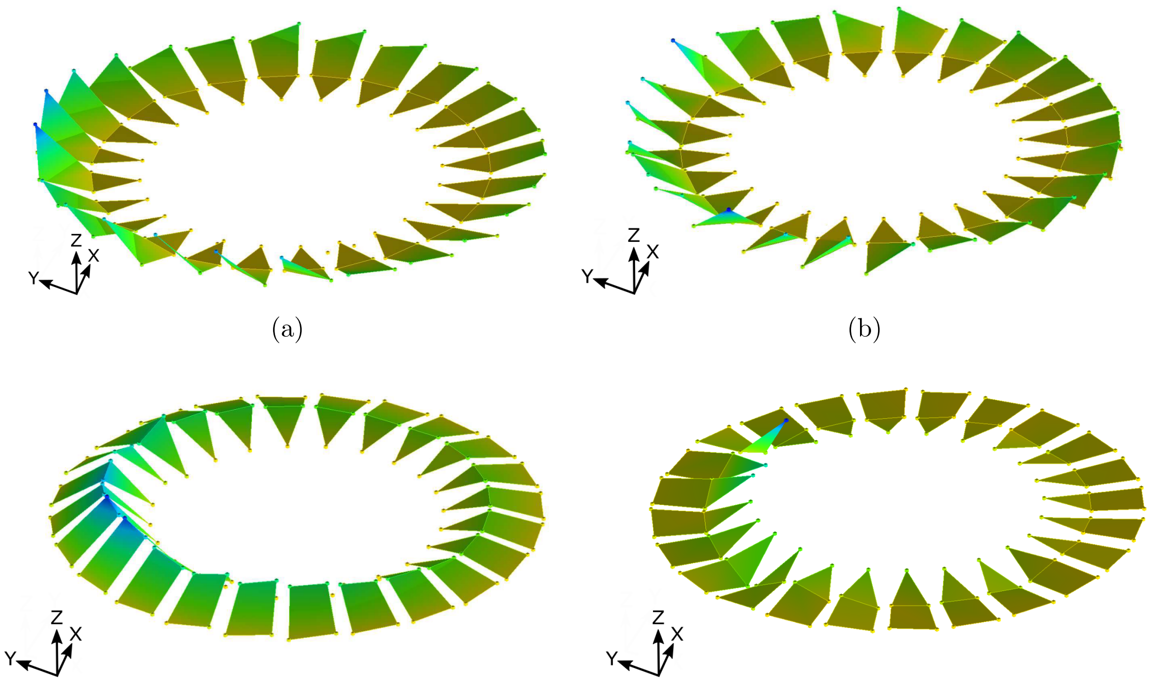

(a) (b)

(c) (d)

Figure D.7: Response of the left point at the top of the blade (a), response of the right point at the top of the blade (b), response of the measurement points at the middle of the blades (c), response of the measurement points at the bottom of the blades (d).

The modes used for the identification process are the three first modes:

- The first mode, shown in Figure D.8, at a frequency of 245.7 Hz, has the 0 nodal diameter as main component.

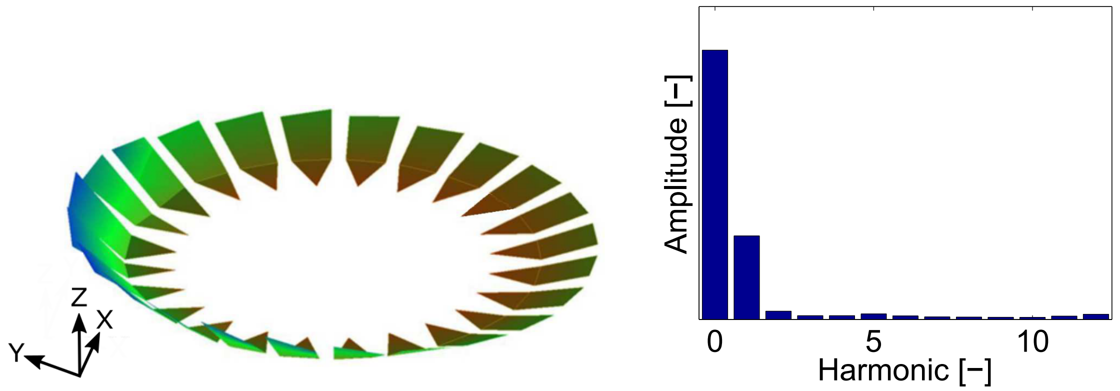

(a) (b)

Figure D.8: Mode shape corresponding to a frequency of 245.7 Hz (a) and his harmonic content (b).

- The second mode shape, shown in Figure D.9, at a frequency of 249.4 Hz, has the 1 nodal diameter harmonic as main component.

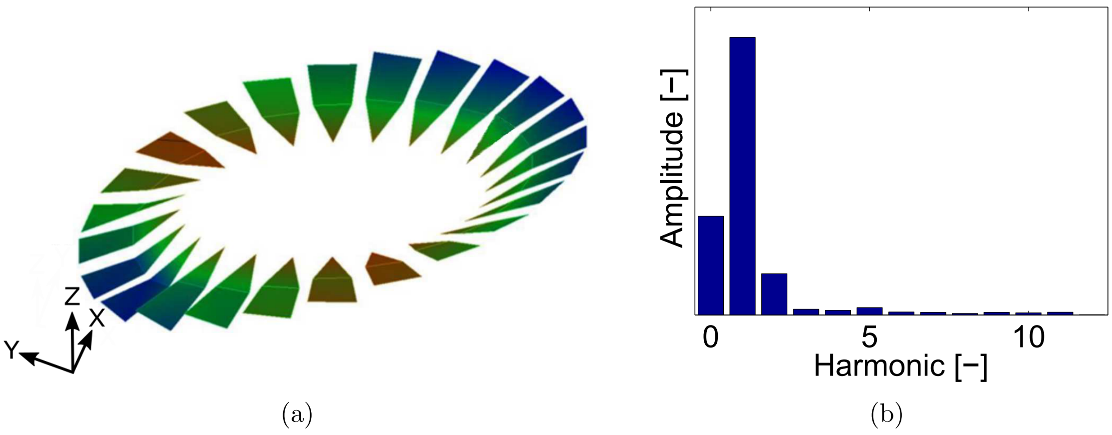

Figure D.9: Mode shape corresponding to a frequency of 249.4 Hz (a) and his harmonic content (b).

- The third mode, shown in Figure D.10 and corresponding to a frequency of 254 Hz, has the harmonics 0, 1 and 2 that participate.

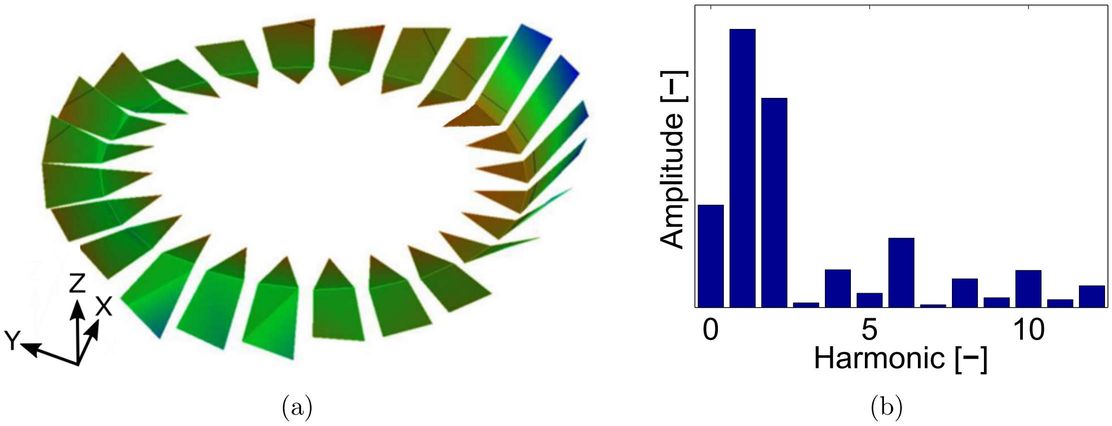

Figure D.10: Mode shape corresponding to a frequency of 254 Hz (a) and his harmonic content (b).

Based on these mode shapes, the CMM identification method is applied. For the identification process, the two measurement points at the top of the blade (the obtained results remain identical when considering the 5 points) are considered. The obtained results are presented on Figure D.11. A mistuning up to 7% is found for the blade 7.

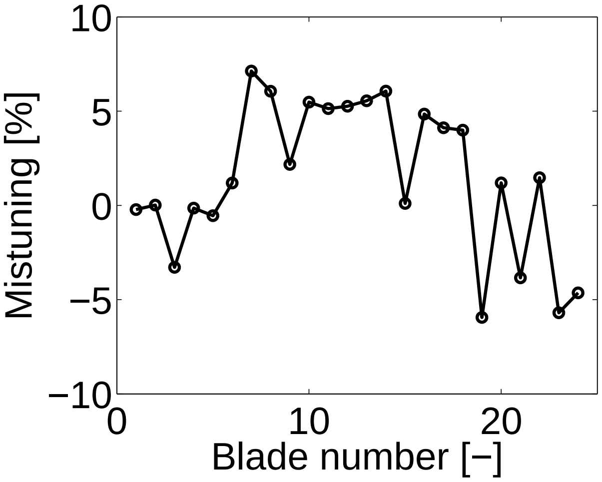

Figure D.11: Identified mistuning.

D.2 Comparison between the measurement with the accelerometers and with the laser

The frequencies and mode shapes obtained with the accelerometers and the laser are compared here.

FRF

Figure D.12 superimposed the sum of the measured FRF obtained with the microaccelerometer and the laser measurements. The considered measurement points are the ones at the top of each blade for both cases.

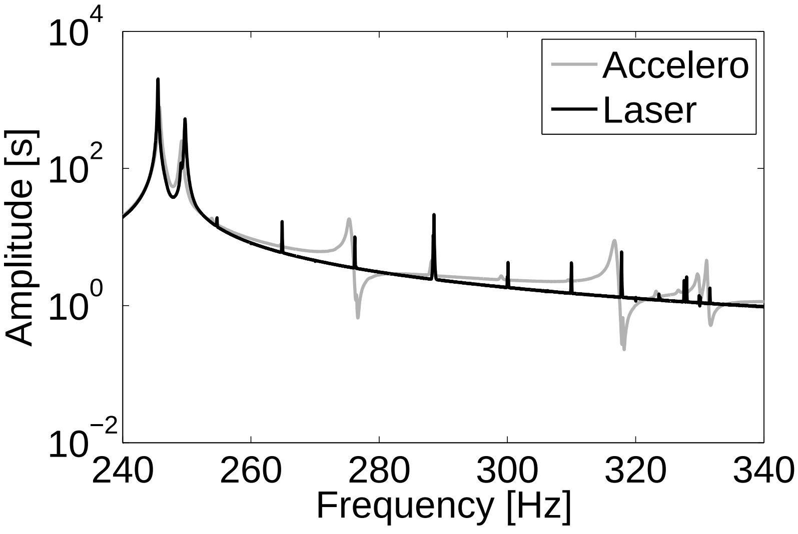

Figure D.12: Comparison between the FRF obtained with the microaccelerometer and the laser measurements.

For low frequencies (four first peaks), a good correspondence is observed between both measurement sets. When the frequency increases, higher frequency shifts are observed between both curves, and the modal damping is also lower for laser measurements. Additional anti-resonances are observed with the microaccelerometer.

Eigenfrequencies and mode shapes

The eigenfrequencies obtained using the stabilization diagram are compared for both measurement sets in Table D.2. The maximum differences between the frequencies of both measurements is -0.34 %. Therefore, the presence of the microaccelerometer on the structure has a negligible effect in terms of the measured eigenfrequencies (if only one peak is detected for one main harmonic, the frequency is repeated in Table D.2).

Main harmonic [-]	Frequency accelero [Hz]	Frequency laser [Hz]	Difference [%]
0	245.67	245.49	0.07
1	249.10	249.08	0.01
1	249.41	249.73	-0.13
2	253.94	254.70	-0.30
2	253.94	254.70	-0.30
3	264.56	264.87	-0.12
3	264.87	264.87	0.00
4	275.27	276.21	-0.34
4	276.25	276.21	0.02
5	288.08	288.43	-0.12
5	288.45	288.55	-0.04
6	298.96	300.11	-0.39
6	299.77	300.11	-0.12
7	309.42	309.99	-0.18
7	309.81	309.99	-0.06
8	316.86	317.79	-0.29
8	316.86	317.79	-0.29
9	323.04	323.63	-0.18
9	323.04	323.63	-0.18
10	326.55	327.55	-0.30
10	326.55	327.96	-0.43
11	329.74	329.89	-0.05
11	329.74	329.89	-0.05
12	330.95	331.58	-0.19

Table D.2: Comparison of the eigenfrequencies of the 1B modes obtained with the microaccelerometer and the laser measurements.

Then, the corresponding mode shapes are compared using the Modal Assurance Criterion (MAC). The MAC number is a quantitative measurement of the alignment of two modes. If the mode shapes are parallel, the MAC is equal to 1, and if the mode shapes are orthogonal, the MAC is equal to 0. The considered measurement points are those at the blade tip. Figure D.13 shows the first mode shapes. The corresponding MAC matrix is given in Figure D.14. The laser mode shapes appear smoother than microaccelometer mode shapes. For the first four mode shapes, the MAC matrix indicates that a good correspondence in the mode shapes has been obtained (MAC value between 0.7 and 1). However, for higher orders, the presence of the accelerometer perturbs the measurements and the measured mode shapes totally differ from the ones measured with the laser vibrometer.

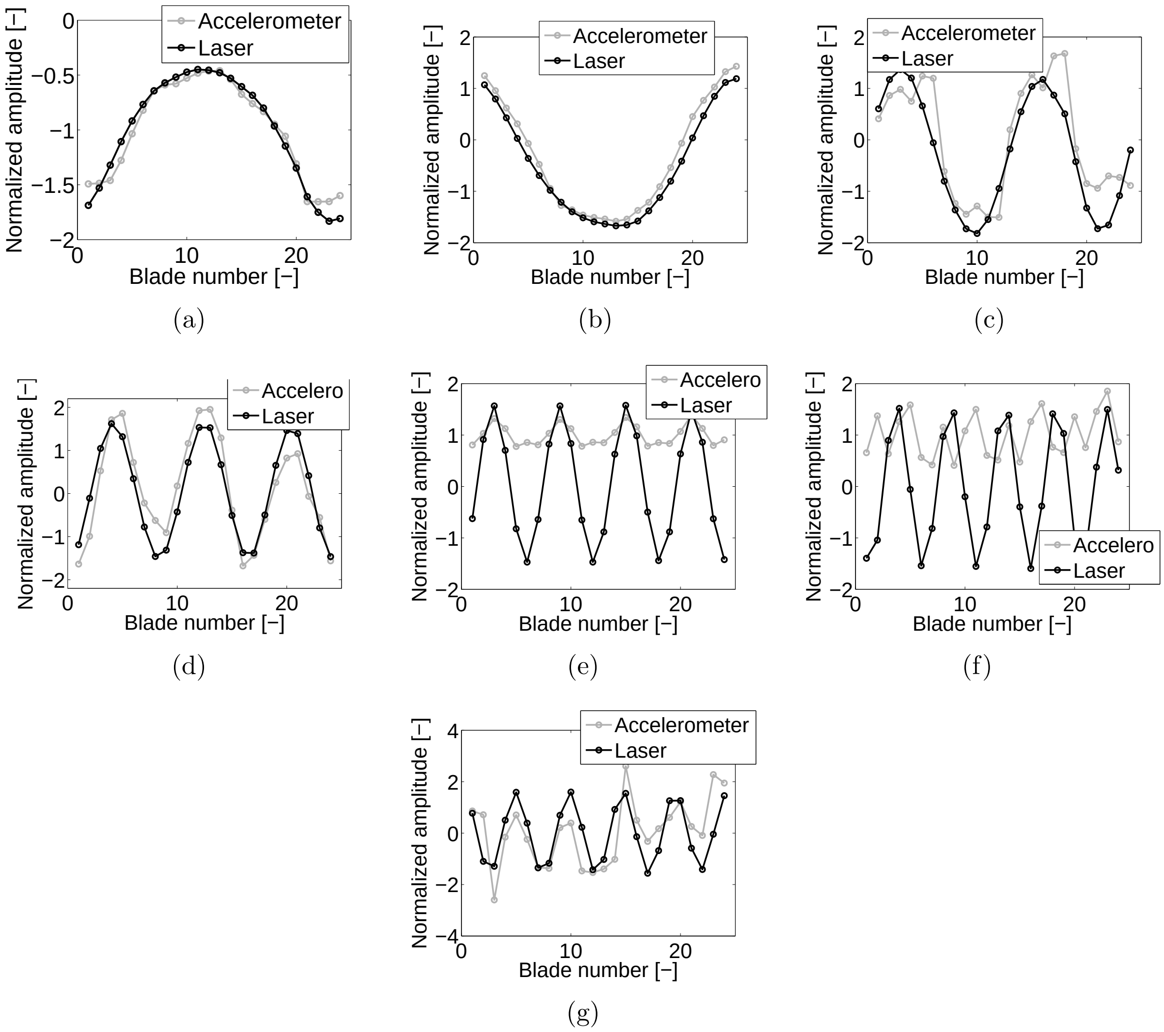

(a) (b) (c)

(d) (e) (f)

(g)

Figure D.13: Comparison between the mode shapes obtained with the microaccelerometer and the laser measurement.

These results show that, even if the effect of the microaccelerometer on the measured frequencies is negligible, it has a large effect on the measured mode shapes, particularly for higher number of nodal diameters.

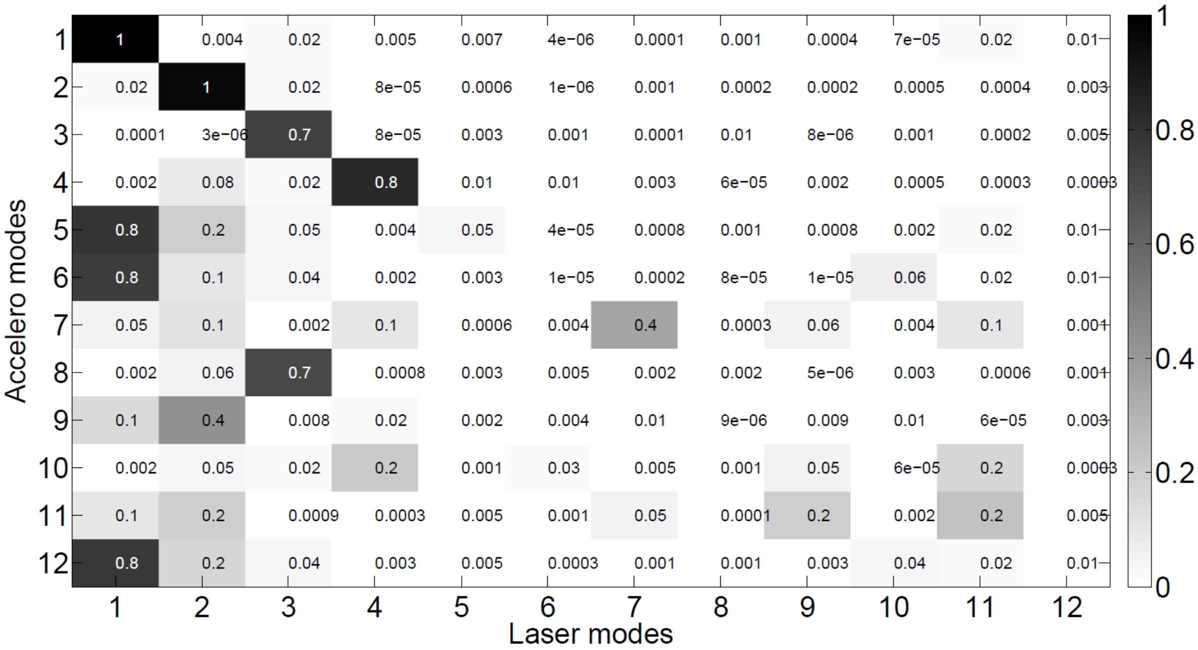

	1	2	3	4	5	6	7	8	9	10	11	12
1	1	0.004	0.02	0.005	0.007	4e−06	0.0001	0.001	0.0004	7e−05	0.02	0.01
2	0.02	1	0.02	8e−05	0.0006	1e−06	0.001	0.0002	0.0002	0.0005	0.0004	0.003
3	0.0001	3e−06	0.7	8e−05	0.003	0.001	0.0001	0.01	8e−06	0.001	0.0002	0.005
4	0.002	0.08	0.02	0.8	0.01	0.01	0.003	6e−05	0.002	0.0005	0.0003	0.0003
5	0.8	0.2	0.05	0.004	0.05	4e−05	0.0008	0.001	0.0008	0.002	0.02	0.01
6	0.8	0.1	0.04	0.002	0.003	1e−05	0.0002	8e−05	1e−05	0.06	0.02	0.01
7	0.05	0.1	0.002	0.1	0.0006	0.004	0.4	0.0003	0.06	0.004	0.1	0.001
8	0.002	0.06	0.7	0.0008	0.003	0.005	0.002	0.002	5e−06	0.003	0.0006	0.001
9	0.1	0.4	0.008	0.02	0.002	0.004	0.01	9e−06	0.009	0.01	6e−05	0.003
10	0.002	0.05	0.02	0.2	0.001	0.03	0.005	0.001	0.05	6e−05	0.2	0.0003
11	0.1	0.2	0.0009	0.0003	0.005	0.001	0.05	0.0001	0.2	0.002	0.2	0.005
12	0.8	0.2	0.04	0.003	0.005	0.0003	0.001	0.001	0.003	0.04	0.02	0.01

Figure D.14: MAC matrix between the mode shapes obtained with the microaccelerometer and the laser measurements.

Identified mistuning

Finally, the comparison between the mistuning identified using both sets of measurements is given in Figure D.15(a). The maximum mistuning remains the same (7 %), but the blade on which the maximum mistuning appears is different (maximum mistuning on blade 7 for the measurements with the microaccelerometer, and on blade 12 for the data with the laser). Figure D.15(b) gives the corresponding error between the mistuning identified for each blade n, defined as

$$\frac{m_{ID}^{Acc}\left(n\right) - m_{ID}^{L}\left(n\right)}{\max\left(m_{ID}^{L}\right)} \,, \tag{D.1}$$

where $m_{ID}^{Acc}\left(n\right)$ refers to the mistuning of blade n obtained with the accelerometer, and $m_{ID}^{L}\left(n\right)$ refers to the mistuning of blade n obtained with the laser. Errors up to 88 % are observed.

These results show that, even if the frequencies are globally the same for the cases with a microaccelerometer and with a laser, the impact of the mode shapes differences between both cases is large. Therefore, the measurements are performed in the thesis only using laser vibrometer.

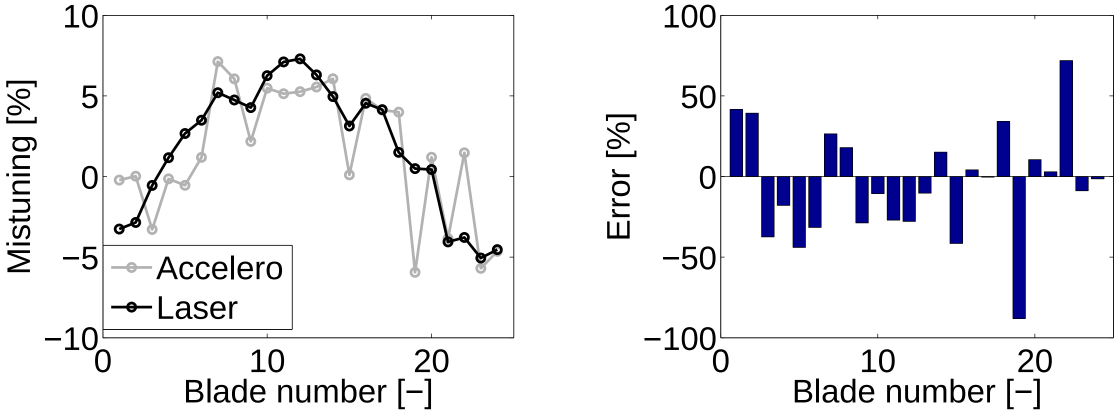

(a) (b)

Figure D.15: Comparison between the mistuning obtained with the microaccelerometer and the laser measurements (a) and the corresponding relative error (b).

Appendix E

Construction of the finite element model based on geometry measurements

In order to construct a CAD of the mono-stage and multi-stage academic structures based on the geometry measurements, different steps are followed. These steps are explained here for the multi-stage structure. The used software used for the post processing of the geometrical measurements is GOM Inspect [127], and to construct the CAD, CATIA V5 [186] is used.

The first step is to define the different geometrical points for each blade, which will be exported to CATIA. More particularly, the eight corner points are selected here, as illustrated in Figure E.1.

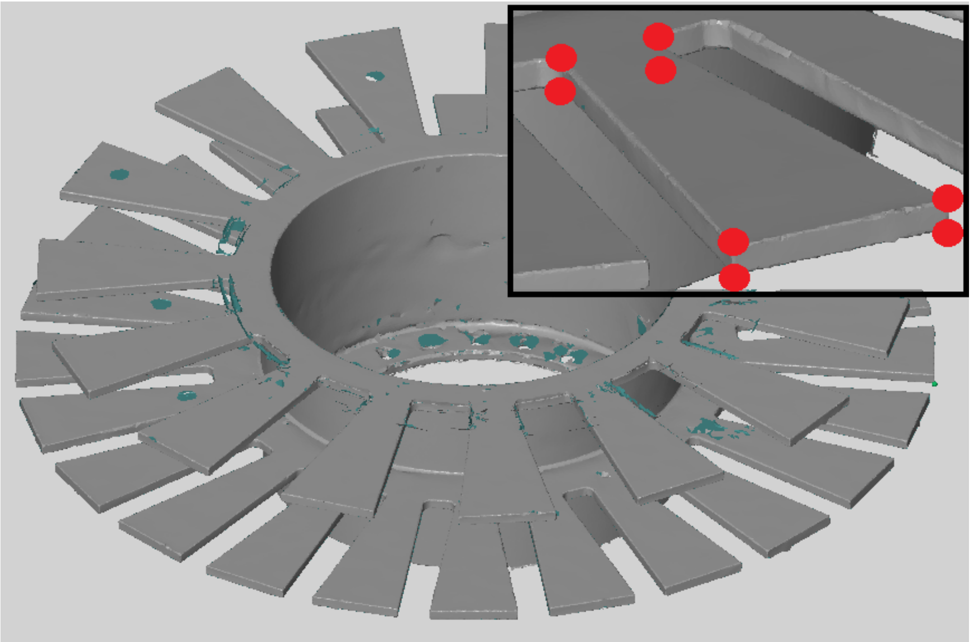

Figure E.1: Exported corner points.

In order to obtain these eight points per blade, the strategy is to generate three planes (Adjusted planes command, as shown in Figure E.2) and to get the intersections of these planes. To create an adjusted plane, the considered surface must be selected (Figure E.3) and the software will considered the best Gaussian adjustment of the selected surface.

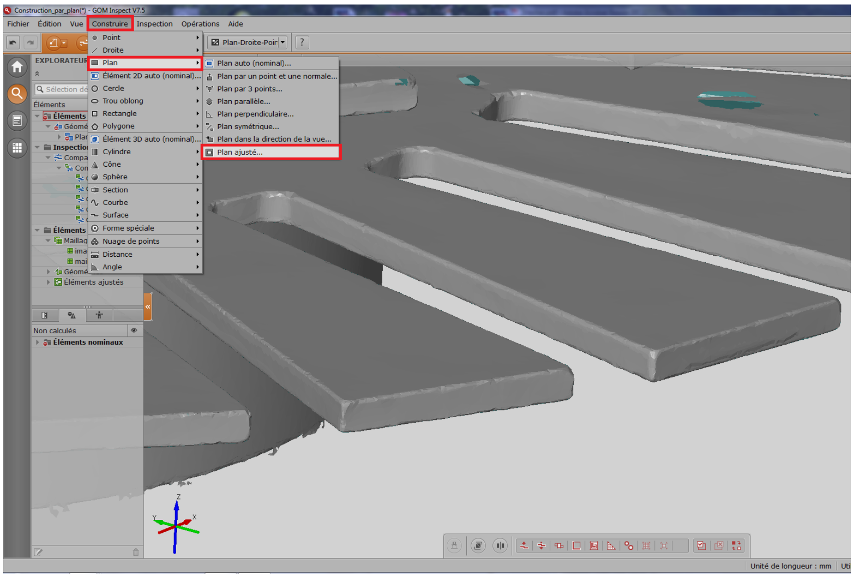

Figure E.2: Adjusted planes command.

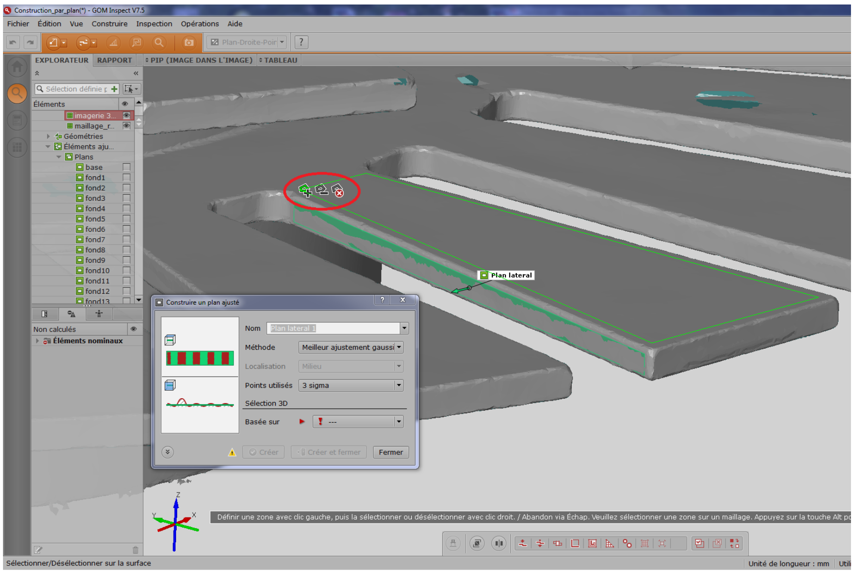

Nom: Plan lateral 1

Méthode: Meilleur ajustement gaussi

Localisation: Milieu

Points utilisés: 3 sigma

Sélection 3D

Basée sur: ---

Définir une zone avec clic gauche, puis la sélectionner ou désélectionner avec clic droit. / Abandon via Échap. Veuillez sélectionner une zone sur un maillage. Appuyez sur la touche Alt po

Figure E.3: Faces selection.

When all planes are created, the points can be generated by intersection of three planes (Figure E.4).

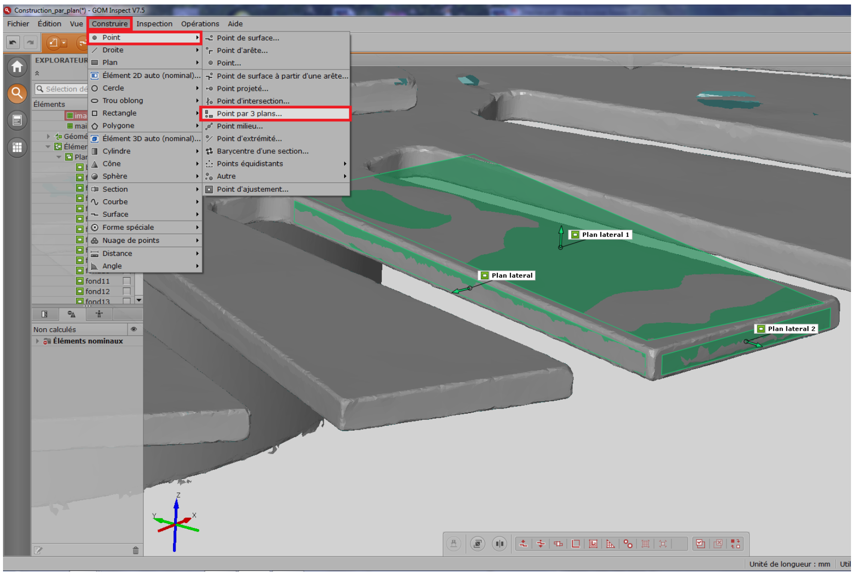

Figure E.4: Points creation by intersection of three planes.

When all points are created, a .CSV file is exported with X Y Z coordinates of each point (Figure E.5).

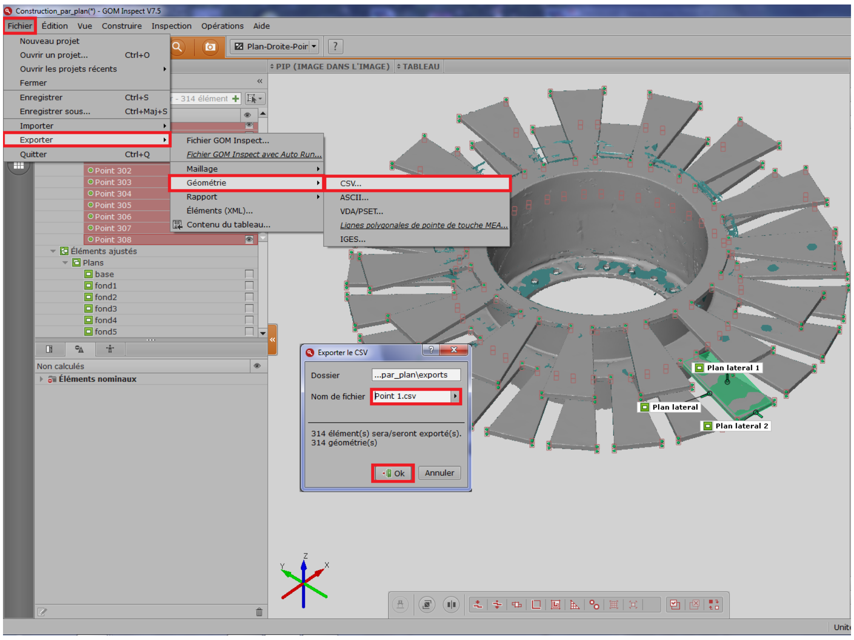

Dossier: ...par_plan\exports

Nom de fichier: Point 1.csv

314 élément(s) sera/seront exporté(s).
314 géométrie(s)

Figure E.5: Points exportation.

The points coordinates of the .CSV files can be imported in CATIA using an Excel macro (Figure E.6). The module used in CATIA for the CAD preparation is the surfacing module, "FreeStyle".

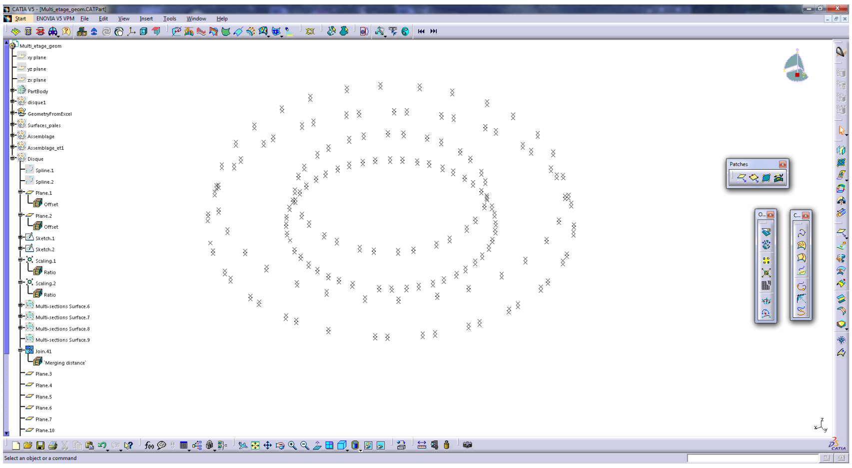

Select an object or a command

Figure E.6: Points in CATIA.

In this module, the surface generation by four points is activated (Figure E.7). This operation must be done for all blade faces i.e., six faces per blade. When all faces are generated, the blade surfaces must be assembled in the "Generative Shape Design" module.

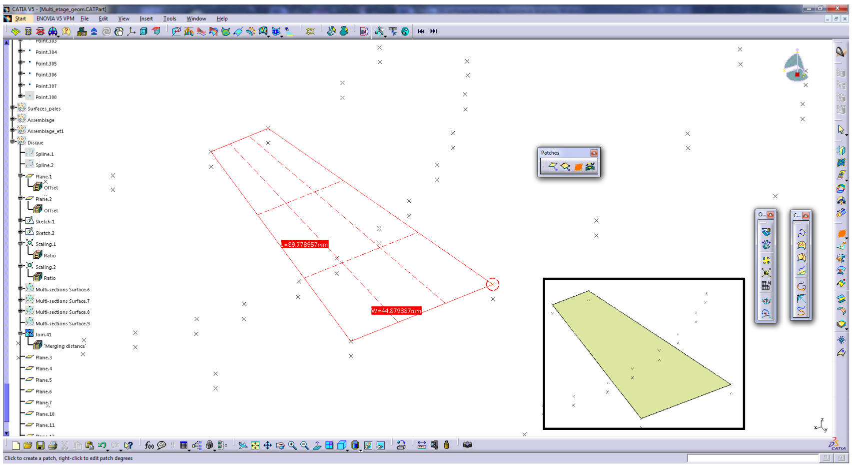

Click to create a patch, right-click to edit patch degrees

Figure E.7: Surface generation by four points.

Then, one all blade surfaces are assembled, they can be filled using the "Part Design" module (Figure E.8).

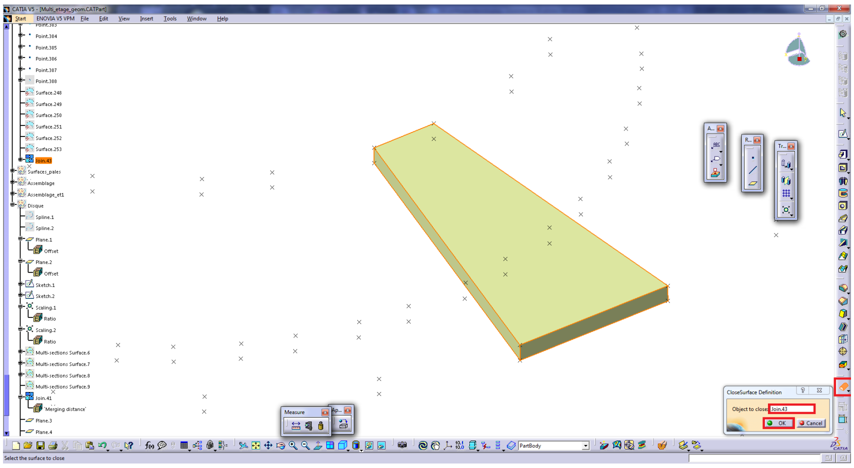

CloseSurface Definition

Object to close: Join.43

Select the surface to close

Figure E.8: Blade filling.

The horizontal part of drum is created in the "GSD" module. The drum is filled after in the "Part Design" module (Figure E.9).

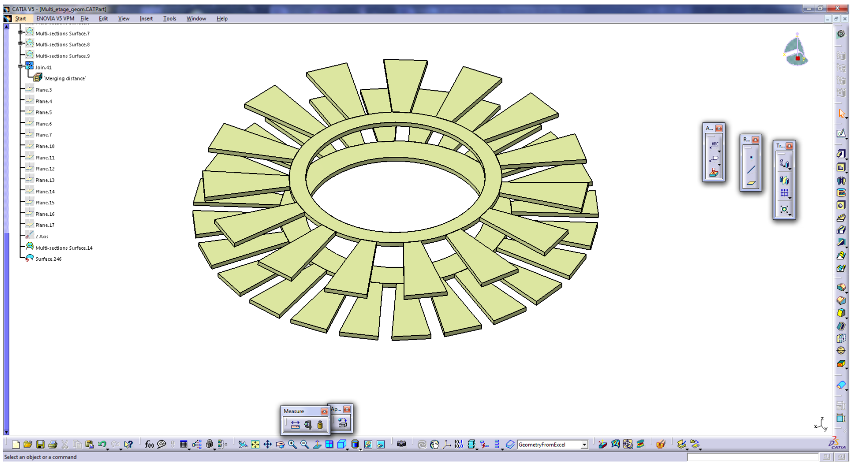

Select an object or a command

Figure E.9: Drum filling.

Then, the vertical part of the drum is created using a sketch on the mid plan of the structure. A 360 degrees revolution around the revolution axis (Z-axis) is realised with the previous sketch. Now a ”mean” CAD of the measured structure has been created (Figure E.10).

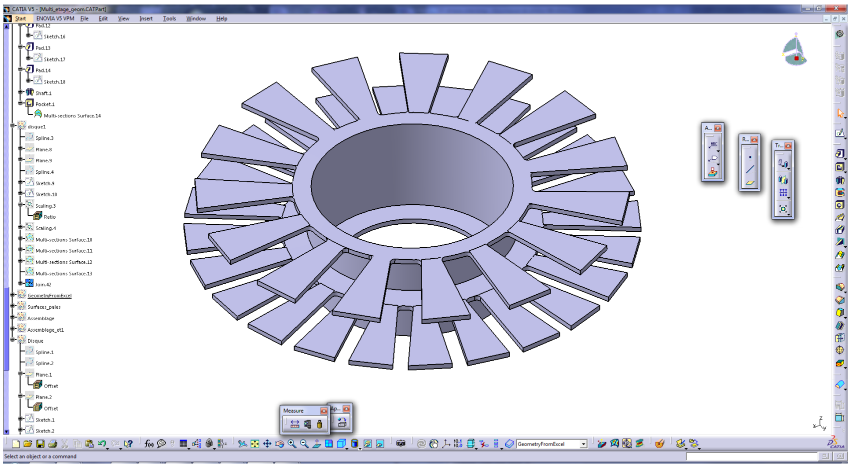

Select an object or a command

Figure E.10: Final CAD.

A refined mesh is generated for this ”mean” CAD. Hexahedral elements are used.

Finally, the coordinates of all geometrical data (Figure E.11) are exported. The elevation of the points on the skin of our finite element model is modified to follow the exact profile of the structure.

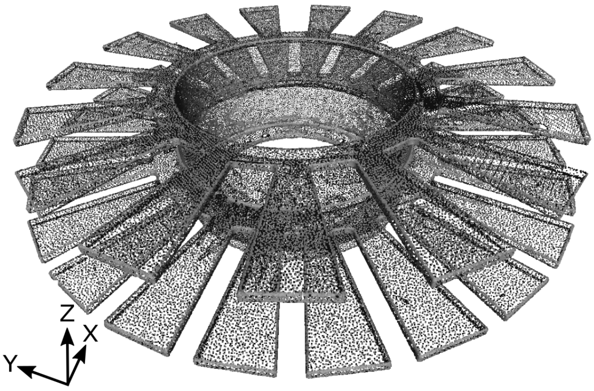

Figure E.11: Set of all geometrical data for the multi-stage structure.

Bibliography

[1] "Engine Alliance," http://www.enginealliance.com/gp7200.html.

[2] R. Bladh, M. P. Castanier, and C. Pierre, "Effects of Multistage Coupling and Disk Flexibility on Mistuned Bladed Disk Dynamics," *Journal of Engineering for Gas Turbines and Power*, vol. 125, no. 1, pp. 121–130, 2003.

[3] M. P. Castanier and C. Pierre, "Modeling and Analysis of Mistuned Bladed Disk Vibration: Current Status and Emerging Directions," *Journal of Propulsion and Power*, vol. 22, pp. 384–396, Mar. 2006.

[4] H. Irretier, "Spectral Analysis of Mistuned Bladed-Disc Assemblies by Component Mode Synthesis," in *Proceedings of the ASME 9th Biennal Conference on Mechanical Vibration and Noise*, (Fairfield, NJ, USA), pp. 115–125, American Society of Mechanical Engineers, 1983.

[5] Z.-C. Zheng and F. R. Wang, "Dynamic Analysis of Blade Groups Using Component Mode Synthesis," in *Proceedings of the ASME 10th Biennal Conference on Mechanical Vibration and Noise*, (Fairfield, NJ, USA), pp. 97–103, American Society of Mechanical Engineers, 1985.

[6] M. J. Kruse and C. Pierre, "Forced Response of Mistuned Bladed Disks Using Reduced-Order Modeling," in *Proceedings of the 37th AIAA/ASME Structures, Structural Dynamics and Materials Conference*, (Reston, VA, USA), pp. 1938–1950, 1996.

[7] M. P. Castanier, G. Òttarsson, and C. Pierre, "A Reduced Order Modeling Technique for Mistuned Bladed Disks," *Journal of Vibration and Acoustics*, vol. 119, no. 3, pp. 439–447, 1997.

[8] M.-T. Yang and J. H. Griffin, "A Reduced-Order Model of Mistuning Using a Subset of Nominal System Modes," *Journal of Engineering for Gas Turbines and Power*, 2001.

[9] R. Bladh, M. P. Castanier, and C. Pierre, "Reduced Order Modeling and Vibration Analysis of Mistuned Bladed Disk Assemblies With Shrouds," *Journal of Engineering for Gas Turbines and Power*, vol. 121, no. 3, pp. 515–522, 1999.

[10] M. P. Mignolet, A. J. Rivas-Guerra, and J. P. Delor, "Identification of Mistuning Characteristics of Bladed Disks From Free Response Data—Part I," *Journal of Engineering for Gas Turbines and Power*, vol. 123, no. 2, pp. 395–403, 2001.

[11] R. Bladh, M. P. Castanier, and C. Pierre, “Component-Mode-Based Reduced Order Modeling Techniques for Mistuned Bladed Disks—Part I: Theoretical Models,” *Journal of Engineering for Gas Turbines and Power*, vol. 123, no. 1, pp. 89–99, 2001.

[12] R. Bladh, M. P. Castanier, and C. Pierre, “Component-Mode-Based Reduced Order Modeling Techniques for Mistuned Bladed Disks—Part II: Application,” *Journal of Engineering for Gas Turbines and Power*, vol. 123, no. 1, pp. 100–108, 2001.

[13] D. M. Feiner and J. H. Griffin, “A Fundamental Model of Mistuning for a Single Family of Modes,” *Journal of Turbomachinery*, vol. 124, no. 4, pp. 597–605, 2002.

[14] S.-H. Lim, R. Bladh, M. P. Castanier, and C. Pierre, “A Compact, Generalized Component Mode Mistuning Representation for Modeling Bladed Disk Vibrations,” in *Proceedings of the 44th AIAA/ASME/ASCE/AMS Structures, Structural Dynamics, and Material Conference*, vol. 2, (Norfolk, Virginia, USA), pp. 1359–1380, 2003.

[15] S.-H. Lim, R. Bladh, M. P. Castanier, and C. Pierre, “Compact, Generalized Component Mode Mistuning Representation for Modeling Bladed Disk Vibration,” *AIAA Journal*, vol. 45, pp. 2285–2298, Sept. 2007.

[16] D. Laxalde and C. Pierre, “Modelling and Analysis of Multi-Stage Systems of Mistuned Bladed Disks,” *Computers & Structures*, vol. 89, pp. 316–324, Feb. 2011.

[17] J. A. Judge, C. Pierre, and S. L. Ceccio, “Experimental Mistuning Identification in Bladed Disks Using a Component-Mode-Based Reduced-Order Model,” *AIAA Journal*, vol. 47, pp. 1277–1287, May 2009.

[18] D. M. Feiner and J. H. Griffin, “Mistuning Identification of Bladed Disks Using a Fundamental Mistuning Model—Part I: Theory,” *Journal of Turbomachinery*, vol. 126, no. 1, pp. 150–158, 2004.

[19] D. M. Feiner and J. H. Griffin, “Mistuning Identification of Bladed Disks Using a Fundamental Mistuning Model — Part II: Application,” *Journal of Turbomachinery*, vol. 126, no. 1, pp. 159–165, 2004.

[20] M. P. Mignolet and C.-C. Lin, “Identification of Structural Parameters in Mistuned Bladed Disks,” *Journal of Vibration and Acoustics*, vol. 119, no. 3, pp. 428–438, 1997.

[21] F. Pichot, F. Thouverez, L. Jezequel, and E. Seinturier, “Mistuning Parameters Identification of a Bladed Disk,” *Key Engineering Materials*, vol. 204-205, pp. 123–132, 2001.

[22] N. E. Kim and J. H. Griffin, “System Identification in Higher Modal Density Regions of Bladed Disks,” in *Proceedings of the 8th National Turbine Engine High Cycle Fatigue Conference*, (Dayton, OH, USA), pp. 1.68–1.82, 2003.

[23] S.-H. Lim, M. P. Castanier, and C. Pierre, “Vibration Modeling of Bladed Disks Subject to Geometric Mistuning and Design Changes,” in *45th AIAA/ASME/ASCE/AHS/ASC Structures, Structural Dynamics, and Materials Conference*, (Palm Springs, California), pp. 1–20, 2004.

[24] F. Pichot, D. Laxalde, J.-J. Sinou, F. Thouverez, and J.-P. Lombard, "Mistuning Identification for Industrial Blisks Based on the Best Achievable Eigenvector," *Computers & Structures*, vol. 84, pp. 2033–2049, Nov. 2006.

[25] D. Laxalde, F. Thouverez, J.-J. Sinou, J.-P. Lombard, and S. Baumhauer, "Mistuning Identification and Model Updating of an Industrial Blisk," *International Journal of Rotating Machinery*, vol. 2007, pp. 1–10, 2007.

[26] S. H. Song, M. P. Castanier, and C. Pierre, "System Identification of Multistage Turbine Engine Rotors," in *Proceedings of ASME Turbo Expo 2007*, (Montreal, Canada), pp. 1–14, 2007.

[27] A. C. Madden, M. P. Castanier, and B. I. Epureanu, "Reduced-Order Model Construction Procedure for Robust Mistuning Identification of Blisks," *AIAA Journal*, vol. 46, pp. 2890–2898, Nov. 2008.

[28] A. Kürhborn and U. Strehlau, "Experimental and Numerical Investigations of HPC Blisks With a Focus on Travelling Waves," in *Proceedings of ASME Turbo Expo 2010*, (Glasgow, UK), pp. 1–13, 2010.

[29] C. M. Firrone and T. Berruti, "An Electromagnetic System for the Non-Contact Excitation of Bladed Disks," *Experimental Mechanics*, vol. 52, pp. 447–459, June 2012.

[30] D. Laxalde, *Etude d'amortisseurs non-lineaires appliqués aux roues aubagées et aux systèmes multi-étages.* PhD thesis, 2007.

[31] C. E. Shannon, "Communication in the Presence of Noise," *Proceedings of the IEEE*, vol. 86, pp. 447–457, Feb. 1998.

[32] M. P. Singh, "SAFE Diagram - A Dresser-Rand Evaluation Tool For Packeted Bladed Disc Assembly," in *TP025*, 1984.

[33] M. P. Singh, J. J. Vargo, D. M. Schiffer, and J. D. Dello, "SAFE Diagram-A design and reliability tool for turbine blading," in *Proceedings of the 17th turbomachinery symposium*, 1988.

[34] J.-C. Golinval, *Mechanical Design of Turbomachinery.* course not ed., 2015.

[35] J. Wildheim, "Excitation of Rotationally Periodic Structures," *Journal of Applied Mechanics*, vol. 46, pp. 878–882, 1980.

[36] J. Wildheim, "Excitation of Rotating Circumferentially Periodic Structures," *Journal of Sound and Vibration*, vol. 75, no. 3, pp. 397–416, 1981.

[37] D. J. Ewins, *Modal testing: theory, practice, and application.* Research Studies Press, second ed., 2000.

[38] D. J. Ewins, "Vibration Characteristics of Bladed Disc Assemblies," *Journal of Mechanical Engineering Science*, vol. 15, pp. 165–186, June 1973.

[39] D. J. Ewins and Z. S. Han, "Resonant Vibration Levels of a Mistuned Bladed Disk," *Journal of Vibration Acoustics Stress and Reliability in Design*, vol. 106, no. 2, pp. 211–217, 1984.

[40] J. A. Judge, C. Pierre, and S. L. Ceccio, "Experimental Validation of Mistuning Identification and Vibration Predictions in Bladed Disks," in *Proceedings of the CEAS/AIAA/AIEA International Forum on Aeroelasticity and Structural Dynamics*, (Madrid, Spain), pp. 89–98, 2001.

[41] J. A. Kenyon and J. H. Griffin, "Experimental Demonstration of Maximum Mistuned Bladed Disk Forced Response," *Journal of Turbomachinery*, vol. 125, no. 4, pp. 673–681, 2003.

[42] C. Hodges, "Confinement of Vibration by Structural Irregularity," *Journal of Sound and Vibration*, vol. 82, pp. 411–424, June 1982.

[43] D. J. Ewins, "The Effects of Detuning Upon The Forced Vibrations of Bladed Disks," *Journal of Sound and Vibration*, 1969.

[44] J. C. MacBain and P. W. Whaley, "Maximum Resonant Response of Mistuned Bladed Disks," *Journal of Vibration Acoustics Stress and Reliability in Design*, vol. 106, no. 2, p. 218, 1984.

[45] S.-T. Wei and C. Pierre, "Localization Phenomena in Mistuned Assemblies with Cyclic Symmetry Part I: Free Vibrations," *Journal of Vibration Acoustics Stress and Reliability in Design*, vol. 110, no. 4, pp. 429–438, 1988.

[46] S.-T. Wei and C. Pierre, "Localization Phenomena in Mistuned Assemblies with Cyclic Symmetry Part II: Forced Vibrations," *Journal of Vibration Acoustics Stress and Reliability in Design*, vol. 110, no. 4, pp. 439–449, 1988.

[47] S.-T. Wei and C. Pierre, "Statistical Analysis of the Forced Response of Mistuned CyclicAssemblies," *AIAA Journal*, vol. 28, pp. 861–868, May 1990.

[48] G. Òttarson and C. Pierre, "On the Effects of lnterblade Coupling on the Statistics of Maximum Forced Response Amplitudes in Mistuned Bladed Disks," in *Proceedings of the 36th AIAA/ASME/ASCE/AHS/ASC Structures*, pp. 3070–3078, 1995.

[49] F. Figaschewsky and A. Kürhborn, "Analysis of Mistuned Blade Vibrations Based on Normally Distributed Blade Individual Natural Frequencies," in *Proceedings of ASME Turbo Expo 2015*, (Montreal, Canada), pp. 1–13, 2015.

[50] C. Siewert and H. Stüer, "Forced Response Analysis of Mistuned Turbine Bladings," in *Proceedings of ASME Turbo Expo 2010*, (Glasgow, UK), 2010.

[51] M. Nikolic, *New Insights Into the Blade Mistuning Problem.* PhD thesis, Imperial College London, University of London, 2006.

[52] Y. J. Chan, *Variability of Blade Vibration in Mistuned Bladed Discs.* PhD thesis, Imperial College London, University of London, 2009.

[53] Y. J. Chan and D. J. Ewins, "A Comprehensive Procedure to Estimate the Probability of Extreme Vibration Levels Due to Mistuning," in *Proceedings of ASME Turbo Expo 2009*, (Orlando, Florida, USA), pp. 1–9, 2009.

[54] Y. J. Chan and D. J. Ewins, "The Amplification of Vibration Response Levels of Mistuned Bladed Disks: Its Consequences and Its Distribution in Specific Situations," *Journal of Engineering for Gas Turbines and Power*, vol. 133, no. 10, p. 102502, 2011.

[55] D. S. Whitehead, "The Maximum Factor by Which Forced Vibration of Blades Can Increase Due to Mistuning," *Journal of Engineering for Gas Turbines and Power*, 1998.

[56] K. R. V. Kaza and R. E. Kielb, "Flutter and Response of a Mistuned Cascade in Incompressible Flow," *AIAA Journal*, vol. 20, pp. 1120–1127, Aug. 1982.

[57] K. R. V. Kaza and R. E. Kielb, "Vibration and flutter of mistuned bladed-disk assemblies," *Journal of Propulsion and Power*, vol. 1, pp. 336–344, Sept. 1985.

[58] O. O. Bendiksen, "Aeroelastic Stabilization by Disorder and Imperfections," in *Proceedings of the XVIth International Congress of Theoretical and Applied Mechanics*, (Lyngby, Denmark), 1984.

[59] B. Shapiro, *Passive Control of Flutter and Forced Response in Bladed Disks Via Mistuning*. PhD thesis, California Institute of Technology, 1999.

[60] H. Yui, *Forced Vibration Charactheristics of Mistuned Bladed Disc Assemblies*. PhD thesis, University of London, 1995.

[61] J. H. Griffin and T. M. Hoosac, "Model Development and Statistical Investigation of Turbine Blade Mistuning," *Journal of Vibration Acoustics Stress and Reliability in Design*, vol. 106, no. 2, pp. 204–210, 1984.

[62] W. C. Hurty, "Dynamic analysis of structural systems using component modes," *AIAA Journal*, vol. 3, pp. 678–685, Apr. 1965.

[63] W. C. Hurty, J. D. Collins, and G. C. Hart, "Dynamic Analysis of Large Structures by Modal Synthesis Techniques," *Computers & Structures*, vol. 1, pp. 535–364, 1971.

[64] R. R. J. Craig and M. C. C. Bampton, "Coupling of Substructures for Dynamic Analyses," *AIAA Journal*, vol. 6, pp. 1313–1319, July 1968.

[65] R. R. J. Craig and C. J. Chang, "Free-Interface Methods of Substructure Coupling for Dynamic Analysis," *AIAA Journal*, vol. 14, pp. 1633–1635, Nov. 1976.

[66] R. R. J. Craig and C. J. Chang, "Substructure Coupling for Dynamic Analysis and Testing," tech. rep., NASA CR-2781, 1977.

[67] G. S. Òttarson, *Dynamic Modeling and Vibration Analysis of Mistuned Bladed Disks*. PhD thesis, University of Michigan, 1994.

[68] M.-T. Yang and J. H. Griffin, "A Reduced Order Approach for the Vibration of Mistuned Bladed Disk Assemblies," *Journal of Engineering for Gas Turbines and Power*, vol. 119, no. 1, pp. 161–167, 1997.

[69] E. Balmès, "Use of Generalized Interface Degrees of Freedom in Component Mode Synthesis," in *Proceedings of the 14th International Modal Analysis Conference*, (Bethel, CT), pp. 1–7, 1996.

[70] E. Balmès, "Optimal Ritz Vectors for Component Mode Synthesis Using the Singular Value Decomposition," *AIAA Journal*, vol. 34, pp. 1256–1260, June 1996.

[71] F. Bourquin and F. D'Hennezel, "Numerical Study of an Intrinsic Component Mode Synthesis Method," *Computer Methods in Applied Mechanics and Engineering*, vol. 97, pp. 49–76, May 1992.

[72] F. Bourquin and F. D'Hennezel, "Intrinsic Component Mode Synthesis and Plate Vibrations," *Computers & Structures*, vol. 44, pp. 315–324, July 1992.

[73] M. P. Castanier, Y.-C. Tan, and C. Pierre, "Characteristic Constraint Modes for Component Mode Synthesis," *AIAA Journal*, vol. 39, pp. 1182–1187, June 2001.

[74] M.-T. Yang and J. H. Griffin, "A Normalized Modal Eigenvalue Approach for Resolving Modal Interaction," *Journal of Engineering for Gas Turbines and Power*, vol. 119, no. 3, pp. 647–650, 1997.

[75] M. E. Brewer, M. P. Castanier, and C. Pierre, "Effects of Harmonic Intentional Mistuning on the Free Response of Bladed Disks," in *Proceedings of the ASME Design Engineering Technical Conferences*, (Las Vegas, Nevada), pp. 1873–1884, 1999.

[76] M. P. Castanier and C. Pierre, "Using Intentional Mistuning in the Design of Turbomachinery Rotors," *AIAA Journal*, vol. 40, no. 10, pp. 2077–2086, 2002.

[77] C. Martel, R. Corral, and J. M. Llorens, "Stability Increase of Aerodynamically Unstable Rotors Using Intentional Mistuning," *Journal of Turbomachinery*, vol. 130, no. 1, p. 011006, 2008.

[78] C. Martel and R. Corral, "Asymptotic Description of Maximum Mistuning Amplification of Bladed Disk Forced Response," *Journal of Engineering for Gas Turbines and Power*, vol. 131, no. 2, p. 022506, 2009.

[79] O. Khemiri, C. Martel, and R. Corral, "Quantitative Validation of the Asymptotic Mistuning Model Using a High Fidelity Bladed Disk Model," in *Proceedings of ASME Turbo Expo 2010*, (Glasgow, UK), pp. 1–10, 2010.

[80] E. P. Petrov, K. Y. Sanliturk, and D. J. Ewins, "A New Method for Dynamic Analysis of Mistuned Bladed Disks Based on the Exact Relationship Between Tuned and Mistuned Systems," *Journal of Engineering for Gas Turbines and Power*, 2002.

[81] E. P. Petrov, "A Method for Forced Response Analysis of Mistuned Bladed Discs with Aerodynamic Effects Included," in *Proceedings of ASME Turbo Expo 2009*, (Orlando, Florida, USA), pp. 1–12, 2009.

[82] E. P. Petrov, "Reduction of Forced Response Levels For Bladed Discs by Mistuning: Overview of the Phenomenon," in *Proceedings of ASME Turbo Expo 2010*, pp. 1–13, 2010.

[83] P. Vargiu, C. M. Firrone, S. Zucca, and M. M. Gola, "A Reduced Order Model Based on Sector Mistuning for the Dynamic Analysis of Mistuned Bladed Disks," *International Journal of Mechanical Sciences*, vol. 53, no. 8, pp. 639–646, 2011.

[84] C. Fitzner, B. I. Epureanu, and S. Filippi, "Nodal Energy Weighted Transformation: A Mistuning Projection and its Application to FLADE$^{\text{TM}}$ Turbines," *Mechanical Systems and Signal Processing*, vol. 42, no. 1-2, pp. 167–180, 2014.

[85] V. Ganine, M. Legrand, H. Michalska, and C. Pierre, "A Sparse Preconditioned Iterative Method for Vibration Analysis of Geometrically Mistuned Bladed Disks," *Computers and Structures*, vol. 87, no. 5-6, pp. 342–354, 2009.

[86] C. Soize, "A Nonparametric Model of Random Uncertainties for Reduced Matrix Models in Structural Dynamics," *Probabilistic Engineering Mechanics*, vol. 15, pp. 277–294, July 2000.

[87] E. Capiez-Lernout and C. Soize, "Nonparametric Modeling of Random Uncertainties for Dynamic Response of Mistuned Bladed Disks," *Journal of Engineering for Gas Turbines and Power*, vol. 126, no. 3, pp. 610–618, 2004.

[88] M. Mbaye, *Conception robuste en vibration et aéroélasticité des roues aubagées de turbomachines.* PhD thesis, Université Paris-Est, 2009.

[89] M. Mbaye, C. Soize, and J.-P. Ousty, "A Reduced-Order Model of Detuned Cyclic Dynamical Systems With Geometric Modifications Using a Basis of Cyclic Modes," *Journal of Engineering for Gas Turbines and Power*, vol. 132, no. 11, p. 112502, 2010.

[90] M. Mbaye, C. Soize, J.-P. Ousty, and E. Capiez-Lernout, "Robust Analysis of Design in Vibration of Turbomachines," *Journal of Turbomachinery*, vol. 135, p. 021008, Nov. 2012.

[91] A. Sinha, "Reduced-Order Model of a Bladed Rotor With Geometric Mistuning," in *Proceedings of ASME Turbo Expo 2007*, (Montreal, Canada), pp. 1–8, 2007.

[92] A. Sinha, "Reduced-Order Model of a Bladed Rotor With Geometric Mistuning," *Journal of Turbomachinery*, vol. 131, p. 031007, July 2009.

[93] V. Vishwakarma, A. Sinha, Y. Bhartiya, and J. M. Brown, "Modified Modal Domain Analysis of a Bladed Rotor Using Coordinate Measurement Machine Data on Geometric Mistuning," in *Volume 7B: Structures and Dynamics*, (San Antonio, Texas, USA), pp. 1–9, 2013.

[94] A. J. Rivas-Guerra, M. P. Mignolet, and J. P. Delor, "Identification of Mistuning Characteristics of Bladed Disks From Free Response Data— Part II," *Journal of Engineering for Gas Turbines and Power*, vol. 123, no. 2, pp. 404–411, 2001.

[95] J. A. Judge, C. Pierre, and S. L. Ceccio, "Identification of Mistuning in Blisks," in *Proceedings of the 6th National Turbine Engine High Cycle Fatigue Conference*, (Dayton, OH, USA), 2001.

[96] J. A. Judge, C. Pierre, and S. L. Ceccio, "Mistuning Identification in Bladed Disks," in *Proceedings of the International Conference on Structural Dynamics Modelling*, (Lisbon, Portugal), 2002.

[97] M. R. Rossi, D. M. Feiner, and J. H. Griffin, “Experimental Study of the Fundamental Mistuning Model for Probabilistic Analysis,” in *Proceedings of ASME Turbo Expo 2005*, (Reno-Tahoe, Nevada, USA), pp. 1–8, 2005.

[98] S.-H. Lim, *Dynamic Analysis and Design Strategies for Mistuned Bladed Disks.* PhD thesis, University of Michigan, 2009.

[99] S.-H. Lim, C. Pierre, and M. P. Castanier, “System Identification in Higher Modal Density Regions of Bladed Disks,” in *Proceedings of the 9th National Turbine Engine High Cycle Fatigue Conference*, (Dayton, OH, USA), 2004.

[100] F. Pichot, *Identification du désaccordage des disques aubagés monoblocs.* PhD thesis, Ecole Centrale de Lyon, 2002.

[101] T. W. Lim and T. A. L. Kashangaki, “Structural Damage Detection of Space Truss Structures Using Best Achievable Eigenvectors,” *AIAA Journal*, vol. 32, no. 5, pp. 1049–1057, 1994.

[102] T. W. Lim, “Structural Damage Detection Using Constrained Eigenstructure Assignment,” *Journal of Guidance, Control, and Dynamics*, vol. 18, no. 3, pp. 411–418, 1995.

[103] W. A. Benfield and R. F. Hruda, “Vibration Analysis of Structures by Component Mode Substitution,” *AIAA Journal*, vol. 9, no. 7, pp. 1255–1261, 1971.

[104] E. Capiez-Lernout, *Dynamique des structures tournantes à symétrie cyclique en présence d’incertitudes aléatoires. Application au désaccordage des roues aubagées.* PhD thesis, Université de Marne-la-Vallée, 2004.

[105] C. Soize, E. Capiez-Lernout, J.-F. Durand, C. Fernandez, and L. Gagliardini, “Probabilistic Model Identification of Uncertainties in Computational Models for Dynamical Systems and Experimental Validation,” *Computer Methods in Applied Mechanics and Engineering*, vol. 198, no. 1, pp. 150–163, 2008.

[106] Y. Bhartiya, *Single and Multi-Stage Bladed Rotors With Geometric Mistuning: Reduced Order Modeling and Mistuning Identification.* PhD thesis, The Pennsylvania State University, 2011.

[107] J. Avalos and M. P. Mignolet, “Maximum Amplification of Blade Response in Mistuned Multi Stage Assemblies,” in *Proceedings of ASME Turbo Expo 2010*, pp. 981–994, ASME, 2010.

[108] S. H. Song, M. P. Castanier, and C. Pierre, “Multi-Stage Modeling of Turbine Engine Rotor Vibration,” in *Proceedings of the International Design Engineering Technical Conferences and Computers and Information in Engineering Conference IDECT/CIE 2005*, 2005.

[109] S. H. Song, M. P. Castanier, and C. Pierre, “Multi-Stage Modeling of Turbine Engine Rotor Vibration,” in *Proceedings RTO-MP-AVT-121*, no. 2005, (Neuilly-sur-Seine, France), pp. 1533–1544, 2005.

[110] D. Laxalde, F. Thouverez, and J.-P. Lombard, "Dynamical Analysis of Multi-Stage Cyclic Structures," *Mechanics Research Communications*, vol. 34, pp. 379–384, June 2007.

[111] D. Laxalde, J.-P. Lombard, and F. Thouverez, "Dynamics of Multi-Stage Bladed Disks Systems," *Journal of Engineering for Gas Turbines and Power*, vol. 129, no. 4, pp. 1058–1064, 2007.

[112] A. Sternschüss and E. Balmès, "Reduction of Multistage Rotor Models Using Cyclic Modeshapes," in *Proceedings of ASME Turbo Expo 2007*, 2007.

[113] A. Sternschüss, E. Balmès, P. Jean, and J.-P. Lombard, "Model Reduction Applied to Multi-Stage Assemblies of Bladed Disks," in *Proceedings of ISMA Conference*, 2008.

[114] A. Sternschüss, E. Balmès, P. Jean, and J.-P. Lombard, "Reduction of Multi-Stage Disk Models : Application to an Industrial Rotor," *Journal of Engineering for Gas Turbines and Power*, vol. 131, no. 1, p. 012502, 2009.

[115] A. Sternschüss, *Multi-Level Parametric Reduced Models of Rotating Bladed Disk Assemblies.* PhD thesis, Ecole Centrale Paris, 2009.

[116] D. Laxalde, F. Thouverez, and J.-P. Lombard, "Vibration Control for Integrally Bladed Disks Using Friction Ring Dampers," in *ASME Turbo Expo 2007*, pp. 1–11, 2007.

[117] A. Sinha, "Reduced-Order Model of a Mistuned Multi-Stage Bladed Rotor," *International Journal of Turbo and Jet Engines*, vol. 25, pp. 145–154, Jan. 2008.

[118] Y. Bhartiya and A. Sinha, "Reduced Order Model of a Multistage Bladed Rotor with Geometric Mistuning via Modal Analyses of Finite Element Sectors," in *Proceedings of ASME Turbo Expo 2010*, pp. 1–10, 2010.

[119] S. H. Song, *Vibration Analysis and System Identification of Mistuned Multistage Turbine Engine Rotors.* PhD thesis, University of Michigan, 2007.

[120] "LMS SAMTECH SAMCEF: Siemens PLM Software," http://www.plm. automation.siemens.com/fr be/products/lms/samtech/.

[121] "LMS Test.Lab: Siemens PLM Software," http://www.plm.automation.siemens.com/fr be/products/ lms/.

[122] B. Peeters, H. Van der Auweraer, P. Guillaume, and J. Leuridan, "The PolyMAX frequency-domain method: a new standard for modal parameter estimation?," *Journal of Shock and Vibration*, vol. 11, no. 3-4, pp. 395–409, 2004.

[123] A. C. Madden, M. P. Castanier, and B. I. Epureanu, "Mistuning Identification of Blisks at Higher Frequencies," in *51st AIAA/ASME/ASCE/AHS/ASC Structures, Structural Dynamics, and Materials Conference*, pp. 1–10, 2010.

[124] D. E. Holland, J. R. Rodgers, and B. I. Epureanu, "Measurement point selection and modal damping identification for bladed disks," *Mechanical Systems and Signal Processing*, vol. 33, pp. 97–108, Nov. 2012.

[125] D. E. Holland and B. I. Epureanu, “A Component Damping Identification Method for Mistuned Blisks,” *Mechanical Systems and Signal Processing*, vol. 41, no. 1-2, pp. 598–612, 2013.

[126] A. Kaszynski, J. A. Beck, and J. M. Brown, “Uncertainties of an Automated Optical 3D Geometry Measurement, Modeling, and Analysis Process for Mistuned IBR Reverse Engineering,” in *Proceedings of ASME Turbo Expo 2013*, (San Antonio, Texas, USA), pp. 1–9, 2013.

[127] “GOM,” http://www.gom.com.

[128] H. Huang, Z. M. Gong, X. Q. Chen, and L. Zhou, “SMART Robotic System for 3D Profile Turbine Vane Airfoil Repair,” *International Journal of Advanced Manufacturing Technology*, vol. 21, no. 4, pp. 275–283, 2003.

[129] V. E. Garzon and D. L. Darmofal, “Impact of Geometric Variability on Axial Compressor Performance,” *Journal of Turbomachinery*, vol. 125, no. 4, pp. 692–703, 2003.

[130] A. Sinha, B. Hall, B. Cassenti, and G. Hilbert, “Vibratory Parameters of Blades from Coordinate Measurement Machine Data,” *ASME Journal of Turbomachinery*, vol. 130, no. 1, pp. 011013–1 – 011013–8, 2008.

[131] J. M. Brown and R. V. Grandhi, “Probabilistic High Cycle Fatigue Assessment Process for Integrally Bladed Rotors,” in *ASME Turbo Expo 2005*, pp. 1–9, 2005.

[132] J. M. Brown, *Reduced Order Modeling Methods for Turbomachinery Design.* PhD thesis, Wright State University, 2008.

[133] J. A. Beck, J. M. Brown, C. J. Cross, and J. C. Slater, “Probabilistic Mistuning Assessment Using Nominal and Geometry Based Mistuning Methods,” in *Proceedings of ASME Turbo Expo 2012* (ASME, ed.), pp. 1–13, 2012.

[134] F. Chen, G. M. Brown, and M. Song, “Overview of Three-Dimensional Shape Measurement Using Optical Methods,” *Optical Engineering*, vol. 39, no. 1, pp. 10–22, 2000.

[135] S. Holtzhausen, S. Schreiber, C. Schöne, R. Stelzer, K. Heinze, and a. Lange, “Highly Accurate Automated 3D Measuring and Data Conditioning for Turbine and Compressor Blades,” *ASME Turbo Expo 2009: Power for Land, Sea, and Air Volume 6: Structures and Dynamics, Parts A and B*, pp. 37–41, 2009.

[136] A. Lange, M. Voigt, K. Vogeler, H. Schrapp, E. Johann, and V. Gummer, “Impact of Manufacturing Variability and Nonaxisymmetry on High-Pressure Compressor Stage Performance,” *Journal of Engineering for Gas Turbines and Power*, vol. 134, no. 3, p. 032504 (8 pages), 2012.

[137] J. de Cazenove, S. Cogan, and M. Mbaye, “Finite-Element Modelling of an Experimental Mistuned Bladed Disk and Experimental Validation,” in *Proceedings of ASME Turbo Expo 2013*, pp. 1–10, 2013.

[138] *Centre Spatial de Liège (CSL)*, http://www.csl.ulg.ac.be/.

[139] M. Pastor, M. Binda, and T. Harčarik, “Modal Assurance Criterion,” *Procedia Engineering*, vol. 48, pp. 543–548, 2012.

[140] “LMS Samtech Boss Quattro,” http://www.plm.automation.siemens.com/fr be/products/lms/samtech/boss-quattro.shtml.

[141] C. Soize, “A Comprehensive Overview of a Non-Parametric Probabilistic Approach of Model Uncertainties for Predictive Models in Structural Dynamics,” *Journal of Sound and Vibration*, vol. 288, pp. 623–652, Dec. 2005.

[142] C. Soize, “Random Matrix Theory for Modeling Uncertainties in Computational Mechanics,” *Computer Methods in Applied Mechanics and Engineering*, vol. 194, pp. 1333–1366, Apr. 2005.

[143] M. P. Mignolet and C. Soize, “Nonparametric Stochastic Modeling of Linear Systems with Prescribed Variance of Several Natural Frequencies,” *Probabilistic Engineering Mechanics*, vol. 23, no. 2-3, pp. 267–278, 2008.

[144] C. Soize, “Stochastic Modeling of Uncertainties in Computational Structural Dynamics - Recent Theoretical Advances,” *Journal of Sound and Vibration*, vol. 332, no. 10, pp. 2379–2395, 2013.

[145] J. A. Kenyon, J. H. Griffin, and N. E. Kim, “Sensitivity of Tuned Bladed Disk Response to Frequency Veering,” *Journal of Engineering for Gas Turbines and Power*, vol. 127, no. 4, p. 835, 2005.

[146] D. Afolabi and O. Mehmed, “On Curve Veering and Flutter of Rotating Blades,” *Journal of Engineering for Gas Turbines and Power*, vol. 116, no. 3, pp. 702–708, 1994.

[147] S. Baik, M. P. Castanier, and C. Pierre, “Mistuning Sensitivity Prediction of Bladed Disks Using Eigenvalue Eigenvalue Curve,” in *The 9th National Turbine Engine High Cycle Fatigue Conference*, 2004.

[148] E. Chatelet, F. D’Ambrosio, and G. Jacquet-Richardet, “Toward Global Modelling Approaches for Dynamic Analyses of Rotating Assemblies of Turbomachines,” *Journal of Sound and Vibration*, vol. 282, no. 1-2, pp. 163–178, 2005.

[149] O. Turhan and G. Bulut, “Linearly Coupled Shaft-Torsional and Blade-Bending Vibrations in Multi-Stage Rotor-Blade Systems,” *Journal of Sound and Vibration*, vol. 296, pp. 292–318, Sept. 2006.

[150] O. Turhan and G. Bulut, “Coupling Effects Between Shaft-Torsion and Blade-Bending Vibrations in Rotor-Blade Systems,” in *Vibration Problems ICOVP 2005*, vol. 111, pp. 505–510, 2007.

[151] R. Rzadkowski and J. Sokolowski, “Coupling Effects between the Shaft and Two Bladed-Discs,” *Journal of Vibration Engineering and Technologies*, vol. 4, no. 3, pp. 249–266, 2005.

[152] R. Rzadkowski and A. Maurin, “Multistage Coupling of Eight Bladed Discs on a Solid Shaft, Part 1. Free Vibration Analysis,” in *Proceedings of ASME Turbo Expo 2012*, (Copenhagen, Denmark), pp. 1–10, ASME, 2012.

[153] B. Segui and E. Casanova, "Application of a Reduced Order Modeling Technique for Mistuned Bladed Disk-Shaft Assemblies," in *Proceedings of ASME Turbo Expo 2007*, pp. 1–11, 2007.

[154] K. X. D'Souza and B. I. Epureanu, "A Statistical Characterization of the Effects of Mistuning in Multi-Stage Bladed Disks," in *Proceedings of ASME Turbo Expo 2011*, 2011.

[155] K. X. D'Souza and B. I. Epureanu, "A Statistical Characterization of the Effects of Mistuning in Multistage Bladed Disks," *Journal of Engineering for Gas Turbines and Power*, vol. 134, no. 1, p. 012503, 2012.

[156] R. J. Guyan, "Reduction of Stiffness and Mass Matrices," *AIAA Journal*, vol. 3, pp. 380–380, Feb. 1965.

[157] O. O. Bendiksen, "Flutter of Mistuned Turbomachinery Rotors," in *Proceedings of ASME Turbo Expo 1983*, (Phoenix, Arizona, USA), pp. 1–9, 1983.

[158] D. Afolabi, "The Frequency Response of Mistuned Bladed Disk Assemblies," *Vibrations of blades and bladed disk assemblies*, pp. 15–21, 1985.

[159] E. F. Crawley and K. C. Hall, "Optimization and Mechanisms of Mistuning in Cascades," *Journal of Engineering for Gas Turbines and Power*, vol. 107, no. 2, p. 418, 1985.

[160] J. Dugundji and D. J. Bundas, "Flutter and Forced Response of Mistuned Rotors Using Standing Wave Analysis," *AIAA Journal*, vol. 22, pp. 1652–1661, Nov. 1984.

[161] A. V. Srinivasan and G. G. Tavares, "Direct Use of Unsteady Aerodynamic Pressures in the Flutter Analysis of Mistuned Blades," *Journal de Physique III*, vol. 5, no. 10, pp. 1587–1597, 1995.

[162] C.-C. Lin and M. P. Mignolet, "An Adaptive Perturbation Scheme for the Analysis of Mistuned Bladed Disks," in *ASME 1995 International Gas Turbine and Aeroengine Congress and Exposition*, 1995.

[163] T. Miyakozawa, *Flutter and Forced Response of Turbomachinery With Frequency Mistuning and Aerodynamic Asymmetry.* PhD thesis, Duke University, 2008.

[164] Y. S. Choi, S. Fleeter, and D. a. Gottfried, "Resonant Response of Mistuned Bladed Disks Including Aerodynamic Damping Effects," *Journal of Propulsion and Power*, vol. 25, no. 6, pp. 1240–1248, 2009.

[165] B. Shapiro, "Symmetry Approach to Extension of Flutter Boundaries via Mistuning," *Journal of Propulsion and Power*, vol. 14, pp. 354–366, May 1998.

[166] F. Moyroud, T. Fransson, and G. Jacquet-Richardet, "A Comparison of Two Finite Element Reduction Techniques for Mistuned Bladed-Disks," in *Volume 4: Manufacturing Materials and Metallurgy; Ceramics; Structures and Dynamics; Controls, Diagnostics and Instrumentation; Education*, (Münich, Germany), pp. 1–11, ASME, May 2000.

[167] E. P. Petrov and D. J. Ewins, "Search for the Best Blade Arrangement in a Mistuned Bladed Disc Assembly," in *7th national turbine engine high cycle fatique (HCF) conference*, (Florida, USA), 2002.

[168] G. Kahl, "Mistuning and Coupling Effect in Turbomachinery Bladings," in *Unsteady Aerodynamics, Aeroacoustics and Aeroelasticity of Turbomachines*, 2006.

[169] I. Sladojevic, E. P. Petrov, A. I. Sayma, M. Imregun, and J. S. Green, "Investigation of the Influence of Aerodynamic Coupling on Response Levels of Mistuned Bladed Discs With Weak Structural," in *Proceedings of ASME Turbo Expo 2005*, pp. 1–9, 2005.

[170] Z. He, B. I. Epureanu, and C. Pierre, "Parametric study of the aeroelastic response of mistuned bladed disks," *Computers & Structures*, vol. 85, pp. 852–865, June 2007.

[171] C. Pierre, T. E. Smith, and D. V. Murthy, "Localization of Aeroelastic Modes in Mistuned High-Energy Turbines," vol. 10, no. 3, 1991.

[172] C. Pierre and D. V. Murthy, "Aeroelastic Modal Characteristics of Mistuned Blade Assemblies - Mode Localization and Loss of Eigenstructure," *AIAA Journal*, vol. 30, pp. 2483–2496, Oct. 1992.

[173] E. Seinturier, C. Dupont, M. Berthillier, and M. Dumas, "A New Method to Predict Flutter in Presence of Structural Mistuning - Application to a wide chord fan stage," in *Symposium on Unsteady Aerodynamics, Aeroacoustics and Aeroelasticity of Turbomachines*, (Lyon, France), pp. 739–748, 2000.

[174] J. de Cazenove, S. Cogan, M. Mbaye, and M. Berthillier, "Forced Response Prediction of a Mistuned Bladed Disk in the Presence of Aeroelastic Coupling and Model Uncertainties," in *10th International Conference on Vibrations in Rotating Machinery*, pp. 281–291, Elsevier, 2012.

[175] R. E. Kielb, D. M. Feiner, J. H. Griffin, and T. Miyakozawa, "Flutter of Mistuned Bladed Disks and Blisks With Aerodynamic and FMM Structural Coupling," in *Proceedings of ASME Turbo Expo 2004*, (New York, USA), pp. 573–579, ASME, 2004.

[176] R. E. Kielb, E. Hong, K. C. Hall, and S. S. Pai, "Probabilistic Flutter Analysis of a Mistuned Bladed Disk," in *Proceedings of ASME Turbo Expo 2006*, (Barcelona, Spain), pp. 1–6, 2006.

[177] G. Dimitriadis, "Course of Aeroelasticity," tech. rep., University of Liège, 2015.

[178] D. N. Gorelov, "Vibrations of Cascade Profiles in Nonuniform Incompressible Flow," *Fluid Dynamics*, vol. 4, no. 4, pp. 19–24, 1969.

[179] A. V. Srinivasan and J. A. Fabunmi, "Cascade Flutter Analysis of Cantilevered Blades," *Journal of Engineering for Gas Turbines and Power*, vol. 106, no. 1, p. 34, 1984.

[180] M. Sadeghi and F. Liu, "Computation of mistuning effects on cascade flutter," *AIAA Journal*, vol. 39, pp. 22–28, Jan. 2001.

[181] R. E. Kielb, "Aeromechanical Design of Turbomachinery Blades," tech. rep., Duke University, 2014.

[182] R. E. Kielb and K. R. V. V. Kaza, "Effects of Structural Coupling on Mistuned Cascade Flutter and Response," in *Proceedings of ASME Turbo Expo 1983*, (Phoenix, Arizona, USA), pp. 1–8, 1983.

[183] R. E. Kielb and K. R. V. Kaza, "Effects of Structural Coupling on Mistuned Cascade Flutter and Response," *Journal of Engineering for Gas Turbines and Power*, vol. 106, no. 1, pp. 17–24, 1984.

[184] D. M. Feiner and J. H. Griffin, "A Reduced Order Model for Transient Analysis of Bladed Disk Forced Response," in *Proceedings of ASME Turbo Expo 2005*, (Reno-Tahoe, Nevada, USA), pp. 1–10, 2005.

[185] B. Peeters, J. Lau, J. Lanslots, and H. V. D. Auweraer, "Automatic Modal Analysis - Myth or Reality?," *Sound and Vibration*, vol. 3, pp. 17–21, 2008.

[186] "CATIA - Dassault Systèmes."

List of Publications

Journal articles

- F. Nyssen, B. I. Epureanu, J.-C. Golinval, "Experimental Modal Identification of Mistuning in an Academic Multi-Stage Drum", *Mechanical Systems and Signal Processing* (under review)
- F. Nyssen, J.-C. Golinval, "Identification of Mistuning and Model Updating of an Academic Blisk Based on Geometry and Vibration Measurements", *Mechanical Systems and Signal Processing*, 68-69, pp. 252-264, February 2016

Conference proceedings

- F. Nyssen, J.-C. Golinval, "Influence of the Inter-stage Coupling Flexibility on the Dynamics of Multi-Stage Rotors", *ASME Turbo Expo 2016*, Seoul, South Korea, 13 to 17 June 2016
- F. Nyssen, J.-C. Golinval, "Experimental Modal Identification of Mistuning in an Academic Blisk and Comparison with the Blades Geometry Variations", *ASME Turbo Expo 2015*, Montreal, Canada, 15 to 19 June 2015
- F. Nyssen, M. Arnst, J.-C. Golinval, "Modeling of Uncertainties in Bladed Disks Using a Nonparametric Approach", *ASME 2014 International Design Engineering Technical Conferences and Computers and Information in Engineering Conference IDETC/CIE 2014*, Buffalo, New York, USA, 17 to 20 August 2014
- F. Nyssen, M. Arnst, J.-C. Golinval, "Nonparametric modelling of multi-stage assemblies of mistuned bladed disks", *5th European Conference on Computational Mechanics*, Barcelone, Spain, 20 to 25 July 2014
- F. Nyssen, M. Arnst, J.-C. Golinval, "Towards a Nonparametric Modelling of Multistage Assemblies of Mistuned Bladed Disks", *ASME Turbo Expo 2014*, Düsseldorf, Germany, 16 to 20 June 2014 (poster)
- R. Beckers, F. Nyssen, H. Benabou, R. Viguié, J. Ligot, D. Simon, J.-C. Golinval, "Calibration of Gauges for Dynamic Strain Measurements on Compressor Bladed Disks", *ASME Turbo Expo 2014*, Düsseldorf, Germany, 16 to 20 June 2014 (poster)
- F. Nyssen, R. Viguié, D. Simon, J.-C. Golinval, "A Methodology for The Appropriation And The Isolation of Nodal Diameter Modes in Cyclic Symmetric Structures", *ASME 2013 International Design Engineering Technical Conference and Computers*

and Information in Engineering Conference IDETC/CIE 2013 - 25th Conference on Mechanical Vibration and Noise, Portland, Oregon, USA, 4 to 7 August 2013

- F. Nyssen, J.-C. Golinval, D. Simon, R. Viguié, "Excitation of nodal diameter mode-shapes of a stator ring of a turbojet engine using a limited number of excitation sources", *ASME Turbo Expo 2013*, San Antonio, Texas, USA, 3 to 7 June 2013
- F. Nyssen, J.-C. Golinval, D. Simon, R. Viguié, "Méthodologie d'excitation de modes à diamètres nodaux d'un anneau statorique de turboréacteur", *3ième Colloque "Analyse Vibratoire Expérimentale"*, Ecole Nationale d'Ingénieurs du Val de Loire (ENIVL), Blois, France, 20 to 21 November 2012